SHEAR-WAVE SPLITTING IN CROSS-HOLE SEISMOLOGY AND CHANNEL WAVES IN ANISOTROPIC WAVEGUIDES

by

Enru Liu

(B.Sc. Geological Institute, Changchun, China)

Thesis submitted for the degree of Doctor of Philosophy

Department of Geology and Geophysics

University of Edinburgh

October 1989

I hereby declare that this thesis has been composed by myself and that the work described is entirely my own unless otherwise explicitly stated in the text.

Enru Liu

To my parents and Yun

(Xiàn-géi wõ de fù-mú hé Líu Yún)

ABSTRACT

Seismic wave propagation through cracked and anisotropic media is studied using synthetic seismograms at subsurface geophones. Synthetic seismograms are calculated for three different models: shear-wave splitting in cross-hole surveys; an examination of internal interfaces on shear-wave polarizations; and modelling channel waves in anisotropic waveguides. All these studies are directly or indirectly related to subsurface observations in borehole seismology.

Firstly, the synthetic modelling of shear-wave splitting in cross-hole surveys has demonstrated that vertical seismic profiles (VSPs) are more useful and informative than cross-hole surveys for estimating azimuths, dips, and aspect ratios of near-vertically aligned fluid-filled cracks (EDA-cracks) from shear-wave data. The modelling of a small field data set further supports this conclusion.

Secondly, the study of shear-wave propagation at internal interfaces has shown that both reflected and transmitted shear-waves may be distorted. The distortion is, however, much more severe for reflection than for transmission. In the presence of anisotropy, the interfaces will only alter the polarization patterns of the shear-waves, and will not alter the (first) initial motions of shear-wave onsets since they are controlled by the symmetry of the anisotropy (the orientation of EDA-cracks). The effect of anisotropy on amplitude-versus-offset is also

demonstrated. It is suggested that surface-to-surface reflection seismics are not as informative as VSPs. This study is of interest when analyzing data from offset VSPs, cross-hole surveys and reflection surveys.

Finally, seismic wave propagation in an anisotropic waveguide is studied. The guided waves (or channel waves) can be used to detect anisotropy. Much of the work on this subject is modelling the observed channel waves data from an in-seam seismic survey. It has been found that anisotropy is characterized by the coupling of channel waves in seismograms (combined Love- and Rayleigh-motion), dispersion anomalies, and particle motion anomalies. The dispersion and particle motion anomalies cannot be explained by isotropic or transversely isotropic models with vertical symmetry axes, but can be modelled when cleat-induced anisotropy is included. We suggest that some of the observed records of hydraulic fracturing events are due to modes trapped between two or more fluid-filled fractures or treatment-induced low-velocity zones.

I speculate that study of channel waves observed in cross-hole surveys may be applied to reservoir description, and will play an important role in monitoring enhanced oil recovery (EOR) in hydrocarbon reservoirs in the future.

ACKNOWLEDGEMENTS

It is a pleasure to acknowledge the considerable debt of gratitude which I owe to my supervisor, Professor Stuart Crampin. This thesis could certainly never have been conceived without Stuart's constant enthusiastic support, constructive criticisms and for encouraging me to travel and finding funds for me to do so, and above all, his patience in improving my English which made this research possible. I consider myself very lucky to have had Stuart as a supervisor.

I thank Dr Chris W. Browitt, head of the Global Seismology Research Group (GSRG) of the British Geology Survey (BGS), who allowed me to use all the facilities in his group. I also thank Professor Ken M. Creer, my University supervisor for accepting me as a student in his department. David Booth helped me many times throughout my first year and discussed problems during the course of this thesis. David B. Taylor and Bob McGonigle helped me using the ANISEIS modelling package. Russ Evans, Charlie Fyfe, John Lovell, Colin MacBeth, Angela McCluskie (GSRG secretary), Phil Wild, and others in the GSRG also helped me whenever there was a problem. The friendly assistance of the staff of the NERC Computer Service in Edinburgh is gratefully acknowledged.

I am also indebted to Peter Jackson and Bruce Roth of the British Coal Corporation, who provided the data for Chapter 4 and Chapter 6, respectively. I thank Bruce for patiently answering my queries. Colin MacBeth kindly allowed me to use his time series analysis program, from which the dispersion analysis in Chapter 6 was made possible.

I must thank David Booth, Gerhard Graham, John Lovell, Colin MacBeth, and Gareth Yardley, who found their valuable time to read and comment on the manuscript. The postgraduate students in BGS gave me constant advice, suggestions, criticism and support: Iain Bush, Dave Campden, Scot Fraser, Gerhard Graham, Heiner Igel, Lou Min, Shiela Peacock, Gareth Yardley, and Li Xiang-yang. I thank in particular Iain and Heiner for numerous discussions.

My postgraduate studentship was financed by the State Educational Committee of the People's Republic of China and the British Council through the Technology Cooporation Awards, which also supported me to attend the 57th Annual International Meeting of the Society of Exploration Geophysicists (SEG) in New Orleans, October 1987, and the 10th, 11th, 12th and 13th United Kingdom Geophysical Assemblies. I thank in particular the staff of the Educational Section of the Chinese Embassy in London and the staff of the British Council in Edinburgh for their help. American Geophysical Union (AGU) and BGS financed my attendance at the 3rd International Workshop on Seismic Anisotropy in Berkeley, California, June 1988. Edinburgh Anisotropy Project (EAP) supported my attendence at the 51st Annual International Meeting of the European Association of Exploration Geophysicists (EAEG) in Berlin, West Germany, June 1989.

Last, but certainly not least, I thank my parents, my brothers and particularly my wife Liu Yun for their constant support and encouragement. Yun also typed part of this thesis. This work would never have been completed without their help.

CONTENTS

CHAPTER 1

INTRODUCTION

"There was initially no way here. It is the footsteps of many people that have formed and widened the path." [*Lu Xun, a modern Chinese writer (1936)*].

1.1 Seismic anisotropy

Ten years ago, Bamford and Crampin (1977) wrote in the preface to a special issue of the *Geophysical Journal* entitled "Seismic anisotropy - the state of the art": *"It is difficult to find more than a passing reference to seismic anisotropy, variously described as aeolotropy and transverse isotropy, in standard seismological texts."* They predicted that *" ... with the increasing resolution of seismic observations, the general neglect of anisotropy must disappear."* Because of lack of observations, Bamford and Crampin were only able to refer to observations of upper mantle anisotropy with the focus on the oceanic upper mantle. Ten years later, Crampin (1987a) was able to claim that anisotropy is a universal phonomenon in the rocks of the Earth. Neglect of anisotropy has finally disappeared in both earthquake and exploration seismology.

Seismic anisotropy in the Earth's rocks may commonly arise as a consequence of stress-aligned micro-cracks, pores or discontinuities (large fractures) in the top 10 to 20 km of the Earth. The earthquake process, fluid transport in geothermal and hydrocarbon reservoirs, and in nuclear waste depositions are all closely tied to the presence of fractures, especially aligned cracks (reviewed in

Chapter 2). Studies of shear-wave propagation through such crack-related anisotropic media have shown that a small degree of anisotropy along the propagation path would in principle result in separation or splitting between shear-waves polarized parallel to and perpendicular to the faces of the aligned cracks. Shear-wave polarizations are also found to be sensitive to the degree and symmetry or orientation of the anisotropic system. Detecting and measuring shear-wave splitting caused by this crack-induced anisotropy offers the possibility of obtaining detailed information about the internal structure and the stress fields of crustal rocks. This phenomenon has particular interest in the exploitation of hydrocarbon reservoirs, where natural fractures are important in production.

1.2 An outline of the work in this thesis

Construction of synthetic seismograms plays an important role in modern seismology. Comparison of synthetics to observed seismograms may help us fully understand wave propagation in the real Earth. In this thesis, we study the propagation of seismic waves through cracked anisotropic media using synthetic seismograms. This work involves the calculation using synthetic seismograms in three different situations; each of which is related or partially related to subsurface observations in borehole seismology, particularly wave propagation in horizontal or near-horizontal planes. The work covered in this thesis falls into three parts:- (a) a synthetic seismogram study of shear-wave splitting in cross-hole surveys (Chapter 3) and a particular simple example examined in Chapter 4,

(b) an examination of internal interfaces on shear-wave polarizations, both transmission and reflection are studied (Chapter 5), and (c) a study of channel waves in anisotropic waveguides in coal seams (Chapter 6) and in cracked reservoirs (Chapter 7).

We begin in Chapter 2 by a general review of the recent advance and development in seismic anisotropy. We will focus on cracked-induced anisotropy and the hypothesis of *extensive-dilatancy anisotropy* (*EDA*). The causes of crustal anisotropy and fluid inclusions in the Earth's crust are discussed. We introduce the Hudson crack model and the ANISEIS fullwave modelling package, which we will use in this thesis.

Chapter 3 describes the synthetic modelling of shear-wave splitting in cross-hole surveys. The important conclusion of this study is that vertical seismic profiles (VSPs) are more useful and informative than cross-hole surveys for estimating azimuths, dips, and aspect ratios of near-vertical cracks from shear-wave data. We provide observations of shear-wave splitting in cross-hole surveys in Chapter 4. Shear-wave splitting is observed and modelled by a simple arrangement of source and geophones in an anisotropic model.

Chapter 5 is a theoretical consideration of shear waves at a single interface. Both transmission and reflection are studied. This is very important because both are frequently encountered in offset VSPs, reflection seismics and cross-hole surveys. It is suggested that reflection seismics are not as informative as VSPs, and there are some difficulties in analyzing shear-wave reflection data in the presence of anisotropy.

Chapter 6 is a study of seismic wave propagations in an anisotropic waveguide. The trapped channel waves (or guided waves) are used to detect cleat-induced anisotropy in coal seams. It shows that coal seams are usually cracked and hence are effectively anisotropic to seismic wave propagation. Anisotropy is characterized by coupling of channel-wave in seismograms, dispersion anomalies, particle motion anomalies and amplitude anomalies. A possible application of the channel wave analysis is studied for a cracked reservoir in Chapter 7. We suggest that some of the observed records of hydraulic fracturing events are due to the trapped modes in either two-fracture formed waveguides or treatment-induced low-velocity zones (LVZ).

Finally, some discussion, suggestions and possible future applications are presented in Chapter 8. Three appendices discuss some special topics, which are related to the major parts of this thesis, and can be regarded as an additional work. The main substance of this thesis has appeared in the following papers: Liu, Crampin and Booth (1989) has been published, Liu and Crampin (1989) has been submitted, and Liu, Crampin and Roth (1989a) has been presented at 51st EAEG Meeting in Berlin, F.R.Germany in June 1989, and (1989b) is in preparation. The first paper was also presented at 57th SEG Meeting in New Orleans, USA in October 1987.

1.3 The most frequently used abbreviations and notations in the text

AVO - Amplitude-versus-offset.

CD or ε - Crack density.

CDP - Common-depth point, a method in reflection seismics.

CHS - Cross-hole survey or inter-well survey

c_{ijkl} - Elastic tensor.

EDA - Extensive-dilatancy anisotropy.

EOR - Enhanced oil recovery

IMOVSP - Inverse multi-offset vertical seismic profile.

LVZ - Low-velocity zone.

NMO - Normal moveout.

PD - Polarization diagram.

ρ - density

Q - Attenuation quality factor.

qP - quasi longitudinal or P-wave.

$qS1$, $qS2$ - Faster and slower split shear-waves.

qSR, qSP - Two split shear-waves at right angle to, and perpendiculat to the plane through crack normal.

R - Radial component

R_{SH}, R_{SV} - Reflection coefficients of SH- and SV-waves.

$SH45SV$ - A shear-wave with equal amplitudes of SH- and SV-waves (polarization angle $\psi = 45°$).

T_{SH}, T_{SV} - Transmission coefficients of SH- and SV-waves.

T - Transverse component

V - Verical component

V_P, V_S - P- and shear-wave velocities in an isotropic medium.

VSP - Vertical seismic profile.

ψ - Polarization angle

λ, μ - Lamé constants in an isotropic medium.

2G - Second generalized channel (surface) wave mode in an *anisotropic* medium, corresponding to the fundamental mode of Love channel (surface) wave in an *isotropic* medium.

CHAPTER 2

SHEAR-WAVE SPLITTING AND EXTENSIVE-DILATANCY ANISOTROPY: A GENERAL REVIEW

In this Chapter, we review some of the recent advances in seismic anisotropy with the focus on shear-wave splitting and the hypothesis of *extensive-dilatancy anisotropy*. Hudson's crack theory and the ANISEIS modelling package, which we will use in this thesis are introduced. This Chapter serves as the introduction of the basic theory of this thesis.

2.1 Shear-wave splitting: the basic theory

Any homogeneous uniform material whose physical properties vary with direction is anisotropic, and its elastic behaviour with respect to appropriate seismic wavelengths can be described by effective elastic constants in one of a range of anisotropic systems. The general theory of wave motion in anisotropic elastic solid is well documented (Love 1944; Musgrave 1954; Duff 1960; Lighthill 1960; Kraut 1963; Dieulesaint and Royer 1980). Crampin (1977, 1981) gives a comprehensive review of seismic wave propagation in anisotropic media.

The equations of motion for waves propagating with infinitesimal displacement in a purely anisotropic medium are expressed as:

$$\rho \partial^2 u_i / \partial t^2 = c_{ijkl} \partial^2 u_k / (\partial x_j \partial x_l); \qquad i, j, k, l = 1,2,3 \qquad (2\text{-}1)$$

where ρ is the density; u_k is the component of displacement in the k-th direction; c_{ijkl} is the forth order tensor of elastic constants; and the suffix summation convention is understood. The elastic tensor c_{ijkl} has the following symmetries: $c_{ijkl} = c_{ijlk} = c_{klij}$. There are 21 elastic constants to describe an elastic system for most general form of rock anisotropy or the most general orientation. Anisotropic systems with fewer than 21 elastic constants occur most commonly mentioned by Crampin (1981). Such symmetrical systems include the monoclinic with 13, orthorhombic with 9, tetragonal and trigonal with 6 (or 7), hexagonal with 5, cubic with 3, and isotropic with 2 independent elastic constants.

Equation (2-1) is a set of three second order differential equations. We now look for a solution in the form of a progressive wave with the slowness vector $\mathbf{q} = (1/V,0,0)$ of a plane wave propagating in the x_1 direction:

$$u_i = u_i^{\circ} F(t - x_1/V), \tag{2-2}$$

In order to calculate the phase velocity V and the wave polarizarion u_i° (the particle displacement direction), we insert (2-2) into the propagation equation of motion (2-1), denoting by F'' the second derivative of F:

$$\partial^2 u_i/\partial t^2 = u_i^{\circ} F'',$$

and

$$\partial^2 u_k/\partial u_j \partial u_l = u_k^{\circ} F''/V^2,$$

so

$$\rho u_i^{\circ} = c_{ilkl} u_k^{\circ}/V^2, \tag{2-3}$$

We introduce a second rank tensor

$$\Gamma_{ik} = c_{ilkl}, \tag{2-4}$$

and the above equation, known as Christoffel equation, becomes

$$\Gamma_{ik} u_k^{\circ} = \rho V^2 u_i^{\circ}, \tag{2-5}$$

The direction dependent velocity and particle displacement can be found by solving the characteristic equation of (2-5)

$$|\Gamma - \rho V^2 \mathbf{I}| = 0, \tag{2-6}$$

for eignvalue ρV^2, $\mathbf{I}$ is identity matrix.

This shows that the polarization u_i° is an eigenvector of the Γ_{ik} tensor with eigenvalue ρV^2. It is easy to prove that the eigenvalues are real and positive (see Dieulesaint and Royer 1980), there are generally three waves with different velocities along any direction of phase propagation, and mutually orthogonal polarizations. These waves correspond to a quasi *P*-wave, *qP*, with approximately longitudinal particle motion, and two quasi shear-waves, *qS1* (faster) and *qS2* (slower), with approximately transverse particle motions (Figure 2.1). The distinct feature of wave propagation in anisotropic media can be immediately seen to be *shear-wave splitting*, where a shear-wave propagation through anisotropic media splits into two components with orthogonal vector displacements (polarizations) travelling at different phase velocities. Both velocities and displacements are fixed for the particular raypath through the anisotropic symmetry system. The

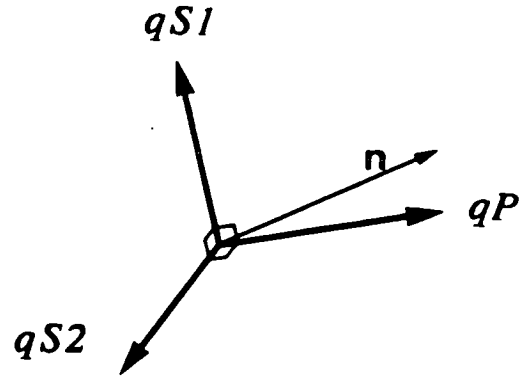

Figure 2.1 In a crystal (an anisotropic medium) the mutually orthogonal polarizations of the three waves can propagate in a given directions **n**, each with its own velocity. The wave whose displacement is closest to **n** is called quasi-longitudinal (*qP*). Its velocity is usually greater than that of the other two waves (quasi-shear waves denoted by *qS1* and *qS2*).

polarization directions and the time delay between two split shear-waves provide constraints on the orientation of the principal axes of strain and the degree of anisotropy. This phenomenon is also known as *shear-wave birefringence* or *double refraction* (similar to the birefringence of light in optics). Figure 2.2 shows a schematic illustration of the shear-wave splitting. The splitting has inserted into the three-dimensional (3D) particle motion characteristic waveforms, which are preserved for any subsequent propagation through isotropic rocks.

2.2 Shear-wave splitting in the Earth's crust

2.2.1 Observations of shear-wave splitting

The theory outlined above shows that shear-wave splitting is a diagnostic feature of some form of seismic anisotropy (its degree and symmetry). Shear-wave splitting was first reliably identified in a series of papers about Turkish-Dilatancy Projects (Crampin *et al.* 1980, 1985; Booth *et al.* 1985; Crampin and Booth 1985). However, after only a few years, this has been confirmed to exist everywhere, wherever a three-component seismometer is used, both in exploration seismics (Major *et al.* 1985; Alford 1986; Becker and Pereberg 1986; Crampin *et al.* 1986; Leary and Li 1986; Li *et al.* 1986; Johnston 1986; Lynn and Thomsen 1986; Willis *et al.* 1986, and others presented at the SEG Summer Workshop in Utah 1989), and in earthquake seismology (reviewed by Crampin 1987; Lovell *et al.* 1989). Previous studies have also suggested that the upper mantle is anisotropic to seismic surface waves (Hess 1964; Bamford *et al.* 1979; Christensen and Salisbury 1979; Crampin and King 1981;

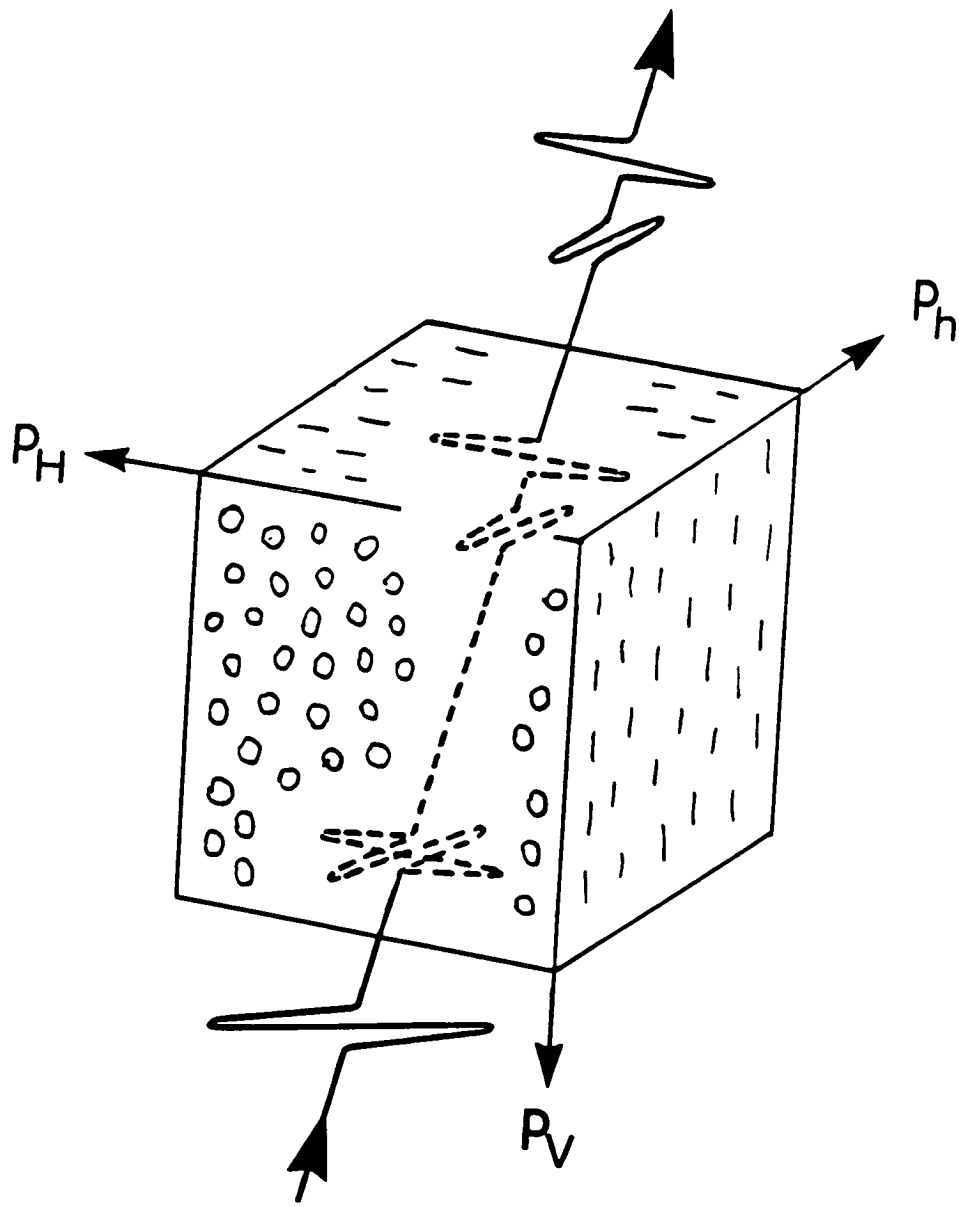

Figure 2.2 Schematic illustration of shear-wave splitting in aligned EDA cracks. The cracks are aligned by the typical stress relationships in the subsurface crust. P_V, P_H, and P_h are the vertical, maximum, and minimum horizontal compressional stresses, respectively. P_V and P_H are at least two or three times greater than P_h.

Kirkwood and Crampin 1981b). Very recently, it has been suggested that the Earth's inner core is also anisotropic (Shearer *et al.* 1988; Sayers 1989). Above all, it is not surprising to suggest that almost the whole Earth is anisotropic.

2.2.1 Causes of seismic anisotropy

Anisotropy in the Earth may arise for several different reasons, but in general, it can be attributed to layering, preferred mineral orientation, lithologically aligned crystals and aligned pores or cracks in the rock mass. The latter is most commonly invoked to explain field observations. Crampin *et al.* (1984a) has described the causes of seismic anisotropy in detail. Booth (1982) and Peacock (1986) have also given comprehensive reviews. I shall briefly summarize these as follows.

(a) Aligned crystals

Crystalline anisotropy occurs when the individual crystals in a crystalline solid have preferred orientations over a volume sufficiently large to affect the transmission of seismic waves (Babuska 1984). Such anisotropy (caused by minerals such as olivine or orthopyroxene) has been widely used to explain the observations in the upper mantle (Hess 1964; Francis 1969; Ave'Lallemant and Carter 1970; Peselnick and Nicolas 1978; Christensen and Salisbury 1979; Fuchs 1983; Silver and Chan 1988).

(b) Lithological anisotropy

A sedimentary solid has lithological anisotropy when the individual grains, which may or may not be elastically anisotropic, are elongated or flattened and these shapes are aligned by gravity or fluid flow when the material is first deposited, or by plastic

deformation thereafter (Crampin *et al.* 1984). Lithological anisotropy has been observed in shales by Kaarsberg (1960); Robertson and Corrigan (1983); White *et al.* (1983); Banik (1984) and Peacock and Crampin (1985), in clays by Puzyrev *et al.* (1984) and Brodov *et al.* (1984), in submarine turbidities by Davis and Clowes (1986).

Peacock (1986) uses the term *intrinsic anisotropy* to cover both crystalline and lithological anisotropy, which are inherent in a rock itself and continuous at all length scales greater than the size of the grain (Crampin *et al.* 1984a), and independent of external conditions such as stress. Direct stress-induced anisotropy can also be classified as intrinsic (Crampin *et al.* 1984a).

(c) Long-wavelength anisotropy

Long wavelength anisotropy occurs when propagation through arrangements of isotropic layers of isotropic blocks may be simulated by propagation through a structurally simpler anisotropic solid. Periodic thin-layers (PTL) or finely layered media are examples of this kind of anisotropy. PTL-anisotropy is widely assumed in sedimentary basins by exploration seismologists. It has also been observed in marine sediments and in calcareous sediments (Johnson *et al.* 1977). The theory is well established (Postma 1955; Helbig 1958; Backus 1962; Levin 1978; Berryman 1979; Helbig 1984). This is sometimes refered to as transverse isotropy with a vertical symmetry axis (Levin 1978; Helbig 1984; Crampin 1986).

(d) Crack-induced anisotropy

When an isotropic rock contains a distribution of inclusions, such

as dry (vapour or gas-filled) or fluid-filled cracks or pores which have preferred orientations, the resulting material will have effective seismic anisotropy. Such crack-induced anisotropy has now been used to explain all the phenomena in the crust (such as the universality and uniformity of the alignment of the faster split shear-waves) which cannot be explained or are only partly explained by other types of anisotropy (Crampin 1987a). It is, therefore, considered to be the most important cause of crustal anisotropy. The remainder of this Chapter is dedicated to a detailed discussion.

The success in modelling the Paris Basin VSP data leads Bush and Crampin (1987) to the conclusion that sedimentary rocks with finely layered structures are cracked and hence have orthorhombic symmetry. In such a medium, shear-waves are not necessarily parallel to the strike of the cracks (Crampin 1988, 1989) due to the effects of shear-wave singularities.

2.3 EDA, fluid and micro-inclusions in the Crust

Observation of shear-wave splitting above small earthquakes in many parts of the world show that most *in situ* rocks in the Earth's crust contain a distribution of stress-aligned fluid-filled cracks or microcracks. Such distributions of aligned cracks are effectively anisotropic to seismic waves (Crampin 1978) and the phenomenon is called *extensive-dilatancy anisotropy* or *EDA* (Crampin *et al.* 1984b; Crampin 1985a; Crampin and Atkinson 1985). Almost all the observations can now be interpreted according to the hypothesis of extensive-dilatancy anisotropy with a few exceptions. Under the right conditions for recording, it is expected that there will be no example of shear waves that do not split.

One of the important causes of extensive-dilatancy anisotropy is the exsistence of fluid inclusions in crustal rocks. EDA-cracks (fluid-filled microcracks, cracks, and pores with preferred orientations) aligned by the contemporary stress fields appear to exist in most rocks in the Earth's crust (Crampin *et al.* 1984b; Crampin 1985a; Crampin and Atkinson 1985). The cracks are either induced by subcritical crack growth of existing cracks in the presence of nonlithostatic stresses (Atkinson 1982, 1984), or opened by horizontal lithostatic stresses resulting from the motion of plates and possibly modified by local tectonic conditions (Nur and Simmons 1969). Prograde metamorphic processes release chemically bound water from most mineral grains within the rockmass (Fyfe *et al.* 1978) and the only way that such water can be released into an intact rock is by hydraulic fracture at high pore pressures into initially-isolated inter- and intra-granular microcracks. Such microfractures are aligned by similar processes that aligned large industry-generated hydraulic fractures which, below the top few hundred metres, usually take up near-parallel near- vertical orientations perpendicular to the minimum horizontal compressional stress. Prolonged metamorphism may lead to the development of large water-filled fractures, as was found down to 12km in the Kola Deep Hole where abundant heavily mineralized water-filled fractures were found at levels (8 km) where the maximum horizontal compressional stress was greatest (Crampin 1985a). The orthogonal minimum horizontal stress at 8 km depth would be much less than the vertical stress, and the fractures would be aligned parallel and vertical.

Lovell *et al.* (1989) give a comprehensive review of this subject. A paper by Hyndman and Shearer (1989) reviews the evidence for water in the lower crust based on magnetotelluric and seismic reflection data.

2.4 Applications and significance

(a) Estimating stress orientation and earthquake prediction

In tectonically active regions where the orientation of the contemporary stress field is known (Major *et al.* 1988; Chen *et al.* 1987; Peacock *et al.* 1988) the polarization of the faster shear-wave is parallel to the maximum principal horizontal stress inferred from independent evidence. Conversely, analysis of shear-wave splitting may help to determine the stress direction in areas where it is not known (Li *et al.* 1988). Distributions of stress-aligned fluid-filled microcracks must be universally expected in the crust. Such EDA-cracks may be modified and manipulated by stress changes, which are suggested to be the main driving mechanisms for many of the large variety of precursors that are intermittently observed before earthquakes. The cracks are aligned by contemporary tectonic stress, and it is expected that changes in the geometry of EDA-cracks may indicate changes of the stress field before earthquakes. The most direct effects of changes of stress are modifications of the configurations of the EDA-cracks in the stressed rockmass. Since the behaviour of shear waves is controlled by three-dimensional variations in the crack geometry, it is hoped that analysis of shear-wave splitting could lead to direct determinations of changes in the crack configuration and hence stress changes, and thus it potentially offers a new technique for the earthquake prediction (Crampin *et al.* 1984b, 1987).

The changes in crack geometry (aspect ratio) before and after earthquakes have recently been reported in several areas including the Anza seismic gap, California (Peacock *et al.* 1988; Crampin *et*

al. 1989), the North Anatolian Fault, Turkey (Chen *et al.* 1987), and Arkansas (Booth *et al.* 1989).

(B) Predicting orientations of industry-generated hydraulic fractures

The orientations of shear-aligned EDA-cracks, which may be estimated by analysis the waveforms and polarizations of shear-waves, predict the orientation of any subsequence hydraulic fractures. This has been confirmed at the hot-dry-rock geothermal experiment in Cornwall (Roberts and Crampin 1986). Crampin and Booth (1989) recently report that the hydraulic pumping dilates pre-existing joints in the *in situ* granite.

(c) Estimating internal structure of hydrocarbon reservoirs

Detailed analysis of shear waveforms in three-component shear-wave vertical seismic profiles yields accurate estimates of the internal structure throughout the rockmass surrounding the well (Crampin *et al.* 1986). This is a new source of direct interpretation, which is suggested to be important for the appraisal and evaluation of hydrocarbon reservoirs and for optimizing production strategies for secondary and tertiary recovery. Analysis of shear-wave anisotropy can also provide information about lithology (Winterstein 1984).

(d) Investigating coal mines

Investigation of such cracks by monitoring shear-waves is likely to yield detailed informaton about stress fields in coal mines. It is necessary to estimate overburden fracture density in order to optimize the use of expensive mining equipment in open-cast mining. Recording shear waves with three-component geophones in cross-hole

or VSPs as appropriate, should yield detailed estimates of crack geometry and crack density. An example of using channel waves to identify cleat-induced anisotropy in coal seams will be given in Chapter 6.

There are many other applications and implications of EDA hypothesis (Crampin 1987a), most of which are being investigated. Crampin (1985b) claims that a shear wavetrain contains at least three or four times more information about the structures along raypath than the equivalent *P*-wave train, and it is clear that monitoring shear waves has a great potential for many Earth Science investigations.

2.5 Hudson crack theory and ANISEIS package

Wave propagation in anisotropic media is substantially different from propagation in isotropic media and many effects (such as velocity variations, polarization anomalies, and shear-wave splitting) occur. It is thus necessary to obtain a full understanding of wave propagation in anisotropic media. The most important and effective way at present is the use of synthetic seismograms. This thesis is aimed at using synthetic modelling using ANISEIS modelling package in order to detect any possible anisotropy and to interpret any observed phenomenon. Anisotropy is simulated by Hudson's formulation for aligned cracks in an isotropic matrix rock.

2.5.1 Hudson's crack theory

Several theories have been developed to calculate the effective elastic constants of media containing aligned circular penny-shaped cracks, including Eshelby (1957); Anderson *et al.* (1974); Garbin and

Knopoff (1973a, b, 1975); O'Connell and Budiansky (1974); Budiansky and O'Connell (1976); Hudson (1980b, 1981) and Nishizawa (1982) and others. They all assume that the dimension of the cracks are small with respect to the seismic wavelengths. Garbin and Knopoff (1973, 1975a, b) derived a first order approximation theory. Hudson (1980b, 1981) developed more general formulations (first-order perturbation, 1981 and second-perturbation, 1980b) for the scattering of seismic waves with wavelength much greater than the crack dimensions by distribution of penny-shaped aligned cracks, either empty (dry) or containing fluid (saturated). We will therefore refer to as Hudson-cracks (also referred as EDA-cracks or Crampin-cracks). Hudson expressed the elastic constants of a medium containing aligned cracks by:

$$c_{ijkl} = c_{ijkl}^{0} + \varepsilon c_{ijkl}^{1} + \varepsilon^2 c_{ijkl}^{2} \qquad (2\text{-}7)$$

The crack density ε is defined number of cracks in a unit volume (Budiansky and O'Connell 1976). c_{ijkl}^{0} are the elastic constants of un-cracked rock; εc_{ijkl}^{1} and $\varepsilon^2 c_{ijkl}^{2}$ are the first and second-order perturbations due to cracks, which are given explicitly by Crampin (1984). The results may be formulated so that real parts model the velocity variation of body waves and imaginary parts attenuation (Crampin 1981). This allows wave propagation through a two-phase cracked solid to be modelled by wave propagation through a homogeneous anisotropic material with complex elastic constants.

Although Hudson originally claimed that his theory is only valid for small aspect ratios, after an extensive comparison with Nashizawa's (1982) cracks which are assummed to be valid for any aspect ratio (from thin flat cracks through circular pores to

elongated needle- shaped pores), Douma (1988) was able to show that Hudson-theory is valid for the aspect ratio up to 0.3 for weak anisotropy (crack density up to 0.06). He finally suggested that in the modelling of real data one may use Hudson-cracks, even if the aspect ratios are not expected to be small, because of its simple analytical forms and possibility of studying wave attenuation effects (due to scattering), which cannot be done with Nishizawa cracks. Recently, group theory has been used to formulate the elastic constants in cracked media (Schoenberg and Douma 1988; Schoenberg and Muir 1989). The results from this theory are in general consistent with Hudson theory (Schoenberg and Douma 1988).

Note that the Hudson's crack theory has been recently further developed by Hudson (1986, 1988). Peacock (1988) and Xu and King (1988) have been testing this widely-used theory in laboratory experiments, and have shown some consistent results.

2.5.2 ANISEIS modelling package (Taylor 1987)

ANISEIS is a flexible interactive computer modelling system for calculating synthetic seismograms from point sources in plane-layered anisotropic and cracked media. It can accomodate a variety of model structures such as vertical seismic profiles, surface to surface reflections, and cross-hole surveys. The adopted reflectivity technique and propagator matrix method are employed in ANISEIS to generate synthetic seismograms in vertically inhomogeneous anisotropic and isotropic models (the reflectivity technique only allows plane horizontal layers). The theory is based on the method developed by Crampin (1970); Crampin and Taylor (1971); Taylor and Crampin (1978). The anisotropic reflectivity technique has been extended by Booth and Crampin (1983a, b). The

propagator matrix method can be found to include anisotropic layers in Crampin (1970); Keith and Crampin (1977a, b, c). ANISEIS offers a variety of point sources and great flexibility in the choice of integration methods both for integration over slowness in the vertical plane and over azimuth in the horizontal plane. Hudson's crack formulations are adapted in ANISEIS for the calculation of synthetic seismograms in cracked media. The cracks are defined by radius, crack density, aspect ratio, and the content of the cracks, which can be either isotropic or anisotropic (Taylor, McGonigle, and Crampin, personal communications).

It is worthing noting that the reflectivity technique is a fullwave modelling technique, *i.e.* not only body waves, but also interface, surface, channel, or any non-geometrical inhomogeneous waves can be included. Such non-geometrical inhomogeneous waves can only be treated by ray methods with some difficult specific modifications (Çerveny 1979). Another disadvantage of the ray method is that it is invalid near caustics, such as shear-wave singularities, and a special treatment has to be introduced (Chapman and Shearer 1989). Such treatments have not yet been developed for the most common singularity, the point singularity. Other modelling techniques, such as finite difference and finite element methods, have also been developed to consider anisotropy, but require large computer storages and are very costly in computer time.

CHAPTER 3

SHEAR-WAVE SPLITTING IN CROSS-HOLE SURVEYS: I, SYNTHETIC MODELLING

[The contents of this Chapter have been published as "Shear-wave splitting in cross-hole surveys: Modeling", by E.Liu, S.Crampin and D.C.Booth in *Geophysics*, 54, 57-65, 1989.]

3.1 Introduction

In Chapter 2 we reviewed the observations of shear-wave splitting in the crust. However, all published records of shear-wave splitting at present involve shear waves generated, recorded, or both generated and recorded at the free surface (such as surface-to-surface reflection surveys, surface-to-subsurface VSPs, and subsurface-to-surface earthquake records). Shear waves, however, may suffer severe scattering both at the free surface and by irregular topography within a wavelength or two of the recording site (Evans 1984; Booth and Crampin 1985). In principle, cross-hole surveys (CHSs) or inter-well seismics, where both source and receiver are subsurface, should be free of many of the difficulties associated with long raypaths and near-surface interference when shear waves are either generated or recorded at the surface (Fehler and Pearson 1984). CHSs should allow shear-wave splitting to be monitored along shorter raypaths at higher frequencies; the resulting shorter wavelengths would increase the resolution with which we could specify the effective anisotropy of EDA cracks within

the rockmass. Such information might not be of direct use in discovering new reservoirs, but should enable fractured beds and the structure of EDA cracks to be identified in known reservoirs and some of the parameters estimated so that the internal structure could be evaluated.

This Chapter will focus on the synthetic modelling in order to compare CHSs with VSPs in extracting information about crack-induced anisotropy. The next Chapter will show some observations.

3.2 Cross-hole seismology in crystalline rocks

Cross-hole seismology has been used to study the seismic and mechanical properties of rocks *in situ*. Bois *et al.* (1972) have used well-to-well measurements for determining compressional velocities in sedimentary rocks. McCann *et al.* (1975, 1986) and Thill (1978) have used inter-borehole acoustic measurements for site investigations in engineering geology. Paulsson and King (1980) have linked variations in seismic velocities of granite to microcrack closure caused by thermal stress. Fehler (1981), Aki *et al.* (1982), and Fehler and Pearson (1984) have studied the effects of heat extraction and hydraulic fracturing on granite in a geothermal site using cross-hole seismic observations. An attenuation study was also made by Fehler and Pearson (1984). Wong *et al.* (1983) have successfully used cross- hole seismic tomographic images to trace a fracture zone between two boreholes separated by 175 metres and their results are very successful. The cross-hole tomographic image technique they applied was based on isotropic

structures. High frequency cross-hole surveys have been very successful in the past few years. However, they are all based on cross-hole seismic images, waveform analysis, or attenuation studies. Since most cross-hole surveys are carried out in crystalline rocks, anisotropy must be expected.

By comparison with vertical seismic profiles and reflection seismics, the major distinction in surveying is that the raypaths for VSPs and reflection surveys are usually within $\pm 45°$ of the vertical (often much closer to vertical); in such cases, the seismic waves have small incidence angles at receivers, so the analysis of the shear-wave motions should be confined to the horizontal plane. The raypaths for CHSs are usually within $\pm 45°$ of the horizontal, and in such cases, the seismic waves arrive at relatively large incidence angles, so it is insufficient to analyze the shear-wave motions only in the horizontal plane, and both horizontal and vertical motions should be considered. Figure 3.1 is a schematic illustration of typical VSPs with near and far offsets and CHSs. The difference between them may require different field techniques and different schemes of analysis when surveying vertically oriented cracks. We shall examine the behaviour of shear waves propagating through cracked rock by analyzing shear-wave splitting on synthetic seismograms along horizontal and nearly horizontal raypaths. This may be compared with the modelling by Crampin (1985b, 1987b) of shear-waves VSPs, where the propagation paths are vertical or nearly vertical.

3.3 Shear-waves with near vertical propagation: characteristics of polarization alignments

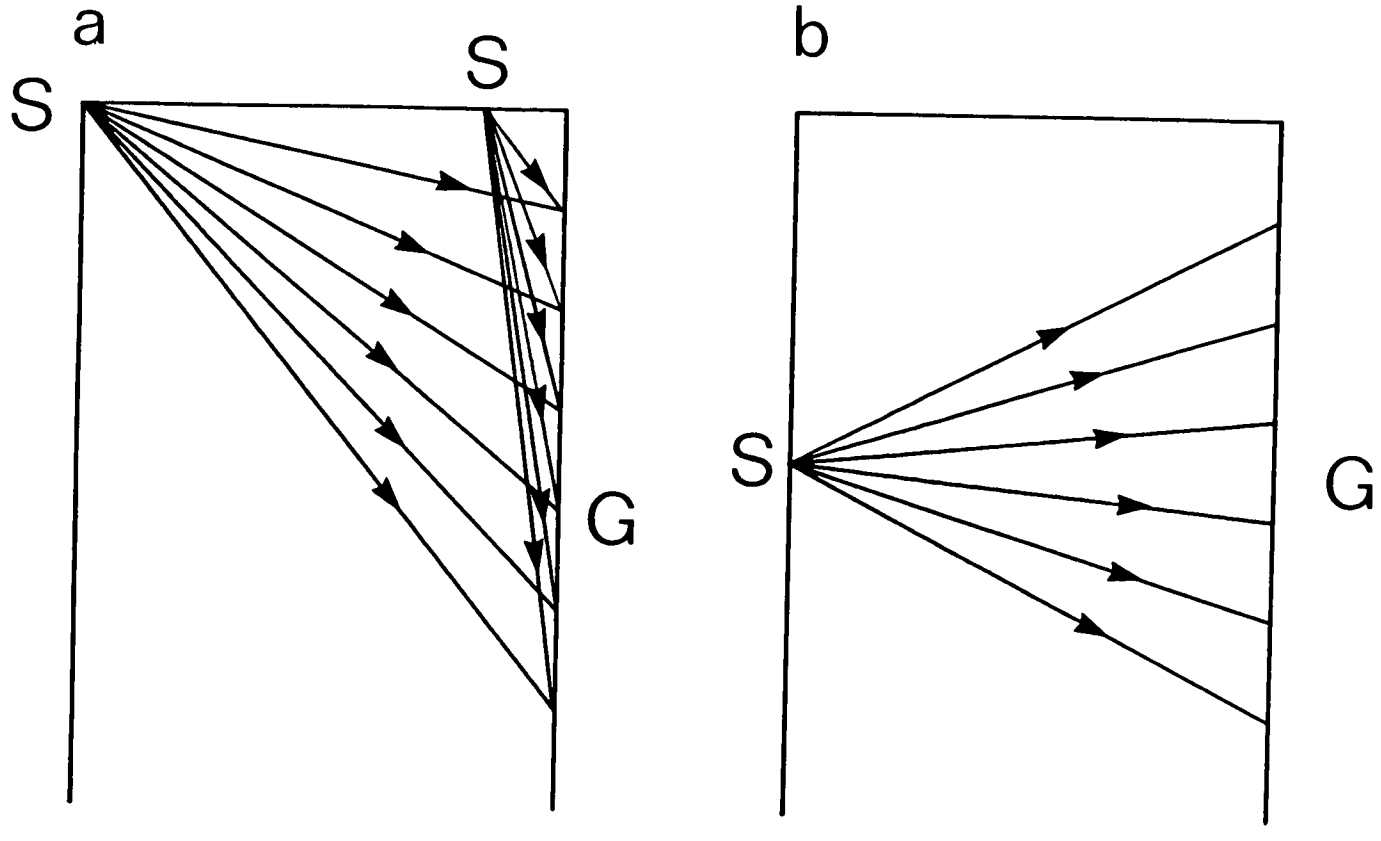

Figure 3.1 Schematic illustration of typical (*a*) VSP and (*b*) CHS surveys (S = Source position, G = Geophone position).

We consider a cracked rock where the dimensions of the cracks are several times smaller than the wavelengths of the shear waves. This is only a small restriction, as the minimum wavelength of observed shear-waves is usually measured in metres (often many tens of metres) and EDA cracks are expected to be principally microcracks with dimensions less than a few mm, or at most open fractures of length one or two metres (Crampin 1987a). A shear-wave propagating nearly vertically through EDA cracks splits into two phases with polarizations parallel and perpendicular to the face of the cracks. The phase with polarization parallel to the cracks meets less acoustic impedance, so travels faster and is less attenuated than the phase with polarizations normal to the crack face. Note that splitting does not occur when the incident shear-wave is polarized parallel (or perpendicular) to the crack face, when only the faster (or slower) phase is excited. When the slower shear wave is excited, additional motion orthogonal to the expected polarizations occurs, behaviour which has been observed on many occasions.

3.3.1 Velocity variation

Figure 3.2 shows the velocity variations of body waves propagating through distributions of thin parallel liquid-filled cracks or EDA-cracks with two crack densities. The elastic constants are listed in Table 3.1. The crack densities are defined by $\varepsilon = CD = Na^3/v$, where N is the number of cracks of radius a in volume v. Figure 3.2a shows the velocity variations for $CD = 0.1$, where the velocity anisotropy is large enough for the group and phase velocities to be clearly separated and a line singularity [cusp where the two shear-wave velocity surfaces intersect (Crampin and Yedlin 1981)] in group velocity is marked with an arrowhead; Figure 3.2b shows the velocity variations for $CD = 0.04$, which is a crack density commonly

Table 3.1 Elastic constants of two materials used in the text

Isotropic matrix rock $V_P = 4.0$, $V_S = 2.309$km/s, $\rho = 2.3\text{gcm}^{-3}$

HAS01 ($CD = 0.1$)

$c_{1111} = 35.628$, $c_{2222} = c_{3333} = 36.670$

$c_{1122} = c_{1133} = 11.864$, $c_{2233} = 12.124$

$c_{3131} = c_{1212} = 9.781$ Pascals x 10^9

HAS04 ($CD = 0.04$)

$c_{1111} = 36.326$, $c_{2222} = c_{3333} = 36.747$

$c_{1122} = c_{1133} = 12.117$, $c_{2233} = 12.222$

$c_{3131} = c_{1212} = 11.191$ Pascals x 10^9

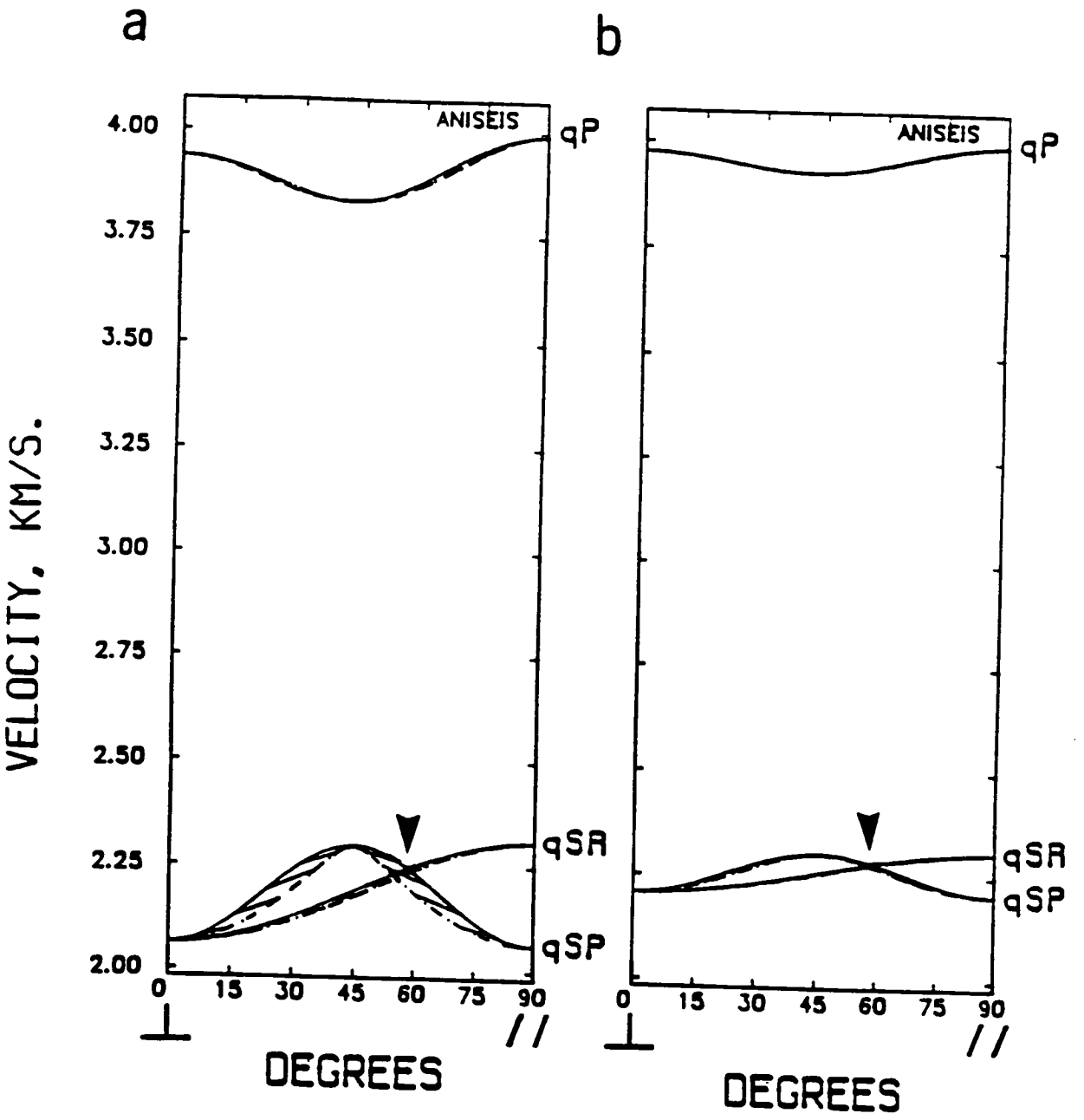

Figure 3.2 Velocity variations of the three body waves [quasi *P*-wave *qP* and quasi *S*-waves (parallel *qSP* and right angle *qSR*)] propagating through distributions of thin parallel liquid-filled cracks in an isotropic rock with velocities V_P = 4.0 and V_S = 2.309 km/s. The propagation directions range from perpendicular (0°) to parallel (90°) to the cracks. The solid lines are the phase velocities and broken lines are the group velocities which are joined to the equivalent phase velocity at every 10° of phase velocity. Arrowheads mark directions where the two velocity surfaces intersect in line singularities. Crack densities are (*a*) CD = 0.1; and (*b*) CD = 0.04.

found in the Earth in sedimentary (Crampin *et al.* 1986), metamorphic (Crampin and Booth 1985), and igneous rocks (Roberts and Crampin 1986). A crack density of 0.04 is equivalent to a crack with a diameter less than 0.7 in each unit cube. This is comparatively weak anisotropy. The three body-waves are a quasi *P*-wave, *qP*, with nearly longitudinal displacement, and two quasi shear-waves, *qSP* and *qSR*, polarized (**P**)arallel, and at (**R**)ight angles, respectively, to the plane through the crack normals.

It is noted that in nearly horizontal propagation of seismic waves through vertically aligned cracks with a horizontal symmetry axis, such modelling is for transversely isotropic medium. The simple model we use here is to demonstrate how shear-wave splitting behaves in cross- hole surveys.

3.3.2 Equal-area projections and polarization alignments

The behaviour of shear-wave splitting along nearly vertical raypaths can be conveniently specified by mapping the polarizations and delays between the split shear waves in equal-area projections (polar maps) over an upper or lower hemisphere of directions. Thus, Figure 3.3a shows a polar map of the horizontal strike of the polarization of the leading (faster) shear-wave for a hemisphere of directions of plane waves propagating through parallel vertical liquid-filled cracks. The cracks strike east-west and have the same crack density as for Figure 3.2b. Figure 3.3a shows that the polarization of the leading shear-wave is parallel to the strike of the cracks for a broad band of directions across the centre of the projection, as suggested by Figure 2.2 (Chapter 2). The abrupt change in polarization either side of the central band is caused by the intersection of the velocity curves of the two shear-wave

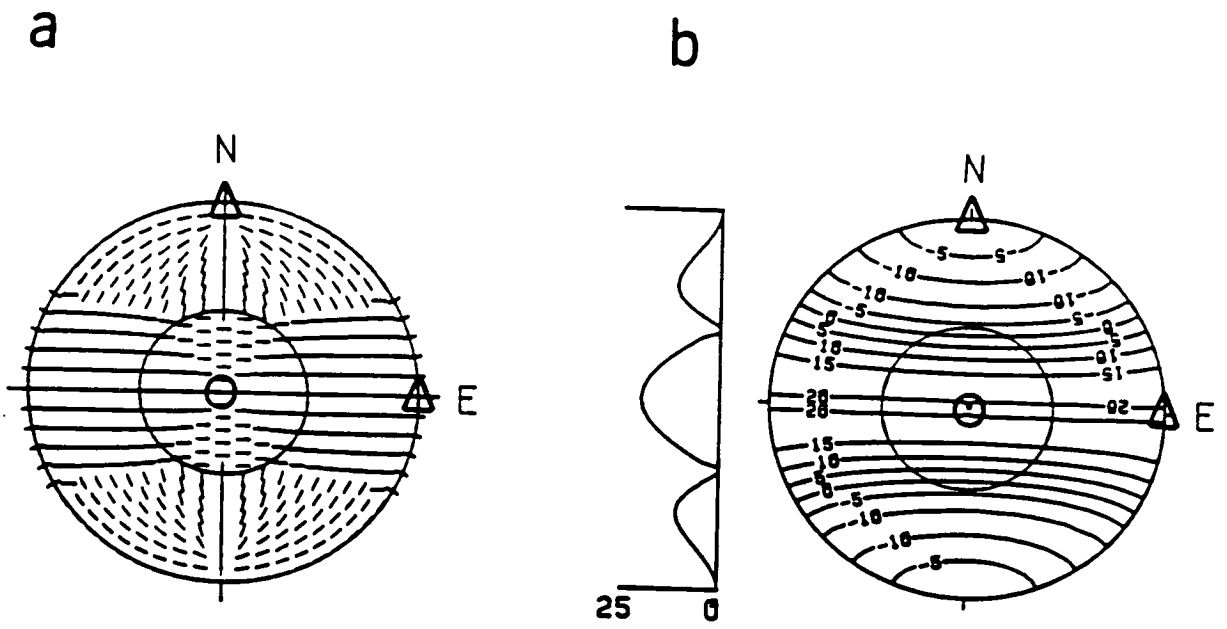

Figure 3.3 Polar equal-area projections over a hemisphere of directions of the (*a*) polarizations in the (R)adial-(T)ransverse plane and (*b*) time delays of plane split shear-waves propagating at the group (ray) velocity through the thin parallel liquid-filled cracks of Figure 3.2b ($CD = 0.04$) aligned vertically and striking east-west. The inner circles mark the shear-wave windows at the free surface at $\arcsin(V_S/V_P) = 35.26°$ and are marked as a scale. The bars in (*a*) are the horizontal components of the displacements of the leading (faster) split shear-wave, and the time delays between the split shear-waves in (*b*) are contoured in milliseconds for a normalized pathlength of 1 km. A north-south section of the delays is to the left of the contour plot. Values for vertical directions are circled, and values for horizontal north and horizontal east are marked with triangles.

polarizations at about 60° from the crack normal (about 30° from the vertical) marked by arrowheads in Figure 3.2. Figure 3.3b shows contoured delays between the split shear-waves for a normalized pathlength. Such polar projections, although suitable for specifying the behaviour of shear waves along raypaths within ±45° of the vertical, are not appropriate for describing the behaviour of shear waves along the more nearly horizontal raypaths expected in CHSs (the raypaths in CHSs are expected to cross the edge of the equal-area projections).

The remarkable feature of shear-wave splitting in parallel vertical cracks displayed in these polar projections is that the faster shear-wave is polarized parallel to the strike of the vertical cracks for a broad band of directions across the centre of the projection, including almost the whole of the shear-wave window [about 35° at the free surface (Booth and Crampin 1985)]. This diagnostic feature is seen in almost all observations of shear waves along nearly vertical raypaths in the crust (Crampin 1987a). The time delays between the split shear-waves reach maximum values in the same broad band. We shall see that CHS experiments in similar crack distributions do not display such diagnostic phenomena.

3.4 Shear-wave with near horizontal propagation: characteristics of polarization variations with direction

3.4.1 Plate Carée projections

The behaviour of shear-wave splitting in CHSs is displayed by cylindrical projections of the polarizations and delays over a full range of raypaths (360° of azimuth and dips from +90° downwards to -90° upwards). Note that such projection is also suitable for

wide-offset VSPs. Figure 3.4 shows Plate Carée cylindrical projections (equal steps of latitude and longitude) of the particle polarizations of the leading split shear-wave to subsurface geophones in (a) horizontal (**R**)adial and (**T**)ransverse and (b) (**V**)ertical and (**T**)ransverse cross-sections for $CD = 0.1$. Thus, Figure 3.4 shows the polarizations of the leading shear-wave arrivals radiating from a point source as seen by (a) horizontal instruments and (b) vertical and transverse instruments on the walls of a cylinder. The cylinder has then been opened out. (Figure 3.4 is a cylindrical map of the radiation in all directions from a point source, whereas Figure 3.3 is a polar map of one hemisphere). Figure 3.4c shows contours and Figure 3.4d, sections of delays between the split shear-waves for plane waves propagating at the group (ray) velocity through the same parallel vertical liquid-filled cracks striking east-west with a crack density of $CD = 0.1$ as in Figure 3.2a.

Figure 3.5 shows the same variations as Figure 3.4 for the smaller crack density of $CD = 0.04$ as in Figure 3.2b. The principal effect of the reduced crack density is the smaller time-delays in Figure 3.5c and 3.5d. There are also minor differences between the shapes of the contours caused by the differences between the variations of group velocity seen in Figures 3.2a and 3.2b. Figure 3.6 shows polarizations and delays of shear waves propagating through the same cracks as Figure 3.5 but with the plane of the cracks dipping at 70°.

3.4.2 Polarization variation with direction

The variations with direction of the polarizations and delays in Figures 3.5 and 3.6 show distinctive patterns in which the

Figure 3.4 Cylindrical projections of the polarizations and time delays of the split shear waves propagating through the thin parallel liquid-filled cracks of Figure 3.2*a* ($C\Delta$ = 0.1) aligned vertically and striking east-west, for the full range of raypath directions from upward (-90°) to downward (90°) to a geophone with azimuths of 0° to 360° east of north (clockwise from north). Polarizations of the leading split shear waves are projected onto (*a*) horizontal, marked (R)adial and (T)ransverse and (*b*) (V)ertical and (T)ransverse cross-sections for a fixed amplitude of displacement. The length of the symbol indicates the amplitude of a normalized leading split shear wave for the appropriate direction. Values for horizontal north and horizontal east are marked with triangles corresponding to the triangle in Figure 3.3. Values for vertical directions (circled in Figure 3.3) lie along the -90° dip coordinates in Figure 3.3. Time delays in (*c*) are contoured in milliseconds for a normalized pathlength of 1 km, and the cross-sections of the contours in (*d*) are at the five specified azimuths in (*c*).

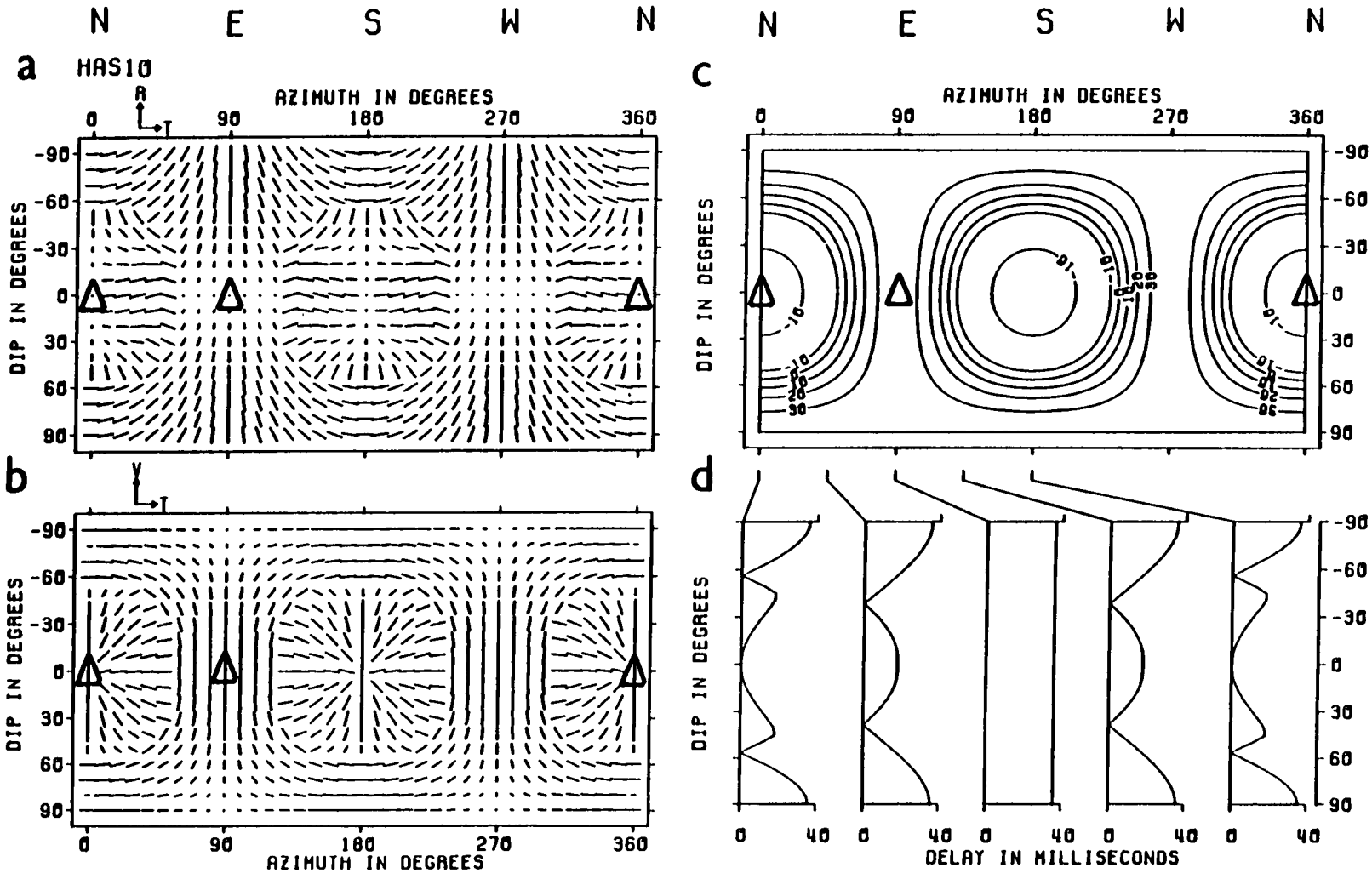
N E S W N
N E S W N
a HAS10
b
c
d
AZIMUTH IN DEGREES
DIP IN DEGREES
DELAY IN MILLISECONDS
0 90 180 270 360
-90 -60 -30 0 30 60 90
0 40

Figure 3.4

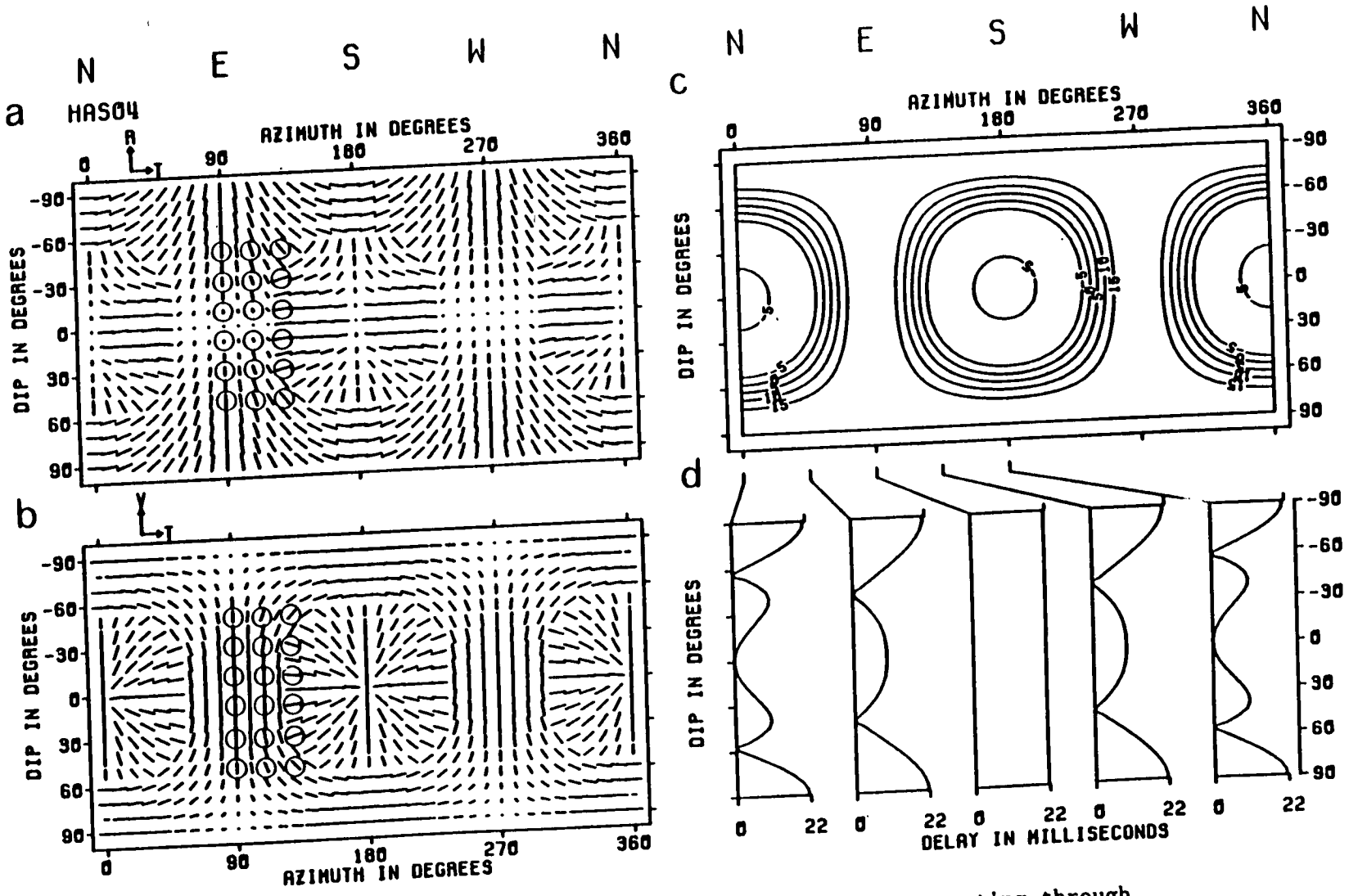

Figure 3.5 Cylindrical projections for shear waves propagating through the thin parallel vertical cracks of Figure 3.2*b* for a crack density of $CD = 0.04$. The circles mark the directions of propagation of the synthetic seismograms in Figure 3.7. Notation as in Figure 3.4.

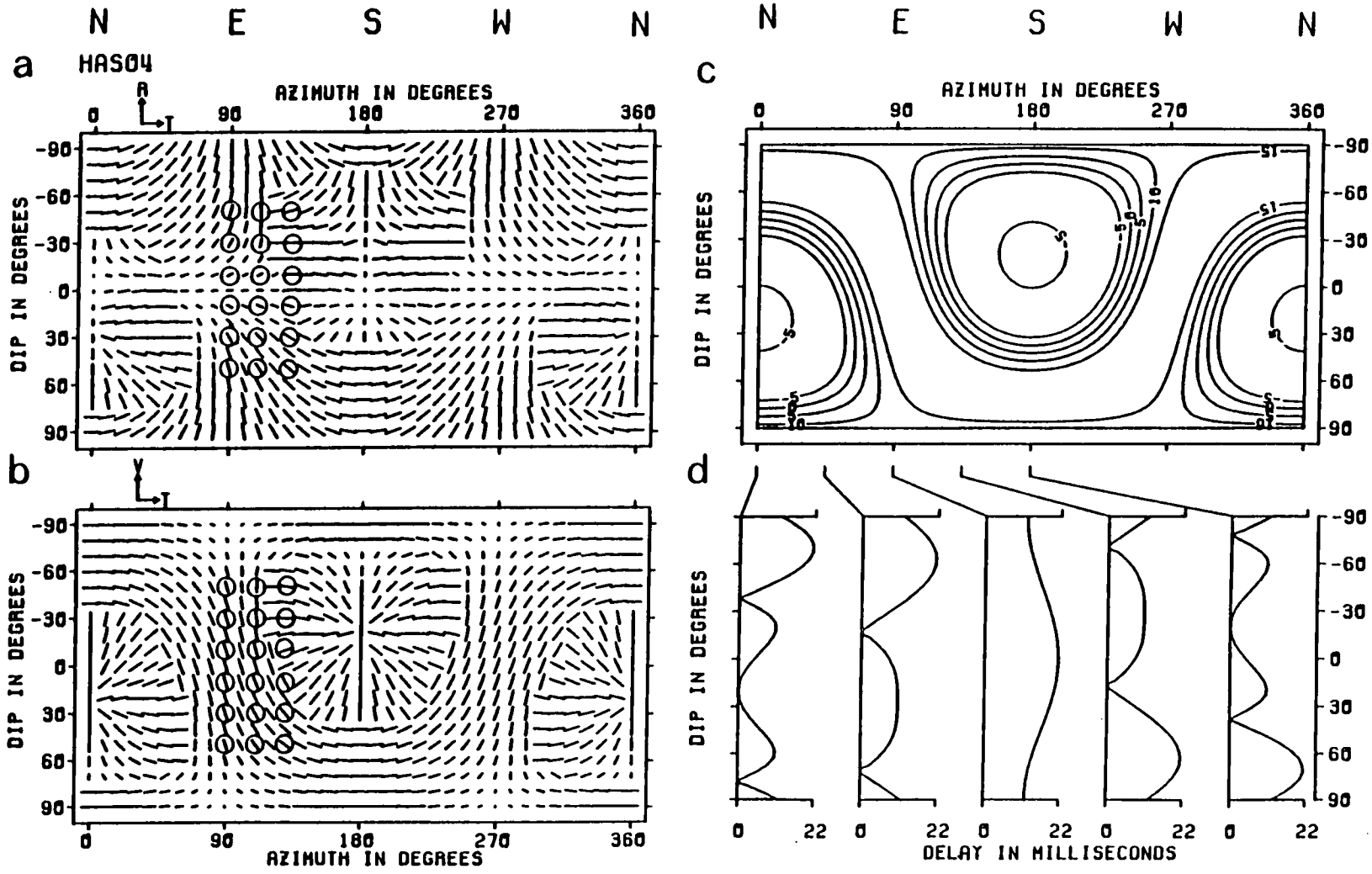

Figure 3.6 Cylindrical projections for the same cracks as Figure 3.5 but dipping at 70° to the north. The circles mark the directions of propagation of the synthetic seismograms in Figure 3.8. Notation as in Figure 3.4.

orientations of the cracks and relative crack densities can be easily evaluated, given observations from a sufficient range of directions. However, the patterns lack any strongly diagnostic features such as the pattern of parallel polarizations in the polar projections in Figure 3.3. In practice, CHS observations are usually confined to raypaths between a limited number of approximately vertical boreholes usually at relative azimuths which have been fixed by other considerations. Thus, in most CHS surveys the behaviour of shear-wave splitting can be examined only along a few vertical stripes at arbitrary azimuths in cylindrical projections. The interpretation of the polarizations and delays in terms of crack orientations and crack densities from a few vertical stripes is possible in noise-free conditions for an appropriate choice of azimuths and range of dips, but the interpretation of a few vertical stripes at arbitrary azimuths, particularly where irregularities in the rock may cause scatter in the observations, is likely to be difficult and inconclusive.

3.5 Synthetic seismograms from adjacent boreholes in an anisotropic medium

The principal effect of shear-wave splitting is to introduce subtle phase and amplitude changes into the different components of motion. These may be observed by meticulously comparing the relative displacements of parallel time series, or by easily recognizable patterns in polarization diagrams (Crampin 1985b) (*Polarization diagrams* or *PDs*, also known as hodograms, are orthogonal cross-sections of the particle displacements for short time intervals

along the wavetrains). The patterns are characteristic of the particular phase and amplitude differences between the different shear-wave phases (Crampin 1985b). Numerous observations suggest that the patterns are stable and can be identified even in the presence of considerable noise.

Figure 3.7 shows synthetic seismograms and polarization diagrams for shear waves from a point source propagating through a uniform space containing the thin parallel vertical cracks of Figure 3.2b striking east-west, giving the same structure as used for Figure 3.5. Synthetic seismograms are shown at six three-component geophones placed in a vertical borehole at depths to give relative dips of -50°, -30°, -10°, 10°, 30°, and 50° from vertical point forces with offset from the borehole at 200m, at azimuths N 90°E, N 110°E, and N 130°E corresponding to the circled arrivals in Figure 3.5. The dominant source frequency is 80 Hz. This geometry gives signals that can be compared directly with the polarizations and delays in Figure 3.5.

The arrowheads in the polarization diagrams in Figure 3.7, marking the initial directions of motion of the leading split shear-waves radiating from a point source, correspond to the polarizations in the marked directions in Figure 3.5. The places where arrowheads are omitted are where there is no splitting either because the radiated shear-wave is polarized very close to one of the fixed polarizations through the anisotropic rock so that the other split shear-wave is not excited, as in Figure 3.7a, or because the time delays between the split shear-waves are too small to cause significant splitting at the dominant period of the signal, as elsewhere in Figure 3.7.

Figure 3.7 Seismograms and polarization diagrams of shear waves through the same uniform space as in Figure 3.5. Six three-component geophones in a vertical borehole are arranged at depths to give the raypaths identified in Figure 3.5 (dips of -50° to 50°) relative to vertical point forces (dominant frequency of 80 Hz) in vertical boreholes offset 200 m at azimuths of (*a*) N90°E, (*b*) N110°E, and (*c*) N130°E. Upper diagrams are three-component synthetic seismograms aligned (V)ertical, and horizontal (R)adial and (T)ransverse to the azimuth of arrival. Lower diagrams are corresponding polarization diagrams for horizontal and vertical-transverse cross-sections of the particle displacements, and labelled (V)ertical, (R)adial, and (T)ransverse. Arrowheads indicate the initial directions of the first motions of the shear waves corresponding to the polarizations identified in Figure 3.5. Seismograms and polarization diagrams show the true relative amplitudes in each vertical column.

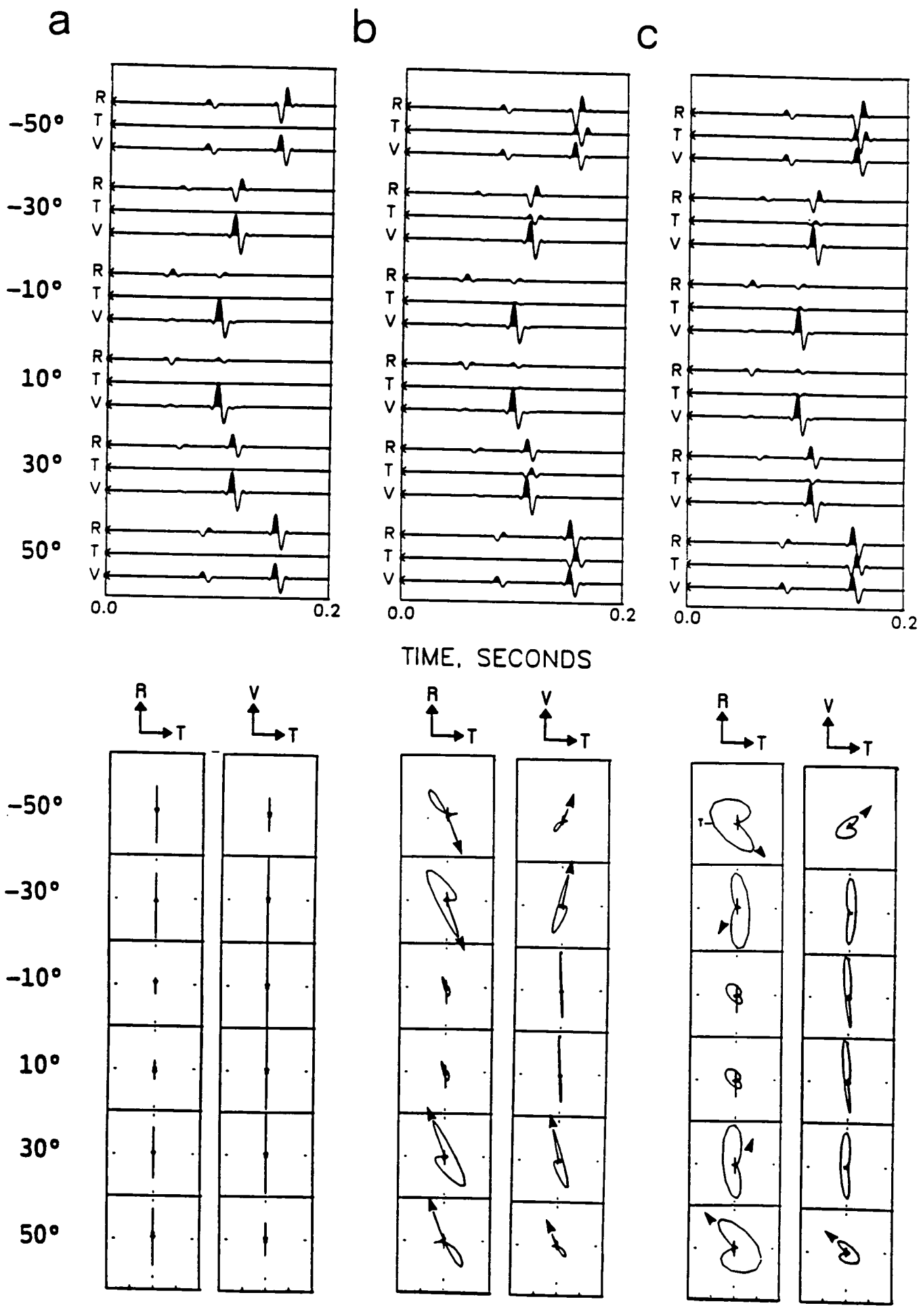

Figure 3.7

Figure 3.8 shows synthetic seismograms and polarization diagrams for shear-waves propagating through the same structure as Figure 3.7 but with cracks dipping 70° to the north, corresponding to the marked raypaths in the cylindrical projection in Figure 3.6. The notation is the same as in Figure 3.7.

The polarization diagrams in Figures 3.7 and 3.8 display patterns of particle displacements with the abrupt changes in direction typical of impulsive single-cycle shear waves propagating through cracked rock (Crampin 1985b, 1987b). The polarizations of the initial motion of the leading split shear waves with curved wavefronts agree remarkably well with the polarizations of the plane waves along the group velocity (ray) directions in Figures 3.5 and 3.6, respectively. The measured inconsistencies are less than 3° and are caused by the different behaviour of group velocity for curved and plane wavefronts in anisotropic rocks. (The point source is about seven wavelengths from the geophone borehole). A plane wave travels at the group velocity and the two polarizations of the shear waves are strictly orthogonal, whereas, a ray from a point source (with a curved wavefront) travels at the group velocity and, in general, will have different polarizations from the plane wave at the same angle of incidence. Consequently, for a point source the two split shear waves will not be strictly orthogonal.

3.6 Discussion

Crampin (1987a) has listed as many as 20 parameters that control the EDA-cracks (Table 3.2), of which at least four may be

Figure 3.8 Seismograms and polarization diagrams for synthetic seismograms through the same uniform space as Figure 3.6 (cracks dipping 70° to the north) along the marked raypaths. Geometry of paths and notation is the same as in Figure 3.7.

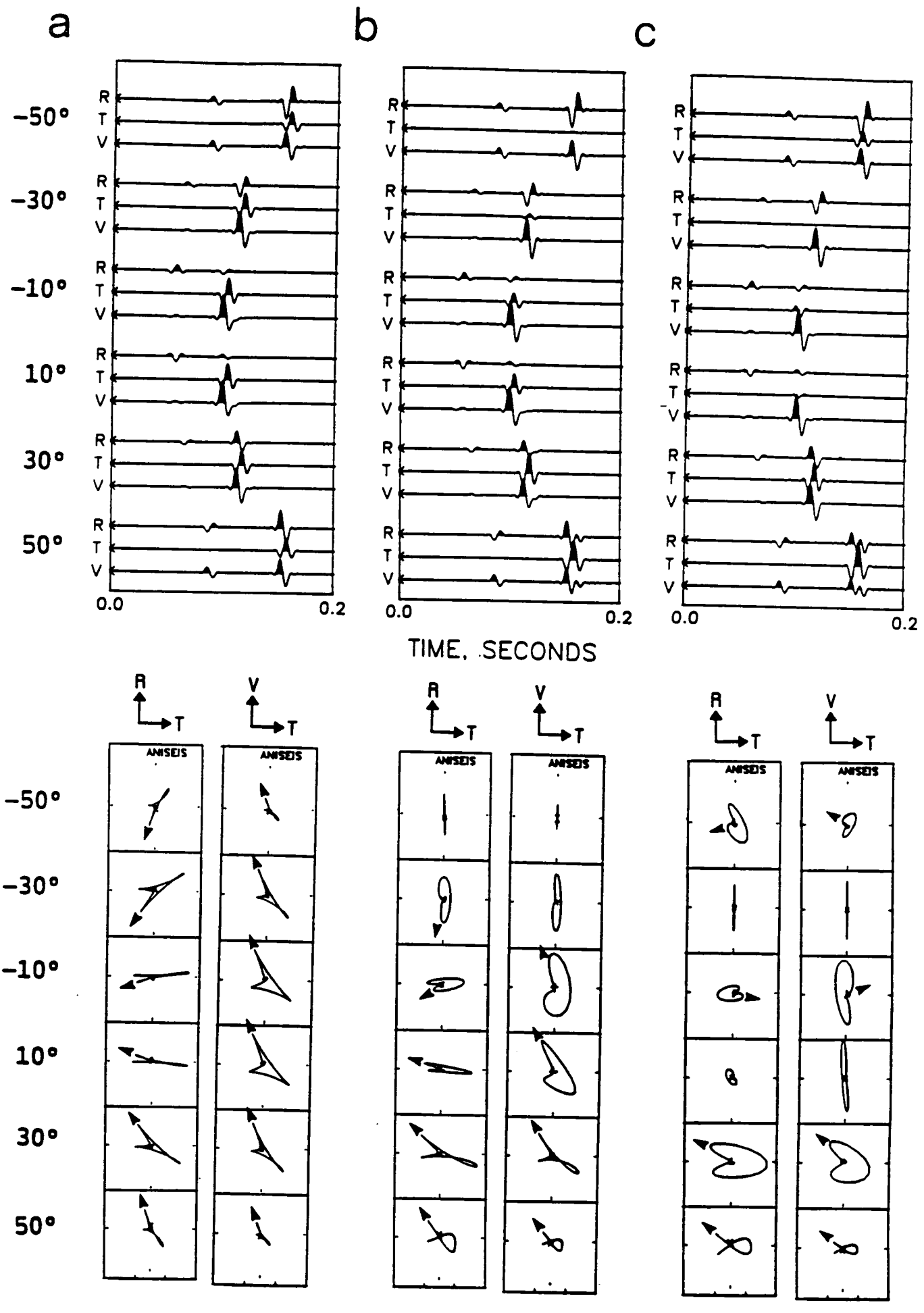

Figure 3.8

Table 3.2 Parameters controlling the EDA-cracks (from Crampin 1987a)

External conditions:	
(1) Lithostatic stress	(2) Deviatoric stress
(3) Temperature	(4) Properties of rockmass
Internal conditions:	
(5) Pore-fluid pressure	(6) Compressibility of pore-fluid
(7) Viscosity of pore-fluid	(8) Debris in crack void
(9) Vapour/liquid ratio in pore-fluid	(10) Properties of pore fluid under high temperatures & pressures
Dynamic conditions:	
(11) Rate of strain	(12) Rate of crack healing
(13) Rate of crack growth	
Crack parameters:	
(14) Orientation	(15) Dimensions
(16) Aspect ratio	(17) Distribution
(18) Smoothness of crack faces	(19) Connectedness (degree of isolation)
(20) Geometry (parallel, biplanar, *etc.*)	

interesting to the reservoir engineer, and may be extracted from seismic observations of shear-wave splitting. These are the crack geometry, particularly the strike and dip of the cracks, the aspect ratio of the cracks, and the crack dimensions.

3.6.1 Strike of the cracks

The polarization of the leading split shear wave propagating along nearly vertical raypaths gives estimates of the strike of the nearly vertical parallel cracks. This type of polarization is observed in many different circumstances in the Earth. There is no such distinctive behaviour in CHSs. The strike could be identified by the symmetrical behaviour at a range of azimuths spanning the direction of strike, but, except by chance, observations between suitable boreholes are unlikely to be available. However, determination of strike might be possible for a range of sources from a horizontal borehole or tunnel with three-component geophones at some distance away from the line of the tunnel.

3.6.2 Dip of the cracks

Dip is difficult to identify from nearly vertical raypaths unless observations are available from a range of azimuths and angles of incidence in an appropriate range of directions. CHSs display the effects of dip as asymmetries in the polarization patterns between upward and downward propagating waves, as in Figure 3.8, where the cracks dip at 70°, in contrast to Figure 3.7, where the cracks are vertical. At azimuths parallel to the strike of the cracks, as in Figure 3.8, the dip can be read directly from the dip of the polarization of the leading shear-wave.

3.6.3 Aspect ratio of the cracks

Changes in aspect ratio change the directions where the two split shear waves intersect [see Figure 1 in Crampin (1987c)] and change the position of the line of transition between the nearly orthogonal polarizations in polar and cylindrical projections in Figures 3.3 to 3.6. A larger aspect ratio increases the width of the broad band of parallel polarizations in polar projections and increases the diameter of the circular features in the cylindrical projections. Such changes in aspect ratio have been identified along nearly vertical raypaths in seismic gaps where the stress is changing before earthquakes (Chen *et al.* 1987; Booth *et al.* 1988; Peacock *et al.* 1988; Crampin *et al.* 1989). It does not seem likely that the position of these transition zones can be easily identified in CHSs.

3.6.4 Crack dimension

The dimensions of EDA cracks may range from submicrometre to a few millimetre in intact rock and up to a few metres in fractured beds (Crampin 1987a). The elastic constants, and hence the velocity variations and shear-wave splitting, are more sensitive to the dimensionless crack density than the crack dimensions [see the theoretical formulations of Hudson (1980b, 1981) or Crampin (1984)]. It is likely that attenuation will be more sensitive to the dimensions of the cracks than to velocity variations. If the cause of attenuation in cracked rock can be established, it is likely to be a particularly valuable technique, because with a known source polarization, the relative attenuation of the split shear-waves can be directly compared as they will have propagated along very similar raypaths. Because frequencies used in CHSs are significantly higher than these used in conventional exploration seismology, stronger attenuation of signals can be expected.

Note that the interpretation here is based on the effects of a single parallel vertical crack set. It is believed that assuming a single crack set is justified. There are now observations of shear-wave splitting from over fifty different locations (see Crampin 1987a). Relatively few of the data show scatter or are difficult to interpret, and the majority show clear patterns of 3D variation; wherever a pattern can be seen, it suggests vertical cracks striking perpendicular to the minimum horizontal stress, as illustrated in Figure 2.2 (Chapter 2). To our knowledge, no shear-wave polarizations anywhere suggest other than nearly parallel vertical cracks. The physical reasons for this have been discussed elsewhere (Crampin 1987a).

In our modelling we only considered a uniform space containing the EDA-cracks. We suggest that channel waves (guided waves) may be observed in the cross-hole surveys if there exists a low velocity zone through which they can travel. Analysis of channel wave particle motions may provide further imformation about *in-situ* cracks (see Chapter 6 for discussion of channel waves in coal seams and Chapter 7 for channel waves in a reservoir).

3.7 Conclusions

The theoretical and numerical examples presented here suggest that information about the internal rock structure causing shear-wave splitting is unlikely to be extracted easily from CHS experiments unless sufficient observations can be made at a range of azimuths. A large number of boreholes at suitable azimuths or a horizontal borehole are not expected to be commonly available. Note, however,

that the dip of near vertical parallel cracks can be estimated from polarization diagrams at a specific range of CHS azimuths.

As always with shear-wave splitting observed in the subsurface (away from the severe interactions with the free surface), detailed interpretation is possible with synthetic seismograms. However, this type of interpretation will be more difficult for CHSs than for VSPs because CHSs appear to give less easily recognized information about the parameters of the cracks, and there will be less control over the initial parameters for the modelling procedure.

We have only modelled synthetic seismograms from borehole shear-wave sources that radiate *SV* waves, reflecting current technology. A source of *SH* waves would produce different patterns of polarization, for example, by exciting the second slower split shear wave with orthogonal polarizations in Figure 3.7a; but the conclusions of this chapter are unlikely to be changed significantly.

Shear-wave CHS surveys will be expensive and consequently rarely attempted. We suggest that the major applications of the results of this chapter are likely to be in interpreting acoustic events induced by hydraulic pumping. Interpreting acoustic events recorded by down-well three-component geophones should yield unique information about the initial stress distribution and the developing system of cracks.

The present conclusions are based on the analysis of synthetic seismograms of cross-hole surveys and the comparison with the modelling of VSP data (for instance, the modelling by Bush 1989).

However, it does not alter the fact that CHSs have high resolution and avoid the interaction with the free surface, which we stated at the beginning of this Chapter. More important, channel waves could be observed in cross-hole surveys, such as in coal seams (Chapter 6).

CHAPTER 4

SHEAR-WAVE SPLITTING IN CROSS-HOLE SURVEYS: II, MODELLING IMOVSP DATA

4.1 Introduction

We have investigated numerically, in Chapter 3, shear-wave splitting in cross-hole surveys using synthetic seismograms, and discussed what crack parameters may be extracted. A particular simple example will be presented in this Chapter.

In order to map the top strata of coal-seams, the Brtish Coal Corporation's (BCC) Western Area Geophysical Services and the Headquarters Geophysical Unit have developed an Inverse Multi-Offset VSP (IMOVSP) technique. Several explosive sources are fired at various levels in a borehole and large geophone arrays are deployed around the drill site. A more detailed description of this technique can be found in Jackson *et al.* (1989). This IMOVSP technique fills in the gap between cross-hole surveys, borehole logging, conventional reflection seismics, in-seam seismics (which will be introduced in Chapter 6), and VSPs. The major advantages of IMOVSPs over conventional VSPs are the shot-to-shot repeatability and its high frequency content. In addition, acquisition is much faster than for offset VSPs (Jackson *et al.* 1989). We now introduce this new technique and attempt to model a small additional data set to one of the IMOVSPs carried out by the BCC in which the shots were recorded in a cross-hole configuration. As there are three

boreholes involved in the surveys and the geometry is similar to the cross-hole surveys, this short chapter can be therefore considered as a continuation and a complement of Chapter 3. There are two purposes of this study: (1) to introduce the IMOVSP technique, and (2) to demonstrate the difficulty of extracting information about cracks from cross-hole data.

4.2 Explosive source in a cylindrical borehole

As an explosive source is used in the IMOVSP survey, we first give a brief introduction of the downhole explosion. In theory, an explosive source only generates *P*-waves. If, however, the explosion is fired in a cylindrical well, shear waves can be produced. Shear waves generated by an explosive source in a borehole are polarized in the plane that includes the direction of propagation and axis of the well. As the well is usually near vertical, the generated shear wave is therefore of *SV*-type. Heelan (1953) demonstrated that *SV*-waves have maximum amplitudes at angles of 45° with respect to the axis of the cavity, and *P*-wave at 90° (Edelmann 1985; White and Sengbush 1963; White 1983). By assuming a straight raypath between the source and geophone (with distance R), Fehler and Pearson (1984) obtained the radiation patterns (amplitudes) of *P*- and shear-waves expressed by the following equations:

$$A_P = K_P [(\lambda + \mu) - \mu \cos^2\phi]/R, \tag{4.1}$$

and

$$A_S = K_{SV} \sin\phi \cos\phi/R = 0.5K_{SV} \sin(2\phi)/R, \tag{4.2}$$

where A_P and A_{SV} are the *P*- and *SV*-wave amplitudes, K_P and K_{SV} are constants, ϕ is the angle from the axis of the borehole, and λ and μ

are the Lamé constants. If attenuation is considered, the factor $\exp[-\pi fR/(QV)]$ should be included, where f is the frequency, and Q is the attenuation quality factor, which is expected to be different for *P*- and shear-waves. Figure 4.1a shows the directions of maximum amplitudes of the *P*- and *SV*-waves generated by an explosion in a cylinder. The maximum amplitude of the *P*-wave is in the direction perpendicular to the borehole axis and the *SV*-wave in the direction of 45° from the borehole axis. Note that this is only a schematic illustration of radiation patterns and the amplitudes of *P*- and shear-waves do not necessarily represent the true amplitudes [Heelen originally indicated that the ratio of maximum amplitudes of *SV*-wave to *P*-wave A_{SVMAX} / A_{PMAX} equals the ratio of compressional-to-shear speeds V_P / V_S, which is 1.732 for the Poisson ratio of 0.25 (White and Sengbush 1963)].

We are unable to apply an explosion in a vertical borehole in the modelling package ANISEIS. Instead, a horizontal force point source will be used, which generates both *P*- and *SV*-motions in purely homogeneous isotropic media. The maximum amplitudes of *P*- and shear-waves radiated from the horizontal force point source are indicated in Figure 4.1b. The *P*-wave radiation patterns from both source-types are similar to the explosion in a cylinder (Figure 4.1a), but the shear-wave radiation patterns are different. *P*- and *SV*-waves are excited by both sources, and no *SH*-wave is generated in homogeneous isotropic media.

4.3 Data and observations

The data available to us is a small addition to one of these IMOVSP surveys, recording out-of-seam shots on the in-seam

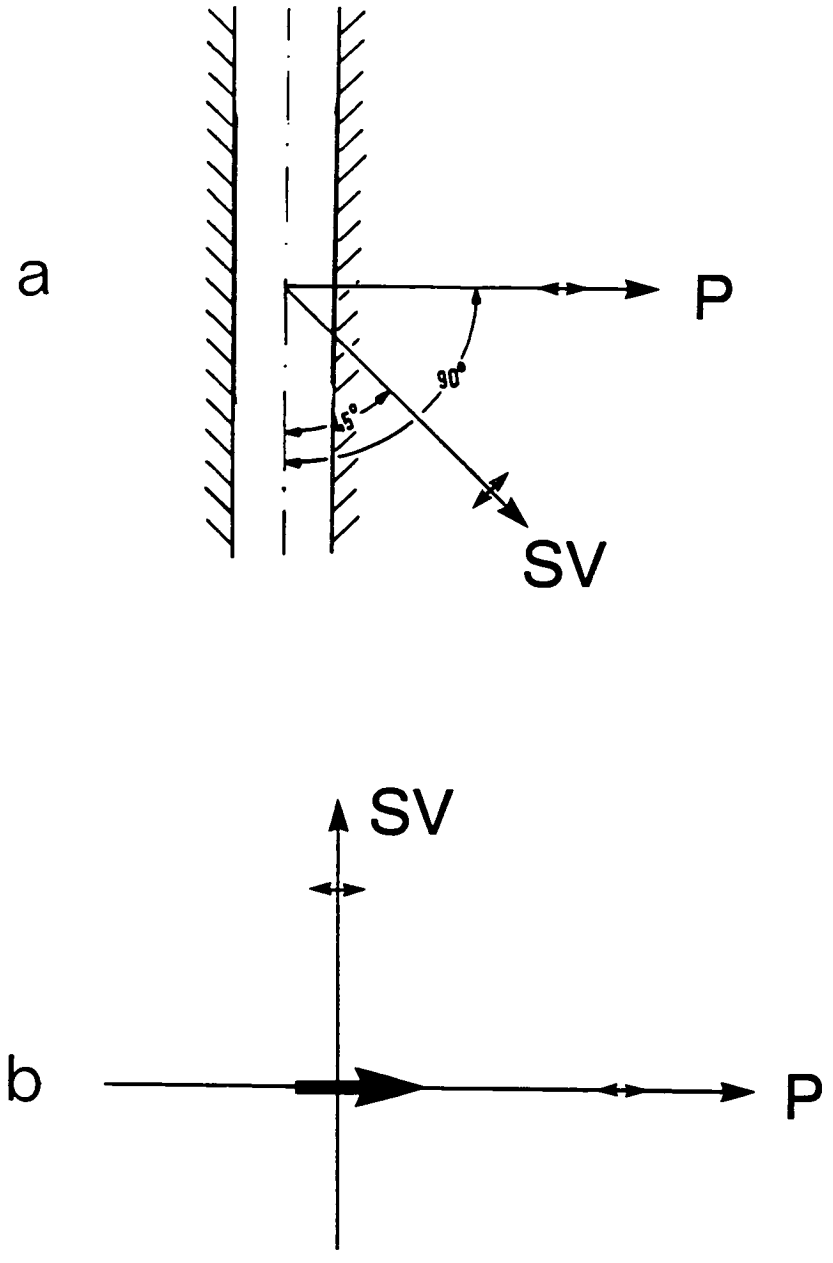

Figure 4.1 (*a*) Directions of maximum amplitudes of *P*- and *SV*-waves generated by a cylindrical cavity suffering a uniform lateral pressure (explosion) and (*b*) Direction of maximum amplitudes of *P*- and *SV*-waves generated by a horizontal force point source in an isotropic medium.

geophones. The location of the relevant shots and geophones in the horizontal plane is shown in Figure 4.2. Three boreholes were involved in the surveys: G1, G2 and S. Geophones were deployed in the same seam in holes G1 and G2, and three relevant shots were fired in hole S. The parameters of shots are grouped in Table 4.1. The data were recorded on a SERCEL 338 system, sampling interval 0.5 millisecond, anti-alias filter set at 750 HZ, 72 db/OCTAVE high cut. The geographical location is Cannock chase, England, the seam is approximately 600 m below ground level.

It is understood that there are at least two coal-seams existing in the area considered, although the seam near the shot points probably has minor effects on the recordings. The coal-seams are typically 2m in thickness. The velocities within the coal-seams and their vicinities are shown in Table 4.2. Such a structure forms a channel (waveguide), however, channel waves were not observed, probably because the sources are too far from the channel containing the geophone.

Three-component seismograms, which have been rotated to radial (towards geophone), transverse (at right angle to the radial in the right-hand coordinate system) and vertical (up) directions, are shown for two geophones located in boreholes G1 and G2 in Figures 4.4 with the recording geometry in Figure 4.3. Analysis of these data can identify four arrivals, which are labelled W1, W2, W3, and W4 in Figure 4.4. The first arrival (W1) appears only in vertical and radial components, travelling with the velocity of direct *P*-wave (3800 m/s). The second arrival (W2) is on all three components, and is the *P* to *S*-conversion at the top coal-seam. The third arrival (W3) with a relative small amplitude is the shear-wave generated by

Table 4.1 Parameters of sources

Shot No.	Source Type	Height (m) above the seam level
207	180′ Cordex	102
208	400gm RDX	67
210	400gm RDX	98

Note: Shot 207 was within a coal seam.

Shot 210 was below a coal seam.

Table 4.2 Isotropic parameters used in the model

Layer	Thickness (m)	V_P (ms^{-1})	V_S (ms^{-1})	Density (gcm^{-3})
Halfspace		3800	2000	2.70
Coal I	2.0	1700	1000	1.40
	102.0	3200	1600	2.20
Coal II	2.0	1700	1000	1.40
Halfspace		3800	2000	2.60

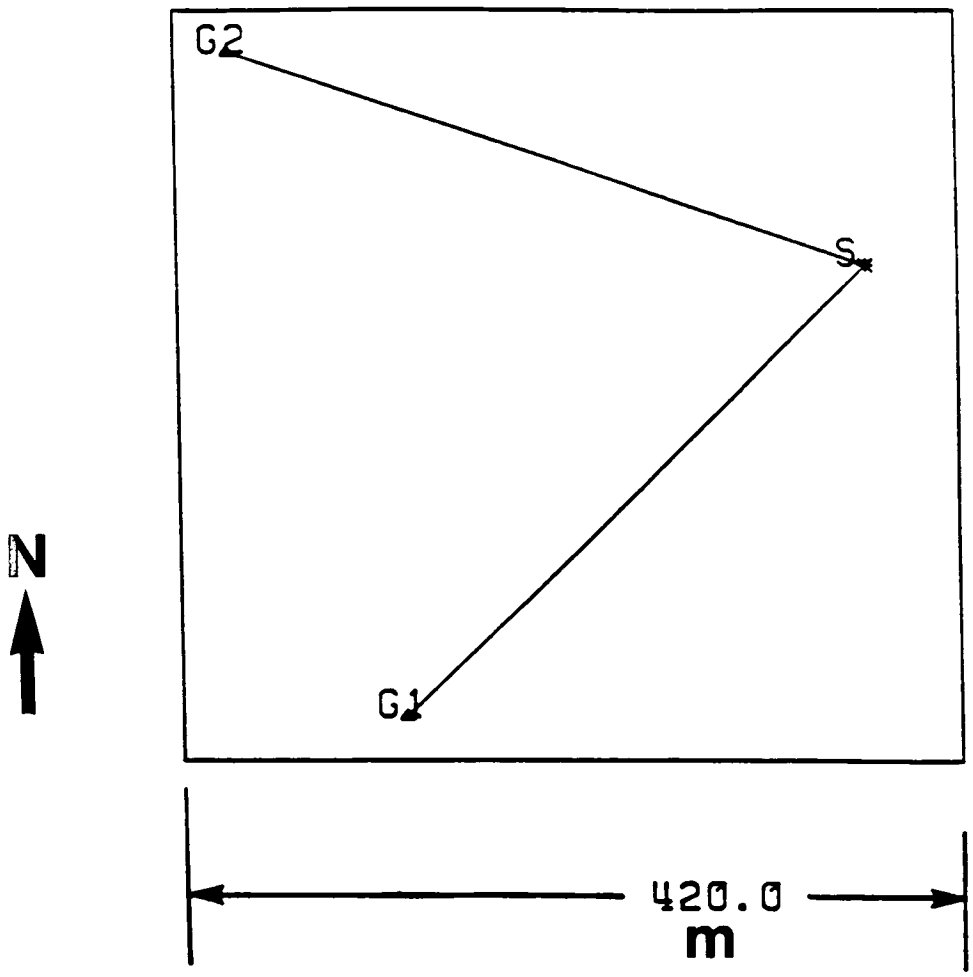

Figure 4.2 Plan of geometry of the IMOVSP. Three boreholes are involved: One source borehole (S) and two receiver boreholes (G1 and G2).

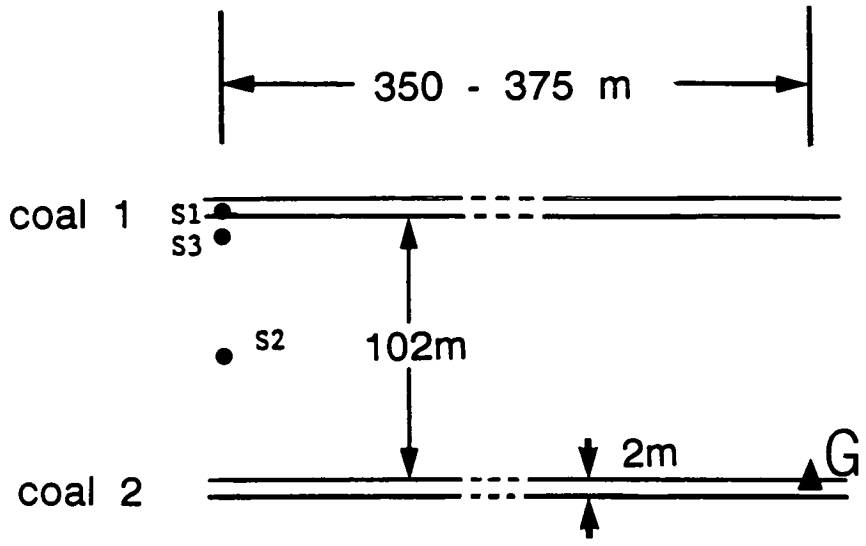

Figure 4.3 The model structure with parameters in Table 4.2.

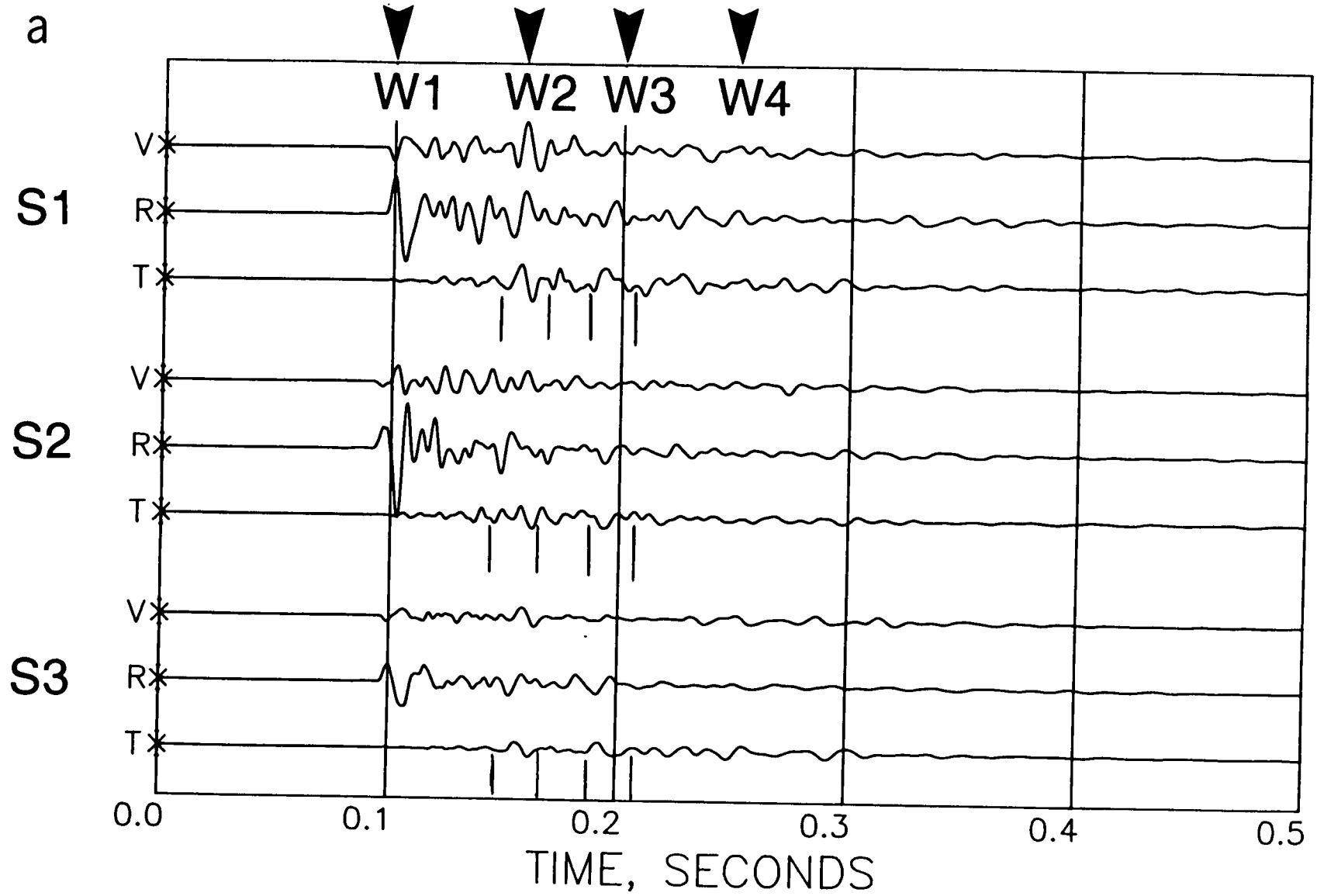

Figure 4.4 Observed three-component seismograms from receiver boreholes (*a*) G1 and (*b*) G2 in Figure 4.2. The solid arrowheads indicate four identical arrivals (W1, W2, W3 and W4).

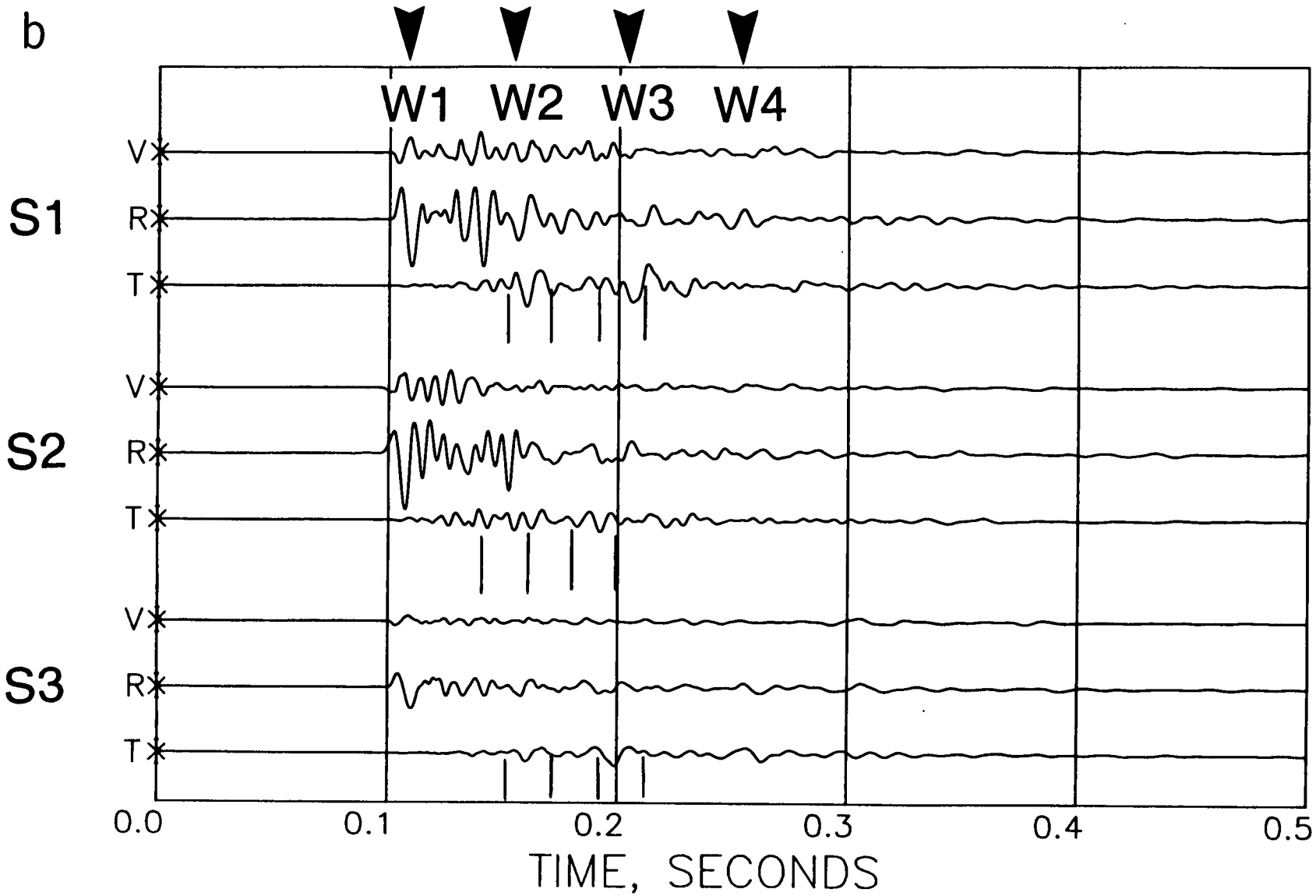

Figure 4.4 (cont.)

the borehole explosion, it travels with the velocity of approximately 2000 m/s, and the last arrival (W4) with small amplitudes is also on all three components, and can be interpreted as *S* to *S*-reflected shear-wave at the top coal-seam. There are also many reverberations between or after these main arrivals, which are the multiple reflections and refractions between the two coal-seams (including conversions between *P*- and shear-waves). If the thickness of the channel and the source frequency are appropriate, channel waves will be expected. In general, seismograms for all three geophones show little difference.

Apart from the first *P* waves, all other three waves appear in all three components. The absence of the *P*-waves in transverse components suggests that the rotation is approximately correct. Figure 4.5 shows the polarization diagrams of the second and third arrivals in the horizontal radial-transverse and vertical-transverse planes for the time window indicated in the seismograms in Figure 4.4. The first motions are marked with large arrowheads. Polarizations are general elliptical with no distinct alignment, but show shear-wave splitting. The observed elliptical particle motions of shear-waves (W2 and W3) cannot be explained by the fact that an explosive source is not expected to produce transverse *SH*-motion, hence the elliptical motions in V-T and R-T planes cannot be attributed to the source radiation patterns. We suggest that these anomalies can be interpreted as a result of anisotropy along the raypaths and can be reproduced by synthetic seismograms.

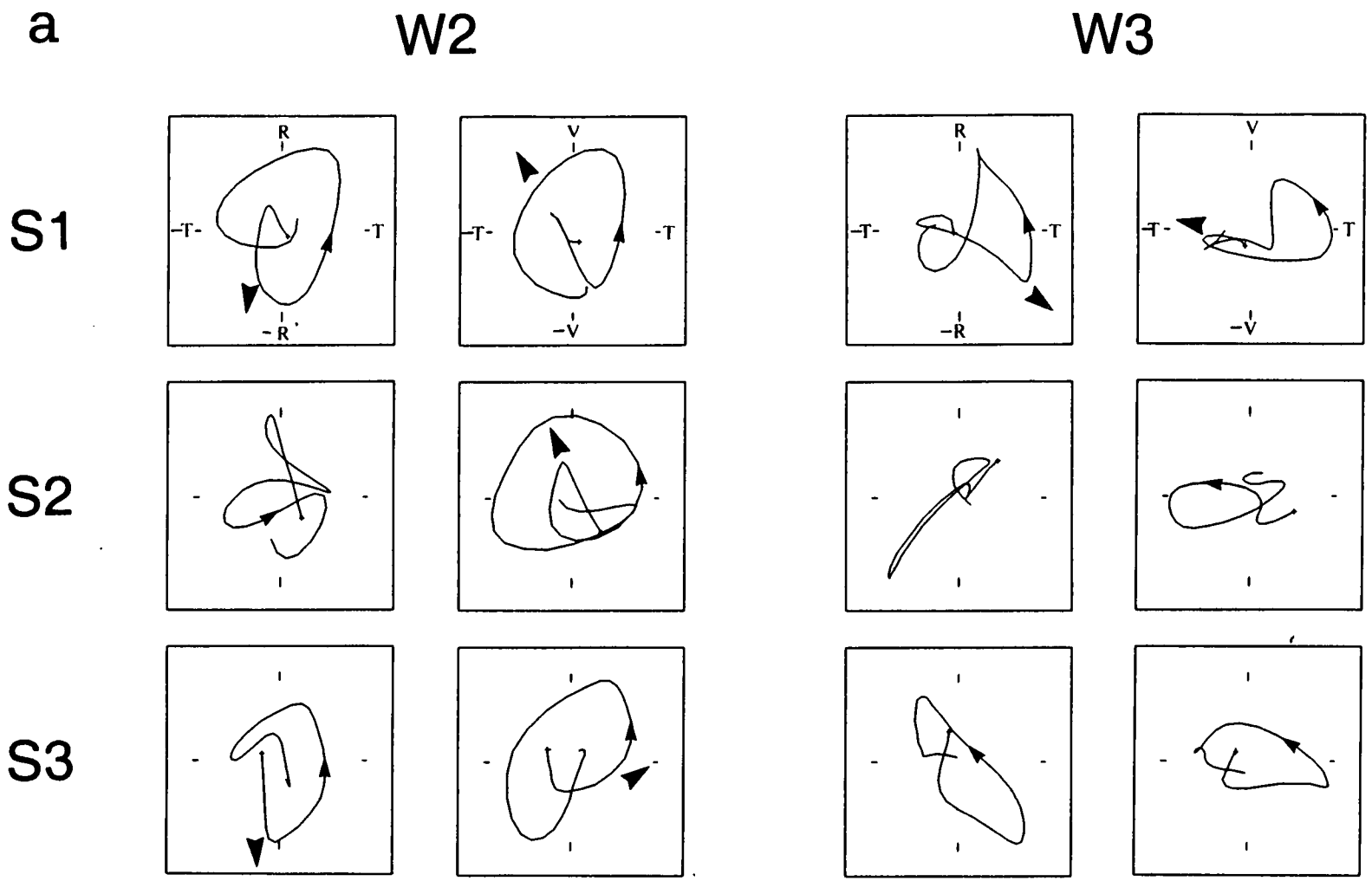

Figure 4.5 Observed particle motion plots of arrivals W2 and W3 of Figure 4.4. (*a*) receiver borehole G1 and (*b*) receiver borehole G2. The first motions of shear-waves are marked with large arrowheads.

Figure 4.5 (cont.)

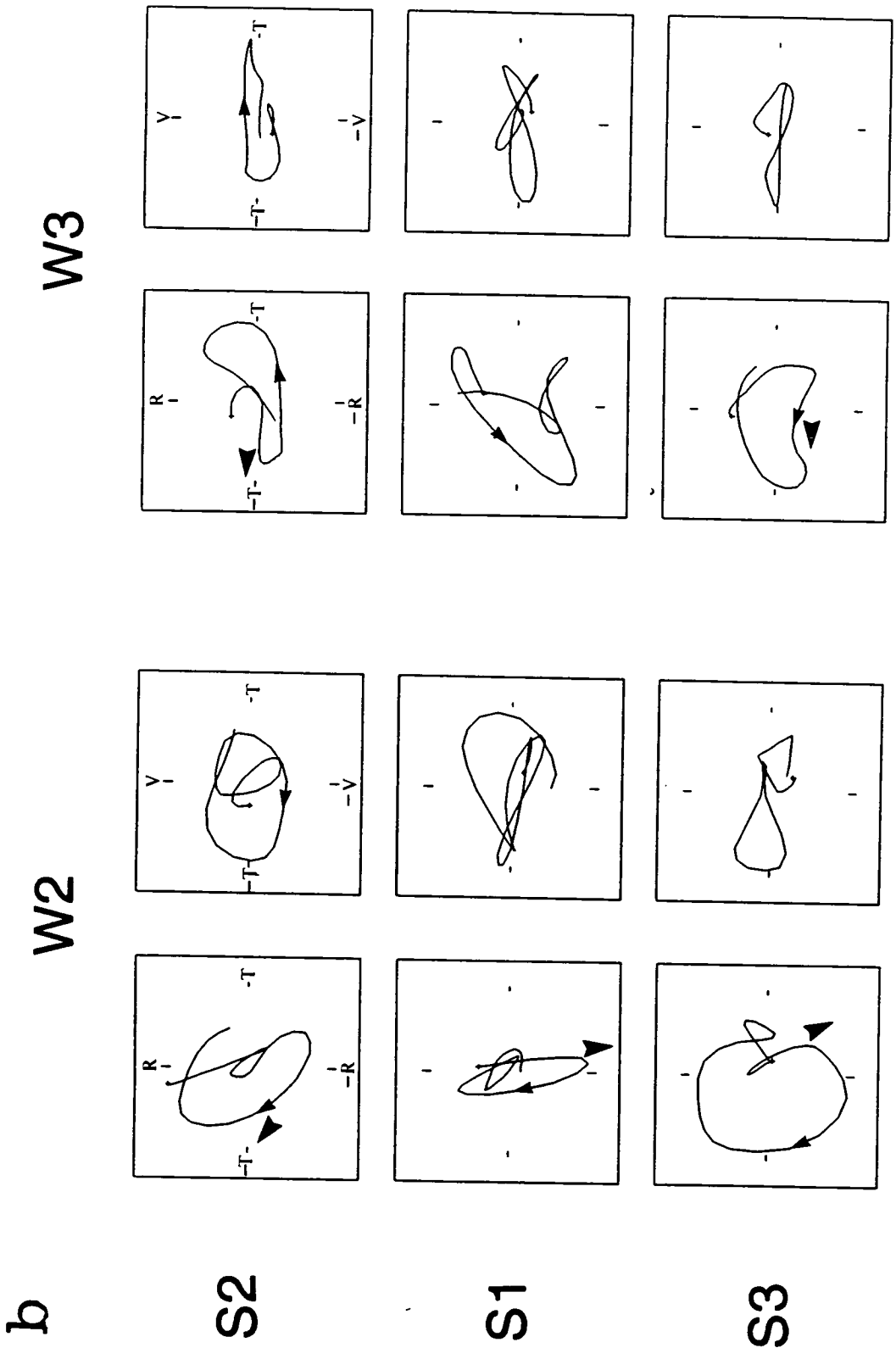

4.4 Synthetic seismograms

There are some difficulties in modelling this data set uniquely because the data are limited and there is not enough coverage of azimuths (2 azimuths) and incident angles (3 very close incident angles) to determine crack orientation with any accuracy. However, the geometry of layout is clear and the general structure is known. We use the trial and error forward modelling procedure to calculate the synthetic seismograms and attempt to match the observations. The dominant source frequency is 70 Hz, which is very close to the observations. The results that we obtain show a fairly good agreement with the observed records, suggesting that anisotropy has to be taken into account if a precise interpretation is required.

The data we have can give no estimate of the dimensions of the cracks. However, most coal-seams are found to be in sedimentary rocks, such as shales and sandstones, which are believed to be finely layered media (transversely isotropic media with a vertical symmetry axis), such layered media are effectively cracked with the vertical crack striking along the local maximum compressional stress (Crampin 1985), it is, therefore, assumed that the channel bounded by two coal-seams to be anisotropic to seismic waves with orthorhombic symmetry (Bush and Crampin 1987). For simplicity, we only consider crack-induced anisotropy (since in transversely isotropic media with vertical symmetry axes a downhole explosive source does not produce transverse *SH*-motion). The cracks within the channel are aligned in the NNW/SSE direction, which is believed to be the strike direction of stress in the United Kingdom (Buchanan 1983, Crampin, Roth, personal communications, etc.).

Figure 4.6 shows the synthetic seismograms at geophones G1 and G2 from three sources at source borehole S calculated for an anisotropic model with the elastic constants in Table 4.3. The model contains vertical aligned fluid-fill cracks (EDA-cracks) in the isotropic medium between two the coal-seams. The crack density is 0.06. The cracks are aligned 10° west of north. Four distinct arrivals can be clearly identified. Their arrival times are approximately in agreement with the observations in Figure 4.4. The major discrepancy between observation and synthetics is the relative amplitudes of the second and third arrivals. The second and third arrivals (*P*-*S* conversion and direct shear waves) are coupled in all three components. Since the coal-seam is characterized by its low-velocity and low-density, reflected waves are expected to have large amplitudes. The waveforms in radial and vertical components are very similar to the observed records except that there are differences in amplitudes. In particular, the third arrivals have large amplitudes. This is caused by the incident source radiation patterns. In our model, a horizontal force point source is applied and the effects of borehole are not considered.

The polarization diagrams are presented in Figures 4.7 with the first motions are marked with large arrowheads. The polarization diagrams show some of the characteristics of the observed records. There are strong elliptical motions of shear-waves after the linear motions of *P*-waves. Because the structure is complicated and shear-waves in synthetic seismograms from all three sources show very similar waveforms and polarizations, it is difficult to compare the first motions of shear-waves with the cylindrical projections in Chapter 3.

Table 4.3 Elastic constants (in Pascals x 10^9) of the material between two coal seams. x_1 is perpendicular to the cracks, x_2 is parallel to the cracks, and x_3 is vertical.

$c_{1111} = 38.82$	$c_{2222} = 38.95$	$c_{3333} = 38.95$
$c_{2233} = 17.35$	$c_{3311} = 17.31$	$c_{1122} = 17.31$
$c_{2323} = 10.80$	$c_{1313} = 9.475$	$c_{1212} = 9.475$

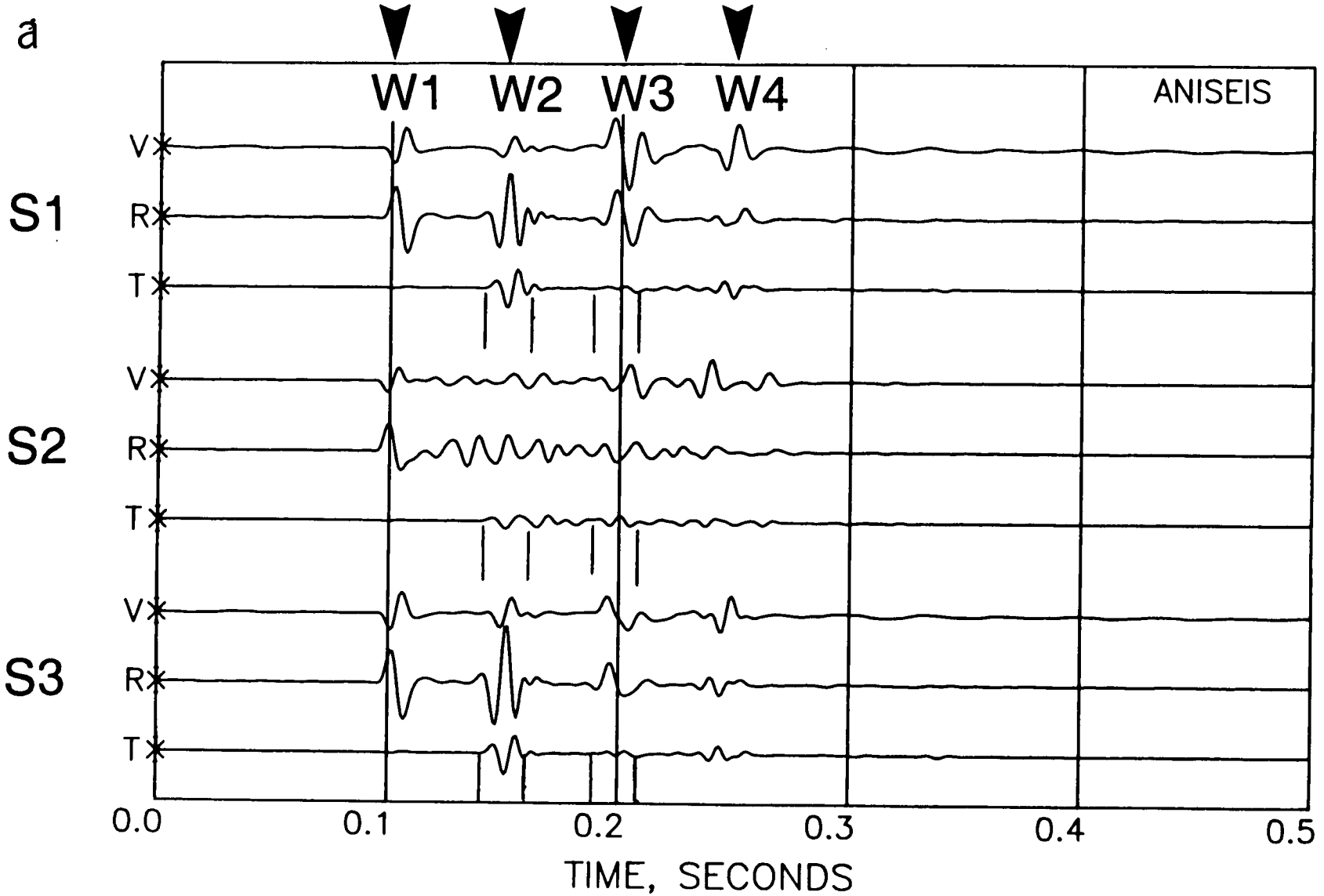

Figure 4.6 Synthetic seismograms calculated for a model structure of Figure 4.3. The notation is the same as Figure 4.4.

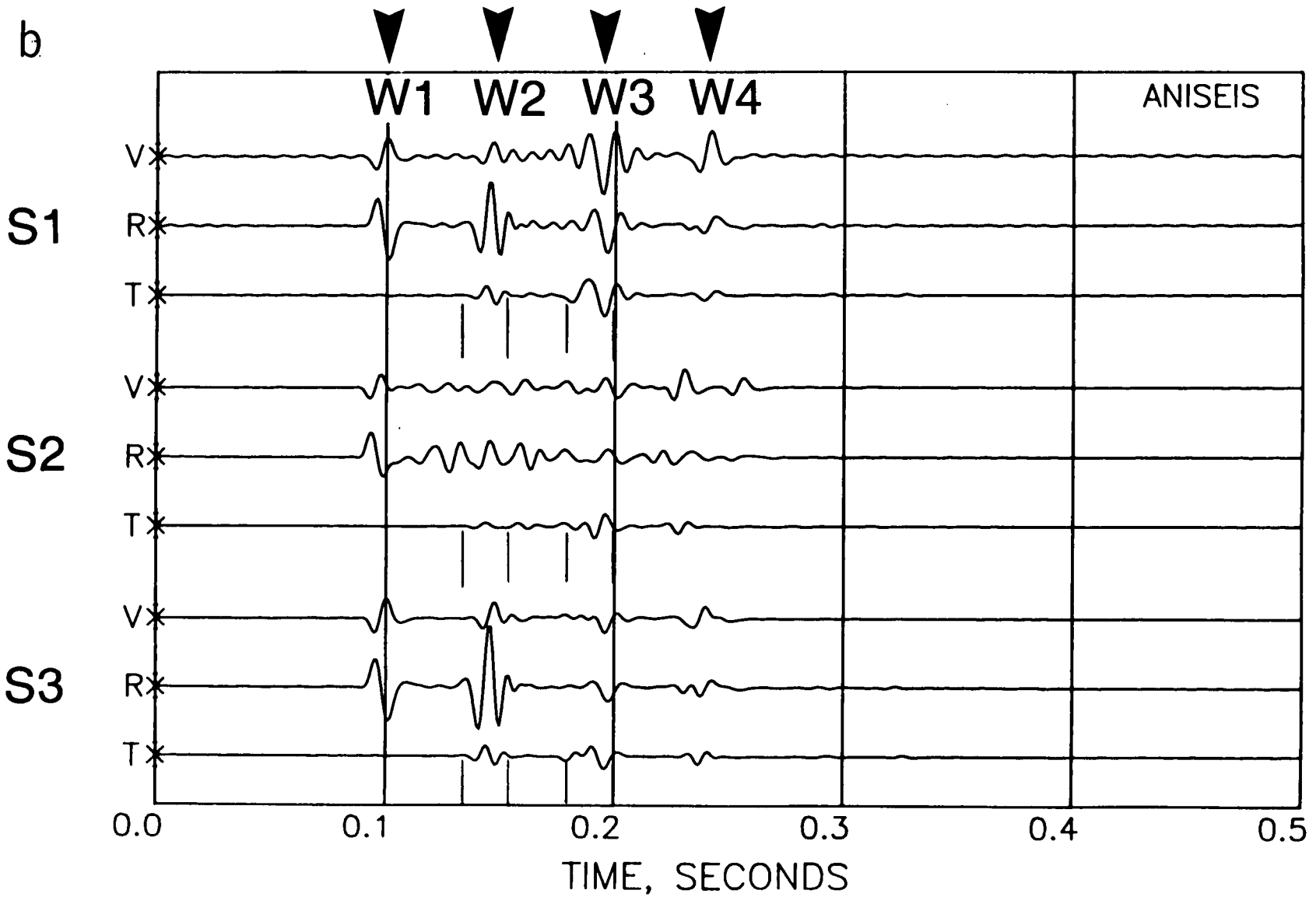

Figure 4.6 (cont.)

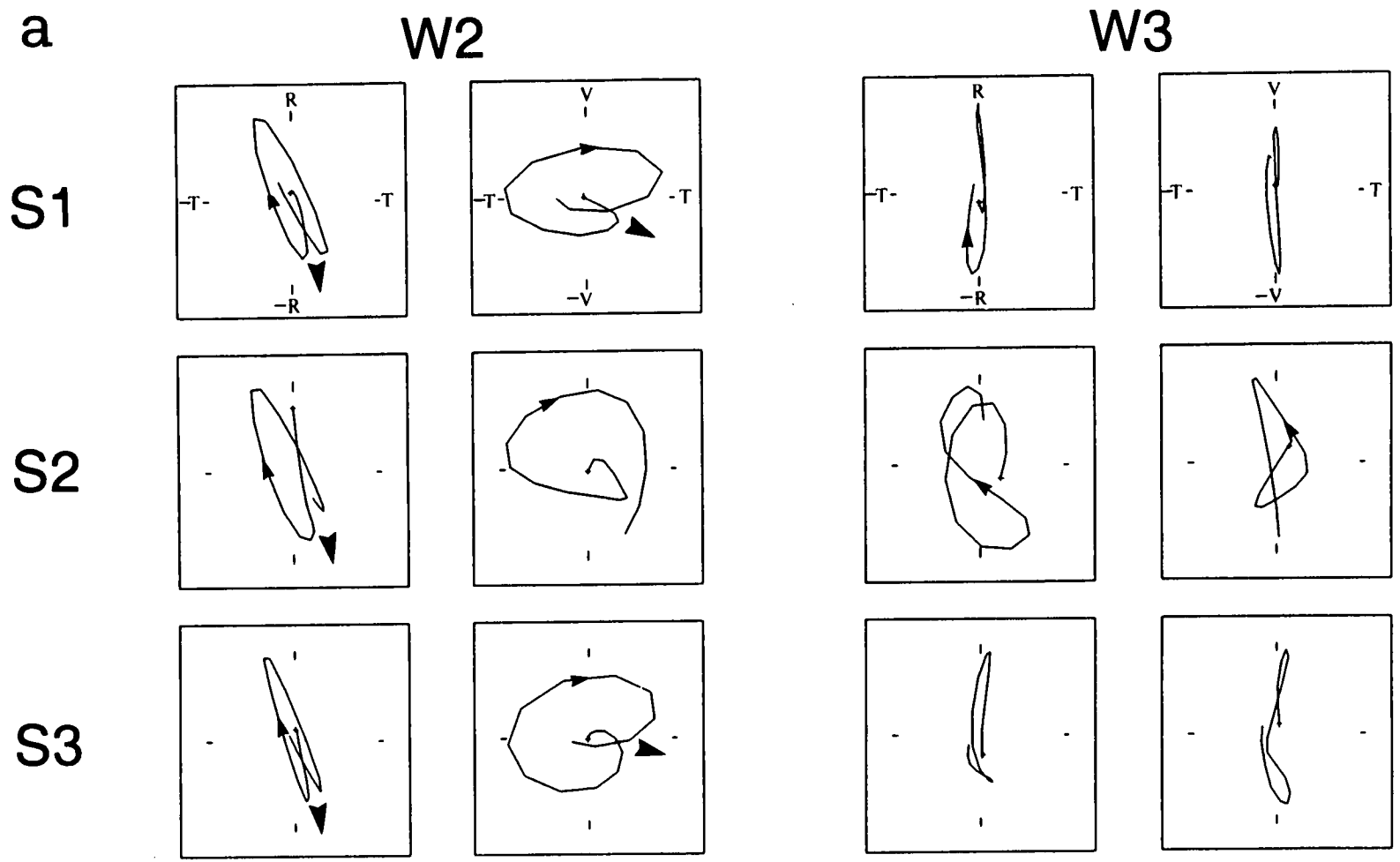

Figure 4.7 Particle motion plots of the synthetic seismograms of Figure 4.6. The notation is the same as Figure 4.5.

Figure 4.7 (cont.)

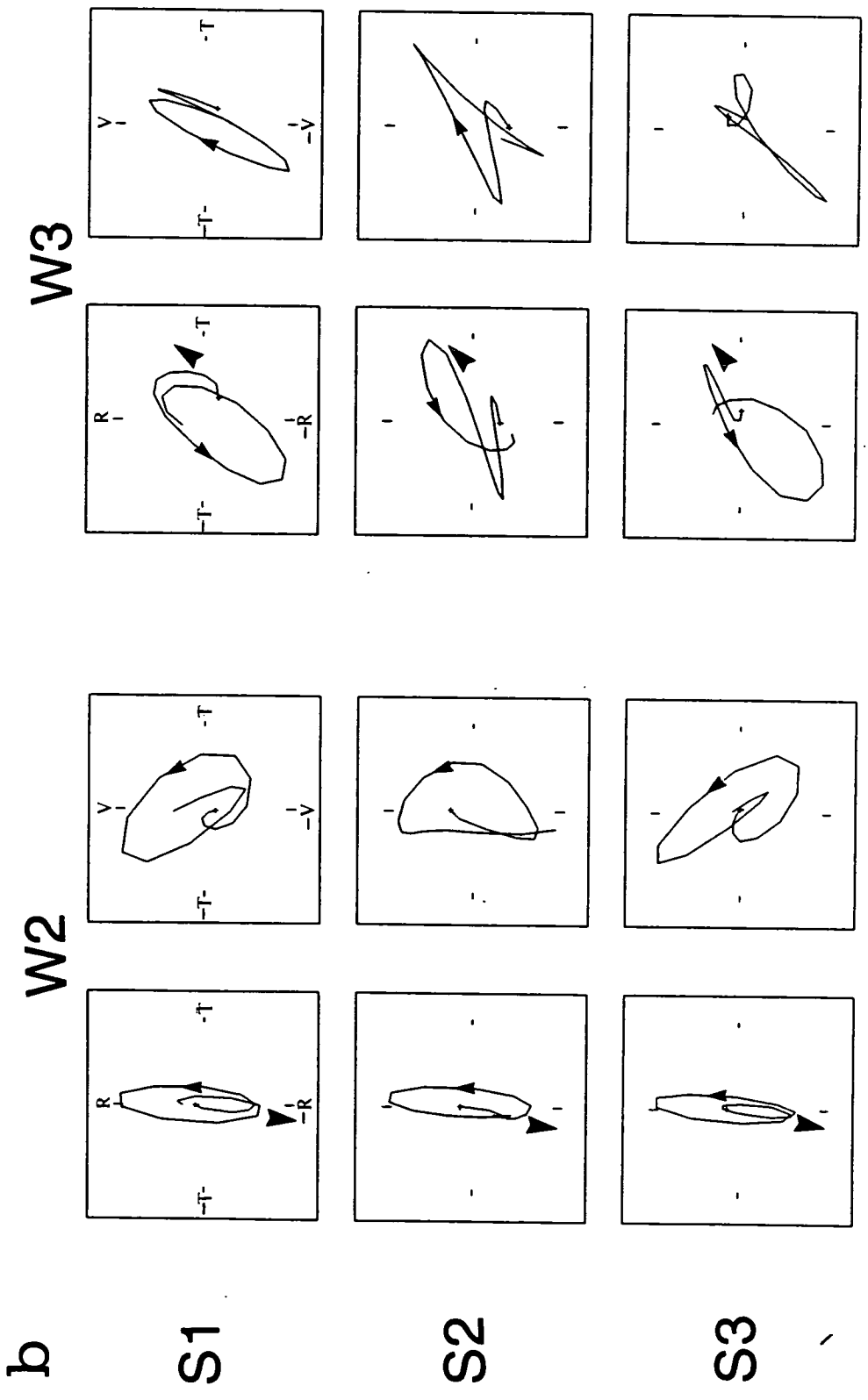

4.5 Discussion and conclusions

The data we have modelled are very limited, it is unlikely to estimate crack parameters accurately. A 10° perturbation in crack strikes only alters the amplitudes slightly, it will not alter the first motions significantly in near horizontal propagations (See Chapter 3). Therefore, we have just obtained a very preliminary match of the observations, and a more detailed modelling would require more data sets. If such data were available, the cylindrical projections in Chapter 3 would help to determine crack parameters.

It is necessary to take the effects of the borehole into account when analyzing the polarizations of shear-waves propagating through boreholes. Borehole effects are most significant when plane waves propagate perpendicular to the boreholes. Thus, borehole effects could be more important in processing and interpreting hole to hole data and wide offset VSP data. However, when the shortest wavelength of interest is about 40 times longer than the borehole's diameter, the effects of the borehole on borehole measurements using a wall-locking geophone are negligible (Schoenberg 1986; Lee 1987).

Shear-wave splitting in cross-hole surveys can be modelled by synthetic seismograms. It is however difficult to extract crack information without enough coverages of incident angles and azimuths. In this preliminary study, we have demonstrated this requirement.

CHAPTER 5

THE EFFECTS OF INTERNAL INTERFACES ON SHEAR-WAVE POLARIZATIONS

5.1 Introduction

In this Chapter we examine the effects on shear waves of *transmission* and *reflection* through interfaces, which leads to the concept of an *internal shear-wave window* analogous to the shear-wave window previously defined for incidence at a free surface. This study may be of interest to wide offset VSPs, cross-hole surveys and reflection seismics. The scattering of shear-wave polarizations at the free surface has been discussed by Nuttli (1961, 1964); Nuttli and Whitmore (1962); Evans (1984); and Booth and Crampin (1985). They showed that shear-waves observed at the free surface may be seriously distorted by interaction with the surface if the angle of incidence is greater than the critical angle $\sin^{-1}(V_S/V_P)$. This angle defines *the shear-wave window*, within which the shear waveforms observed at the surface are similar to the waveforms of the incident waves (Booth and Crampin 1985). The particle motions of shear waves arriving outside the window are severely distorted and the waveforms of the incident wave cannot easily be recovered from observations at the free surface. Recent studies have shown that interaction with internal interfaces may also distort shear-wave polarizations. Cormier (1984) has concluded that interaction with irregular internal interfaces could lead to distortions of shear-wave polarizations of up to 10°. Douma and Helbig (1987) calculated the change in polarization of a plane shear wave polarized intermediate to *SV* and *SH* at a range of angles of

incidence to a plane interface between halfspaces of sandstone and halite. They find (Figure 5.3a) that the deviation of the *transmitted* shear-wave is greatest (3°) at an angle of incidence of 30°.

Douma and Helbig (1987) suggest that such effects (interface effects on transmitted shear-waves) might have serious implications for the study of anisotropy-induced shear-wave splitting. Shear-wave splitting is caused by internal structures, usually by some form of effective anisotropy, but internal interfaces can cause differences in the response of the polarizations of shear-waves that might be mistaken for anisotropy-induced splitting. If internal interfaces cause difficulties in interpreting anisotropy-induced shear-wave splitting, as suggested, the effects need to be quantified. This Chapter is aimed at a thorough examination of interface interferences on shear-wave polarizations. We calculate synthetic seismograms of shear waves incident on internal interfaces, and assess the effects of internal interfaces on measurements of anisotropy. Both transmission (Part I) and reflection (Part II) will be considered for completeness. This Chapter, we suggest, may be considered as a continuation and an addendum of the paper by Booth and Crampin (1985) on the shear-wave window at the surface, and also an extension of the paper by Douma and Helbig (1987).

We consider two examples: incidence at a Low-to-High impedence contrast, L/H, [the case considered by Douma and Helbig (1987)], and incidence at a High-to-Low impedence contrast, H/L. The parameters of the materials are listed in Table 5.1.

Table 5.1 Velocities and densities of sandstone and halite.

	V_P (m/s)	V_S (m/s)	ρ (gcm^{-3})
Sandstone	3074	1904	2.65
Halite	4618	2697	2.16

Elastic constants of anisotropic medium with matrix rock of halite (for transmission model) (Unit is Pascals x 10^9)

	(1,1)	(2,2)	(3,3)	(2,3)	(1,3)	(1,2)
(1,1)	45.868					
(2,2)	14.579	46.044				
(3,3)	14.579	14.621	46.044			
(2,3)	0.000	0.000	0.000	15.711		
(1,3)	0.000	0.000	0.000	0.000	12.505	
(1,2)	0.000	0.000	0.000	0.000	0.000	12.505

Elastic constants of anisotropic medium with matrix rock of sandstone (for reflection model)

	(1,1)	(2,2)	(3,3)	(2,3)	(1,3)	(1,2)
(1,1)	24.558					
(2,2)	5.380	24.601				
(3,3)	5.380	5.387	24.601			
(2,3)	0.000	0.000	0.000	9.607		
(1,3)	0.000	0.000	0.000	0.000	8.728	
(1,2)	0.000	0.000	0.000	0.000	0.000	8.728

5.2 Effects of interfaces on transmitted shear-waves (Part I)

Analytical solutions are only available for plane waves incident on plane welded interfaces. This classic and fundamental problem has been previously treated in many investigations (Ewing *et al.* 1957; Brekhovskikh 1960; Aki and Richards 1980), but in none of these references or others are the results presented in the form that we shall use.

5.2.1 Polarization angles

We consider a plane shear wave with relative *SH* and *SV* amplitudes A_{SH} and A_{SV}, respectively, incident on a plane boundary from material 1 to material 2 (Figure 5.1). The polarization angle or vibration angle (ψ) of the transmitted shear-wave in the plane parallel to the plane of constant phase is related to the amplitude and transmission cofficients (Ingram 1952; Nuttli and Whitmore 1962; Douma and Helbig 1987) by:

$$\psi_t = \tan^{-1}(B\, R_t), \qquad (5\text{-}1)$$

Where $B = A_{SH}/A_{SV}$, $R_t = T_{SH}/T_{SV}$. The ratio $B = A_{SH}/A_{SV}$ specifies the polarization angle of the incident wave. T_{SH} and T_{SV} represent the transmission coefficients of *SH*- and *SV*-waves, respectively, which are functions of the material properties ρ_1, V_{S1}, V_{P1} and ρ_2, V_{S2}, V_{P2} and angle of incidence j_1. For simplicity, V_P and V_S are replaced by α and β, respectively in the following equations:

$$T_{SH} = 2\rho_1\beta_1\cos_j 1/\Delta,$$

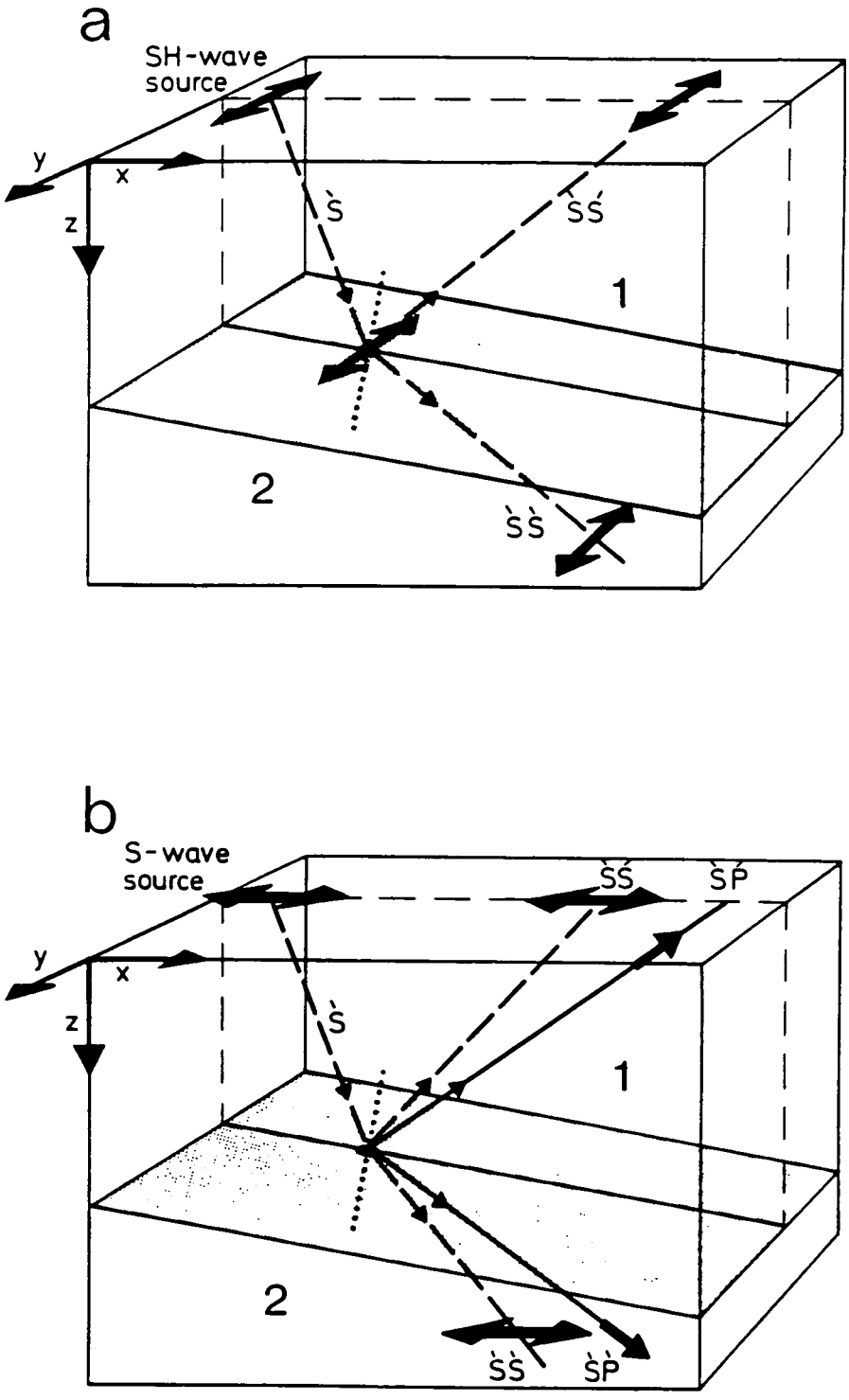

Figure 5.1 A shear-wave incident on an isotropic solid-to-solid interface from material 1 to material 2. (*a*) incident *SH*-wave, and (*b*) incident *SV*-wave.

and

$$T_{SV} = (2\rho_1 \cos j_1/\beta_1) E\beta_1/(\beta_2 D), \tag{5-2}$$

where

$$\Delta = \rho_1\beta_1 \cos j_1 + \rho_2\beta_2 \cos j_2,$$

$$E = b\cos i_1/\alpha_1 + c\cos i_2/\alpha_2,$$

$$D = (\det \mathbf{M})/\alpha_1\alpha_2\beta_1\beta_2,$$

$$G = a - d\cos i_1 \cos j_2/\alpha_1\beta_2, \tag{5-3}$$

$$a = \rho_2(1-2\beta_2^2 p^2) - \rho_1(1-2\beta_1^2 p^2),$$

$$b = \rho_2(1-2\beta_2^2 p^2) + 2\rho_1\beta_1 p^2,$$

$$c = \rho_1(1-2\beta_1^2 p^2) + 2\rho_2\beta_2 p^2,$$

and

$$d = 2(\rho_2\beta_2^2 - \rho_1\beta_1^2).$$

$\mathbf{M}$ is the coefficient matrix containing all the parameters defined in Figure 5.1. i_1, i_2, j_1, j_2 are linked by Snell's Law: $\alpha_1/\sin(i_1) = \alpha_2/\sin(i_2) = \beta_1/\sin(j_1) = \beta_2/\sin(j_2) = 1/p$, where j_1 is the angle of incidence of the shear-wave and p is the ray parameter. Figure 5.2 defines the shear-wave polarization angle ψ.

Figure 5.3 shows the polarization angle and phase difference of the transmitted shear-wave, for an incident wave with equal amplitudes of *SH*- and *SV*-waves ($\psi_i = 45°$, and $B = 1$, which we shall call *SH45SV*), as functions of the angles of incidence for the two different interfaces (Table 5.1): (a) polarization angle and (b) phase difference for the L/H sandstone-to-halite interface; and (c)

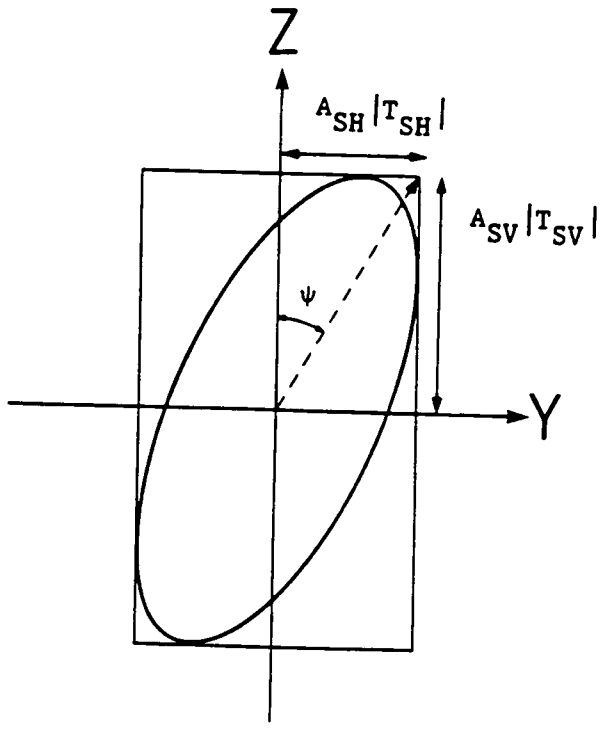

Figure 5.2 Definition of polarization angle ψ of a shear wave in the plane of constant phase. A_{SH} and A_{SV} are the amplitudes of *SH*- and *SV*-components, respectively, of the incident shear-waves. T_{SH} and T_{SV} are the transmission coefficients of *SH*- and *SV*-waves, respectively.

and (d) similar values for the H/L halite-to-sandstone interface. Figure 5.3a is a recalculation of Figure 9 in the paper by Douma and Helbig (1987), but for a full range of angles of incidence from 0° to 90°. We see that at normal incidence (i = 0°), the polarization and phase of the transmitted wave are unchanged. The deviation of the polarization and phase of the transmitted wave increases as the angle of incidence increases, reaching 3° for L/H and 2° for H/L at the smallest critical angle, $\sin^{-1}(V_{S1}/V_{P2})$ for L/H and $\sin^{-1}(V_{S2}/V_{P2})$ for H/L. Beyond these critical angles, the incident wave is totally reflected, and there are several inhomogeneous interface waves, with energy propagating parallel to, and decaying exponentially away from, the interface.

5.2.2 Interface waves

When a linearly polarized plane shear-wave is transmitted through an isolated isotropic-to-isotropic interface, within the innermost window (incidence less than the smallest critical angle), the phase and the (linear) motion of the incidence wave are preserved. The particle motion becomes elliptical only for the angles of incidence greater than the smallest critical angle. There are usually three possible critical angles for L/H ($V_{P1} < V_{P2}$, $V_{S1} < V_{S2}$) defined, in order of increasing angle, by:

$$\alpha_{c1} = \sin^{-1}(V_{S1}/V_{P2}),$$

$$\alpha_{c2} = \sin^{-1}(V_{S1}/V_{P1}), \qquad (5\text{-}4)$$

and

$$\alpha_{c3} = \sin^{-1}(V_{S1}/V_{S2}),$$

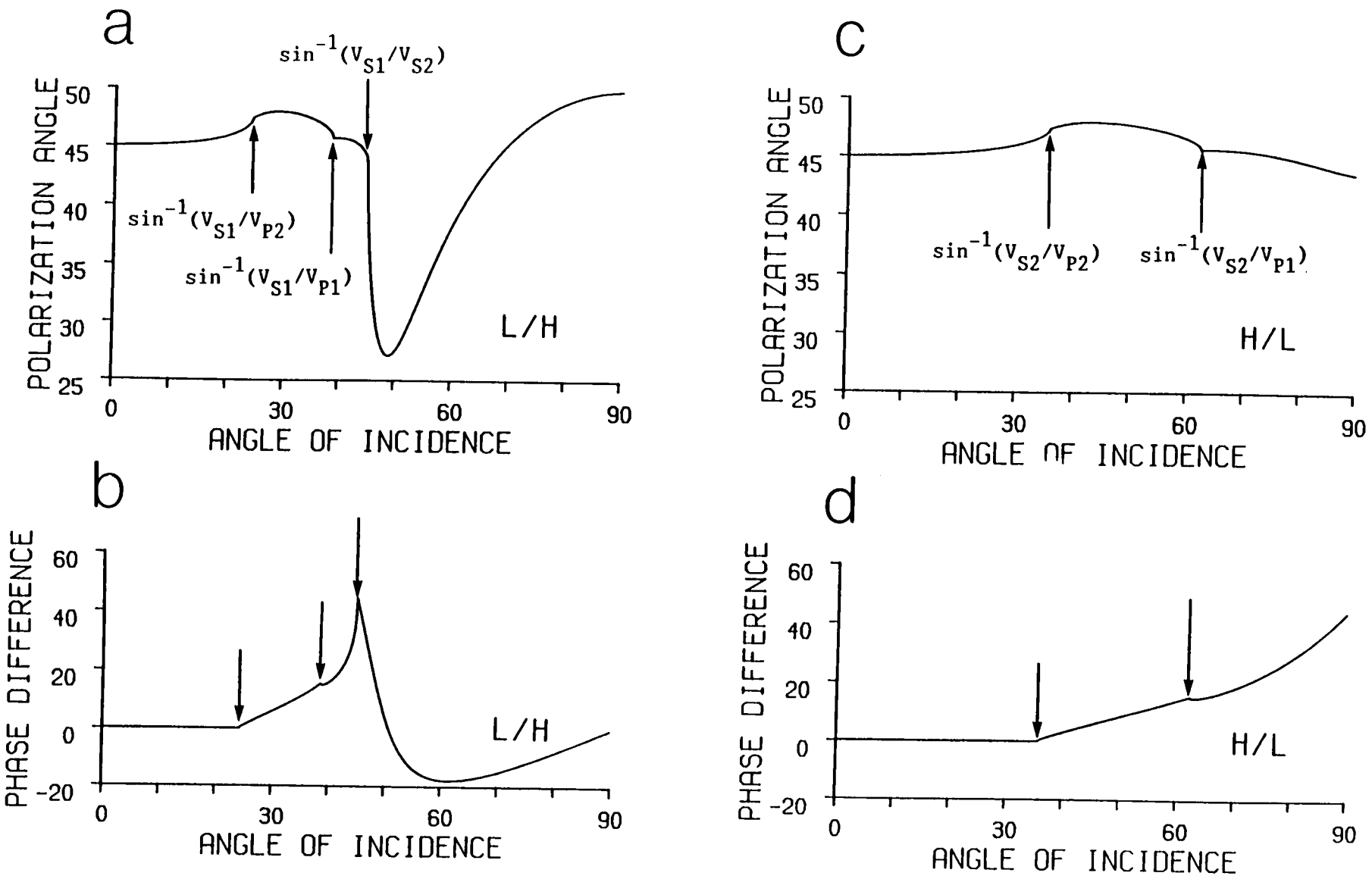

Figure 5.3 (*a*) and (*c*) Polarization angle ψ of transmitted shear waves, and (*b*) and (*d*) phase differences, as functions of incident angles j_1 for (*a*) and (*b*) sandstone-to-halite interface, L/H, and (*c*) and (*d*) halite-to-sandstone interface, H/L. The raypaths at critical angles of incidence are marked with arrows.

and two critical angles for H/L ($V_{P1} > V_{P2}$, $V_{S1} > V_{S2}$, $V_{P1} > V_{S2}$) defined by:

$$\alpha_{c4} = \sin^{-1}(V_{S2}/V_{P2}),$$

and (5-5)

$$\alpha_{c5} = \sin^{-1}(V_{S2}/V_{P1}).$$

As the angle of incidence exceeds the smallest critical angle, the coefficients of the previously real transmitted wave become complex (Appendix A), and the resultant inhomogeneous interface waves are elliptically polarized. The polarization ellipse in the plane containing *SH*- and *SV*-components was described by Smith and Ward (1974); Kanasewich (1981); and Bullen and Bolt (1985), and is determined by the following equation:

$$\sin^2(\Delta\phi) =$$

$$y^2/(A_{SH}\,T_{SH})^2 + z^2/(A_{SV}\,T_{SH})^2 - 2yz\cos(\Delta\phi)/(A_{SH}A_{SV}\,T_{SH}T_{SV}), \quad (5\text{-}6)$$

where the phase difference ($\Delta\phi$) is $\Delta\phi = \phi_{SH} - \phi_{SV}$, and ϕ_{SH} and ϕ_{SV} are the phase angles of *SH*- and *SV*-waves, respectively.

The equation (5-6) is also valid for wave propagation in anisotropic media, where two split shear-waves denoted by q_{S1} (faster) and q_{S2} (slower) will replace *SH* and *SV*-wave in isotropic media, and $\Delta\phi$ becomes the phase difference caused by time delay between two split shear-waves (Shih *et al.* 1988). The equation (5-6) becomes linear in two cases: (1) $\Delta\phi = 0, \pi, 2\pi \ldots n\pi$, where

n is an integer, and (2) only one of the shear-wave (*SH* or *SV* in isotropic media, and q_{S1} or q_{S2} in anisotropic media) is excited by the source.

As angles of incidence exceed the critical angles at which the reflected or refracted ray grazes the interface, that ray ceases to exist as a body ray. There is a redistribution of energy flux among the remaining waves leaving the interface, accompanied by phase shifts, and there are exponentially decreasing inhomogeneous interface waves (three for L/H and two for H/L). Each interface wave carries energy parallel to the interface with velocity equal to the phase velocity of the incident shear-wave along the interface (Hudson 1980a; Kennett 1983). A schematic illustration of all possible interface waves at a solid-to-solid interface is shown in Figure 5.4 (after Çerveny and Ravindra 1971).

The polarization angles show abrupt changes at the three critical angles (24.34°, 38.27°, and 44.91°) for L/H (Figure 5.3a) and two (35.73° and 61.32°) for H/L (Figure 5.3b), which correspond to the excitation of transmitted *P*-wave, reflected *P*-wave, and transmitted shear-wave grazing the interface (for H/L the transmitted shear-wave cannot become imhomogeneous). Particular for L/H, if the angle of incidence is greater than the greatest critical angle of α_{c3} = 44.91°, the transmitted shear-wave becomes evanescent and all the waves except the reflected shear-wave generated by the incident shear-wave become inhomogeneous, and are replaced by the corresponding interface waves with complex coefficients. Under these circumstances, the deviation of the polarization angle is up to 20°, and the phase difference between the *SH*- and *SV*-waves is up to ±20°. It follows therefore, that the critical angle α_{c3} =

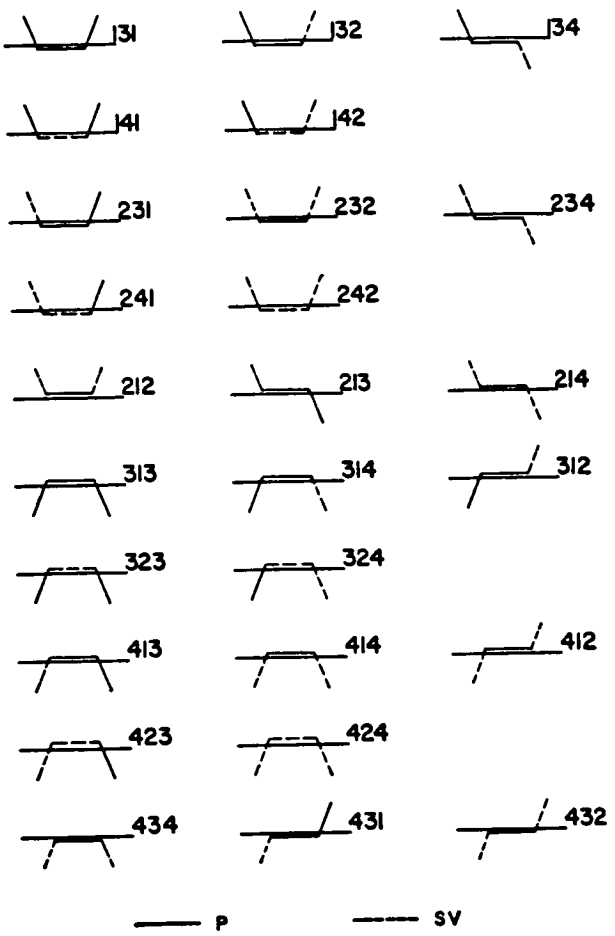

Figure 5.4 Schematic representation of all the possible types of *P* and *SV* head waves (26) for a single isotropic solid-to-solid interface. these waves cannot exist simultaneously. Each type of head wave is characterized by three numbers (see details in Cerveny and Ravindra, 1971, P.117).

$\sin^{-1}(V_{S1}/V_{S2})$ is crucial for L/H. We see that particle motions are strongly elliptical for L/H, if the critical angle α_{c3} is approached, whereas, they are less elliptical for H/L as the largest deviation is only 4°, which in many circumstances may be negligible.

5.2.3 Polarizations of shear-waves with curved wavefronts at isotropic-to-isotropic interfaces

The variations of PDs of transmitted *SH45SV*-waves radiated from a point source 1 km above L/H and H/L interfaces have been calculated for an equi-spaced grid of geophones with the simple geometry of Figure 5.5. The lines in Figure 5.5 mark the raypaths at critical angles of incidence for the L/H interface. The source time function is

$$F(t) = \exp(-2\pi f t)\sin(2\pi f t), \qquad (5.7)$$

where f is dominant frequency, which is 25 Hz in the modelling. Figure 5.6 shows the source pulse and its Fourier spectrum. The PDs for L/H and H/L are presented in Figures 5.7 and 5.8, respectively. No distance-dependent normalization has been applied to the particle motions and *true* relative amplitudes are shown for a fixed amplitude incident wave. Note that the PDs in Figures 5.7 and 5.8 refer to vertical, and horizontal radial and transverse planes.

The raypaths at critical angles of incidence are drawn in Figures 5.7 and 5.8. The critical raypaths mark successive increases of ellipticity of the polarization diagrams for the near-interface recording points. At greater distance from the interface, the polarization diagrams only show minor differences on either side of

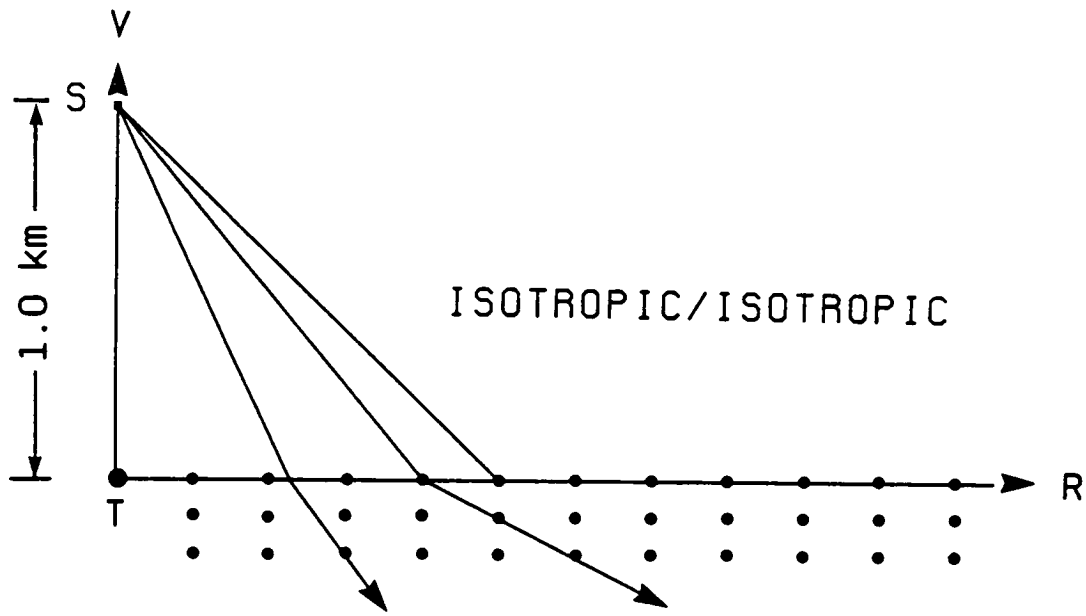

Figure 5.5 Schematic illustration of the model for shear-wave propagation across a plane isotropic-to-isotropic interface at a range of angles of incidence. A 20 Hz point source is located 1 km above the interface. The transmitted shear-waves are recorded at depths of 0.001, 0.1, and 0.2 km below the interface. Three critical angles defined by $\alpha_{C1} = \sin^{-1}(V_{S1}/V_{P2})$, $\alpha_{C2} = \sin^{-1}(V_{S1}/V_{P1})$, $\alpha_{C3} = \sin^{-1}(V_{S1}/V_{S2})$ for L7H are indicated. The wavelengths of the shear waves are 95 m in the sandstone and 135 in the halite.

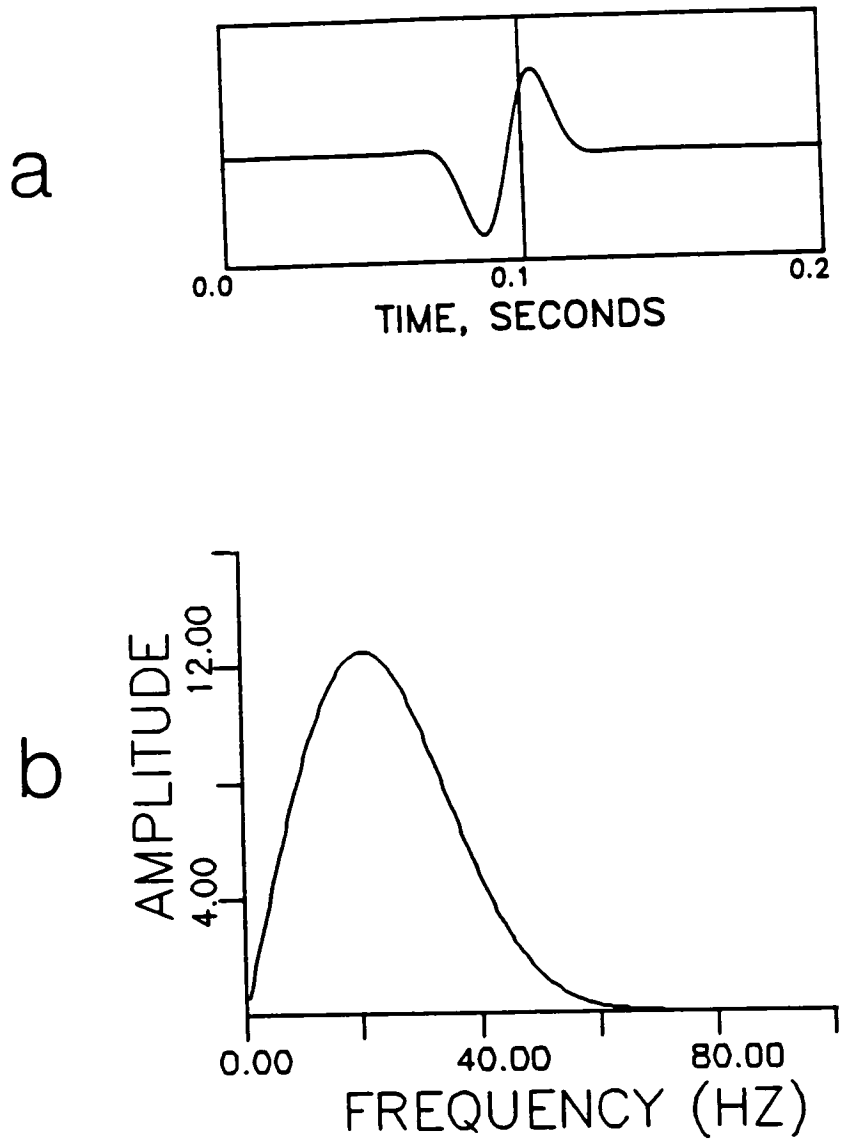

Figure 5.6 (*a*) source time function in our modelling, and (*b*) spectrum of source time function (*a*) with dominant frequency of 20 Hz.

the raypath of critical incidence. The vertical-transverse plane for the L/H interface in Figure 5.7 shows most ellipticity, but in all cases the ellipticity is comparatively weak except at large angles of incidence. Note that for H/L in Figure 5.8, shear-wave particle motion displays very little ellipticity. The results shown here are in general consistent with the theoretical behaviour of plane shear waves at an internal interfaces in Figure 5.3. The small differences are caused by the differences between plane and curved wavefronts at an interface.

The presence of several critical angles of incidence at a plane interface makes the behaviour of shear waves at an internal interface more complicated, but the effects (of transmission) are less severe, than the behaviour at the free surface. At the free surface, a shear wave arriving outside the shear-wave window is very severely distorted (Booth and Crampin 1985). At an internal interface, except for large angles of incidence, the principal effects of the interface are confined to interface waves at and beyond the critical angles. We may define an internal shear-wave window in the same way as that at the free surface as the range of incident angles, within which the shear-waves are recorded with little distortion at the interface. Critical angles are exactly defined and mark abrupt changes of particle motions only for plane waves, similar to the behaviour at the shear-wave window at the free surface (Booth and Crampin 1985), On curved wavefronts as in Figures 5.7 and 5.8, the effects of the critical angle are spread over a range of angles, the exact behaviour for any particular geometry depending on the curvature of the wavefront and the frequency of the incident shear wave.

Figure 5.7 Polarization diagrams of shear-waves on sagittal plane, marked (V)ertical and (R)adial; in the (V)ertical and (T)ransverse plane; and the horizontal (R)adial and (T)ransverse plane, transmitted through a sandstone-to-halite (L/H) interface from a point source with the geometry in Figure 5.5. The incident pulse is a 20 Hz *SH45SV*-wave. The raypaths at the critical angles of incidence are shown.

Figure 5.8 The notation is the same as in Figure 5.7, but for halite-to-sandstone (H/L) interface.

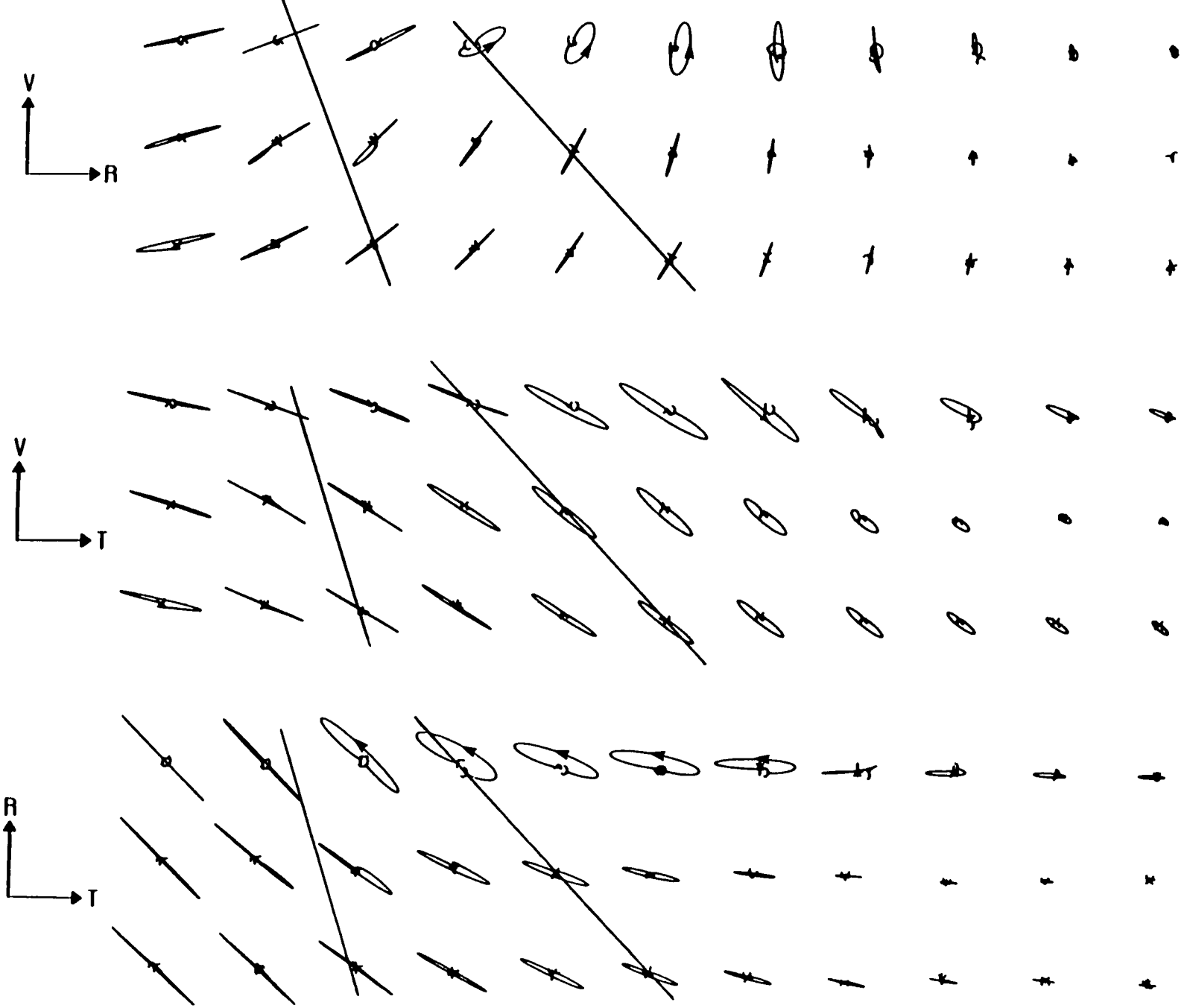

Figure 5.7

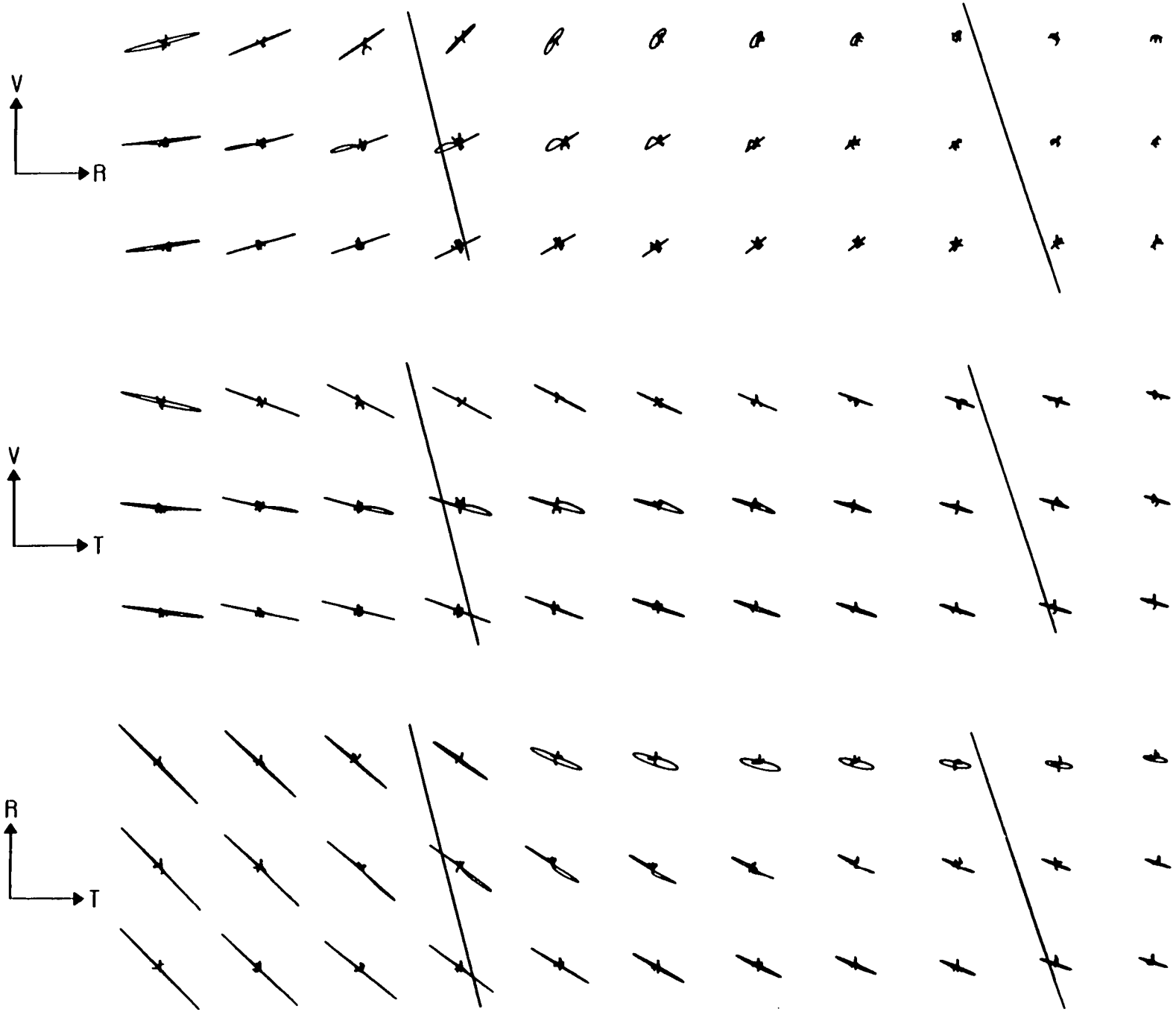

Figure 5.8

5.2.4 Comparison of the effects of interfaces and anisotropy-induced shear-wave splitting

We calculate the behaviour of shear waves at an isotropic-to-anisotropic interface (Figure 5.9), where the anisotropy is caused by EDA-cracks. Figure 5.10 shows the variations of velocities of seismic body waves in parallel fluid-filled microcracks, and equal-area projections of the polarizations and delays between the split shear-waves in three dimensions (see detailed explaination in Chapter 3).

Figures 5.11, 5.12, 5.13, and 5.14 show polarization diagrams of shear waves below an isotropic/anisotropic interface with the same geometry as the L/H interface as in Figure 5.7 with the cracks striking 0°, 30°, 60°, and 90°, respectively, clockwise from the transverse direction, relative to the source/geophone spread. The velocities of the uncracked matrix are the same as halite in Figure 5.7 so that the behaviour of shear wave at isotropic/isotropic and isotropic/anisotropic interfaces may be compared directly. The effects of the anisotropy only begin to be visible when the pathlength through the anisotropy is long enough for shear-wave splitting to separate the two waves. Consequently, the polarizations of shear-waves immediately below the interface are very similar to those for the isotropic/isotropic interface in Figure 5.7, and a change from linear to elliptical motion occurs at the critical angle of incidence.

At receivers further from the interface, the shear waves propagate for greater distances through the effective anisotropy and the effects of the anisotropy-induced shear-wave splitting become dominant on the polarization diagrams, particularly in the

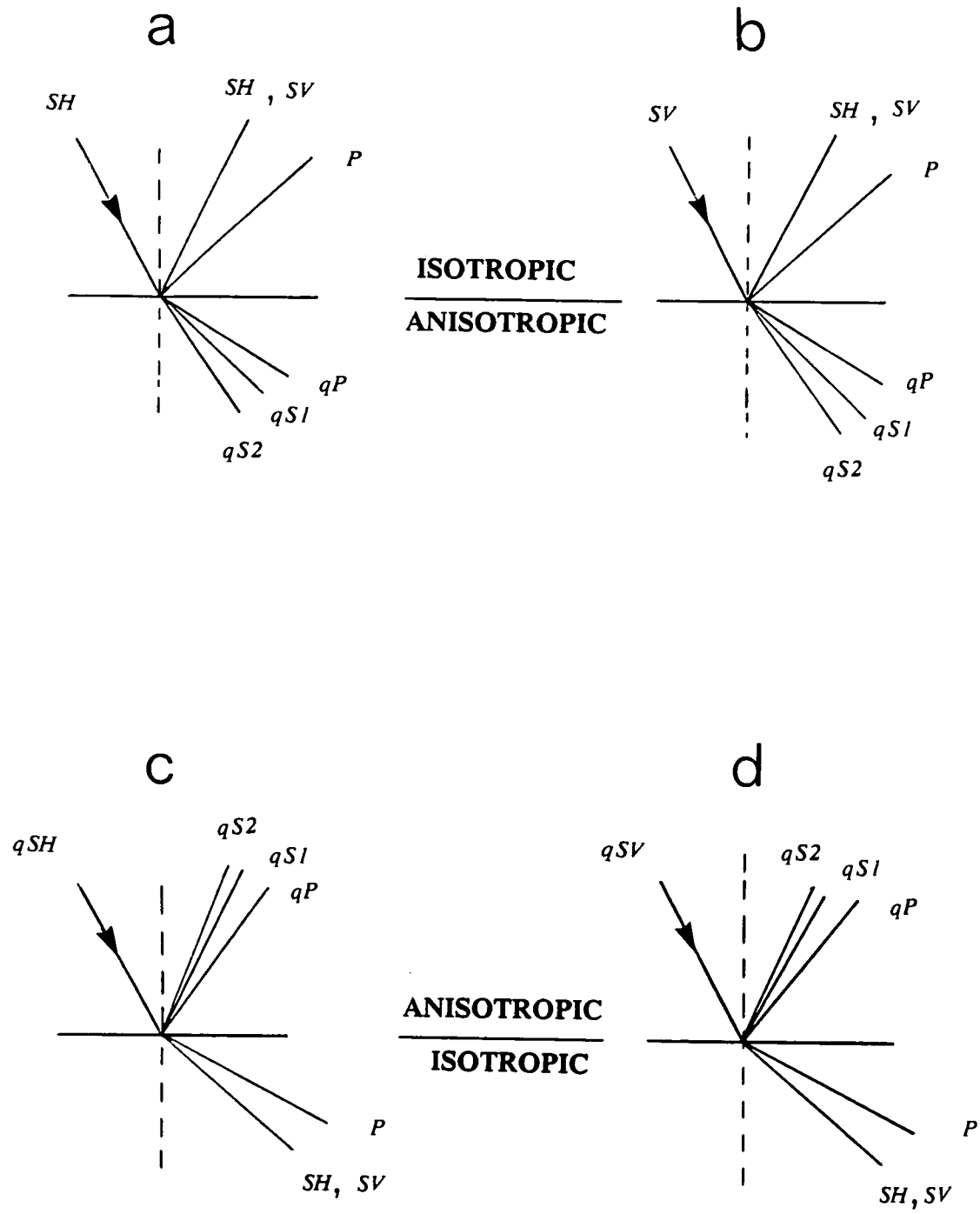

Figure 5.9 Schematic diagrams of reflected and transmitted waves generated by (*a*) *SH*-wave and (*b*) *SV*-wave incident from an isotropic-to-anisotropic interface, and (*c*) *qSH*-wave and (*d*) *qSV*-wave from an anisotropic-to-isotropic interface.

Figure 5.10 Theoretical behaviour of seismic waves in rocks containing thin parallel liquid-filled microcracks calculated with the techniques of Crampin (1984) using the formulations of Hudson (1980b, 1981). The crack density is $\mathcal{CD} = 0.1$, and the velocities in the uncracked isotropic matrix are those of halite (Table 5.1). (*a*) velocity variations with propagation directions from normal (0°) to parallel (90°) to the cracks. The shear-wave *qSR* is polarized at (**R**)ight angles, and *qSP* (**P**)arallel, to the plane of incidence through the crack normal. (*b*) Horizontal equal-area projections out to 90° of the polarizations (top) and time delays (bottom) of split shear-waves passing through the cracked rock with the crack vertical and striking east-west. The inner circle represents the shear-wave window at the free surface at the critical angle incidence angle of 35°. The bars in the polarization plot are horizontal projections of the polarizations of the leading (faster) split shear-waves. The delays are normalized to milliseconds per 1 km pathlength. To the left is a north-south section of the contoured plot.

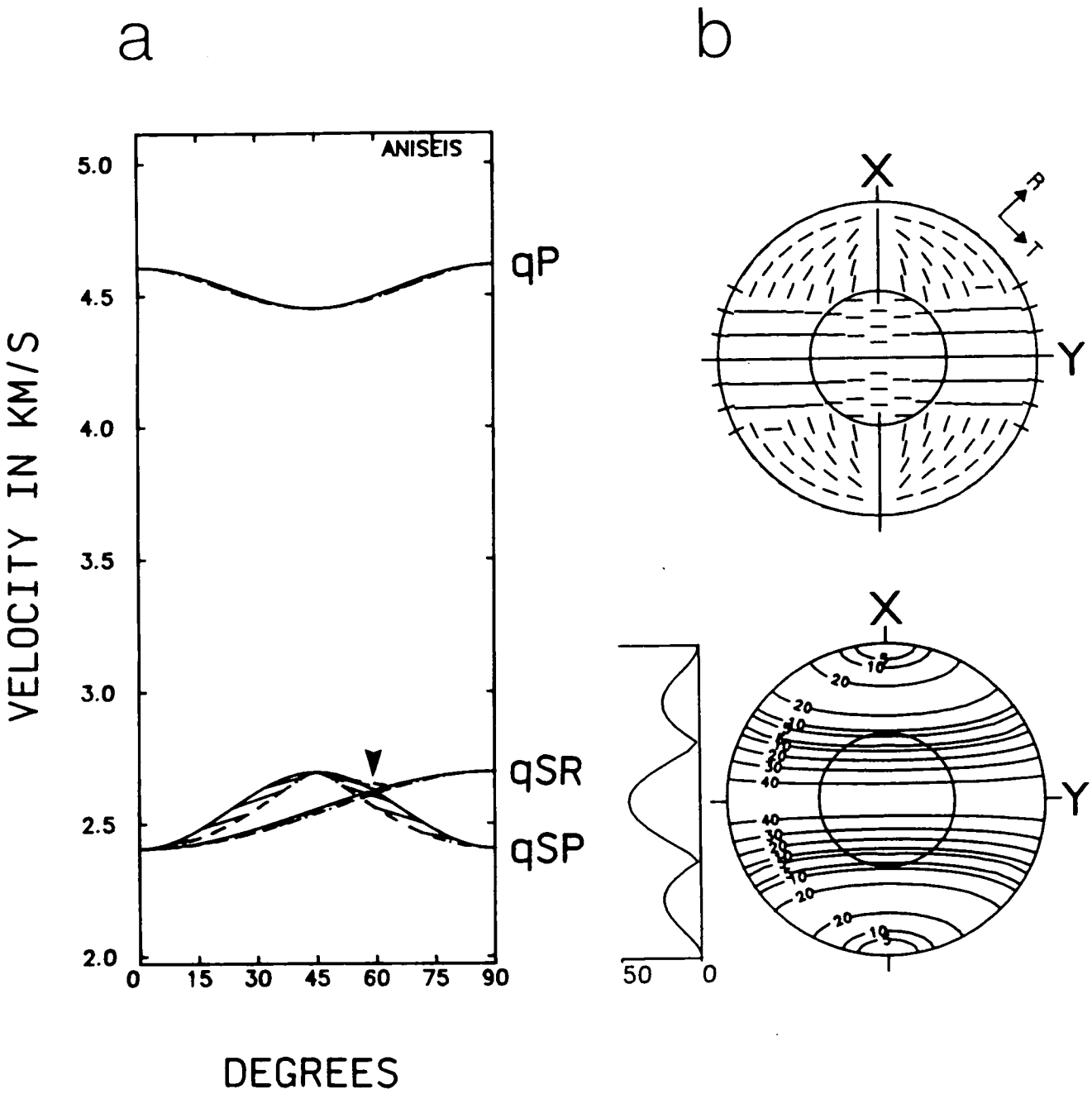
a
b
ANISEIS
5.0
4.5
4.0
3.5
3.0
2.5
2.0
VELOCITY IN KM/S
qP
qSR
qSP
0
15
30
45
60
75
90
DEGREES
X
Y
R
T
50
0

Figure 5.10

Figure 5.11 Same as Figure 5.7, but for an istropic-to-anisotropic interface. The anisotropy is a distribution of parallel vertical thin fluid-filled cracks in a halite matrix with crack density 0.1 in Figure 5.10, with crack striking perpendicular to the source/geophone spread. The takeoff directions of initial shear-wave motion are marked with large arrowheads and the direction with small arrowheads.

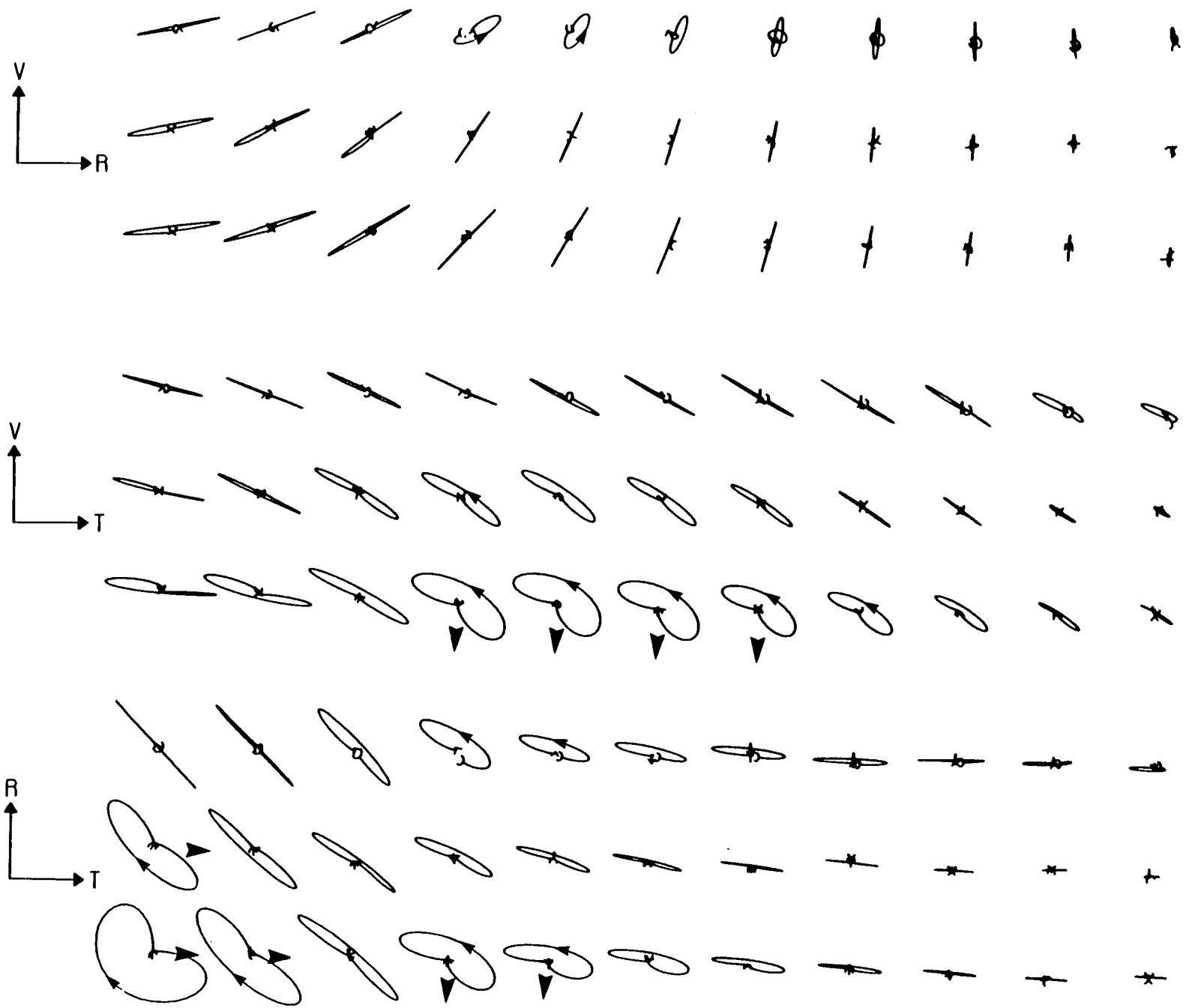

Figure 5.11

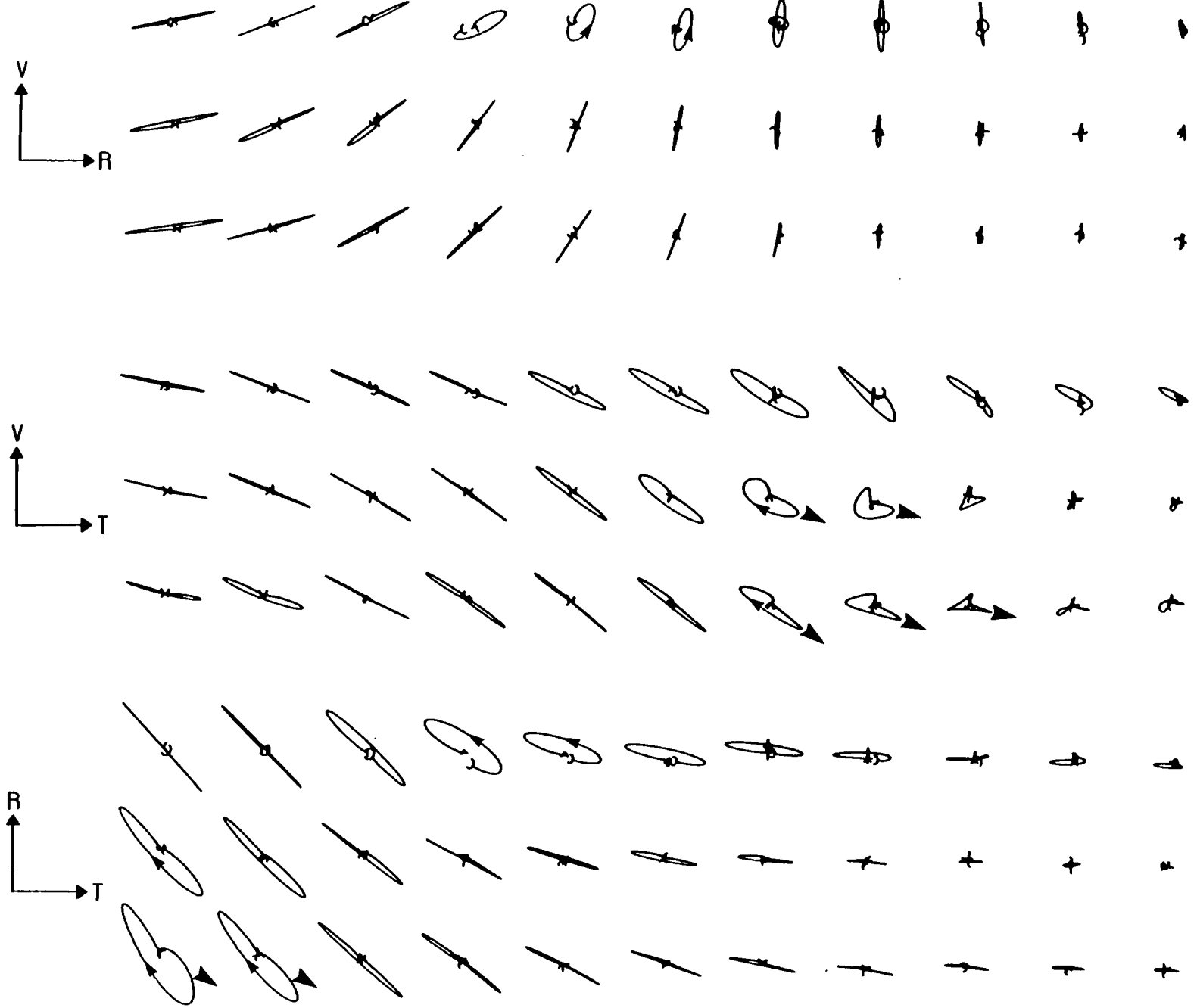

Figure 5.12 Same as Figure 5.11, but crack striking 30° clockwise from transverse direction.

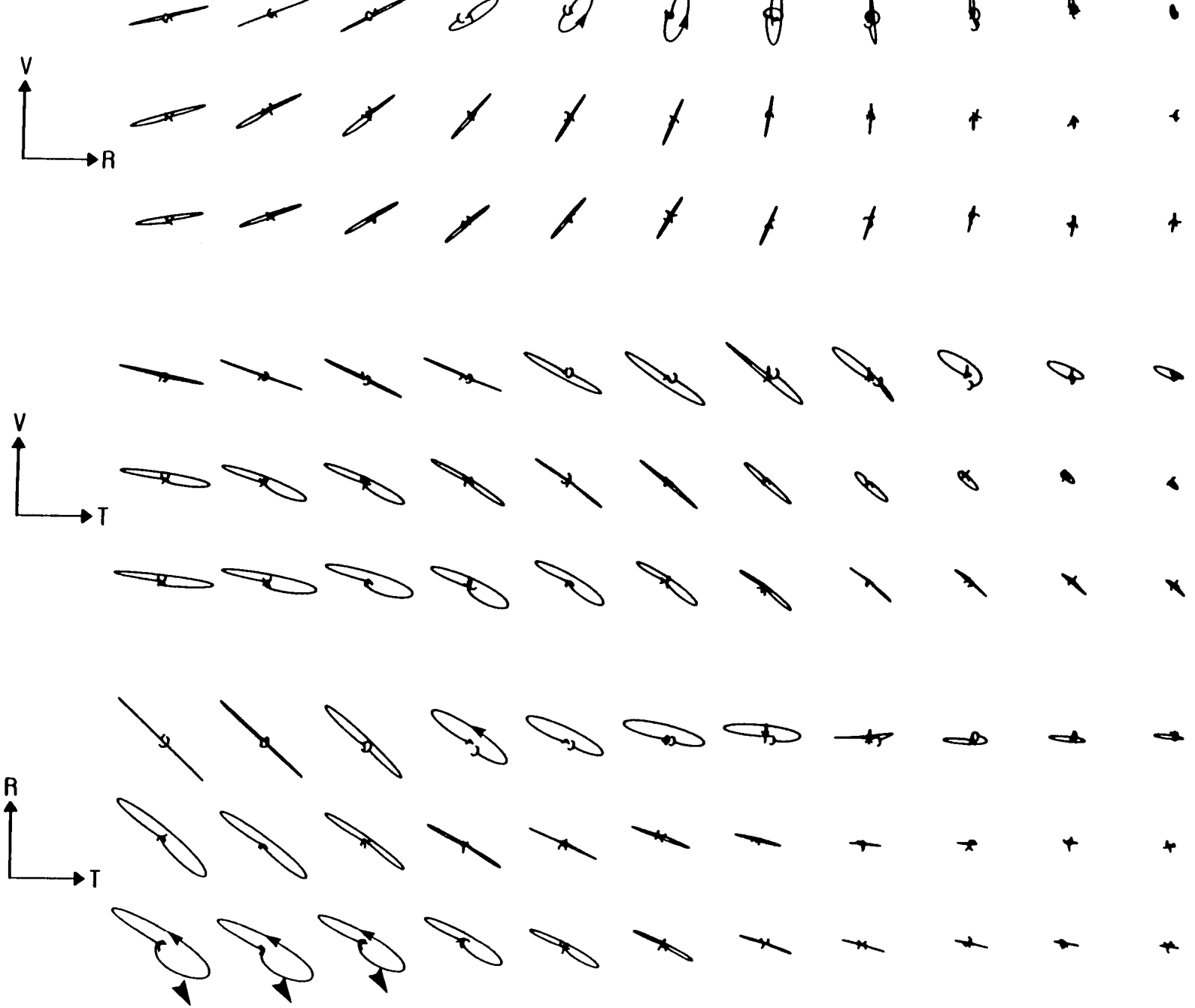

Figure 5.13 Same as Figure 5.11, but crack striking 60° clockwise from transverse direction.

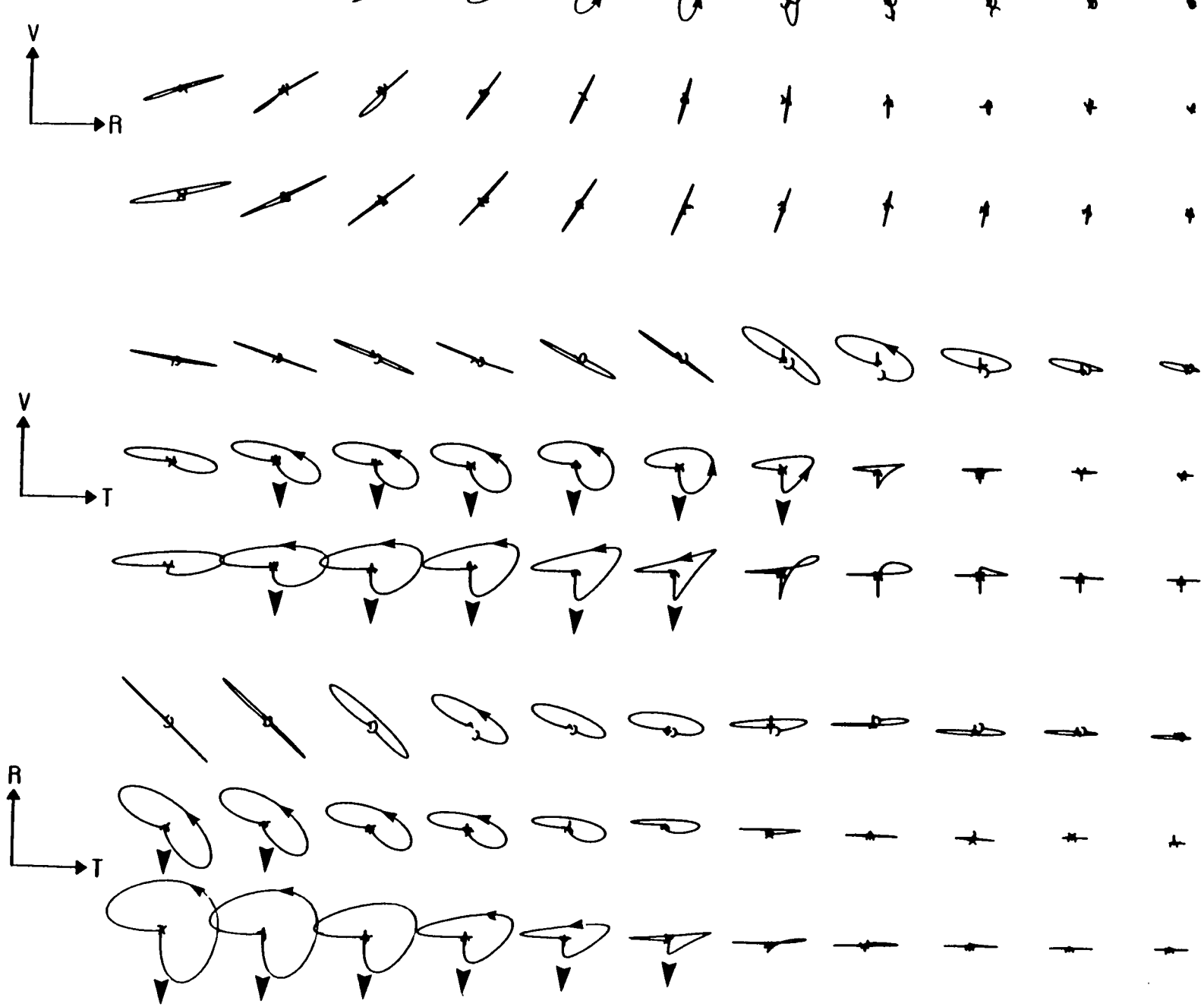

Figure 5.14 Same as Figure 5.12, but crack striking 90° clockwise from transverse direction.

horizontal and transverse planes. The shear-wave polarization diagrams in the horizontal plane show strong ellipticity (pronounced splitting) at small angles of incidences, where the first motions marked with arrowheads are parallel to the strikes of the aligned cracks in all cases as in the equal-area projection of the polarizations (of plane-wave) in Figure 5.10.

In Figures 5.11 and 5.12, there is a sudden change in shear-wave PDs in the horizontal (radial-transverse) planes for the deeper geophones, where the rotation direction of particle motions changes from clockwise to linear and then to anticlockwise. This phenomena is caused by the behaviour of shear waves through the cracked medium shown in Figure 5.10. The change in the direction of rotation is due to the intersection of the velocity curves of the two split shear-wave polarizations at 60° from the crack normal (30° from vertical) marked with an arrowhead in Figure 5.10a. The polarization of the faster split shear-wave changes by approximately 90° on crossing this intersection. In Figures 5.13 and 5.14, the raypaths do not cross this intersection. In Figure 5.7 without anisotropy, the shear-waves are linearly polarized except at large angles of incidence.

The shear-wave splitting is a diagnostic characteristic of shear waves propagating through cracked and anisotropic solids. The orientations of the split shear-waves are determined by the anisotropic symmetry of the medium in which the geophone is situated, not the polarization of the incident shear-wave. Thus, any disturbance to the shear-wave polarizations caused by the interface, may change the relative properties of the split shear-waves into which the initial pulse splits, but will not alter

the polarizations of the split components. The shear-wave splitting in Figures 5.11 to 5.14 shows several distinctive differences from the elliptical polarizations associated with interfaces in Figures 5.7 and 5.8. Within the shear-wave window [incidence angle less than $\sin^{-1}(V_{S1}/V_{P2})$ for L/H and $\sin^{-1}(V_{S2}/V_{P2})$ for H/L], the linear polarizations of the incident wave are preserved by the interface, whereas when enough anisotropic path has been traversed to separate the split shear-waves, distinct shear-wave splitting may be seen. In particular, the polarization of the leading (faster) split shear-wave is controlled by the orientation of the anisotropy (the strike of the EDA-cracks) not the polarization of the incident wave. This means that the small distortions in polarization introduced by the interface suggested by Figure 5.3, will modify the details of the pattern in the PDs, but will not alter the polarization direction of the leading split shear-wave.

The polarizations of the faster split shear-waves in Figures 5.11 to 5.14 for incidence angles less than about 45°, are similar to the polarizations in the equal-area projection in Figure 5.10 for plane wave propagation. At wider angles of incidence the equal-area projections are less satisfactory, and the polarizations (heavy arrows) in these figures compare well with theoretical polarizations for plane wave propagation in the Plate Carrée projection in Liu *et al.* (1989) and also Chapter 3.

5.2.5 The effect of source orientations

Figure 5.15 shows polarization diagrams in the horizontal radial-transverse plane for six equi-spaced values of the source polarization from 0° to 90°. The model of an isotropic layer (250 m) above a cracked anisotropic layer (350 m) overlying an isotropic

Table 5.2. VSP model parameters used in Figure 5.15

	Thickness (m)	V_P (m/s)	V_S (m/s)	ρ (gcm^{-3})
Isotropic	250	4000	2310	2.3
Anisotropic	350	Matrix velocities as above. Vert. Parall. Cracks. CD = 0.1		
Isotropic halfspace	∞	4500	2598	2.6

Elastic constants of the anisotropic layer

	(1,1)	(2,2)	(3,3)	(2,3)	(1,3)	(1,2)
(1,1)	35.628					
(2,2)	11.864	36.670				
(3,3)	11.864	12.124	36.670			
(2,3)	0.000	0.000	0.000	12.273		
(1,3)	0.000	0.000	0.000	0.000	9.781	
(1,2)	0.000	0.000	0.000	0.000	0.000	9.781

Figure 5.15 Synthetic polarization diagrams in the radial-transverse plane of 20 Hz shear-waves propagating through a model containing 6 geophones spanning an anisotropic layer (Table 5.2), calculated for six different source orientations with values indicated below each column. This is a VSP model with the offset of 50 m, and 6 geophones are down a borehole. The anisotropy is simulated by thin vertical aligned fluid-filled cracks striking 30° from transverse directions (clockwise) with crack density $CD = 0.1$. The takeoff directions of initial shear-waves are marked with arrowheads.

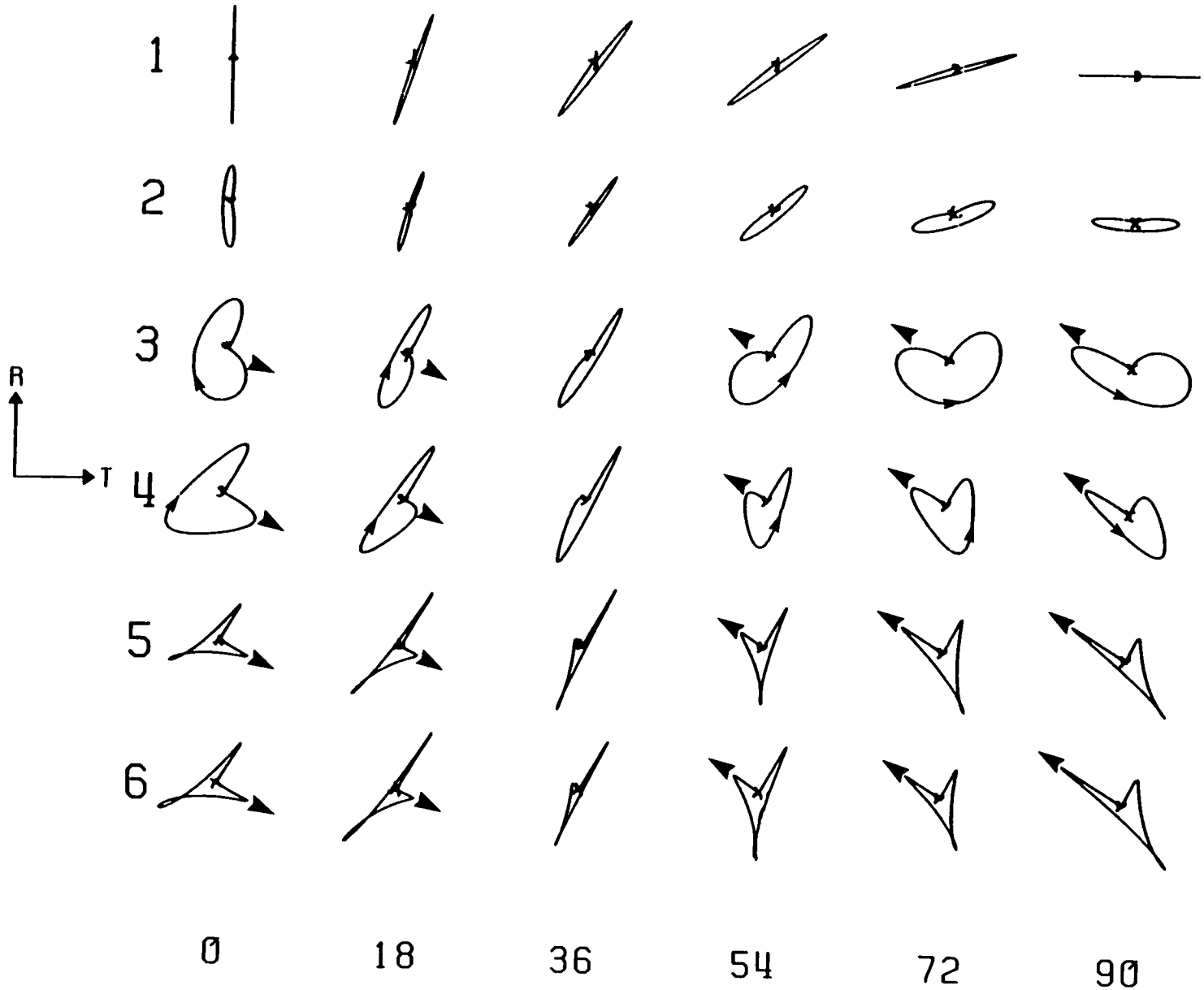

Figure 5.15

halfspace is given in Table 5.2. The cracks strike 30° clockwise from the transverse direction as in Figure 5.12. This is a VSP model with an offset of 50 m and six geophones are located down a borehole every 100m between 200 and 700m from the surface. The uppermost geophone is in the isotropic layer, the second is immediately below the interface between the two layers, and the other four geophones are in the anisotropic layer and the halfspace. It is seen that the shear waves at the upper geophones in the isotropic layer are linearly polarized in the same directions as the incident waves (source polarization). The second geophone shows a little ellipticity due to the effect of a short path in the anisotropic medium. The PDs at the deeper geophones (3 to 6) all display shear-wave splitting. The directions of polarization of the leading faster shear-waves (marked with arrowheads) are all parallel and in the fixed direction determined by the particular path through the anisotropic symmetry, despite the different polarizations of the incident shear-waves. This direction is fixed for a particular raypath to a geophone (see Figure 5.10). The pattern traced out in the PDs varies with the polarization of the incident wave, but the initial takeoff angle (shown by the arrowheads in Figure 5.15) is the same for parallel cracks as indicated by the projections of the polarizations in Figure 5.10.

Shear-wave splitting occurs when a shear-wave passes through anisotropic rock, whereas elliptical motions due to interface scattering exist only when a shear-wave is incident upon an interface with angles of incidence larger than the critical angles. The ellipticity caused by interfaces is most marked when the shear wave is recorded near the interface. The split phases have polarizations parallel and perpendicular to the plane of incidence.

5.3 Effects of interfaces on reflected shear-waves (Part II)

As a complete investigation of interface effects, we now turn to reflected shear-waves. The procedure follows that for transmitted shear-waves. We first examine the plane wave polarization of a reflected shear-wave at two kinds of interfaces (L/H and H/L). Synthetic seismograms are then calculated for a simple model to show the distortion of particle motions due to the plane boundary. We shall also demonstrate the effect of anisotropy on amplitude-versus-offset (AVO) and limitation of reflection seismics in analyzing shear-wave data in the presence of anisotropy.

5.3.1 Polarization angles

The polarization angle (ψ_r) of a plane shear-wave reflected at an interface is defined in the same way as for the transmission (5.1):

$$\psi_r = \tan^{-1}(B\, R_r), \tag{5.8}$$

where $B = A_{SH}/A_{SV}$, $R_r = R_{SH}/R_{SV}$, and R_{SH} and R_{SV} represent the reflection coefficients of *SH*- and *SV*-waves, respectively, which are functions of the material properties ρ_1, V_{P1}, V_{S1}, and ρ_2, V_{P2}, V_{S2} and angle of incidence j_1 (for simplicity, V_P and V_S are replaced by α and β, respectively, in the following equations).

$$R_{SH} = [\rho_1\beta_1\cos(j_1) - \rho_2\beta_2\cos(j_2)]/\Delta, \tag{5.9}$$

and

$$R_{SV} = -\left\{ b\,\frac{\cos(j_1)}{\beta_1} - c\,\frac{\cos(j_2)}{\beta_2} \right\} E/D +$$

$$\left\{ a + d \frac{\cos(i_2)\cos(j_1)}{\alpha_2 \beta_1} \right\} Gp^2 / D. \qquad (5.10)$$

The parameters Δ, E, D, G, a, b, c, and d are all functions of the properties of the materials [equation (5.3)].

Figure 5.16 shows the amplitudes of the reflection coefficents of plane *SV*- and *SH*-waves incident at the isotropic-to-isotropic interfaces. The curves are similar to those (square root energy-ratios) calculated with the program listed in Young and Braile (1976) as used by Crampin (1987b). The behaviour is complicated for wide incident angles, where the behaviour of the coefficients for L/H and H/L velocity contrasts is different. There is a zero point (indicated by an arrow), which corresponds to the incident angle of 15.03° for *SV*-wave (Figure 5.16a) and 26.48° for an *SH*-wave (Figure 5.16b), for the L/H interface (sandstone-to-halite), and 19.53° for an *SV*-wave (Figure 5.16c) and 39.15° for an *SH*-wave (Figure 5.16d) for the H/L interface (halite-to-sandstone). At these angles of incidence, there is no corresponding reflected wave. Table 5.3 is a summary of the critical angles and zero value incident angles. The presence of these zero values in reflection coefficients makes reflected shear-waves more complicated than the corresponding transmitted waves. This can be clearly seen in the polarization angle and phase difference curves in Figure 5.17, which we are now described.

Figure 5.17 show the polarization angle ψ_r and phase difference of the reflected shear-wave, for an incident *SH45SV*-wave, as functions of incident angle for two different interfaces (with the same notation as in Figure 5.3). Like transmitted shear-waves, the polarization and phase of the incident wave are preserved at normal

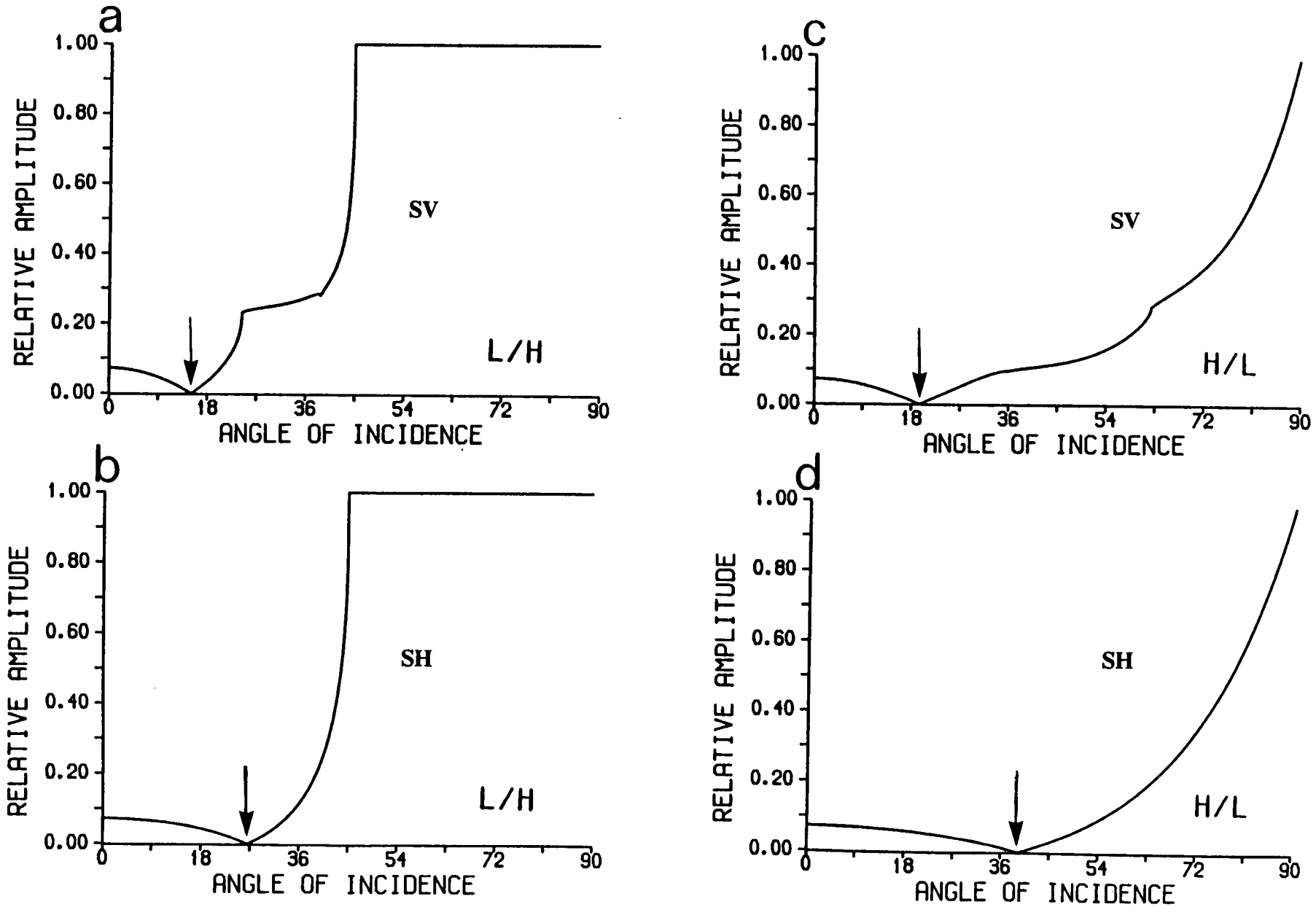

Figure 5.16 (*a*) and (*c*) Reflection coefficients of *SV*-waves, and (*b*) and (*d*) *SH*-waves, as functions of incident angles for (*a*) and (*b*) sandstone-to-halite interface, L/H, and (*c*) and (*d*) halite-to-sandstone interface, H/L. The incident angles at which reflection coefficients are zero are marked with arrows.

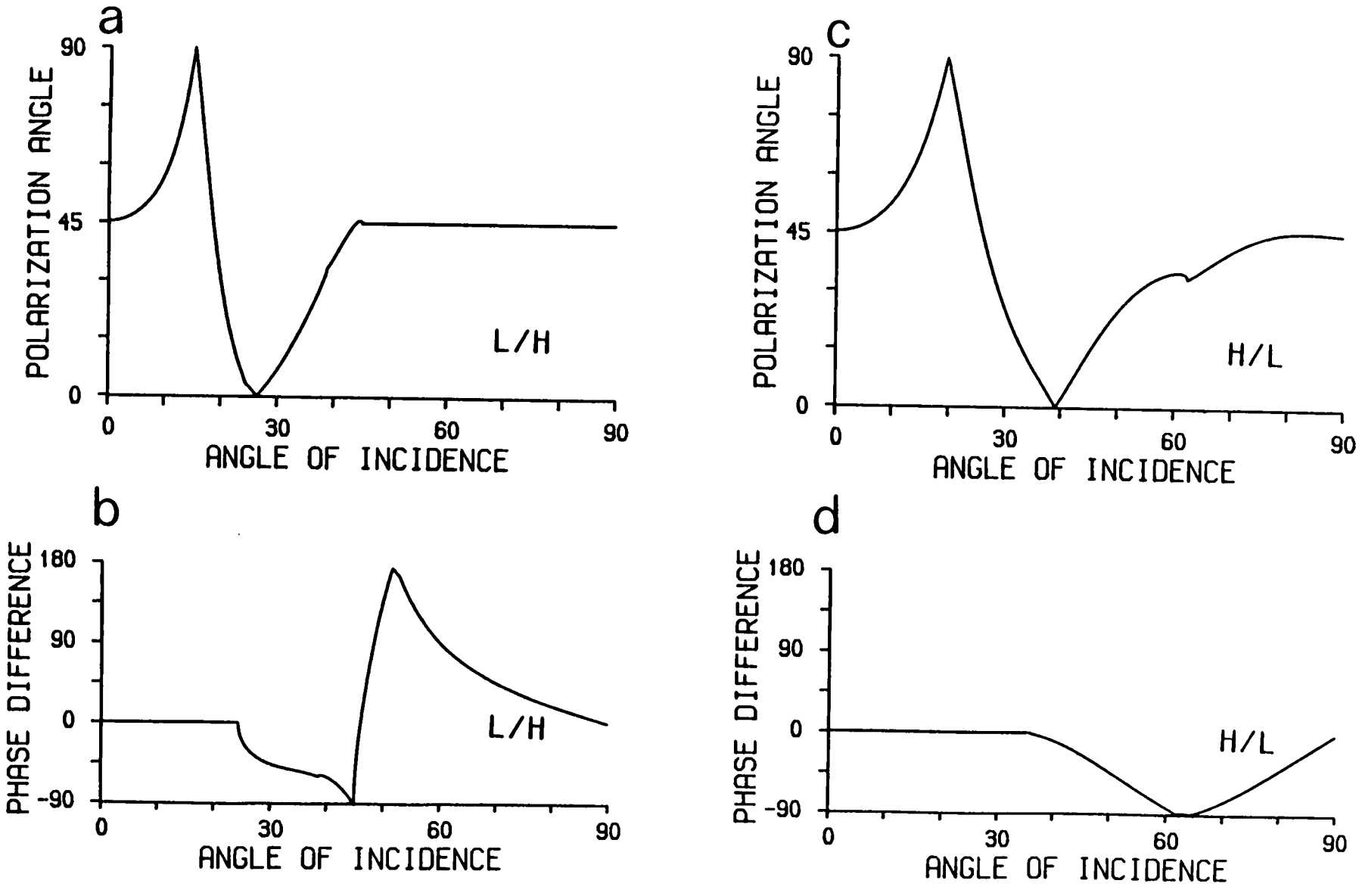

Figure 5.17 Same as Fingure 5.3, but for reflected shear-waves.

Table 5.3 Summary of special incidence angles in the text

	Critical angles			Zero values in refl. coefficients	
	α_1	α_2	α_3	*SV*	*SH*
L/H	24.34	38.27	44.91	15.03	26.48
H/L	35.73	61.32	——	19.53	39.15

Note: L/H: sandstone/halite interface

H/L: halite/sandstone interface

incidence (j_1 = 0°). When the angle of incidence is small (less than about 5°), there is only a small change in polarization. At the angle where the *SV*-wave reflection coefficient becomes zero (R_{SV} = 0) , the polarization is pure *SH*-motion (ψ_r = 90°). Similarly, at the angle where the *SH*-wave reflection coefficient becomes zero (R_{SH} = 0), the polarization is pure *SV*-motion (ψ_r = 0°). The maximum polarization change can be as large as 90° irrespective of the incident shear-wave polarization (between pure *SH*-motion and pure *SV*-motion). After the above changes the reflected shear-wave polarization returns to the source polarizations when the angle of incidence is greater than the largest critical angle (α_{c3} = 44.91°). Unless the source is of pure *SH*-motion (ψ_r = 90°) or pure *SV*-motion (ψ_r = 0°), such a sequence of change of reflected shear-wave polarizations is always possible if there is a sufficient coverage of the incident angles. For the H/L interface (Figure 5.17c) the behaviour of polarization angles is similar to these for the L/H interface at small angles of incidence. At the angle of incidence greater than the largest critical angle (α_{c5} = 61.32°), the polarization angle changes gradually until it reaches the source polarization (ψ_r = 45°), instead of keeping constant as for the L/H interface.

As with the polarization variations, the relative phase differences between *SH*- and *SV*-waves also show considerable change (Figure 5.17b, d). At small angles of incidence there is no phase difference, consequently the shear-wave polarizations radiated from the source will be either preserved as a shear-wave penetrates isotropic plane boundaries, or the polarity will be reversed. If

the phase difference is not 0° or 180°, the resultant shear-wave particle motion will be elliptical. The ellipse depends on the phase shift between the *SH*- and the *SV*-waves (equation 5.6). When phase changes are considered, change in reflected shear-wave polarization can be as large as 180°.

Comparing Figure 5.17 with its counterpart for transmitted shear-waves (Figure 5.3), it is easily seen that the distortion of the polarization angle and the phase of the incident shear-wave after reflection is much more severe than that for transmitted shear-waves. We will demonstrate, in the following section, how the reflected shear-wave polarization is distorted in synthetic seismograms.

5.3.2 Distortion of particle motions of synthetic seismograms from a point source

Figures 5.19 and 5.20 show three-component seismograms calculated for the model shown in Figure 5.18 for L/H and H/L interfaces, respectively. The corresponding polarization diagrams are presented in Figures 5.19d (L/H) and 5.20d (H/L) (direct waves are not included in the calculations). The seismograms and the particle motions are plotted with *true* relative amplitudes and no normalization has been applied. The source is the same as previous modelling for transmitted waves (equation 5.7). *Note that the effect of the free surface has not been considered*, and therefore any anomaly we shall see is due to the reflecting boundary.

The minima in Figures 5.19 and 5.20 are indicated in synthetic seismograms by arrowheads, which are in different positions for the radial and transverse components. This is a result of zero values

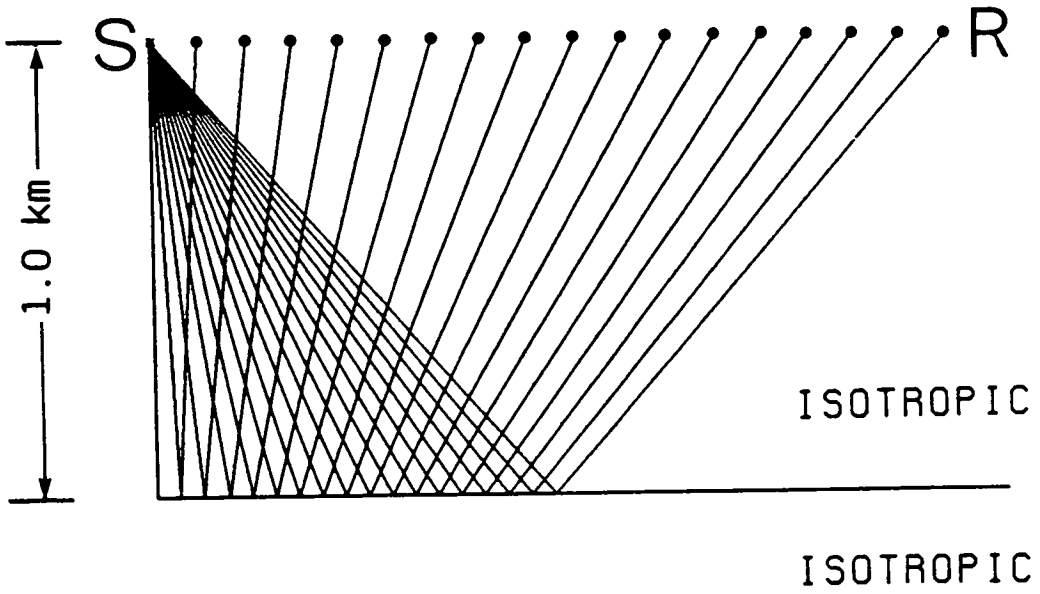

Figure 5.18 Raypaths of a reflection model. Both source (S) and the line of receivers (R) are located 1 km above the interface. The receivers are 100 m apart.

Figure 5.19 Synthetic seismograms of the vertical, and horizontal radial and transverse components (*a* to *c*) and polarization diagrams (*d*) of shear-waves reflected at a sandstone-to- halite interface (L/H) from a point source with the geometry in Figure 5.18. The incident pulse is a 20 Hz *SH45SV*-wave. The seismograms and PDs are plotted with true relative amplitudes and no normalization has been applied. The free surface effect is not included. The incident angles corresponding to the minima of amplitudes in radial and transverse components are indicated by a solid arrow in (*b*) and (*c*). The change of polarization is also indicated in (*d*) (see details in the text).

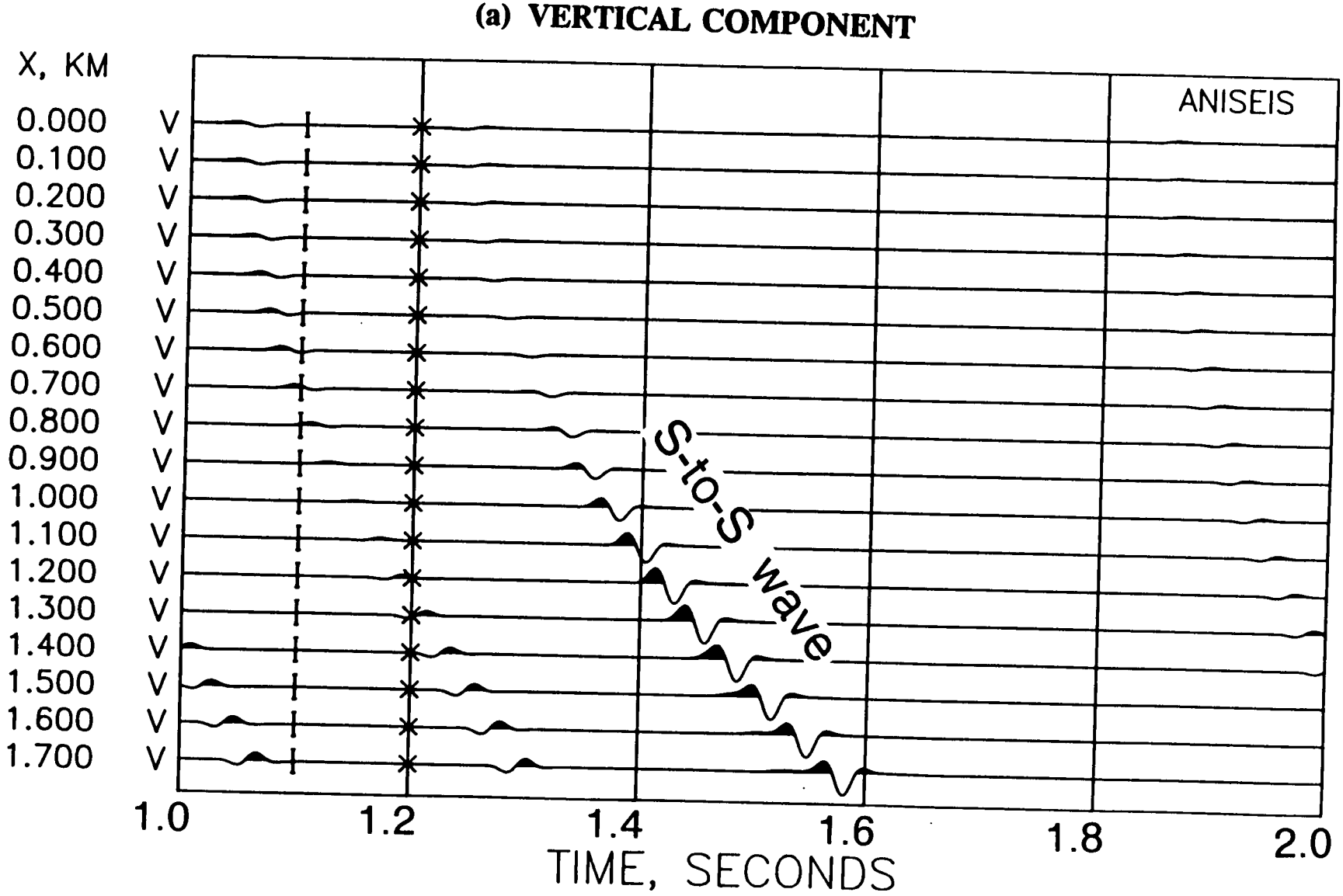
(a) VERTICAL COMPONENT
X, KM
0.000 V
0.100 V
0.200 V
0.300 V
0.400 V
0.500 V
0.600 V
0.700 V
0.800 V
0.900 V
1.000 V
1.100 V
1.200 V
1.300 V
1.400 V
1.500 V
1.600 V
1.700 V
ANISEIS
S-to-S wave
1.0
1.2
1.4
1.6
1.8
2.0
TIME, SECONDS

Figure 5.19 (a)

(b) RADIAL COMPONENT

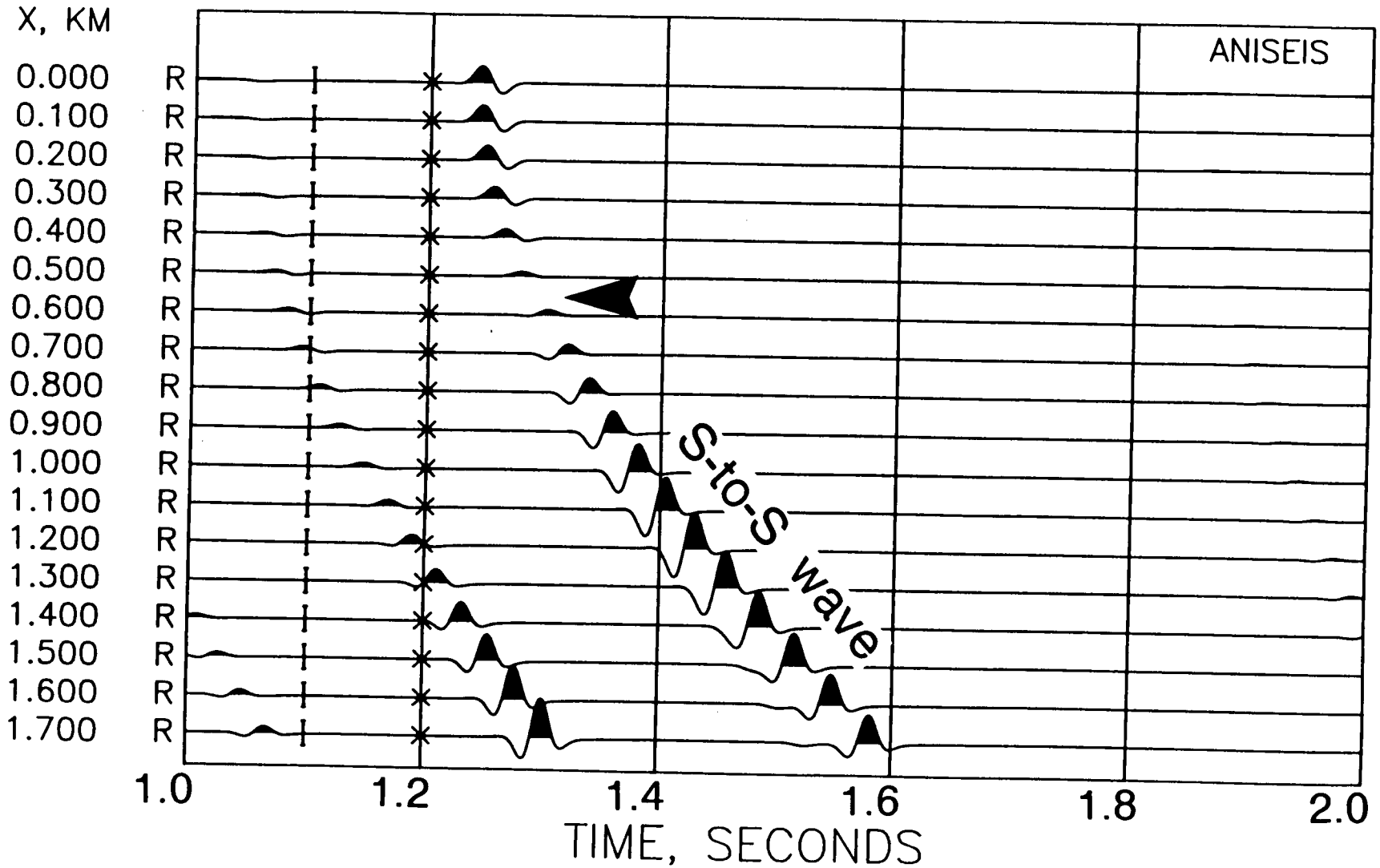

Figure 5.19 (b)

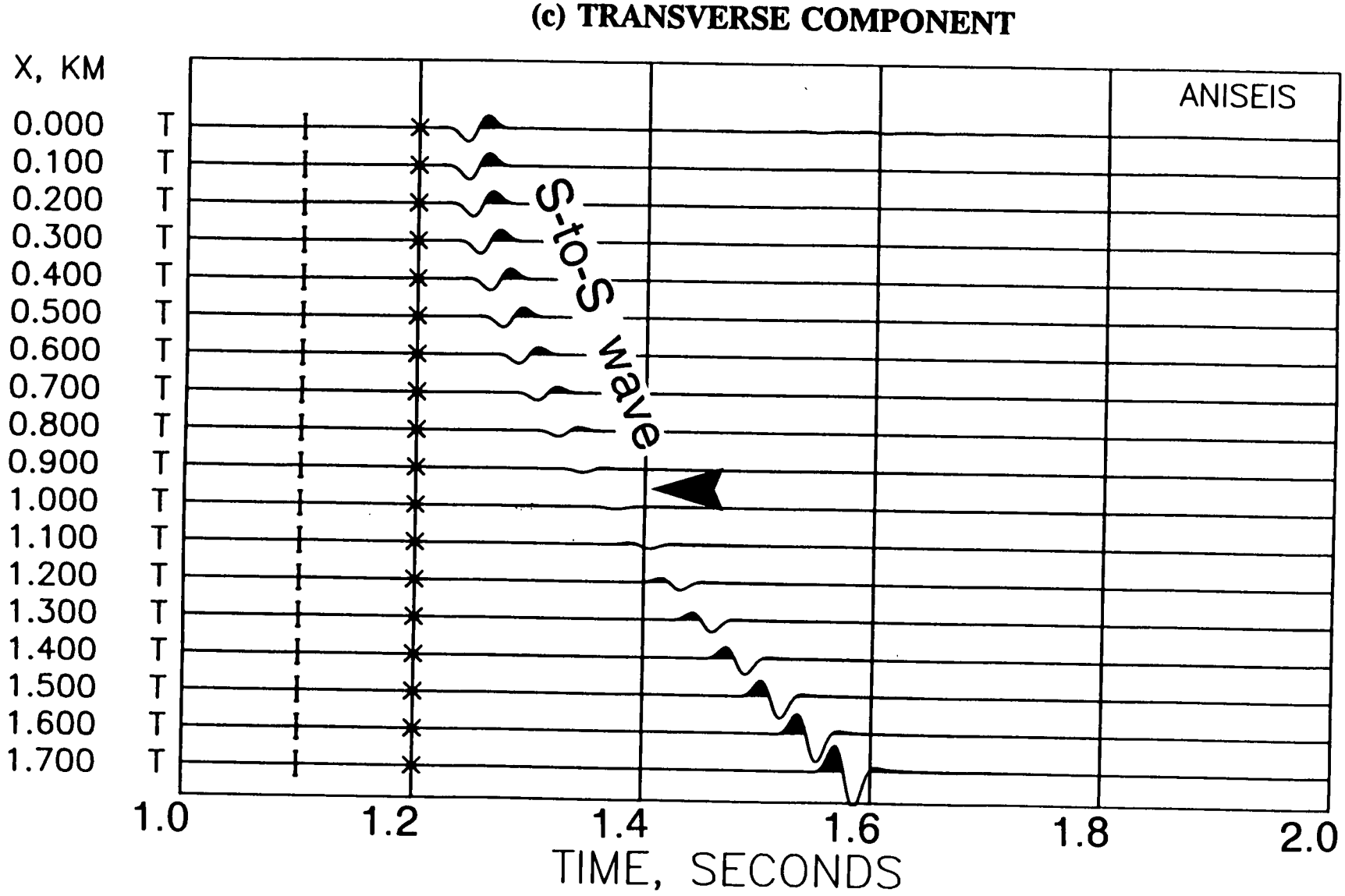
(c) TRANSVERSE COMPONENT
X, KM
0.000 T
0.100 T
0.200 T
0.300 T
0.400 T
0.500 T
0.600 T
0.700 T
0.800 T
0.900 T
1.000 T
1.100 T
1.200 T
1.300 T
1.400 T
1.500 T
1.600 T
1.700 T
ANISEIS
S-to-S wave
1.0
1.2
1.4
1.6
1.8
2.0
TIME, SECONDS

Figure 5.19 (c)

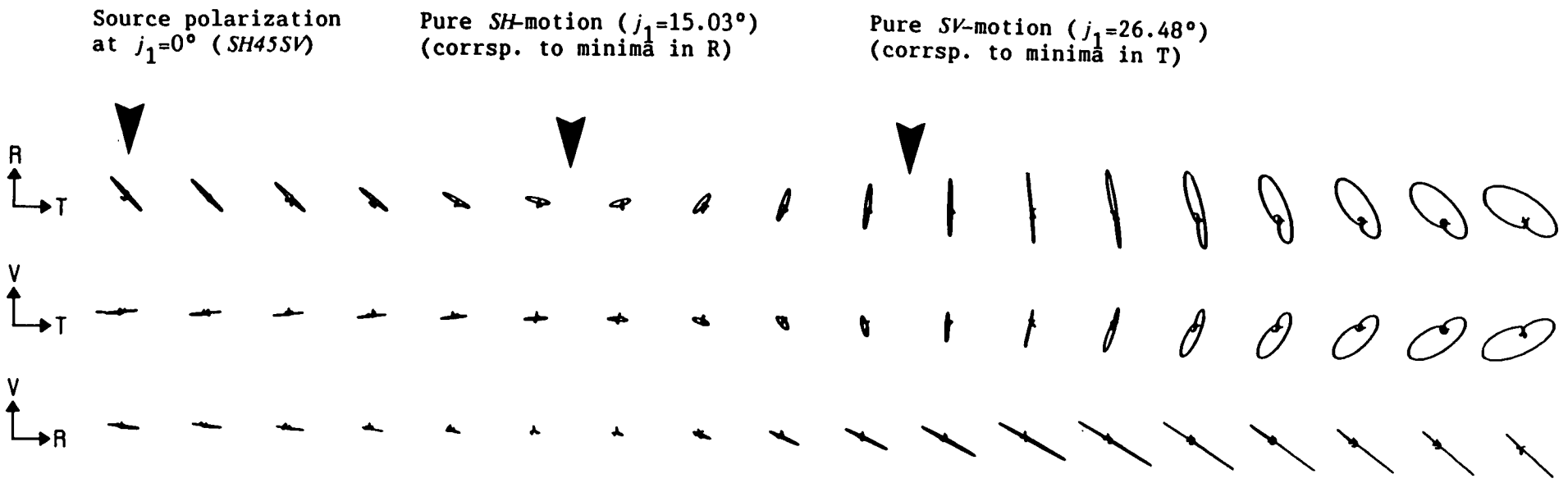
Source polarization
at j_1=0° (*SH45SV*)
Pure *SH*-motion (j_1=15.03°)
(corrsp. to minima in R)
Pure *SV*-motion (j_1=26.48°)
(corrsp. to minima in T)
R
T
V
T
V
R

Figure 5.19 (d)

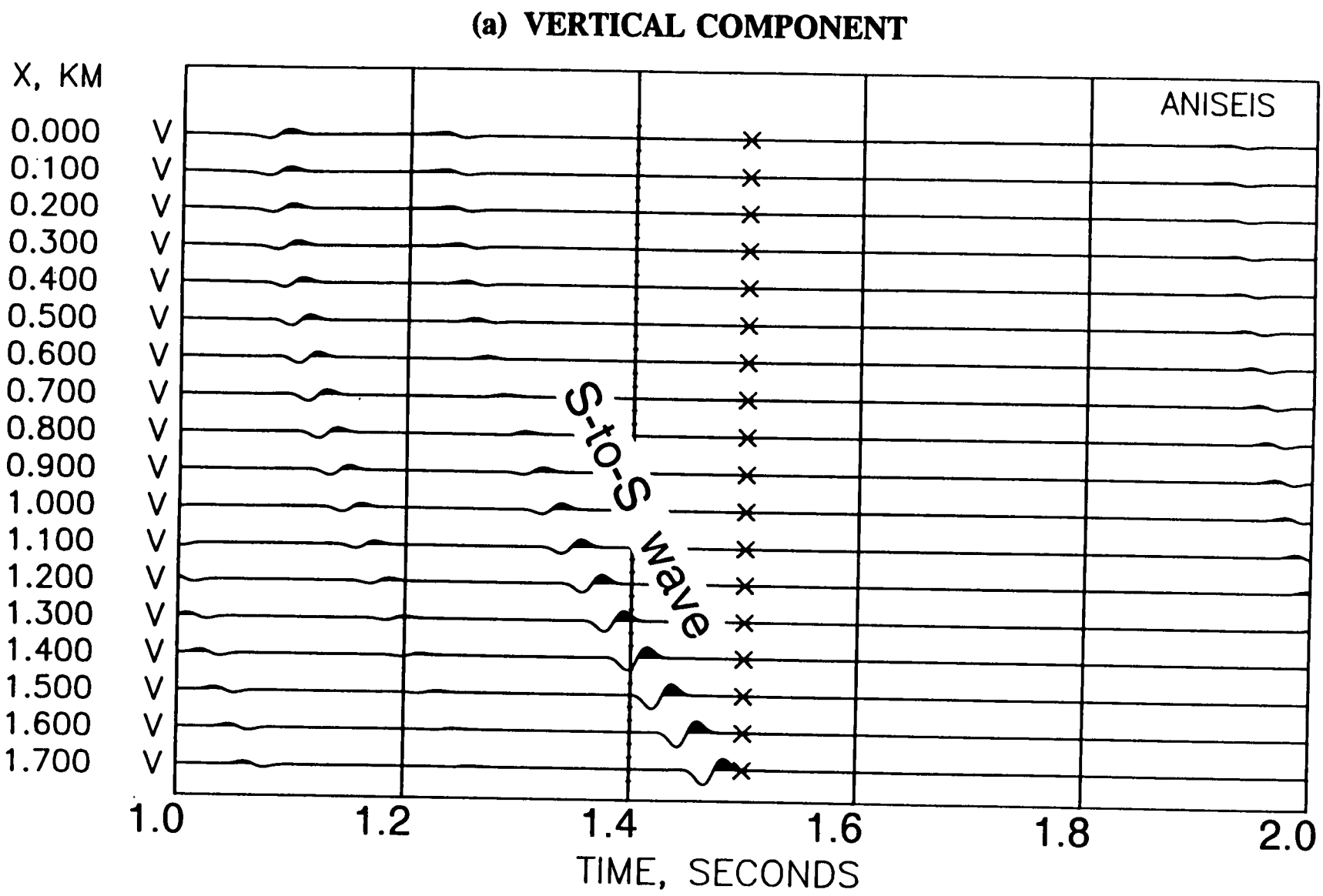

Figure 5.20 Same as Figure 5.19, but for the halite-to-sandstone interface (H/L).

Figure 5.20 (a)

(b) RADIAL COMPONENT

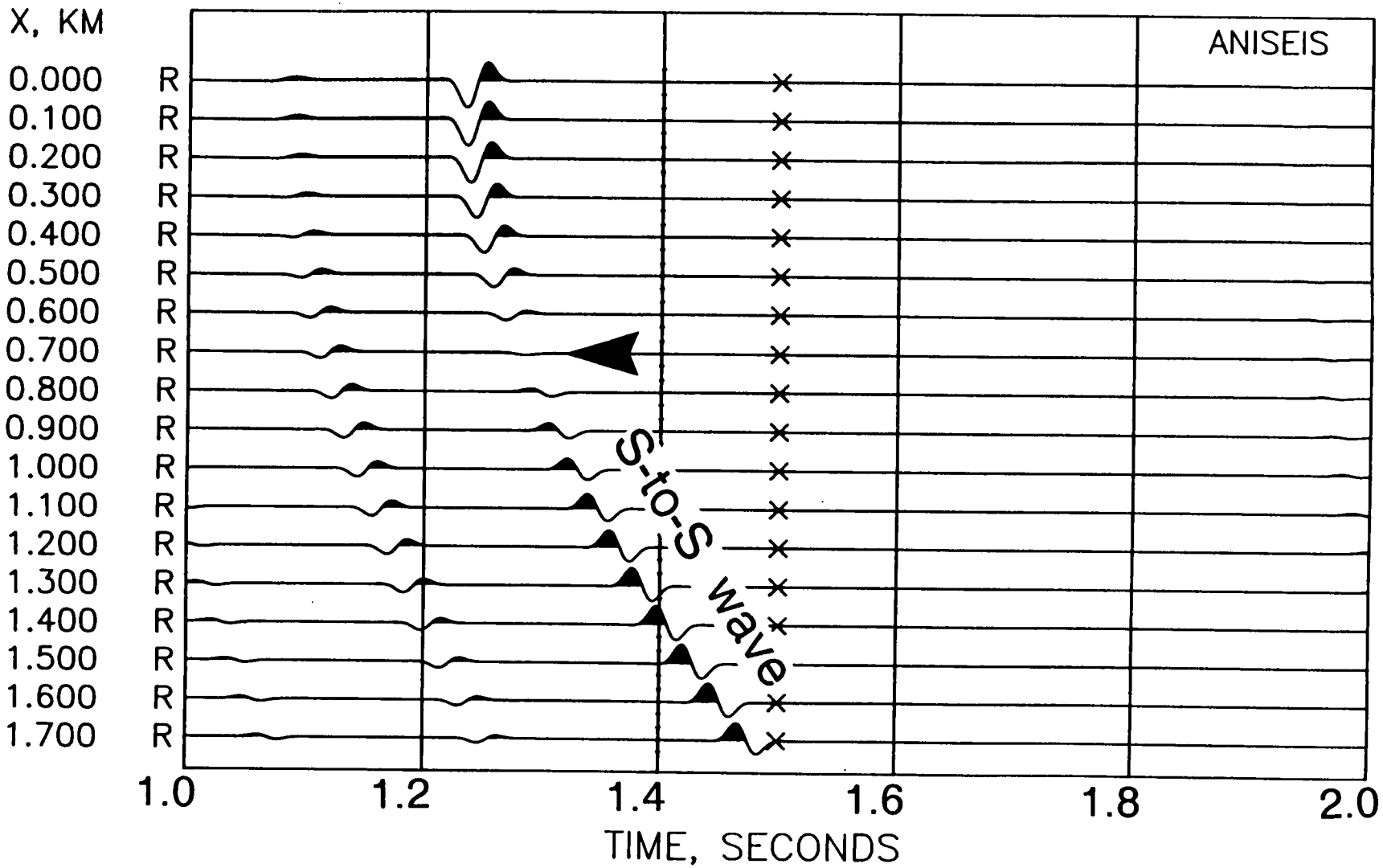

Figure 5.20 (b)

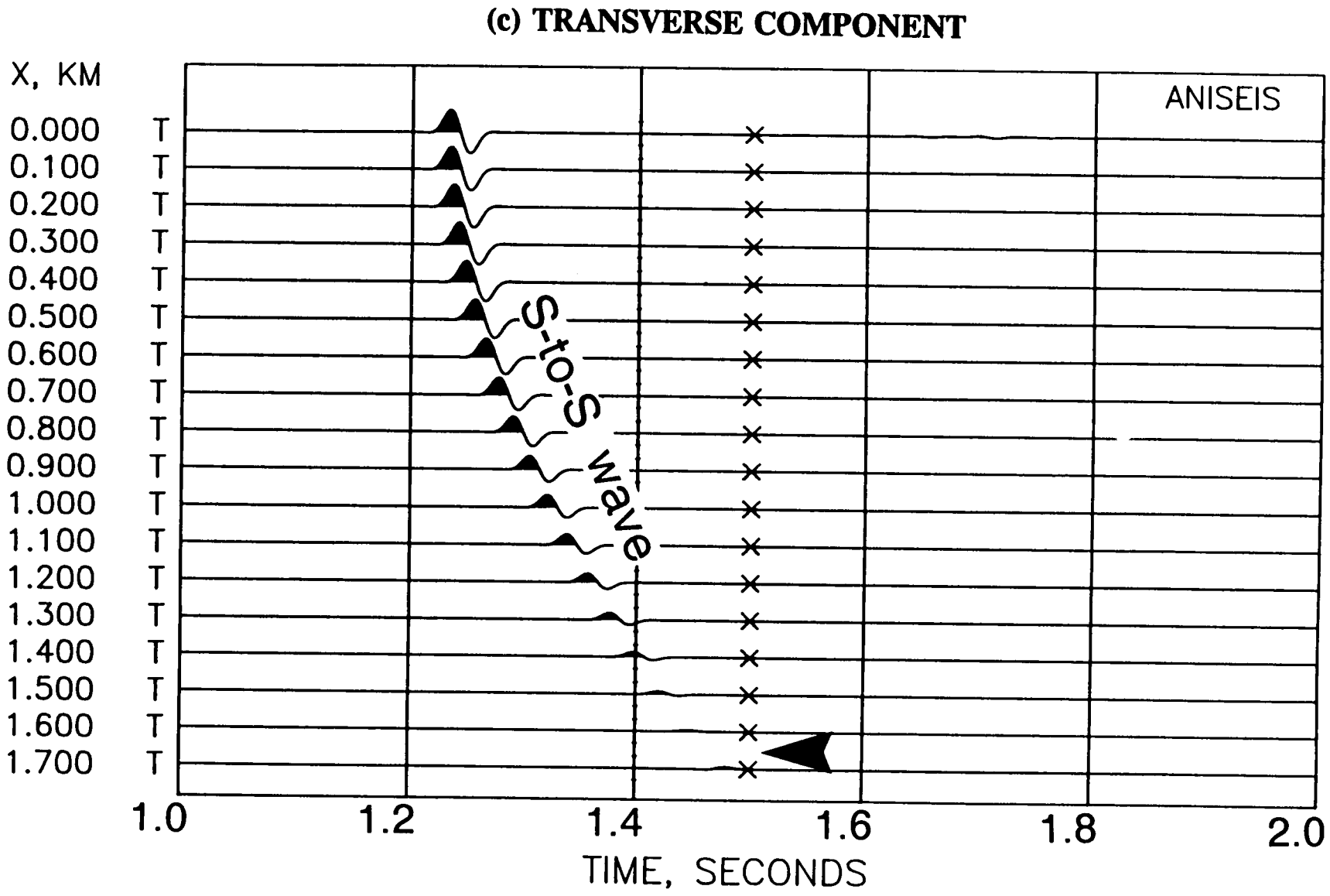
(c) TRANSVERSE COMPONENT
X, KM
0.000 T
0.100 T
0.200 T
0.300 T
0.400 T
0.500 T
0.600 T
0.700 T
0.800 T
0.900 T
1.000 T
1.100 T
1.200 T
1.300 T
1.400 T
1.500 T
1.600 T
1.700 T
ANISEIS
S-to-S wave
1.0
1.2
1.4
1.6
1.8
2.0
TIME, SECONDS

Figure 5.20 (c)

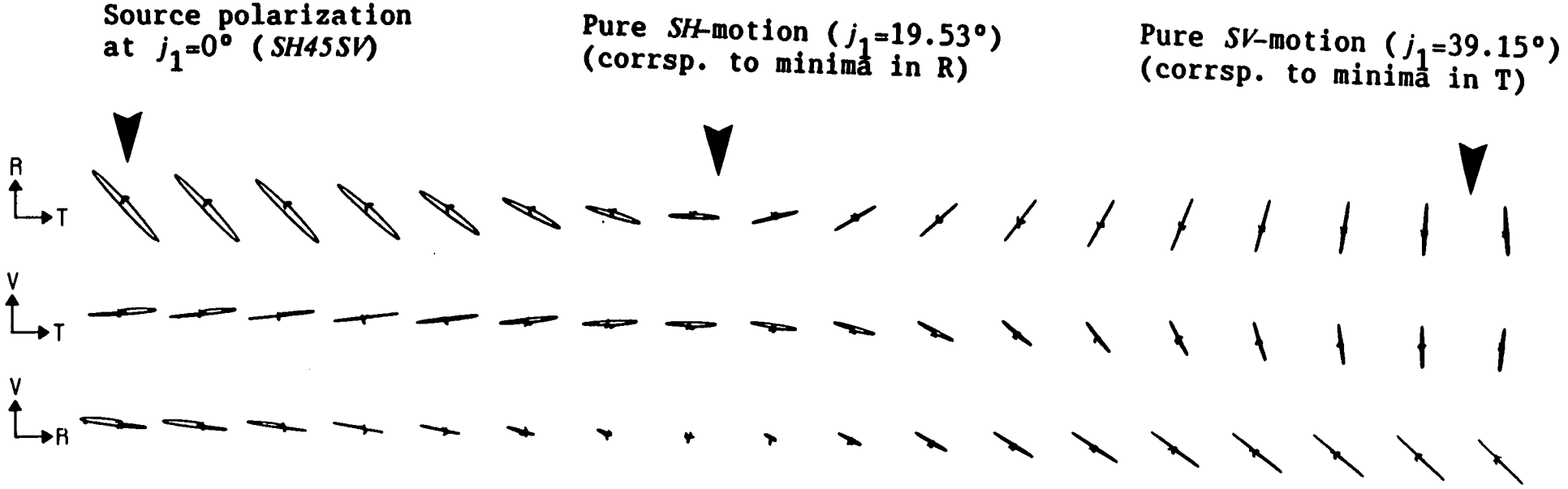
Source polarization
at j_1=0° (*SH45SV*)
Pure *SH*-motion (j_1=19.53°)
(corrsp. to minima in R)
Pure *SV*-motion (j_1=39.15°)
(corrsp. to minima in T)
R
T
V
T
V
R

Figure 5.20 (d)

in the corresponding reflection coefficients (Figure 5.16). The incident angles at which clear polarization changes can be noticed are also shown on particle motion plots in Figures 5.19d and 5.20d, where the polarization of reflected shear-wave swings 90° across the whole range of the incidence angles. Comparing Figures 5.19 and 5.20 with Figure 5.17 for plane wave propagation, we can see a good match, and the sequence of the polarization variations that we described in the previous section (5.3.1) are reproduced by the synthetic seismograms for the curved wavefronts. At large incident angles strong elliptical motions are observed, particularly in the horizontal radial- transverse plane. The seismograms also show largest amplitudes at large incident angles as a result of the *total reflection* of the incidence energy. This is also consistent with the reflection coefficients in Figure 5.16 (the variation of amplitude with offset is called amplitude-versus-offset or AVO, which is of special interest in reflection seismics, see section 5.3.4).

Note that if receivers are located close to the interface, interference of reflected shear-waves with direct waves and interface waves might be expected, which will be similar to the free surface effects. This makes the particle motions even more complicated. Care must be taken when analyzing particle motions of reflected shear-waves in VSPs, where receivers are usually close to underground interfaces.

5.3.3 Effects of anisotropy

We calculate the behaviour of shear-waves at an anisotropic-to-

isotropic interface (see the schematic illustration in Figure 5.9), using the same geometry as the model in Figure 5.18. Anisotropy is caused by EDA-cracks as for Figures 5.11 to 5.14, but the isotropic matrix rock is sandstone (the elastic consitants are in Table 5.1). Figures 5.21 and 5.22 show synthetic seismograms and polarization diagrams with the cracks striking in the transverse direction.

There are three clear features which are due to the presence of anisotropy: (1) the polarization of shear-wave onsets (marked with small arrowheads) is parallel to the strike of the cracks at small angles of incidence, (2) the polarizations at wide angles of incidence are complicated and it is difficult to pick the first arrival (which changes from the transverse direction to linear polarization of the source and then to the radial direction, Figure 5.22), and (3) both radial (Figure 5.21b) and transverse (Figure 6.21c) components reach their mimima at the same incident angle (indicated with arrowheads), which demonstrates the effects of anisotropy on amplitude-versus-offset. The general polarization patterns are much more complicated than those for transmitted shear-waves in Figure 5.11.

As we have demonstrated in Figure 5.15 the first (initial) motion of split shear-waves is independent of the source orientations. It is expected that however complicated the effects of interfaces are, the first motion should be determined by the symmetry of anisotropy. The effect of interfaces only makes the already complicated particle motions of reflected shear-waves even more complicated even in the noise-free synthetic data.

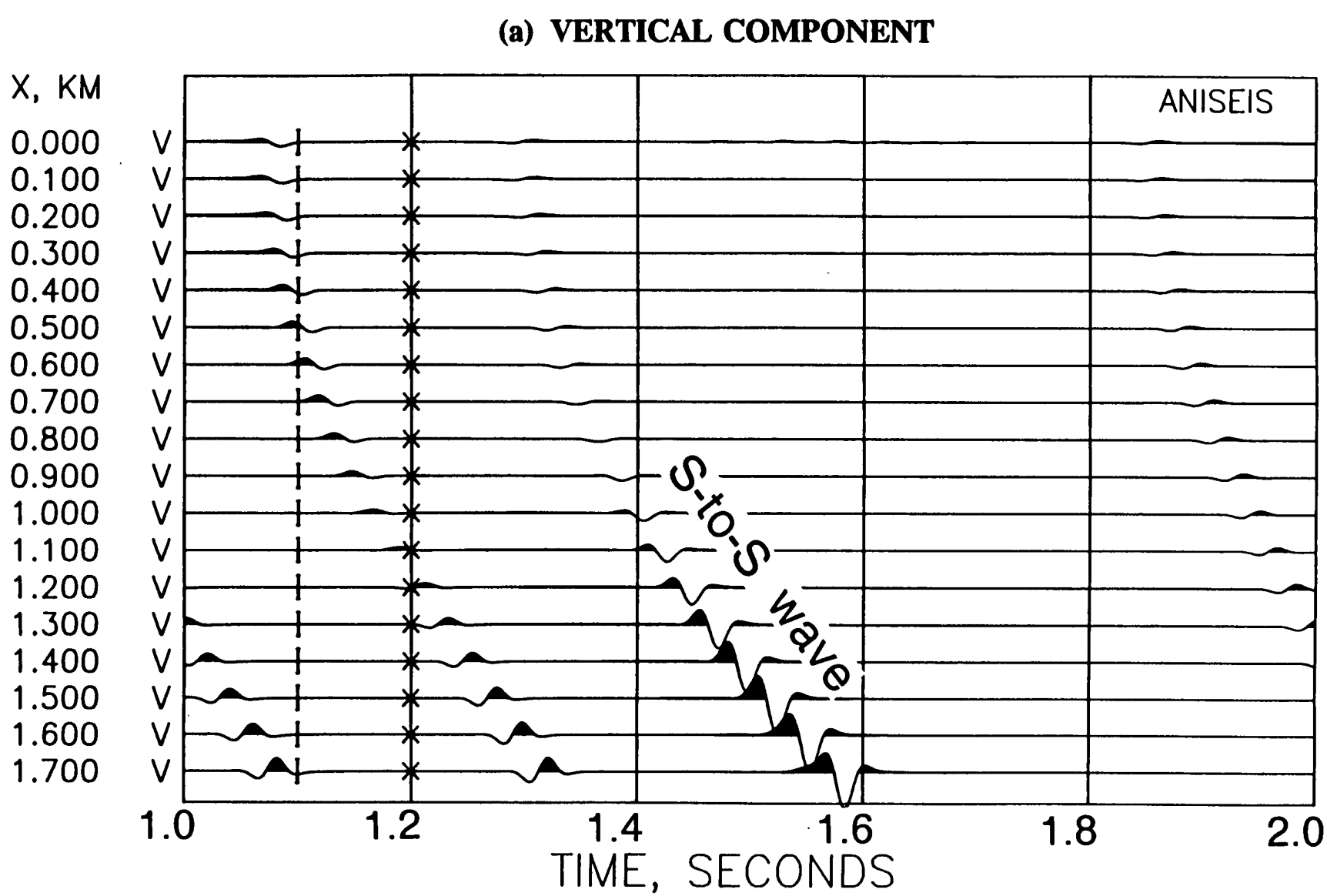

Figure 5.21 Same as Figure 5.19 (*a* to *c*), but for an anisotropic medium with the isotropic matrix velocities same as sandstone.

Figure 5.21 (a)

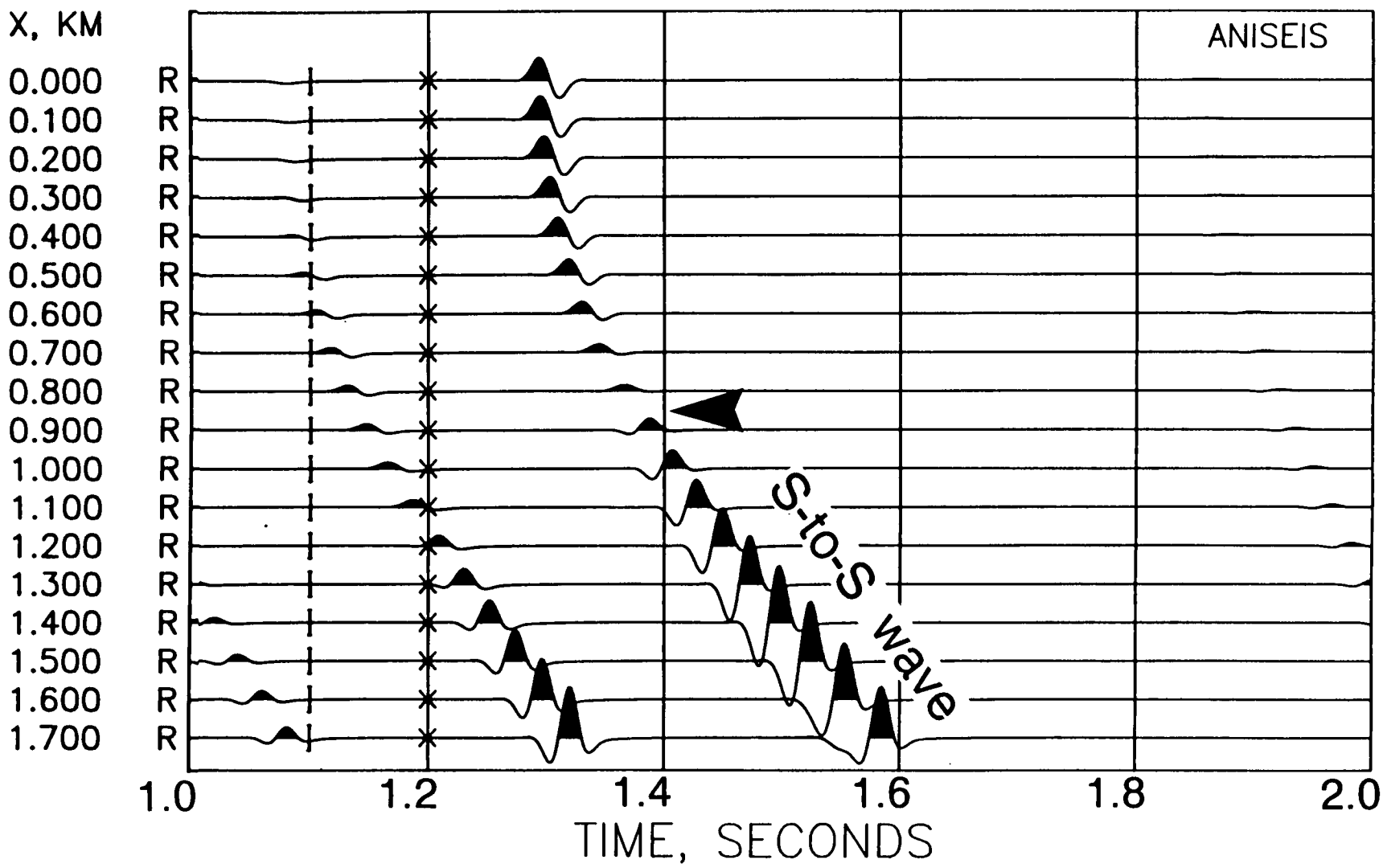
(b) RADIAL COMPONENT
X, KM
0.000 R
0.100 R
0.200 R
0.300 R
0.400 R
0.500 R
0.600 R
0.700 R
0.800 R
0.900 R
1.000 R
1.100 R
1.200 R
1.300 R
1.400 R
1.500 R
1.600 R
1.700 R
ANISEIS
S-to-S wave
1.0
1.2
1.4
1.6
1.8
2.0
TIME, SECONDS

Figure 5.21 (b)

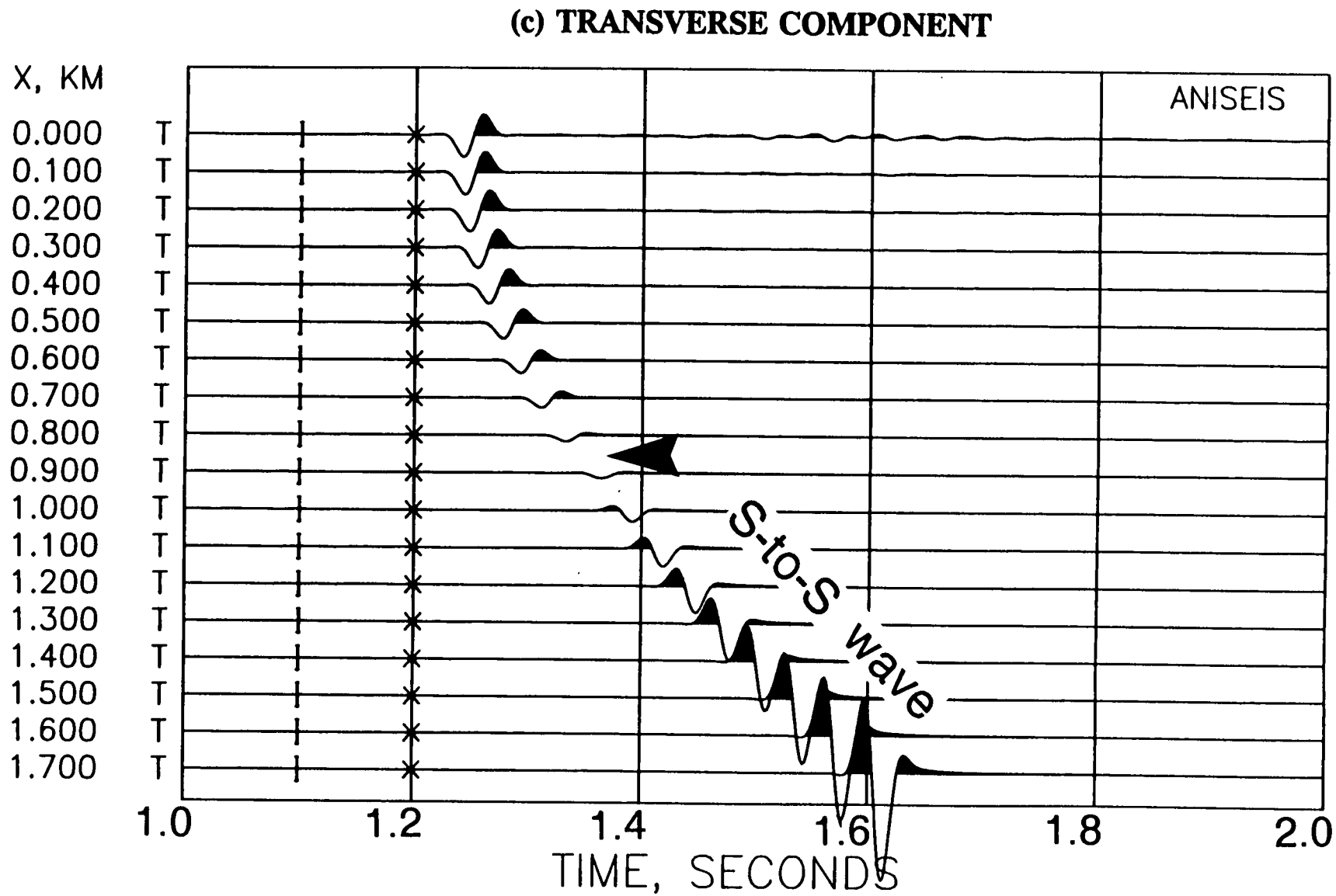
(c) TRANSVERSE COMPONENT
X, KM
0.000 T
0.100 T
0.200 T
0.300 T
0.400 T
0.500 T
0.600 T
0.700 T
0.800 T
0.900 T
1.000 T
1.100 T
1.200 T
1.300 T
1.400 T
1.500 T
1.600 T
1.700 T
ANISEIS
S-to-S wave
1.0
1.2
1.4
1.6
1.8
2.0
TIME, SECONDS

Figure 5.21 (c)

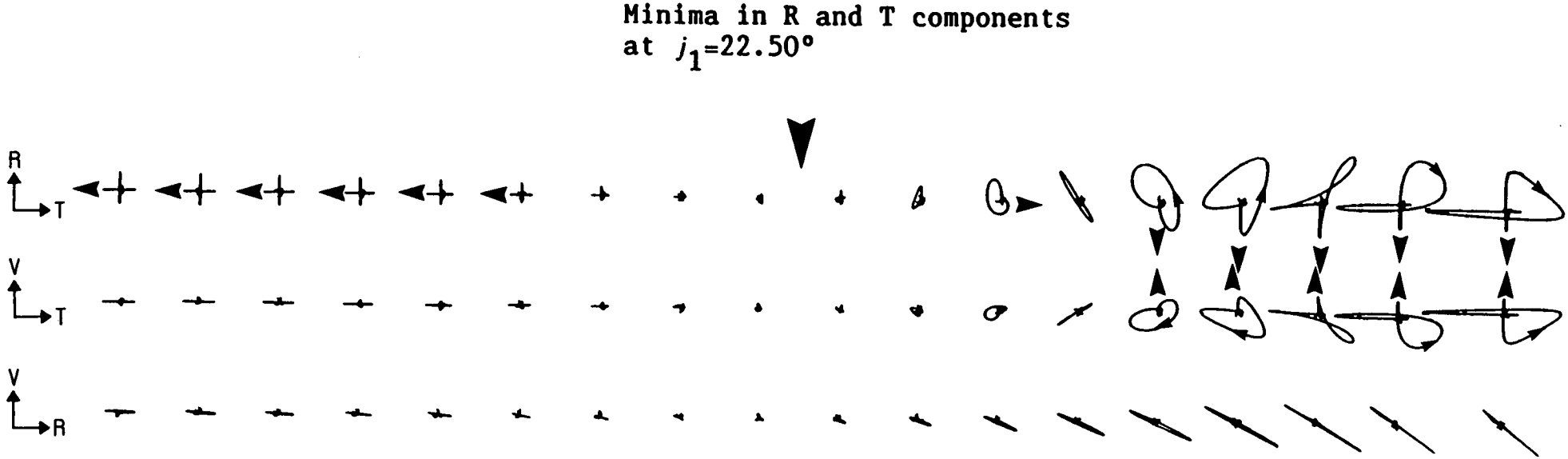

Figure 5.22 Same as Figure 5.19 (*d*), but corresponding to the seismograms of Figure 5.21. The takeoff directions of initial shear-wave motions are marked with large arrowheads and the direction with small arrowheads.

Note that in Figure 5.22 of the particle motion plots, the delays of two split shear-wave are larger for the near-offset geophones (short raypaths) than that for the far-offset geophones (long raypaths). This is because when the offset increases, the raypath moves towards the crack normal [the delay of two split shear-waves reaches its maximum across the centre of the equal-area projection (in case of the nearly-vertical propagation) in Figure 5.10b].

5.3.4 On shear-wave reflection seismics

Reflection seismics, especially common depth point (CDP) method is commonly used during the execution of seismic surveys. The principles and procedures of the CDP method are well described in the literature, for example, Waters (1978), and the method has been very succussful in prospecting for oil. However, there are some difficulties in analyzing shear-wave reflection data to evaluate anisotropic parameters: (1) the free surface effects, including a *S*-*P* conversion, topography and a near surface low-velocity zone (or weathering zone) (see 5.1 Introduction); (2) amplitude-versus-offset (reflection maxima and minima), and (3) polarization changes due to reflectors under isotropic conditions (as shown in this study).

There is a increasing interest in reflection coefficients and amplitude-versus-offset studies (Rendeman and Levin 1980; Ostrander 1984; Levin 1986; Keys 1989). When this thesis was nearly completed an example of porosity identification using *P*-wave amplitude variation with offset was published (Chacko 1989). The amplitude and polarization of reflected shear-waves are closely linked. Rendleman and Levin (1980) pointed out that a *P*-wave reflected from a plane interface attains its maximum amplitude at an offset greater

than that corresponding to the critical angle. Levin (1986) and Keys (1989) studied the zero values in reflection coefficients and the polarity reversal of *P*-waves at a solid-to-solid boundary.

However, they did not discuss shear waves. From Figure 5.17, we can see that for plane shear waves there are also minima and maxima, which are similar to Rendleman and Levin's (1980) Figure 1. Although the reflection coefficient of a curved wavefront is not shown here, we expect that there might also be a minimum and a maximum. In fact, we have already shown the amplitude variation of curved wavefronts in synthetic seismograms in Figures 5.19 and 5.20, which are well predicted by Figure 5.17, as is also Keys's (1989) polarity reversal. Anisotropy also has effects on reflection amplitude- versus-offset. For instance, Wright (1987) concluded that anisotropy (transverse isotropy with a vertical symmetry axis in his case) should be taken into account in amplitude-offset studies of *P*-waves and the reflection-offset trend expected under isotropic conditions can be reversed under anisotropic conditions at incident angles that are useful for exploration. Similar conclusions are expected for shear-waves, as we have shown in Figure 5.21 for more general anisotropy.

The reflected shear-wave polarizations are much more complicated than the corresponding transmitted shear-waves. Such a severe distortion of polarizations makes it difficult to extract information about anisotropy. Recently, the modelling by Li and Crampin (1989) and Yardley and Crampin (1989) for reflection data show complicated particle motions. Li and Crampin also demonstrate that conventional stacking and normal moveout (NMO) correction can degrade shear-wave data. Even if we ignore the possible presence of

several layers with different crack orientations (as discussed by Yardley and Crampin), existence of anisotropy in the near surface low-velocity zone makes it more difficult to pick the first arrival of shear-waves. Even in such noise-free modelling, it is hard to do so, and it will be very difficult to pick the first motions in real data with any accuracy.

Our discussion here does not mean that conventional *P*-wave reflection processing or CDP data processing is incorrect. However, it does mean that it will fail in the analysis of shear-wave data when anisotropy exists. This contradiction can be easily explained by the fact that conventional CDP data processing is mainly based on *P*-wave travel time. Only recently have shear-waves and AVO study become more and more interesting in exploration seismics. This is a challenge for reflection seismics and new processing techniques need to be developed, and current processing techniques require some modifications. Fortunately, exploration seismologists are beginning to realize this. For example, Li and Crampin (1989) have been developing new techniques to process shear-wave reflection data. Note that travel time has not been considered in this study since an interface has no effect on travel time, and any technique based on travel time analysis is not affected by the isotropic-to-isotropic interface.

5.4 Dependence on velocity contrasts and source frequency

There are many parameters involved here. The polarization of both reflected and transmitted shear-waves from an interface depend on velocity and density contrasts and the frequency of incident waves. The critical angles for incident shear-waves at an interface are

determined by the values of velocity and density of two materials across the boundary. For example, if $V_{P1} < V_{S2}$, for a L/H interface there will be two interface waves rather than three. If velocity contrasts are very small, all critical angles tend to increase, and the boundary will have very little effect.

It should also be noted that even though the transmission and reflection coefficients of a plane wave are independent of frequency, for a point source they vary with frequency as the curvature of the point source is mainly determined by the dominant source frequency. Therefore, the polarizations in all the synthetic seismograms in this Chapter are also dependent upon frequency. The variation of polarizations with frequency will be similar to that discussed by Booth and Crampin (1985). The 20 Hz signal we used here is typical for sources used in exploration seismology. Nevertheless, the analysis above is a general case, and a small change in any parameter will not alter the conclusions significantly.

5.5 Discussion

We have investigated the effects of a single internal interface on the polarization of both transmitted and reflected shear-waves. In summary, the shear-wave polarization at a single interface is complicated and several effects need to be considered. However, it is important to know that for a pure *SH*-source or a pure *SV*-source, the internal interface does not cause elliptical particle motion since both *SH*- and *SV*-waves are decoupled. Hence in order to avoid such interfences, inline (*SV*-polarized) or cross-line (*SH*-polarized) shear-wave sources are suggested.

In the modelling of the wide-offset VSPs in the Paris Basin, Bush (1989) has found that the particle motions were elliptical even for an isotropic layered model. Igel (1989) in a recent interpretation of the Varian hole data from California has attributed the strong anomalies observed to be mainly due to the effect of dipping interfaces near an existing large fault. He finds that the deviation of the polarization is up to 40° for the top geophones with a far offset (shear-waves propagate almost parallel to the free surface in his case). He suggested that such a large unusual deviation is unlikely to be caused only by anisotropy ,and some sort of heterogeneity and dipping interfaces are likely.

Observed shear-waves polarizations are usually very complicated and it is not easy to pick up the first arrivals with any accuracy. Many factors could be responsible for those complications. The most important factors apart from anisotropy are heterogeneity, internal interfaces (including dipping interfaces) and the free surface (if observation is on the surface as in earthquake observations and reflection seismics). We name these non-linear polarization generalized by these features as *quasi shear-wave splitting*, in order to distinguish them from the shear-wave splitting due to anisotropy. Understanding the effects of the various factors is critical in investigating the anisotropy-induced shear-wave splitting. Theory and observations have now suggested that anisotropy-induced splitting is a widespread phenomenon, and the results of this Chapter may help to distinguish between the shear-wave splitting caused by anisotropy and others (irregular polarizations).

5.6 Conclusions

This study on the effects of internal interfaces on shear-wave polarizations can be readily divided into two parts: transmitted waves; and reflected waves.

The conclusions from Part I on transmission are:

(1) There are several concentric shear-wave windows associated with the interaction of shear waves with an internal interface. These windows mark ranges of angles of incidence, formed by successive critical angles, where the behaviour of transmitted shear-waves is controlled by the same relationships.

(2) Within the innermost window, for angles of incidence less than $\sin^{-1}(V_{S1}/V_{P2})$, for L/H and $\sin^{-1}(V_{S2}/V_{P2})$, for H/L interfaces, the polarization of the incident shear-wave in an isotropic structure is essentially preserved with only minor deviations of direction of the angle of polarization. Beyond this first critical angle, various interface waves excite motion largely confined to the immediately neighbourhood of the interface. These waves induce elliptical motions close to the interface. For arrivals outside the innermost window (wide angle arrivals), the transmitted wave may have elongated elliptical motion, particularly in the vertical transverse section for the L/H interface.

(3) The effects of anisotropy are different from isotropy. Passage through the inner shear-wave window into an anisotropic layer produces shear-wave splitting, with the delay between the split shear-waves progressively increasing with the length of the

anisotropic raypath. This gives the typical polarization diagrams of shear-wave splitting with orthogonal changes of direction which cannot be mistaken for the interface-induced, elongated ellipticity. At wider angles of incidence, the behaviour of shear waves at isotropic-to-isotropic and isotropic-to-anisotropic interfaces are similar only near the interface when there has been insufficient anisotropic path length to cause significant shear-wave splitting and the effect of the interface is dominant. The interpretation of the splitting could only be mistaken if the delay between the split shear-waves is very small, as a consequence of a short anisotropic raypath, or of very weak anisotropy.

The important result is that initial polarization of the shear-waves in PDs is controlled by the anisotropy (the orientation of EDA-cracks, say). The small changes in orientation of the wave caused by the interface will only affect details of the PD patterns not the initial polarization, thus visual identification of polarization directions in PDs will not be affected, and if synthetic seismograms are used for interpretation, the effects of the interface will be modelled in any case. We conclude that the interaction of shear waves with internal interfaces (transmission) is unlikely to be a serious complication in observations and interpretations of anisotropy-induced shear-wave splitting, although it may contribute to the usually observed complexity of the waveforms following the initial onset of the faster split shear-waves.

These conclusions are important in that it suggests that analysis of anisotropy-induced shear-wave splitting is possible and meaningful. It therefore provides a theoretical base for the

possibility of the automatic analysis of shear-wave polarization and time delays such as the techniques developed by Shih *et al.* (1988), Nicoletis *et al.* (1988), Igel and Crampin (1989), and MacBeth and Crampin (1989a, b, c).

The conclusions from Part II on reflection are:

(1) The shear-waves can be distorted in reflections. The distortion is much more severe than for transmitted shear-waves. The deviation of polarizations can be as large as 180° (from pure *SH*- to pure *SV*-waves with polarity reversal) and the phase difference changes also over 180°. This is partly due to the zero values and partly due to the inversion of the phase in reflection coefficients of *SV*- and *SH*-waves.

(2) The distortion of polarizations of reflected shear-waves is closely linked with reflection maxima and minima. Anisotropy can also affect amplitude-versus-offset and should be taken into account in AVO study.

(3) Where anisotropy exists, particle motions become more irregular. Therefore it is difficult to pick the first motions of shear-waves in reflection data, even in noiseless synthetic data. There are some difficulties of analyzing shear-wave reflection data when anisotropy is present. This study further supports the idea that the VSP technique is more efficient and informative than reflection seismics in obtaining information about crack-induced anisotropy.

This study implies that any technique to extract the anisotropy information (such as first motion and time delays) from shear-wave *reflection* data based on *source polarizations* may fail completely since the source polarization is not preserved after the reflection except at normal incidence. This applies to the method of Igel and Crampin (1989).

CHAPTER 6

CHANNEL WAVES IN ANISOTROPIC WAVEGUIDES: I, MODELLING OF IN-SEAM SEISMIC DATA

6.1 Introduction

In this Chapter, we analyze and model the channel wave data recorded from an in-seam seismic survey. Our modelling will be compared with the observations, and the results show satisfactory agreement in amplitude, dispersion and polarization.

In-seam seismics, since it was first introduced by Krey in 1963, has been accepted as a routine technique in the United Kingdom to map coal-seams and to detect faults (Mason *et al.* 1980; Buchanan *et al.* 1981). Krey *et al.* (1982), Krajewski *et al.* (1987) have also used the technique in Germany, and Greenhalgh *et al.* (1986) and Mason *et al.* (1985) in Australia. Coal-seam guided channel waves are used in in-seam seismics. A very good introductory paper on this technique can be found in Jackson (1985). However, almost all the channel wave analyses so far have been based on dispersion and attenuation characteristics. Although anisotropy is occasionally reported, it has in general been neglected. One form of anisotropy present in coal-seams is that due to aligned cleats (Terry 1959; Williamson 1967; Buchanan *et al.* 1983; Szwilski 1984; Ward 1984). Anisotropy is necessary to improve the resolving power for estimating/imaging in-seam faulting. Such improvement would lead to more refined planning on the basis of seismic results (Buchanan *et al.* 1983).

Synthetic seismograms have been shown to be a powerful tool to data interpretations. The finite-difference method has been used by Korn and Stöckl (1982), Bodoky and Bodoky (1983), and Kerner and Dresen (1985) to model in-seam channel waves. Franssens *et al.* (1985) use the propagator matrix method to generate synthetic seismograms of channel waves in order to model leaking modes. These papers all assume isotropic coal-seams. Recent advances in the recognization of seismic anisotropy in most crustal rocks has lead to a renewed interest in the effects of anisotropy. We attempt to extend the scope of synthetic seismograms by including anisotropy as a parameter of channel waves. We use the anisotropic reflectivity technique to compute synthetic seismograms of channel waves in anisotropic coal-seams. Some anomalies, including the coupling of the Love (*SH*-motion) and Rayleigh (*P*- and *SV*-motion) mode channel waves into generalized modes with a three-dimensional particle motion, cannot be explained by propagation through an isotropic coal-seam. For instance, transverse motion is often observed from a radial source, and radial motion from a transverse source, which would not be expected in a plane-layered homogeneous isotropic structure, unless there were lateral reflections which is not uniformly the case. Synthetic seismograms are used as a basis for modelling the observed channel waves. The results are used to show some of the properties which might be expected for channel waves where there is aligned crack-induced anisotropy. We first review the background theory of the in-seam seismics and channel waves. A satisfactory fit of synthetics to observations is then presented. Anisotropy is characterized by coupling, dispersion anomalies, and particle motion anomalies.

6.2 Coal-seam as a dispersive, attenuative and anisotropic waveguide

Coal is a porous, visco-elastic, low-velocity, and low-density material that occurs in approximately parallel seams surrounded by higher-velocity and higher-density country rocks. Consequently, a coal-seam behaves as a waveguide to seismic energy generated within the seams. Body waves, generated by a source inside the coal-seam, will generate dispersive channel waves propagating parallel to the sedimentary geological bedding rock-coal-rock interfaces, as a result of multiple internal reflections of seismic wavefronts incident upon roof and floor. The theory of seismic wave propagation in coal-seams is well established (Krey 1963; Buchanan 1978) and it is known that dispersive waves in the forms of attenuated quasi-Love (*SH*-motion) and quasi-Rayleigh (*P*- and *SV*-motion) waves are supported (channel waves are also known as seam waves, or guided waves, or trapped modes). The general waveguide theory can be found in Brekhovskikh (1960).

6.2.1 Dispersion

Channel waves, like all interface waves or surface waves, are dispersive, that is the wave-speed varies with the frequency of the wave. Thus a coal-seam is a dispersive waveguide. The dispersion has been studied in many papers dealing with in-seam seismics. It is possible to calculate the dispersion of seismic waves in anisotropic structures using the technique of Crampin (1970), Crampin and Taylor (1971), although this has not yet been done for anisotropic internal layers as in coal-seams. Breitzke *et al.* (1987) suggested that the dispersion curves of Love- and Rayleigh-surface and channel-waves are equivalent if the depth of coal-seams is 5 to 10 times of seam thickness as the free surface

effect is negligible. However, there are some computing difficulties to adopt Crampin's program to channel waves directly, and a slight modification is required (Crampin and Lou, personal communications). It is easy to extend phase recursion technique of Räder *et al.* (1985) to multilayered *transversely isotropic* media with a vertical symmetry axis (Appendix B). Note that in transversely isotropic media, two kinds of channel waves, Rayleigh- and Love-waves, are decoupled.

6.2.2 Attenuation

In isotropic media, attenuation (absorption) has been included in the theory of channel waves (Buchanan 1978). To take account of attenuation of energy we assume the amplitude variation $\exp(-\gamma r)$, where γ is the attenuation coefficient and r is the distance travelled. It is assumed that γ is proportional to frequency at all frequencies of interest, Buchanan (1978) used the complex Lamé constant for Love wave propagation:

$$\mu = \mu_o[1 + i\varepsilon], \tag{6-1}$$

where i is the imaginary unit, and ε is less than one, usually $\varepsilon \ll 1$.

The use of complex Lamé constant is not related to a real stress-strain law (Buchanan 1978); nevertheless, it enables the effects of attenuation to be included very easily in most situations where the attenuation is weakly dependent on frequency. Crampin (1981) uses complex elastic constants to model anisotropic attenuation. It follows that the corresponding complex velocity V can be written as:

$$V = V_0[1 + i\varepsilon/2], \qquad (6\text{-}2)$$

where higher orders of ε have been omitted. The Quality factor Q is then given by $Q = 1/\varepsilon$, which is related to the attenuation coefficient γ by $Q^{-1} = (\gamma V_0/\pi f)$, where f is the frequency (the inverse of the quality factor Q^{-1} is called the internal friction or dissipation factor).

A coal-seam is an attenuative waveguide. The value of Q varies in different coal-seams. In Germany, Krey *et al.* (1981) found Q to be between 45 and 60; in Britain, Buchanan *et al.* (1983) estimated Q to be 45, and in Australia, Greenhalgh *et al.* (1985) found very low values of Q between 20 and 30. They attributed this intrinsic absorption to be a result of high moisure conditions, shallow depths and the strong cleating. Our constant Q model is based on the above theory. Note that the introduction of attenuation will inevitably lead to dispersion in the waveforms as it propagates. For a constant Q, the dispersion relationship has a logarithmic character (Futterman 1962; Aki and Richards 1980). Buchanan (1978) concluded that dispersions due to boundary conditions and attenuation are coupled.

6.2.3 Anisotropy

Coal is likely to be transversely isotropic with a vertical axis of symmetry due to the finely depositional layering and the presence of the overburden. Coal also contains an oriented cracked structure of parallel cleats, aligned perpendicular to the bedding plane. The coal may be extensively cracked or jointed along these cleat or cleavage planes (Terry 1959; Ward 1984), and in many areas the direction of the major cleats is approximately constant (Williamson

1967; Buchanan 1983; Szwilski 1984; Jackson 1985, 1989). Such aligned cleats are expected to induce strong anisotropy, and have important bearing upon the mining of coal (Spears and Caswell 1986). Krey (1963) suggested that anisotropy should be taken into account if a precise interpretation of observed data is required. Buchanan *et al.* (1983) concluded that the effect of ignoring anisotropy is to introduce an error into the inferred position of any reflector in coal-seams. He shows that velocity anisotropy measured from group velocity dispersion curves in coal-seams is up to 14%. The observation of high attenuation by Greenhalgh *et al.* (1985) was interpreted as partly due to strong cleating. It is clear that cleats in coal-seams can introduce strong anisotropy to channel waves.

6.3 Observations

We use the data obtained from the Harworth in-seam seismic transmission survey through a typical coal panel as a basis for the modelling. The data were recorded by the British Coal Corporation. Figure 6.1 shows a horizontal plan of the geometry of the two sets of data. The 2.4m thick coal-seam is a 150m wide panel between two roadways. Shot Hole 6, B, and Shot Hole 9, C, are 150m apart, and the geophones are in groups of usually 3 (or 4), each in 2m deep holes 10m apart at E, F, G, and H. The source is a nylon rod in 2m deep holes, oriented either perpendicular to the wall of the roadway, or at 45° horizontally either side. The rod is struck at the exposed end and the buried end generates an impulsive impact parallel to the rod. The best model of the source is a pulse of

GEOMETRY OF IN-SEAM SEISMICS

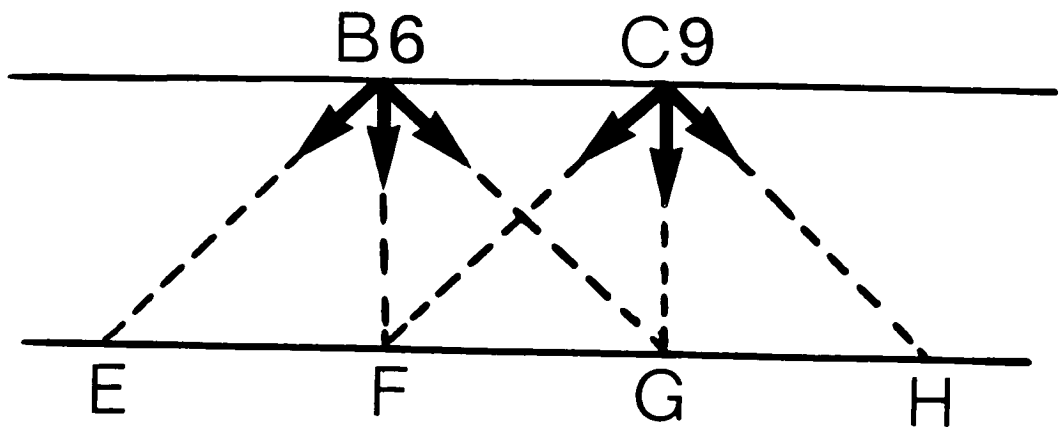

Figure 6.1 Horizontal plan of the Harworth in-seam seismics. Parallel lines are the two roadways between a panel 150 m wide. Shot hole 6, B, and Shot hole 9, C, are 150 m apart. E, F, G, and H are geophone locations. Impact source directions are marked with arrowheads.

several cycles (see next section), and suggests that there are some near-source reverberations (possibly along the nylon rod). Both geophones and source hole are approximately in the centre of the seam.

The three-component geophones are initially oriented vertical and horizontal [perpendicular (**X**) and parallel (**Y**) to the face], but in all displays in this Chapter, the horizontal geophones have been rotated into horizontal (**R**)adial and horizontal (**T**)ransverse directions. The rotation is carried out by the following standard rotation matrix assuming straight raypaths between source and geophones:

$$\begin{bmatrix} \mathbf{R} \\ \mathbf{T} \end{bmatrix} = \begin{bmatrix} \cos\theta & \sin\theta \\ -\sin\theta & \cos\theta \end{bmatrix} \begin{bmatrix} \mathbf{X} \\ \mathbf{Y} \end{bmatrix} \qquad (6\text{-}3)$$

where θ is the angle of rotation. Similarly, all figures display the true relative amplitudes of the seismograms (no automatic gain control has been applied). The sample rate is 0.5 milliseconds.

Figures 6.2(a) to 6.2(g) compare the series of recordings from Shot Holes 6 and 9 for each of the seven source/geophone path geometries. Note that Shot Hole 9 was recorded with only horizontal geophones. The general oscillatory nature of the signals showing dispersion is expected from channel waves in a low-velocity waveguide. Four features are immediately obvious:

1) The distinctive character of the signal on each (rotated) geophone component (**R**, **T**, and **V**) for each shot suggests that the rotations of the components are approximately correct. The rotated seismograms are a valid way of displaying the seismograms.

Figure 6.2 Comparison of observed seismograms for source holes 6 and 9, for the source/geophone geometry indicated to the left. Arrows indicate impact source directions.

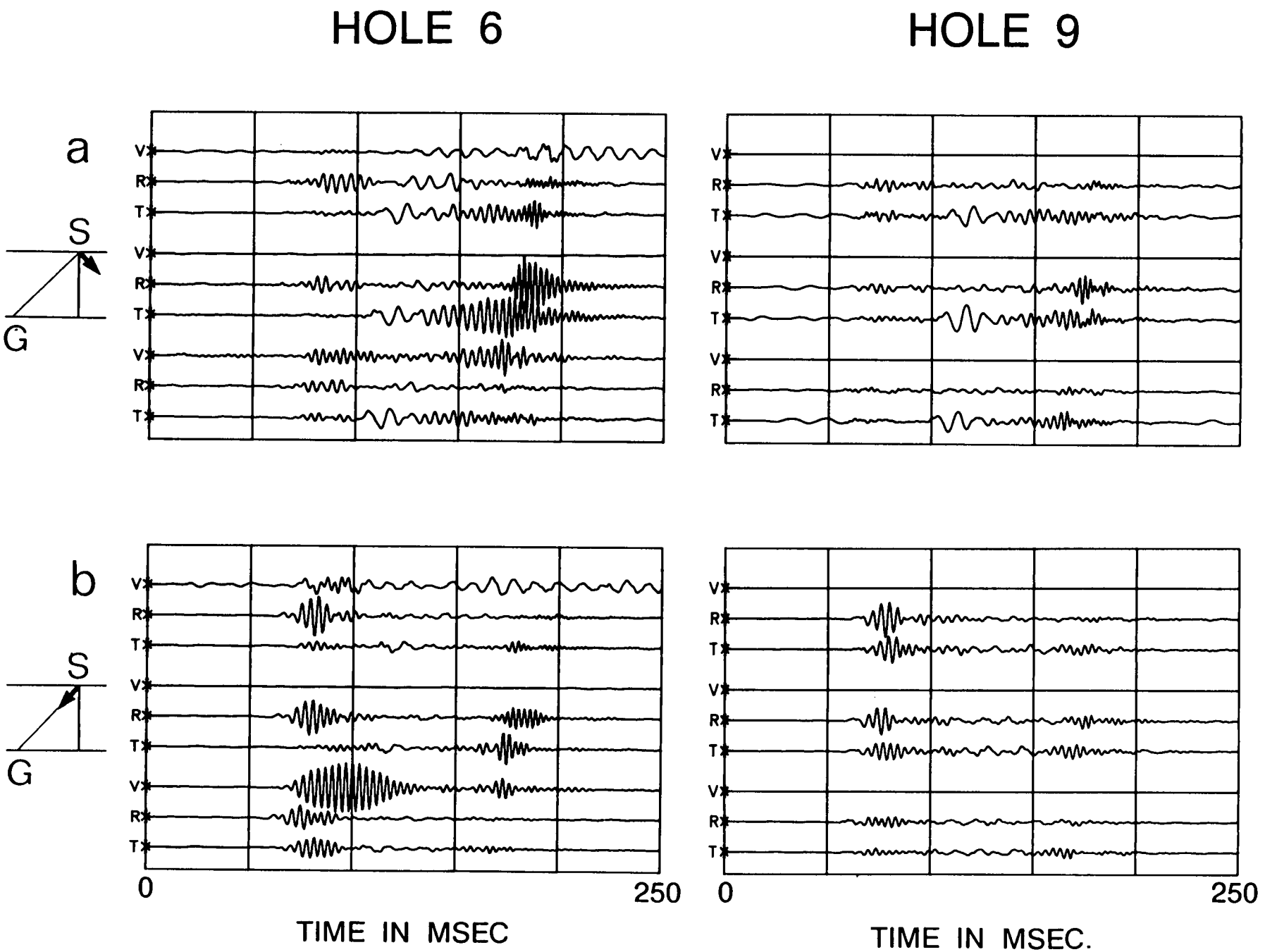

Figure 6.2 (cont.)

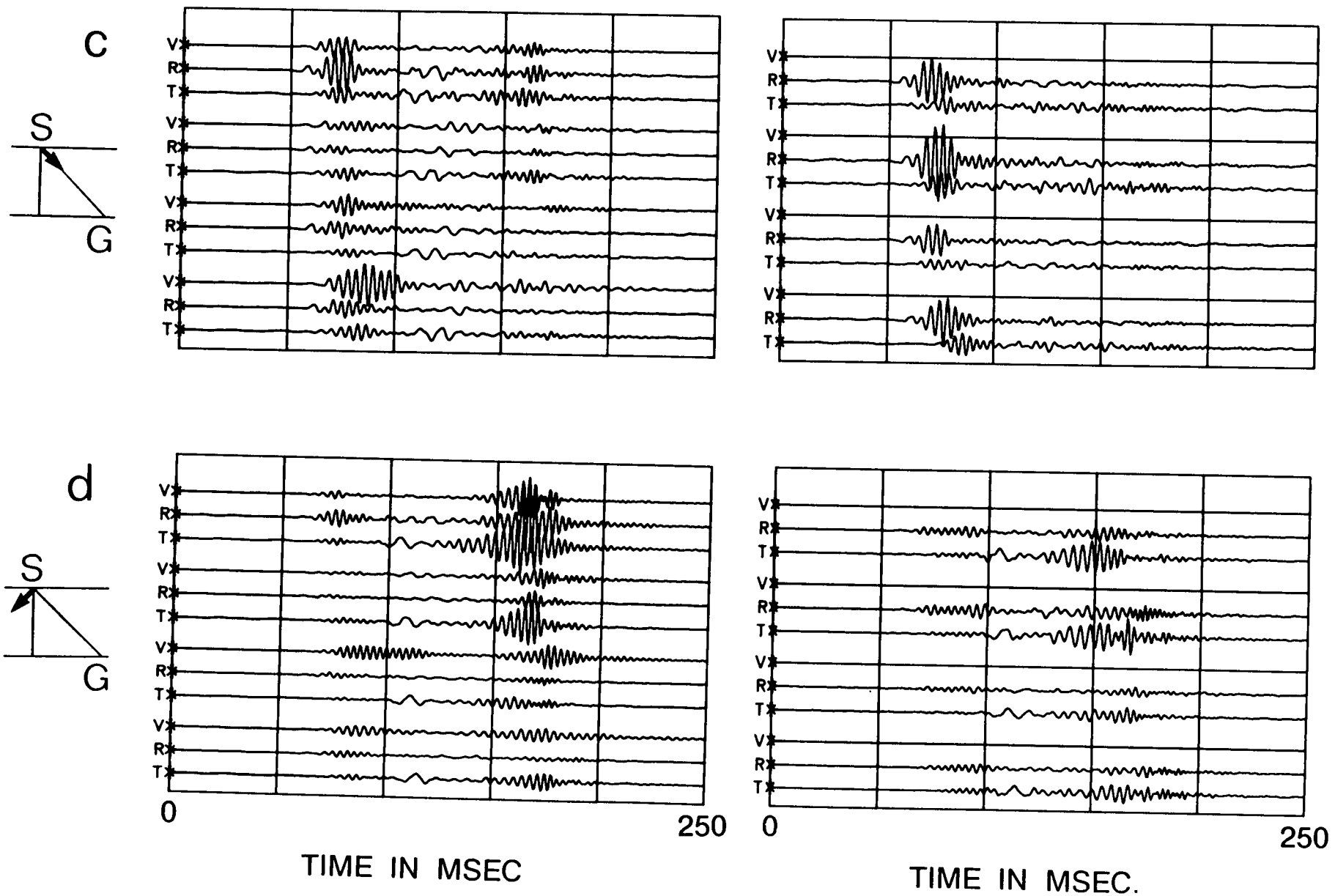

Figure 6.2 (cont.)

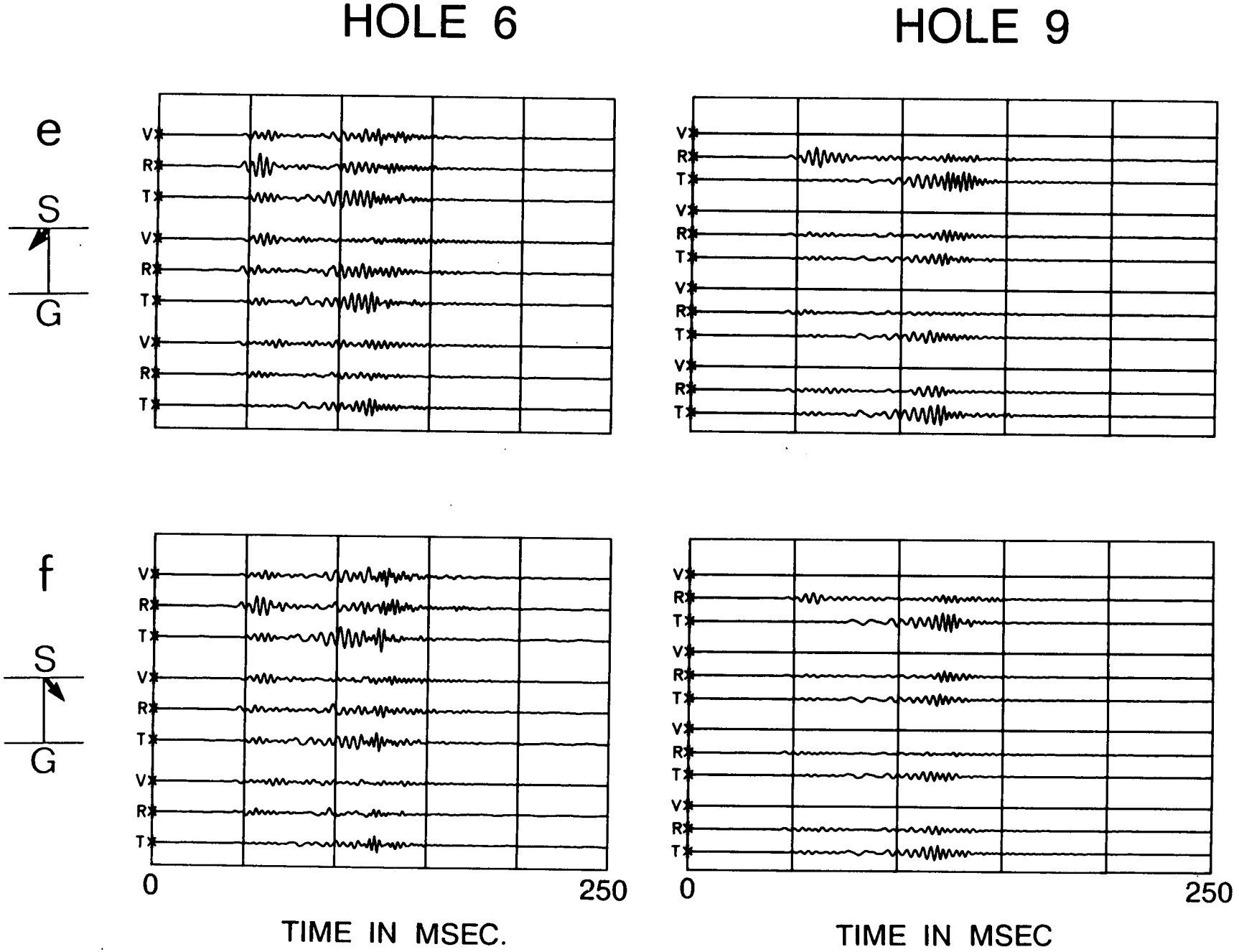

Figure 6.2 (cont.)

Figure 6.2 (cont.)

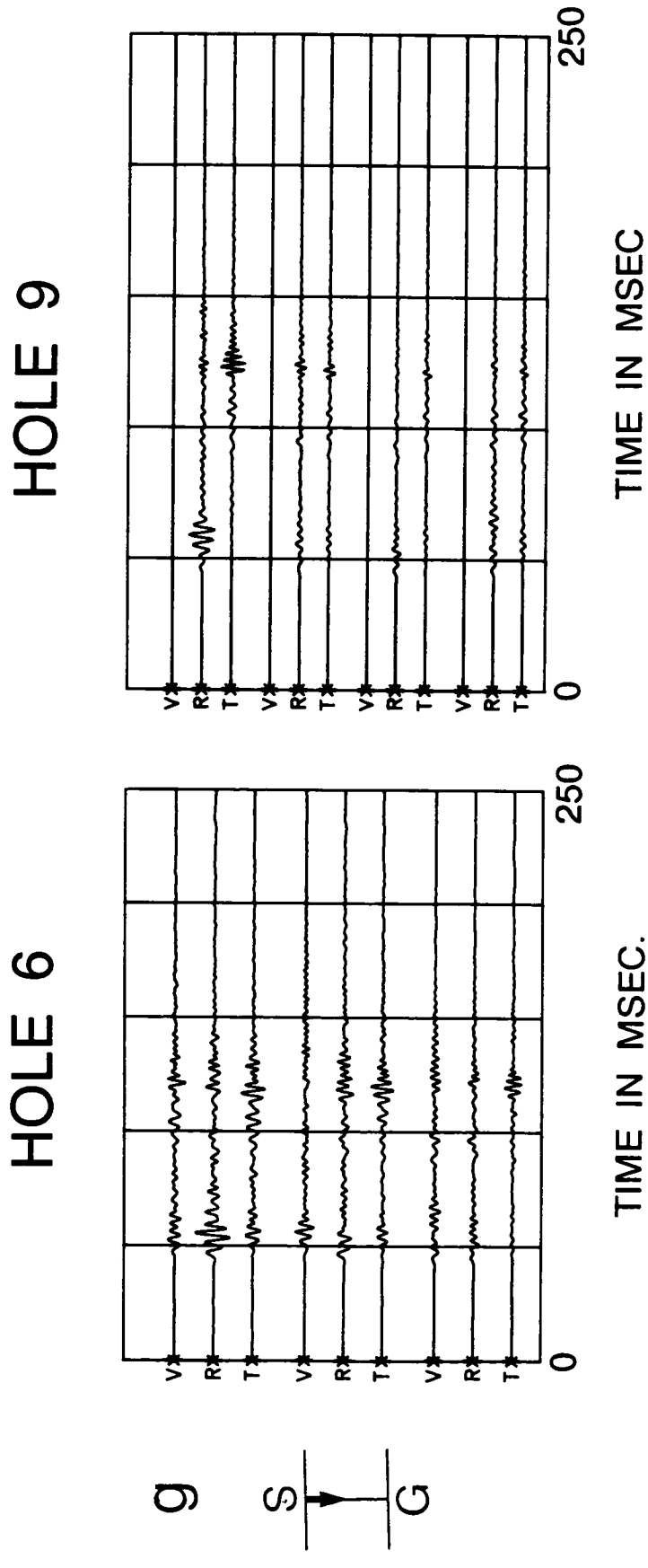

2) The variability of the records from geophones, only 10m apart, suggests that near-geophone inhomogeneities, minor differences in the positions of the geophones within the coal-seam, and possibly geophone-to-rock coupling, can seriously disturb the seismograms. Nevertheless, despite variability, the seismograms in each set do show general similarities, which suggests that the idealized modelling we shall be attempting should be meaningful and possible. It is also worth noting, that the behaviour of channel waves may be very sensitive to small details of the source/path/geophone geometry. This suggests that some of the differences between seismograms from neighbouring geophones may be due to small differences in the position of the geophones with respect to the centre of the seam, and recorded components not being *exactly parallel* and *perpendicular* to the roadway face (possibly 5° to 10° deviated from the expected direction, Roth, personal communication).

3) Seismograms in general show data in all three components. In particular, the radial motion is observed from the transverse source and the transverse motion from the radial source, which cannot simply be explained by isotropic models. Seismograms also show dispersion and amplitude variations with respect to the direction of raypaths.

4) The seismograms from Shot Hole 9 show less variability than those from Shot Hole 6. Consequently, we shall attempt to match synthetic seismograms to observations from Shot Hole 9.

It is noted that *shear-waves* may suffer severe interactions with the free surface (the wall of the roadway) (Booth and Crampin 1985) and internal interfaces (Chapter 5). Lagasse and Mason (1975) found

that the effect of this boundary is to produce a surface or roadway wave confined to the free coal surface. Roadway waves are dispersive and exist as guided modes (Krajewski *et al.* 1987). However, we can find no distinctive feature in Figure 6.2 which is the result of these interactions (although the observations are not wholely appropriate for clearly displaying such features). There are two possible reasons: the interactions may be there and we have not identified them; or the wavelengths of the signals (generally between about 12m and 6m) are too large for a face with a thickness of 2.4m, to cause much disturbance. In view of the fact that we obtain reasonably satisfactory matches of observed to synthetic seismograms, where the modelling has not taken into account the presence of the roadway face, suggests that the second mechanism is probably the reason why we do not see more obvious signs of free-surface interactions.

6.4 Matching synthetic to observed seismograms

Model 1 (Table 6.1) was initially suggested for the isotropic structure around the Harworth seam (Roth, personal comunication). However, after investigating a number of trial models, we had to increase the isotropic shear-wave velocity of the coal-seam from 1000m/s to 1200m/s (Model 2 in Table 6.1) in order to match the arrival times and dispersion of the main signals. The Poisson's ratio of the isotropic reference model is 0.257 for coal, which has been cited in many papers (for example, Krey 1963; Dressen and Fregstätter 1976). Note that microcracks have a significant effect on seismic velocities, and it is seldom that velocities measured in samples in the laboratory match observed velocities, because it is

Table 6.1 Isotropic models

		Velocity (m/s)		Density (g/cm^3)	Thickness (m)
		V_P	V_S	ρ	H
Model 1	Country rock	3500	2000	2.60	∞
	Coal seam 1	2100	1000	1.35	2.4
	Country rock	3500	2000	2.60	∞
Model 2	Country rock	3500	2000	2.60	∞
	Coal seam 2	2100	1200	1.35	2.4
	Country rock	3500	2000	2.60	∞

difficult to retain *in situ* crack geometry.

We also found that it is necessary to introduce relatively strong attenuation, in order to match the dominant frequencies, amplitudes, and dispersion characteristics of the signals. In our model, the attenuation factor Q is 50 for the coal-seam and 100 for the country rocks. The attenuation factor in country rocks is smaller than Q = 150 cited by Krey *et al.* (1982), but a value for Q of 50 is thought to be typical for British coal-seams (Buchanan *et al.* 1983). Matching synthetic modelling, therefore, provides an alternative technique for estimating attenuation in both coal-seams and country rocks. Note that *in situ* attenuation will probably be controlled by the crack geometry, and will result in the attenuation being strongly anisotropic (varying with direction, Crampin 1984). In this study, we have only used an isotropic attenuation (constant attenuation) as we descibed previously.

We model fullwave synthetic seismograms, and try to match synthetic to observed seismograms by forward modelling by an essentially trial and error technique. However, a variety of relevant information can be obtained by visual examination of the seismograms, and this provides starting parameters for the modelling. The source time function in our modelling is:

$$F(t) = t_p^2 \exp(2\pi f t_p / d)\sin(2\pi f t_p), \qquad (6\text{-}4)$$

where $t_p = t - t_{p0}$, t_{p0} is the origin time, d is a damping factor, f is dominant frequency in Hz. Figure 6.3 show the source pulse with a dominant frequency of f = 270 Hz and damping factor of d = 4.

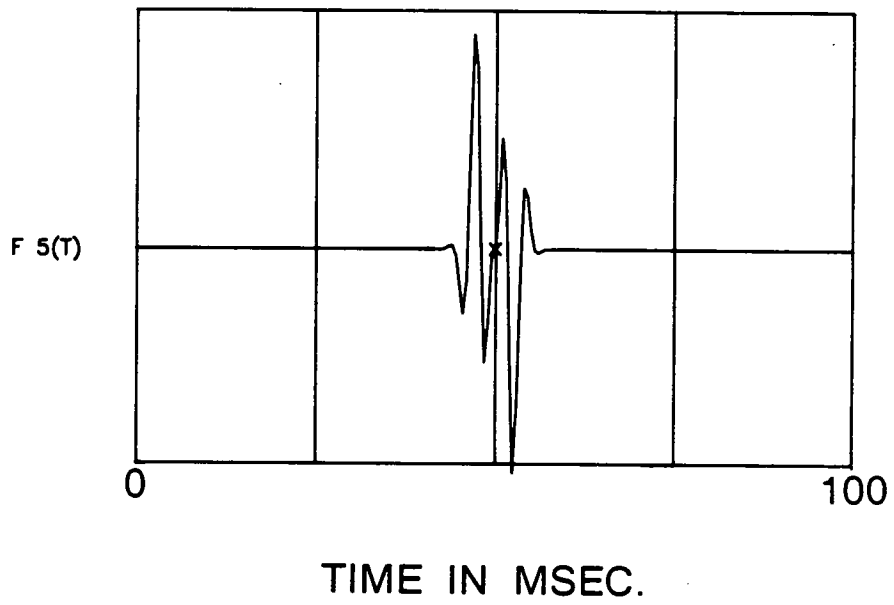

Figure 6.3 Source time function from equation (6-4) with the dominant frequency of 270 Hz and damping factor of 4.

6.4.1 Isotropic modelling

Figure 6.4 shows examples of the signals from four (horizontal) source orientations (parallel, and at ±45° and 90° to the direction of the geophones) propagating through the isotropic Model 2. Both source impacts and recording geophones are in the centre of the seam. Figure 6.4 shows wavetrains isolated on separate components and symmetrical features for ±45° sources quite unlike the wavetrains on the observed seismograms which generally show motion on all three-components. Channel waves in purely isotropic layered structures have pure Rayleigh type-motion (*P*- and *SV*-motion) and pure Love-type motion (*SH*-motion). This absence of coupling between components demonstrates that anisotropy is required to explain the observed seismograms. It should be noted, however, that the radial motion would show coupling to the vertical motion, if the geophones were displaced from the centre of the seam. The symmetry of geophones exactly in the centre of a parallel seam between similar country rock cancels the vertical motion.

6.4.2 Anisotropic modelling

After having obtained an approximate fit of arrival time and amplitudes of synthetic seismograms to observations by using the isotropic model, anisotropy was introduced by simulating thin parallel EDA-cracks. The best estimates of the crack densities were found by trial and error to be $CD = 0.08$ for the coal-seam and $CD = 0.06$ for the country rocks giving the elastic constants in Table 6.2. The cracks (or cleats) are aligned 20° clockwise from the roadways in Figure 6.1, which is believed to be the direction of major cleat in the Harworth seams (Roth, personal communication).

Table 6.2 Elastic constants (in Pascals x 10^9) of the country rocks and the coal seams used for the final model of synthetic seismograms. x_1 is perpendicular to the cracks, x_2 is parallel to the cracks, and x_3 is vertical.

Coal seam 2	$c_{1111} = 5.95$	$c_{2222} = 5.95$	$c_{3333} = 5.95$
	$c_{2233} = 2.07$	$c_{3311} = 2.06$	$c_{1122} = 2.06$
	$c_{2323} = 1.94$	$c_{1313} = 1.62$	$c_{1212} = 1.62$
Country rock	$c_{1111} = 31.74$	$c_{2222} = 31.84$	$c_{3333} = 31.84$
	$c_{2233} = 11.04$	$c_{3311} = 11.01$	$c_{1122} = 11.02$
	$c_{2323} = 10.40$	$c_{1313} = 9.08$	$c_{1212} = 9.08$

Figure 6.4 Synthetic seismograms calculated for the istropic structure in Table 6.1, for four source/geophone geometry as indicated.

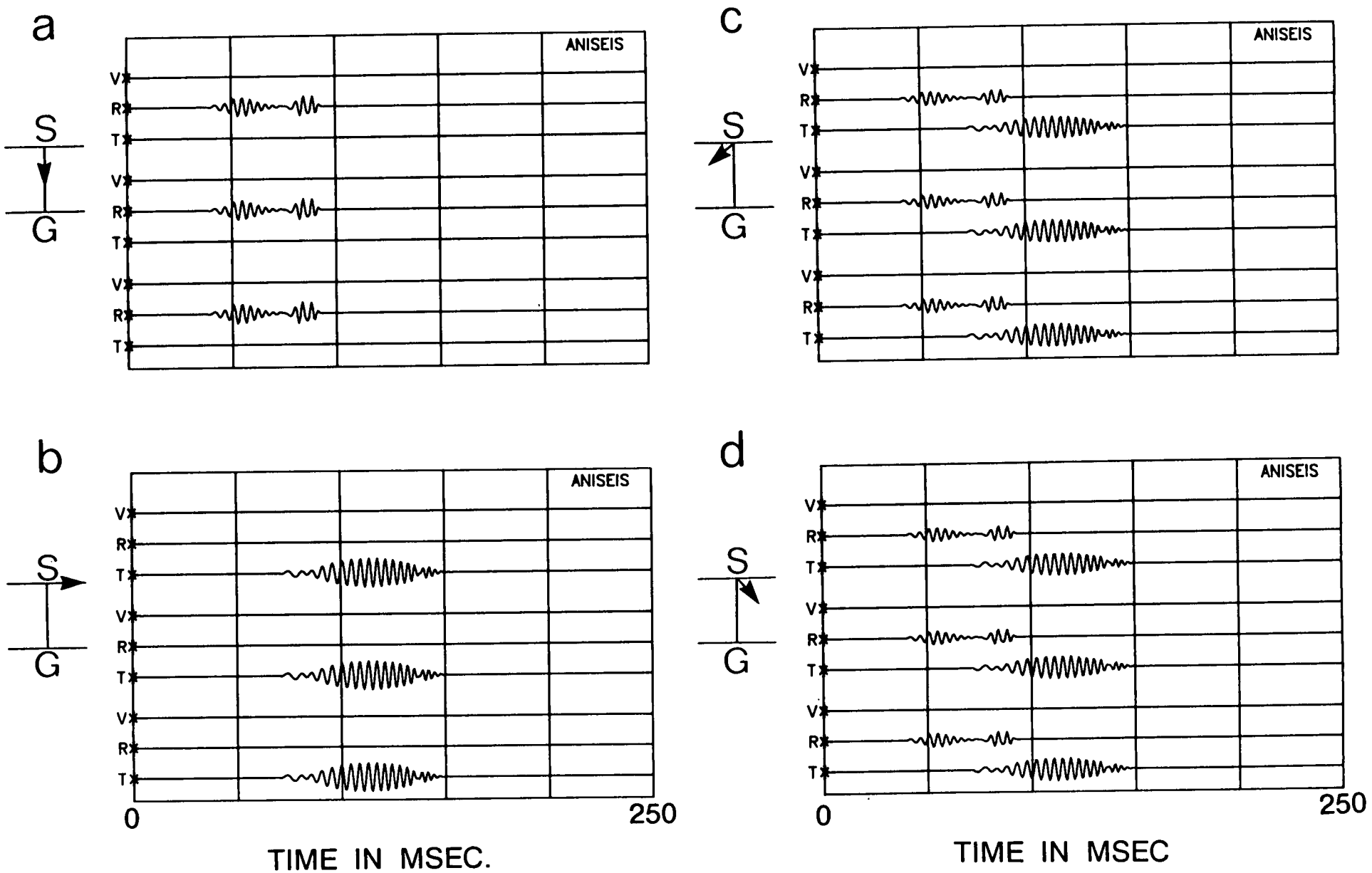

Figure 6.5 compares synthetic seismograms with the observations from Source site 9. The seismograms have been calculated for Model 2, where the isotropy of both country rock and coal-seam has been replaced with the anisotropic parameters in Table 6.2. The synthetic seismograms show many of the general features exhibited in the observations.

The principal arrivals in the synthetic seismograms are:

1) A large amplitude oscillatory wavetrain seen principally on the radial component, which begins near the arrival time of a *P*-wave in the country rock propagating parallel to the seam (a *P* head-wave in the country rock).

2) A large amplitude oscillatory wavetrain, initially low-frequency (about 100 to 150Hz), which begins at shear-wave arrival times in the country rock, and seen principally on the transverse component, it continues as a dispersive train with principally *SH*-motion (Love wave or generalized second modes, see later this chapter). This is likely to be a complicated signal probably composed of several modes of motion.

In the synthetic seismograms, both these signals are generalized mode channel waves as a result of the anisotropy of the model. In anisotropic structures, the separate families of modes with Rayleigh-type motion and Love-type motion in isotropic structures break down, and combine into one family of generalized modes with coupled motion in three dimensions. In order to identify these

Figure 6.5 Comparison of synthetic and observed seismograms for shot hole 9. The synthetic seismograms have been calculated for an anisotropic model with parameters in Table 6.2. The recording source/geophone geometry as indicated.

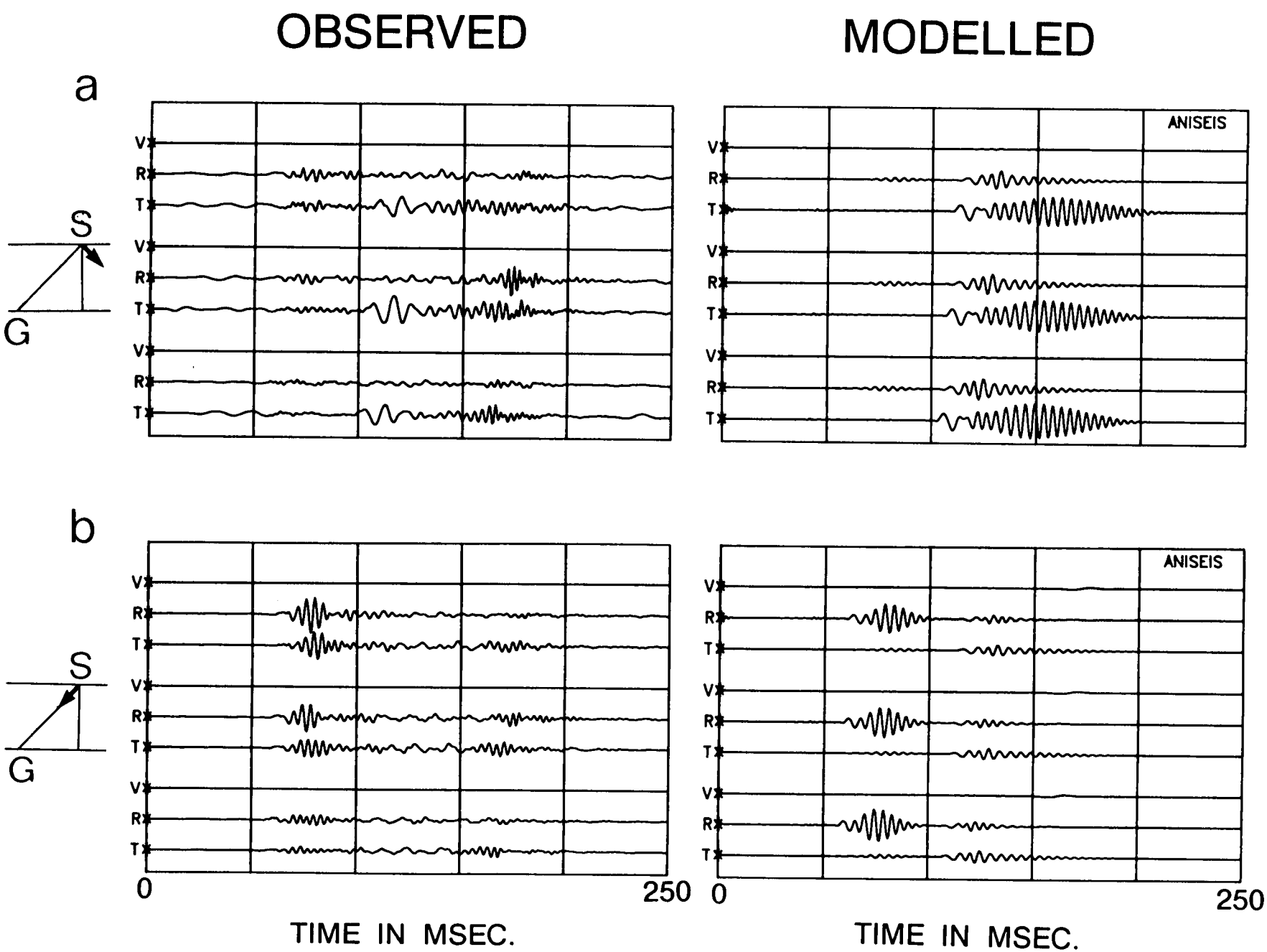

Figure 6.5 (cont.)

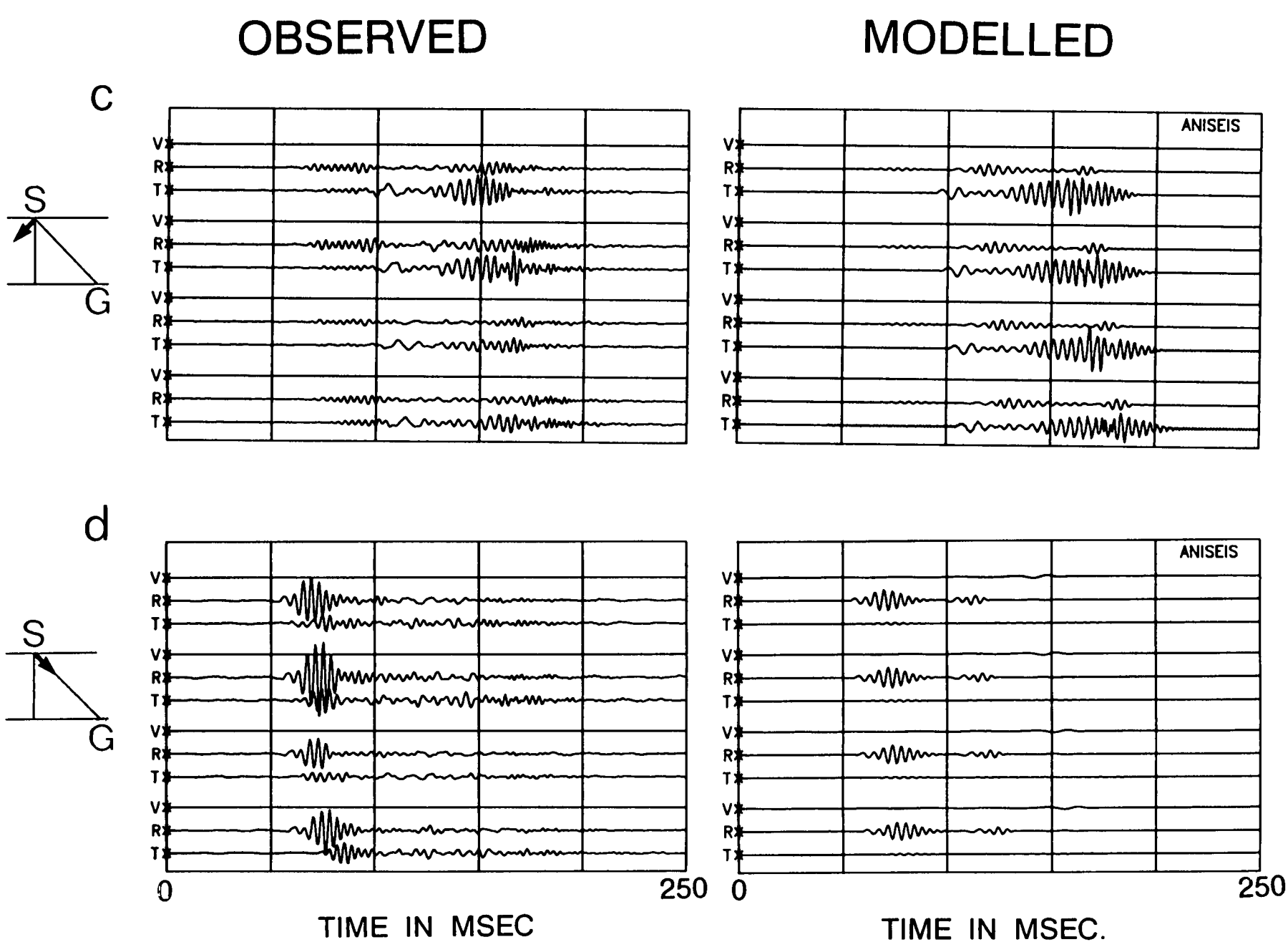

Figure 6.5 (cont.)

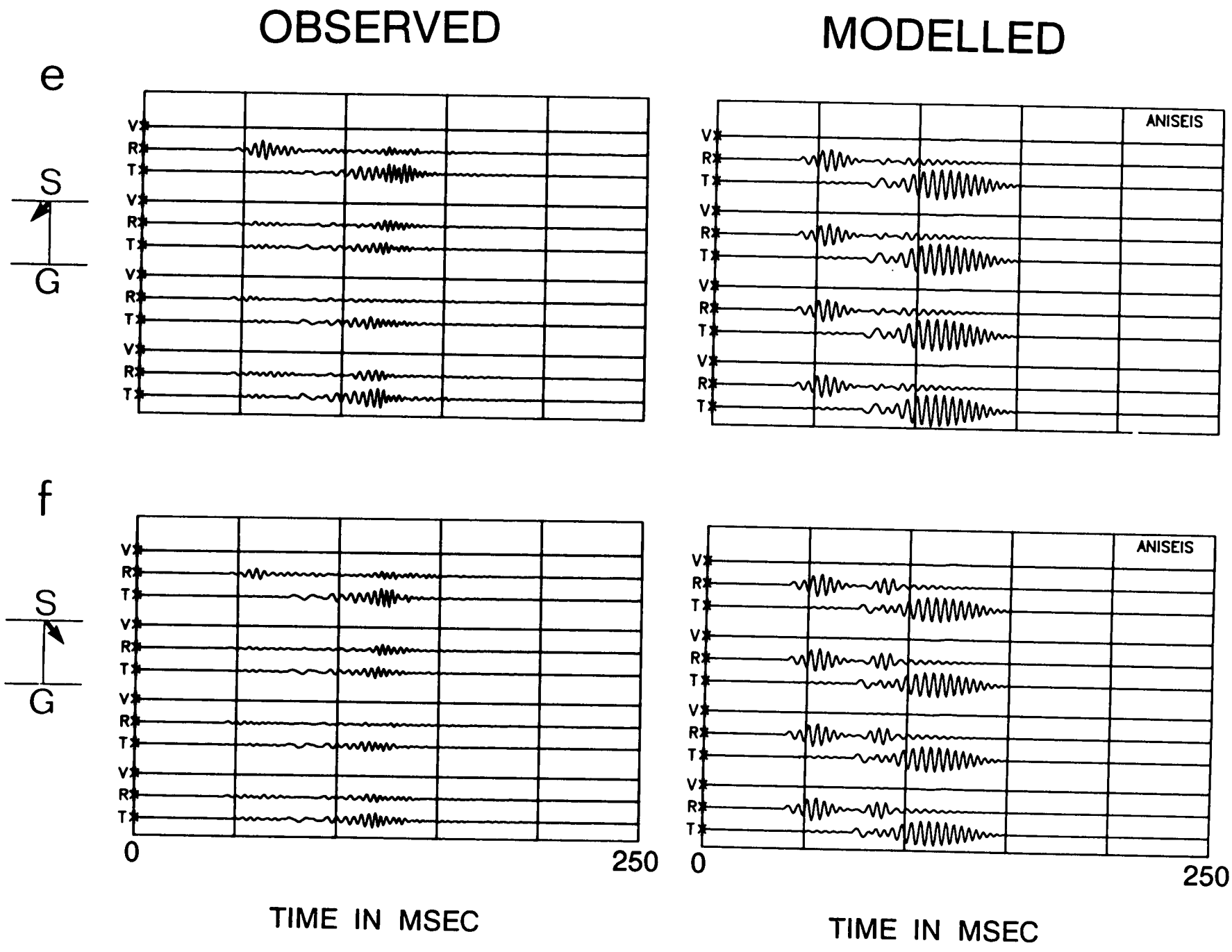

Figure 6.5 (cont.)

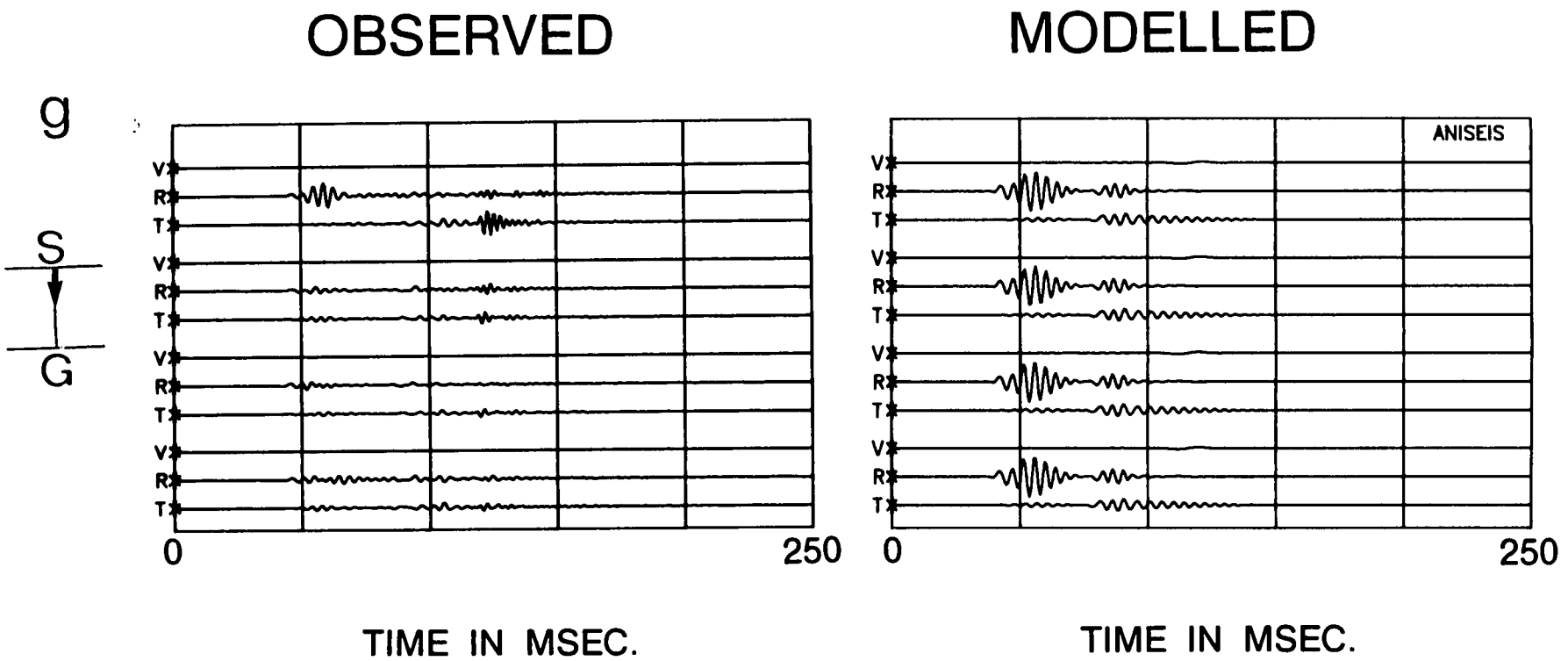

Figure 6.5 (cont.)

arrivals more exactly, it is necessary to calculate dispersion characteristics of various channel wave modes numerically. As the anisotropic dispersion program is currently under modification, in this analysis we will only concentrate on the match of synthetics to observations. Anisotropy is characterized by dispersion and particle motion anomalies which we will discussed later.

6.4.3 Comparison of the Fourier spectrum

As a comparsion, an example of the Fourier spectral amplitudes of Love waves (transverse motions) is shown in Figure 6.6(*a*) for raypath path CF. It shows that the dominant frequency is up to 500 Hz. There are typically three peaks (arrowheads) at the frequencies of 150 Hz, 250 Hz and 420 Hz. Figure 6.6(*c*) shows "unwound" Fourier spectral phase, that is, the phase is not allowed to oscillate between $-\pi$ and π, but is made continuous. For a pure noiseless signal this curve would be perfectly smooth (Burton 1974). The observed signals show smooth phases, suggesting that resolution of the field observations is high. On the bottom of each diagram (Figure 6.6*b* and *d*) is the corresponding diagram from the synthetic seismograms in Figure 6.5. The agreement beween the synthetics and the observations is relatively good, and three peak frequencies are well matched. However, relative amplitudes between peak frequencies are not modelled. This is probably due to the constant attenuation in our model [in most cases, attenuation Q is a linear function of frequency, not constant for all frequencies, Buchanan *et al.* (1983)]. Note that the recording geophone show flat response (Roth, personal communication).

6.5 Dispersion characteristscs

Figure 6.6 Comparison of amplitude (*a* and *b*) and "unwound" phase (*c* and *d*) spectrums of observed (*a* and *c*) and synthetic (*b* and *d*) seismograms for raypath CF in Figure 6.1. Arrowheads indicate the three peak frequencies.

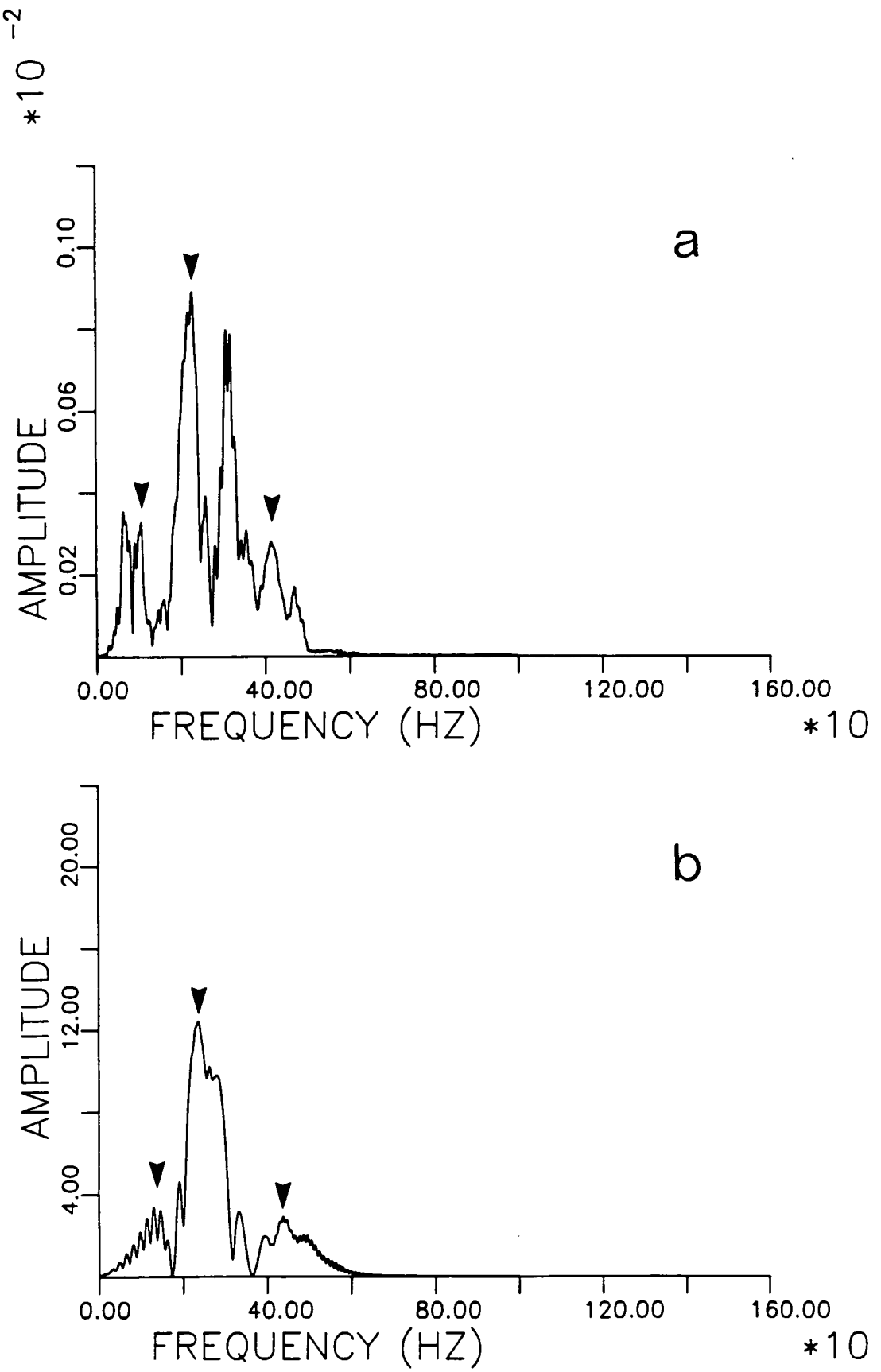

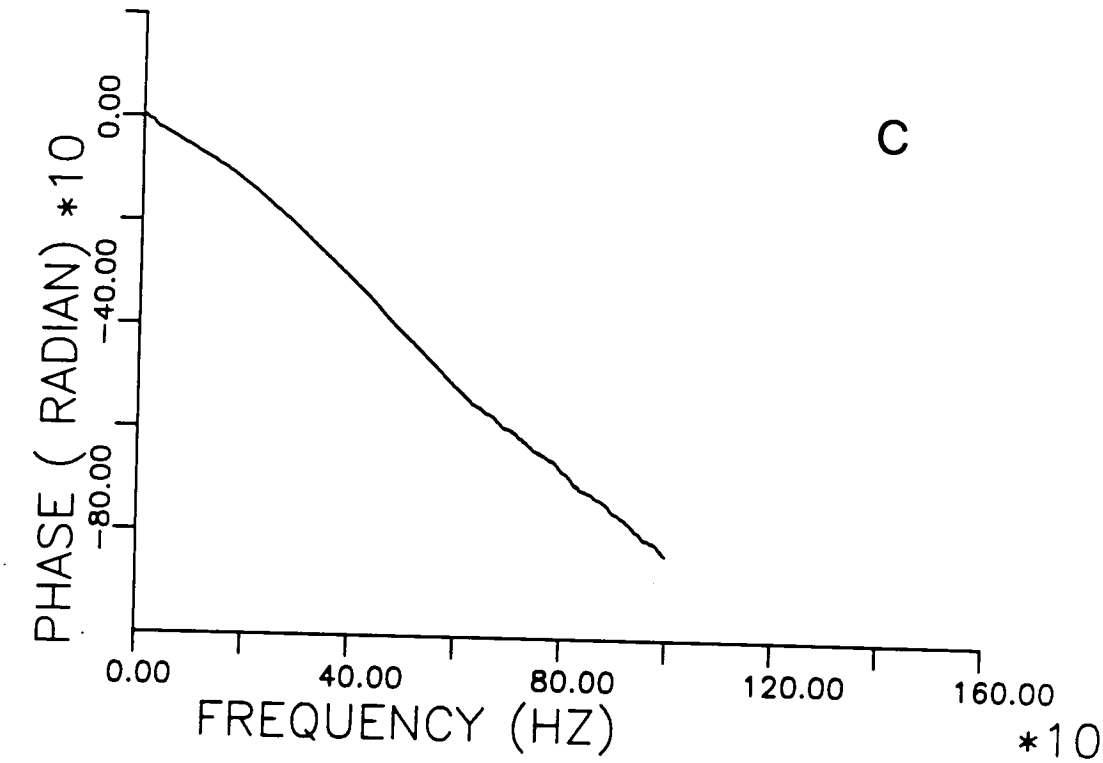
c
PHASE (RADIAN) *10
0.00
-40.00
-80.00
0.00
40.00
80.00
120.00
160.00
FREQUENCY (HZ)
*10

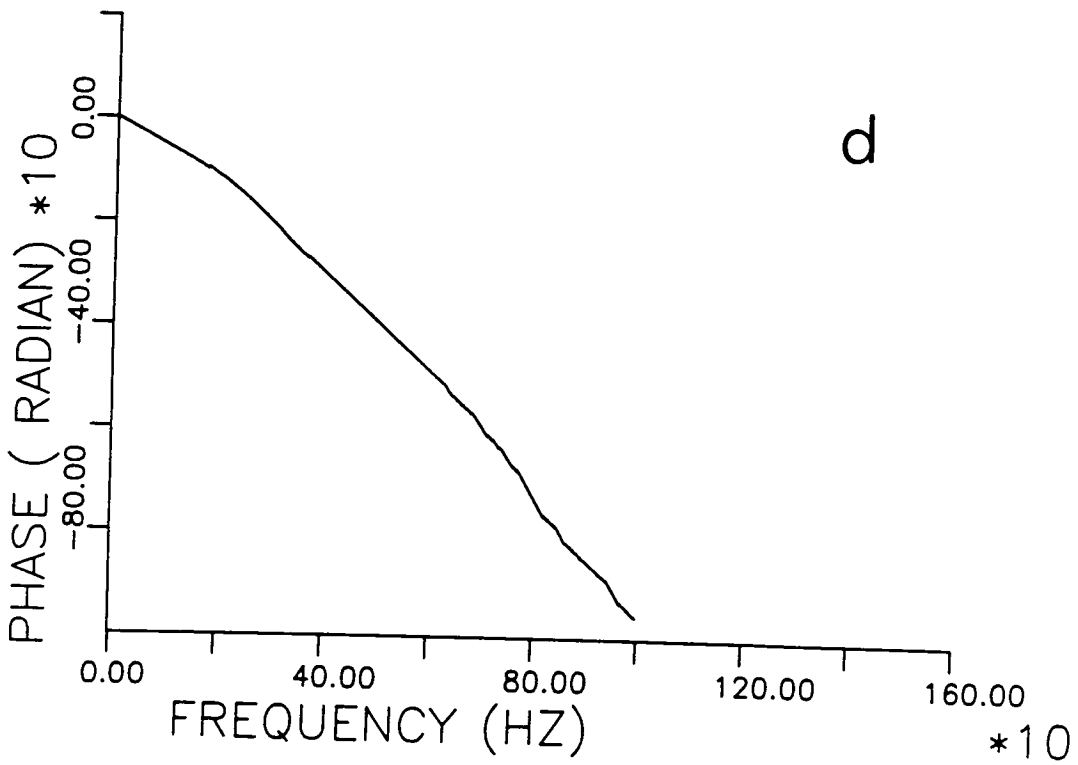
d
PHASE (RADIAN) *10
0.00
-40.00
-80.00
0.00
40.00
80.00
120.00
160.00
FREQUENCY (HZ)
*10

6.5.1 Group velocity dispersion

Dispersion is a major feature of channel waves. It can be extracted by the multiple-filter technique of Dziewonski *et al.* (1969) as modified by Burton and Blamey (1972). Each trace is time-windowed and the arrival times transformed into group velocity-frequency space. In effect, each trace is passed through a bank of overlapping filters to separate arrival times of different frequencies. The filtered in-phase and quadrature spectra, for each frequency point, are then transformed back into the time domain and combined to form a smoothed envelope of instantaneous amplitude. The complete set of amplitudes for all signal frequencies therefore describe the signal in both the velocity and frequency domains. The amplitudes are normalized with respect to the maximum value, and then results displayed as a contour diagram in the velocity-frequency domain. The group velocity can be found by following the ridge representing the signal across the diagram.

A typical contour diagram of instantaneous amplitude in the group velocity-frequency plane is shown for the recording path CH of Figure 6.1 in Figure 6.7. The inferred group velocity dispersion from the contour is marked with "+ + +" and plotted in Figure 6.8. Table 6.3 is a list of output of the group velocity dispersion data picked up from the contour. The lower cutoff frequency is towards zero, indicating that the channel (coal-seam) is nearly symetrical.

One of the advantages of the in-seam seismics is that it is usually possible to make accurate velocity estimates by locating shots and geophones on the opposite sites of a block of unmined coal. This is demonstrated in the following. Dispersions from two groups of geophones closely located at positions F and H are plotted

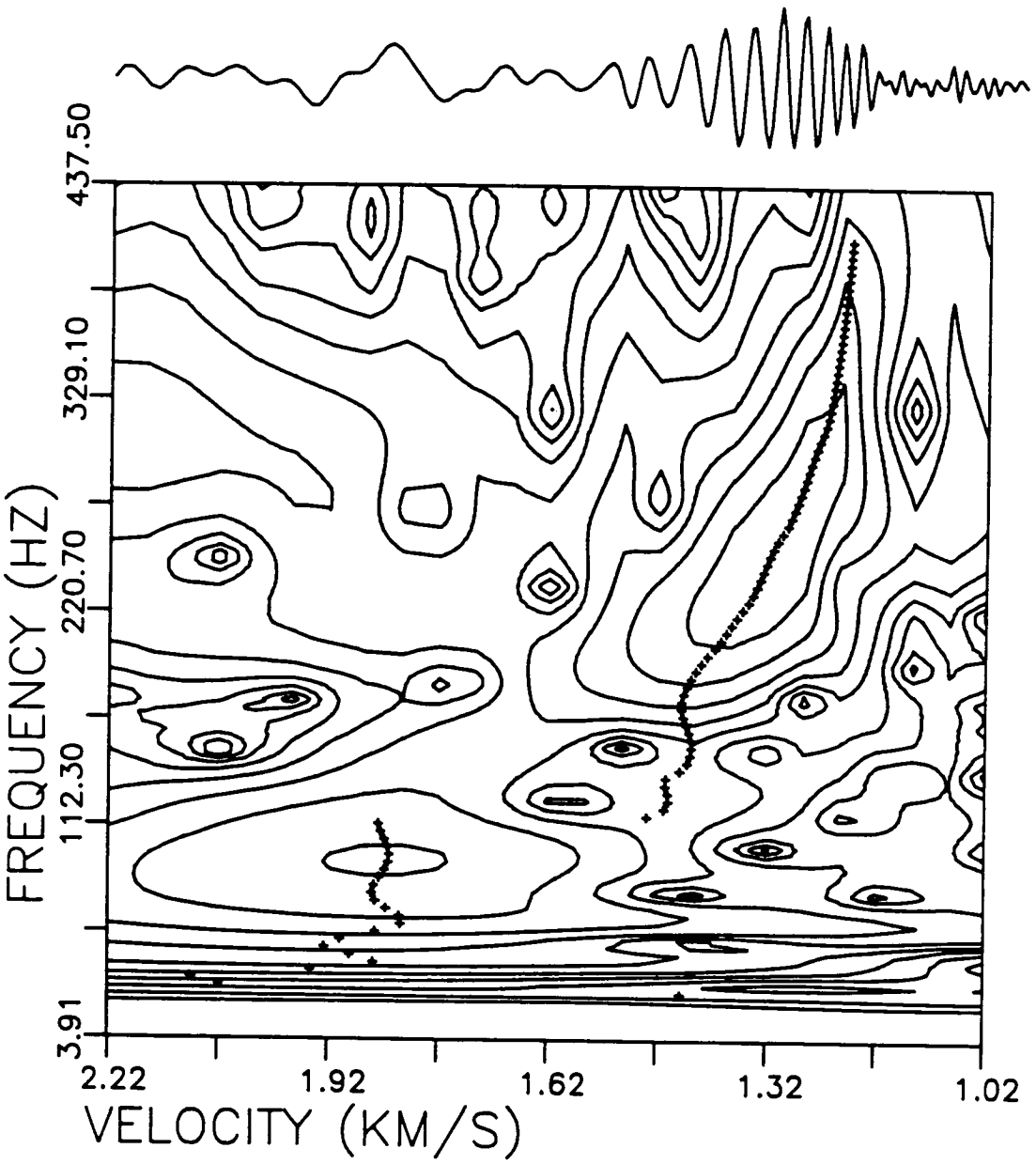

Figure 6.7 A typical contour plot of the multiple filter analysis of the traces for the first geophones for raypath CH of Figure 6.1. Group velocities inferred from the contour and picked automatically are denoted by "+ + +".

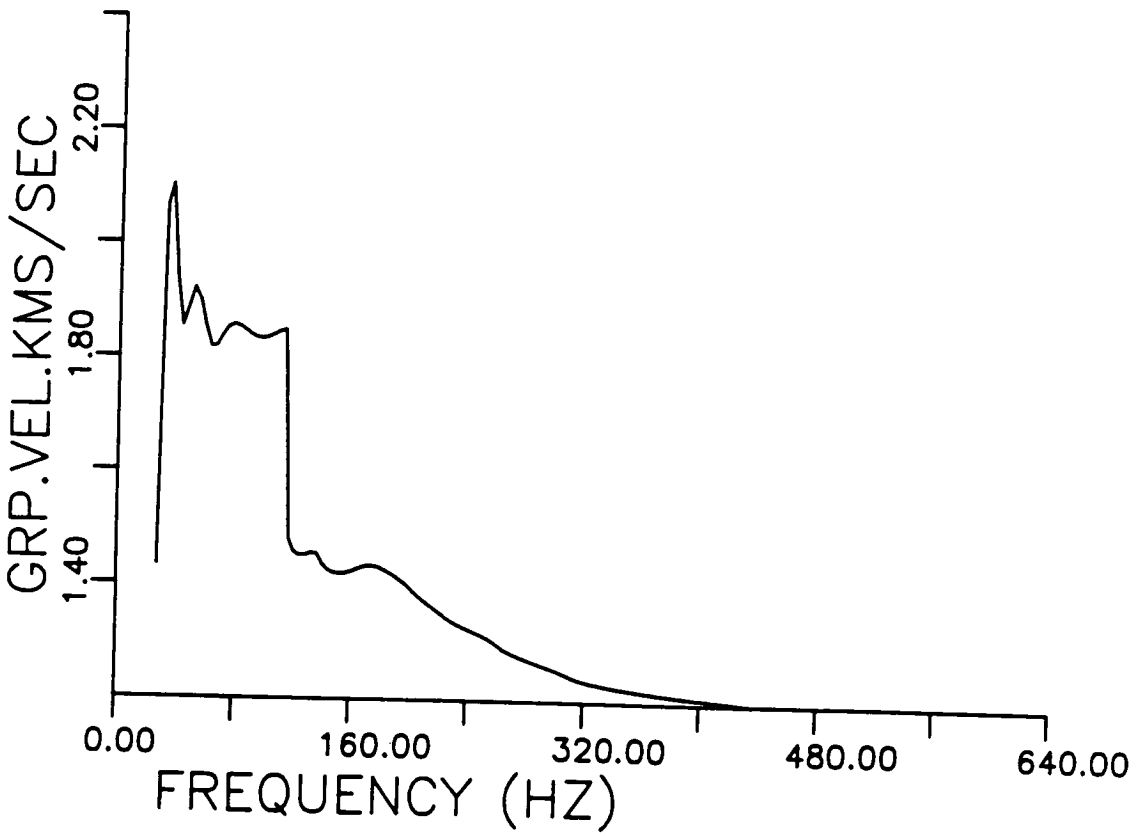

Figure 6.8 Un-smoothed dispersion curves inferred from Figure 6.7. The dispersion data are listed in Table 6.3.

Table 6.3 List of the output of the group velocity dispersion data plotted Figure 6.8.

	FREQUENCY	PERIOD	G VELOCITY
1	0.39062E+01	0.25600E+00	0.12670E+01
2	0.78125E+01	0.12800E+00	0.26988E+01
3	0.11719E+02	0.85333E-01	0.85570E+00
4	0.15625E+02	0.64000E-01	0.12545E+01
5	0.19531E+02	0.51200E-01	0.11370E+01
6	0.23437E+02	0.42667E-01	0.10185E+01
7	0.27344E+02	0.36571E-01	0.13719E+01
8	0.31250E+02	0.32000E-01	0.20205E+01
9	0.35156E+02	0.28444E-01	0.21215E+01
10	0.39062E+02	0.25600E-01	0.19611E+01
11	0.42969E+02	0.23273E-01	0.18651E+01
12	0.46875E+02	0.21333E-01	0.18902E+01
13	0.50781E+02	0.19692E-01	0.19203E+01
14	0.54687E+02	0.18286E-01	0.18994E+01
15	0.58594E+02	0.17067E-01	0.18518E+01
16	0.62500E+02	0.16000E-01	0.18179E+01
17	0.66406E+02	0.15059E-01	0.18201E+01
18	0.70312E+02	0.14222E-01	0.18388E+01
19	0.74219E+02	0.13474E-01	0.18536E+01
20	0.78125E+02	0.12800E-01	0.18581E+01
21	0.82031E+02	0.12190E-01	0.18545E+01
22	0.85937E+02	0.11636E-01	0.18478E+01
23	0.89844E+02	0.11130E-01	0.18405E+01
24	0.93750E+02	0.10667E-01	0.18350E+01
25	0.97656E+02	0.10240E-01	0.18335E+01
26	0.10156E+03	0.98462E-02	0.18364E+01
27	0.10547E+03	0.94815E-02	0.18413E+01
28	0.10937E+03	0.91429E-02	0.18466E+01
29	0.11328E+03	0.88276E-02	0.18497E+01
30	0.11719E+03	0.85333E-02	0.14831E+01
31	0.12109E+03	0.82581E-02	0.14572E+01
32	0.12500E+03	0.80000E-02	0.14506E+01
33	0.12891E+03	0.77576E-02	0.14515E+01
34	0.13281E+03	0.75294E-02	0.14558E+01
35	0.13672E+03	0.73143E-02	0.14559E+01
36	0.14062E+03	0.71111E-02	0.14420E+01
37	0.14453E+03	0.69189E-02	0.14254E+01
38	0.14844E+03	0.67368E-02	0.14213E+01
39	0.15234E+03	0.65641E-02	0.14203E+01
40	0.15625E+03	0.64000E-02	0.14206E+01
41	0.16016E+03	0.62439E-02	0.14238E+01
42	0.16406E+03	0.60952E-02	0.14285E+01
43	0.16797E+03	0.59535E-02	0.14361E+01
44	0.17187E+03	0.58182E-02	0.14396E+01
45	0.17578E+03	0.56889E-02	0.14374E+01
46	0.17969E+03	0.55652E-02	0.14325E+01
47	0.18359E+03	0.54468E-02	0.14262E+01
48	0.18750E+03	0.53333E-02	0.14205E+01
49	0.19141E+03	0.52245E-02	0.14141E+01
50	0.19531E+03	0.51200E-02	0.14074E+01
51	0.19922E+03	0.50196E-02	0.14000E+01
52	0.20312E+03	0.49231E-02	0.13915E+01
53	0.20703E+03	0.48302E-02	0.13815E+01
54	0.21094E+03	0.47407E-02	0.13726E+01
55	0.21484E+03	0.46545E-02	0.13653E+01
56	0.21875E+03	0.45714E-02	0.13586E+01
57	0.22266E+03	0.44912E-02	0.13522E+01
58	0.22656E+03	0.44138E-02	0.13459E+01
59	0.23047E+03	0.43390E-02	0.13394E+01
60	0.23437E+03	0.42667E-02	0.13326E+01
61	0.23828E+03	0.41967E-02	0.13265E+01

Table 6.3 (cont.)

62	0.24219E+03	0.41290E-02	0.13220E+01
63	0.24609E+03	0.40635E-02	0.13179E+01
64	0.25000E+03	0.40000E-02	0.13140E+01
65	0.25391E+03	0.39385E-02	0.13100E+01
66	0.25781E+03	0.38788E-02	0.13058E+01
67	0.26172E+03	0.38209E-02	0.13013E+01
68	0.26562E+03	0.37647E-02	0.12963E+01
69	0.26953E+03	0.37101E-02	0.12904E+01
70	0.27344E+03	0.36571E-02	0.12835E+01
71	0.27734E+03	0.36056E-02	0.12765E+01
72	0.28125E+03	0.35556E-02	0.12713E+01
73	0.28516E+03	0.35068E-02	0.12670E+01
74	0.28906E+03	0.34595E-02	0.12633E+01
75	0.29297E+03	0.34133E-02	0.12600E+01
76	0.29687E+03	0.33684E-02	0.12571E+01
77	0.30078E+03	0.33247E-02	0.12543E+01
78	0.30469E+03	0.32821E-02	0.12517E+01
79	0.30859E+03	0.32405E-02	0.12492E+01
80	0.31250E+03	0.32000E-02	0.12466E+01
81	0.31641E+03	0.31605E-02	0.12440E+01
82	0.32031E+03	0.31220E-02	0.12411E+01
83	0.32422E+03	0.30843E-02	0.12380E+01
84	0.32812E+03	0.30476E-02	0.12345E+01
85	0.33203E+03	0.30118E-02	0.12303E+01
86	0.33594E+03	0.29767E-02	0.12272E+01
87	0.33984E+03	0.29425E-02	0.12249E+01
88	0.34375E+03	0.29091E-02	0.12228E+01
89	0.34766E+03	0.28764E-02	0.12208E+01
90	0.35156E+03	0.28444E-02	0.12190E+01
91	0.35547E+03	0.28132E-02	0.12172E+01
92	0.35937E+03	0.27826E-02	0.12155E+01
93	0.36328E+03	0.27527E-02	0.12140E+01
94	0.36719E+03	0.27234E-02	0.12124E+01
95	0.37109E+03	0.26947E-02	0.12110E+01
96	0.37500E+03	0.26667E-02	0.12096E+01
97	0.37891E+03	0.26392E-02	0.12082E+01
98	0.38281E+03	0.26122E-02	0.12069E+01
99	0.38672E+03	0.25859E-02	0.12057E+01
100	0.39062E+03	0.25600E-02	0.12045E+01
101	0.39453E+03	0.25347E-02	0.12033E+01
102	0.39844E+03	0.25098E-02	0.12023E+01
103	0.40234E+03	0.24854E-02	0.12012E+01
104	0.40625E+03	0.24615E-02	0.12002E+01
105	0.41016E+03	0.24381E-02	0.11992E+01
106	0.41406E+03	0.24151E-02	0.11982E+01
107	0.41797E+03	0.23925E-02	0.11973E+01
108	0.42187E+03	0.23704E-02	0.11964E+01
109	0.42578E+03	0.23486E-02	0.11954E+01
110	0.42969E+03	0.23273E-02	0.11945E+01
111	0.43359E+03	0.23063E-02	0.11935E+01
112	0.43750E+03	0.22857E-02	0.11924E+01

in Figure 6.9. Although seismograms (Figure 6.2) show more irregular, dispersion characteristics seem stable. This demonstrates that the multiple filter technique used here is reliable and also the velocity estimates by in-seam seismics is accurate. It is, therefore, possible to stack the dispersions from a group of closed located geophones to give a composite section comprising all transverse traces (we call this the dispersion stacking, which similar to Buchanan's dispersion stacking technique, Buchanan *et al.* 1983).

6.5.2 Dispersion anomalies

The rotated seismograms in Figure 6.2 shows that the transverse motion (Love wave) is coupled to a small radial motion. The dispersion curves of radial (dashed line) and transverse components (solid line) from raypath CH, CG and CF are compared in Figure 6.10. Only six typical examples are given. It is seen that both radial and transverse components have identical dispersion features, that is dispersion curves of the radial and the transverse components for frequency larger than 150Hz are almost the same, implying that both components record the same mode. This could be, however, due to the incorrect rotation by equation (6-3), but can be distinguished from elliptical particle motions (see next section). In fact, because radial and transverse components are constantly ½π out of phase, poor rotation of the observed seismograms alone cannot explain this observation (incorrect rotation causes residual coupling, which will be discussed in section 6.6.3).

Apart from the coupling discussed above, another anomaly inferred from dispersion analysis is the azimuthal variation of dispersion curves. The stacked dispersion curves of raypath CH, CG, and CF are

Figure 6.9 Comparison of dispersion curves of Love waves from a group of geophones (3) closely located at (*a*) position F, and (*b*) position H (source location is at position C). Similar characteristics in each group implies the accuracy of velocity estimates and also the possibility of dispersion stacking technique.

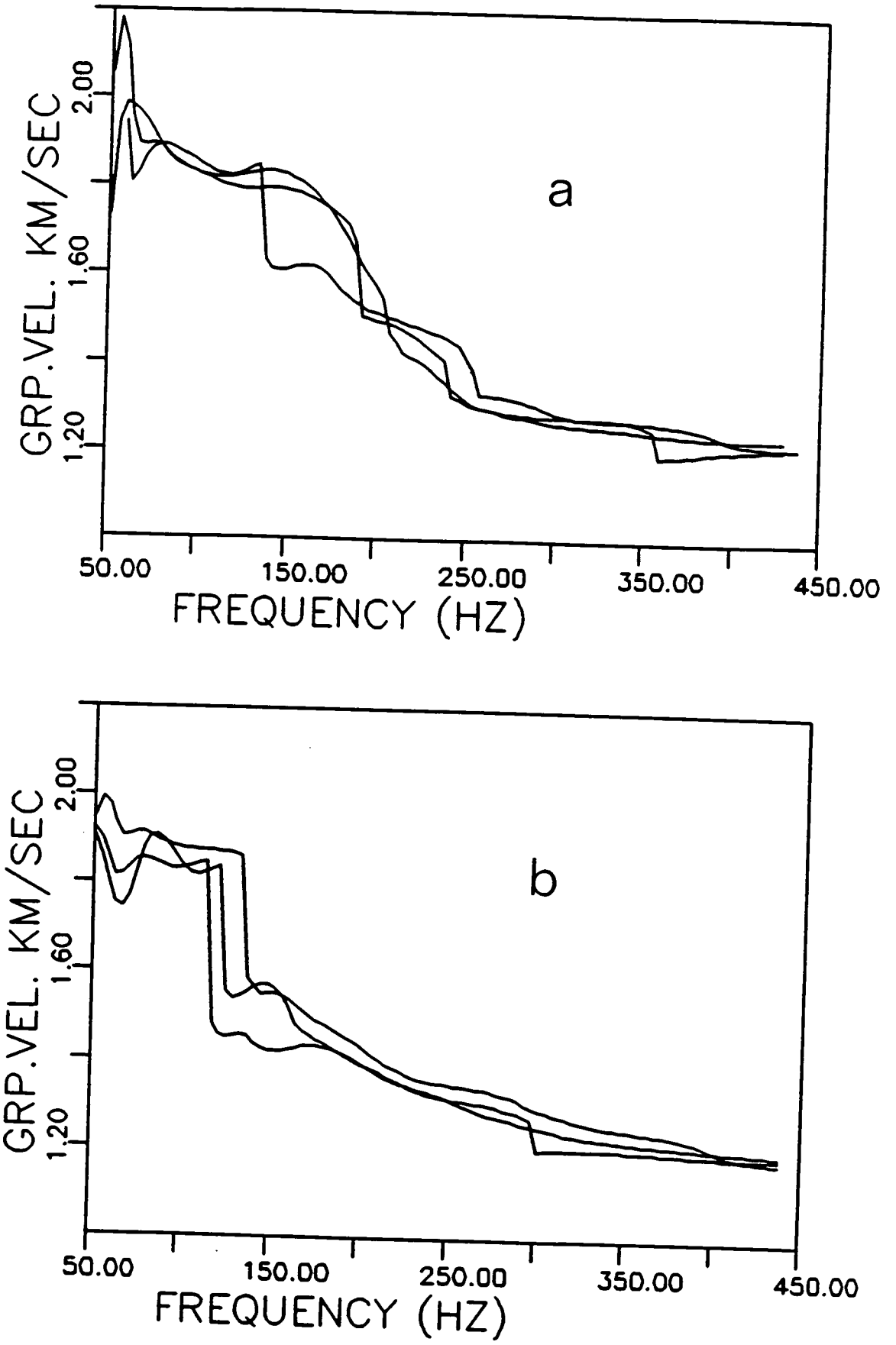

Figure 6.10 Comparison of Love channel wave dispersion characteristics of (R)adial and (T)ransverse components from transverse source (impact direction perpendicular to the raypath) for (*a*) geophone 1 and (*b*) geophone 2 of raypath CH, and (*c*) geophone 1 and (*d*) geophone 2 of raypath CF. (*e*) and (*f*) for geophone 2 of raypath CG for impact source orientations 45° to the right and left, respectively. Similar dispersion characteristics in radial and transverse components indicate the coupling of Love waves.

Figure 6.10 (cont.)

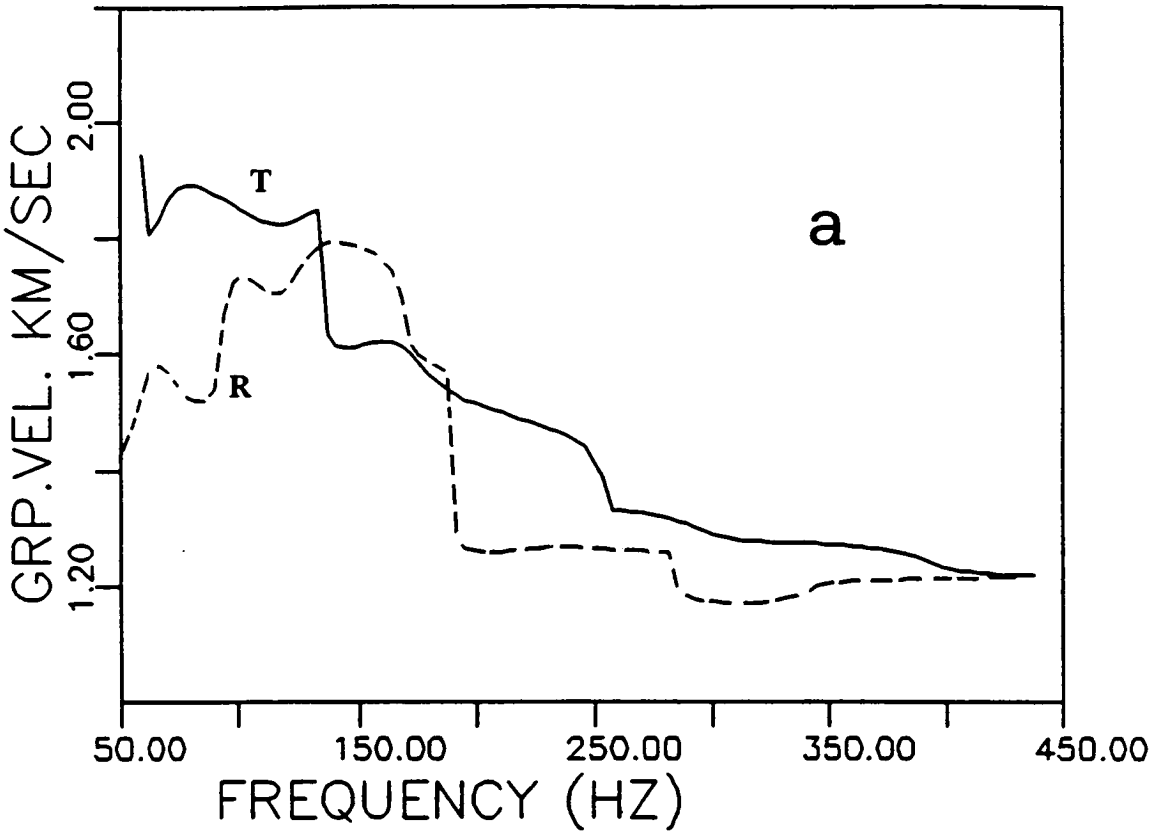

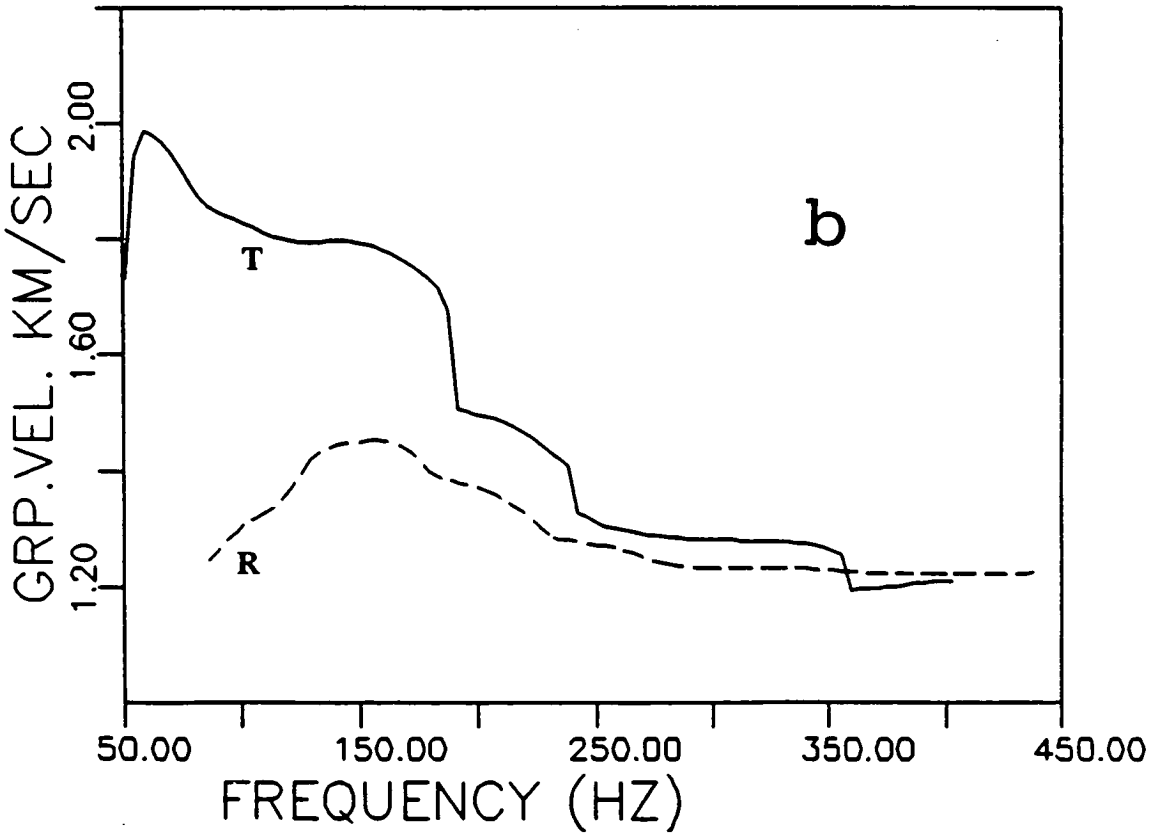

Figure 6.10 (cont.)

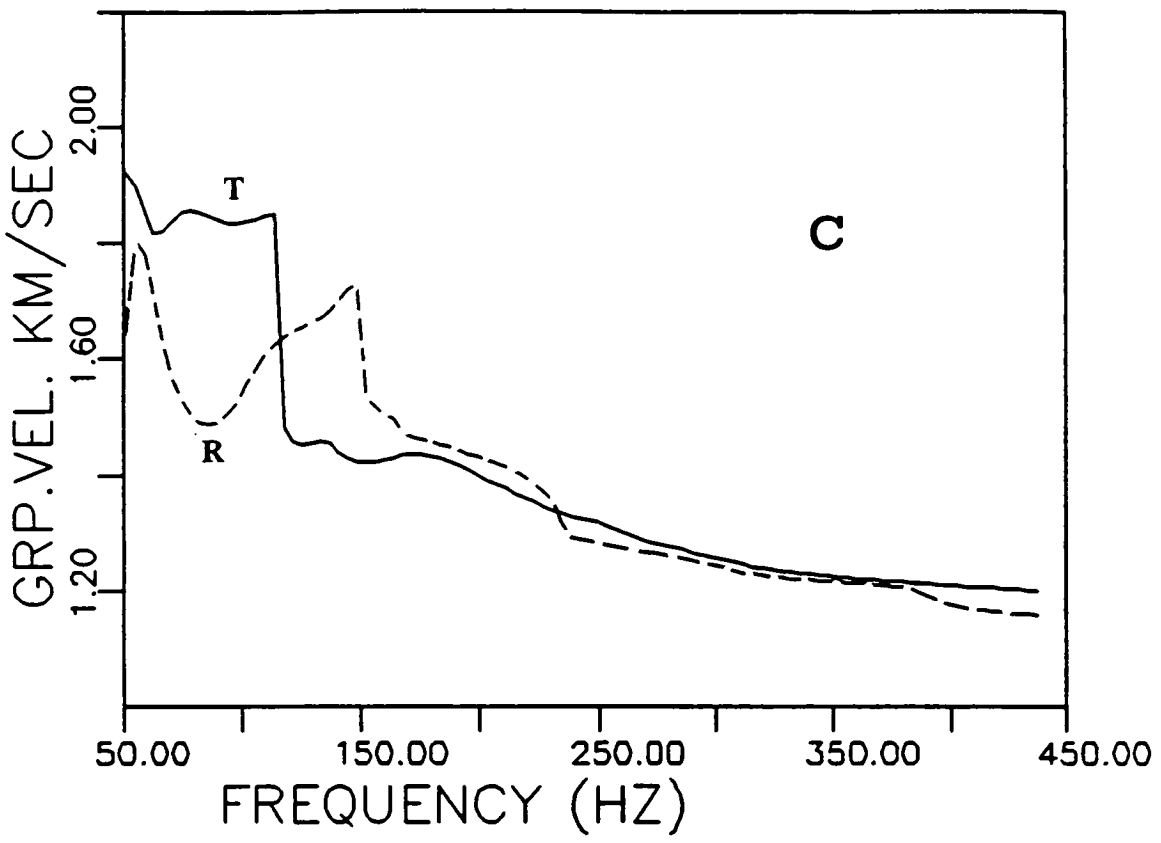

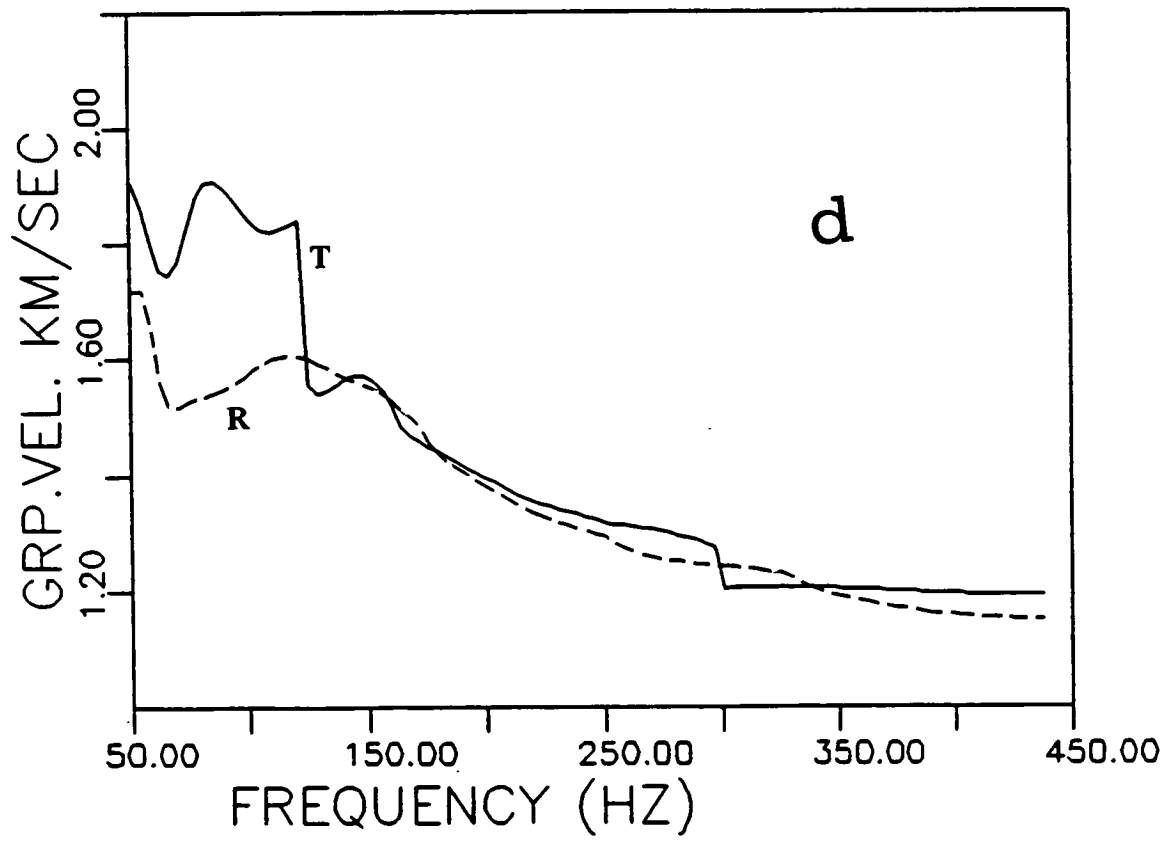

Figure 6.10 (cont.)

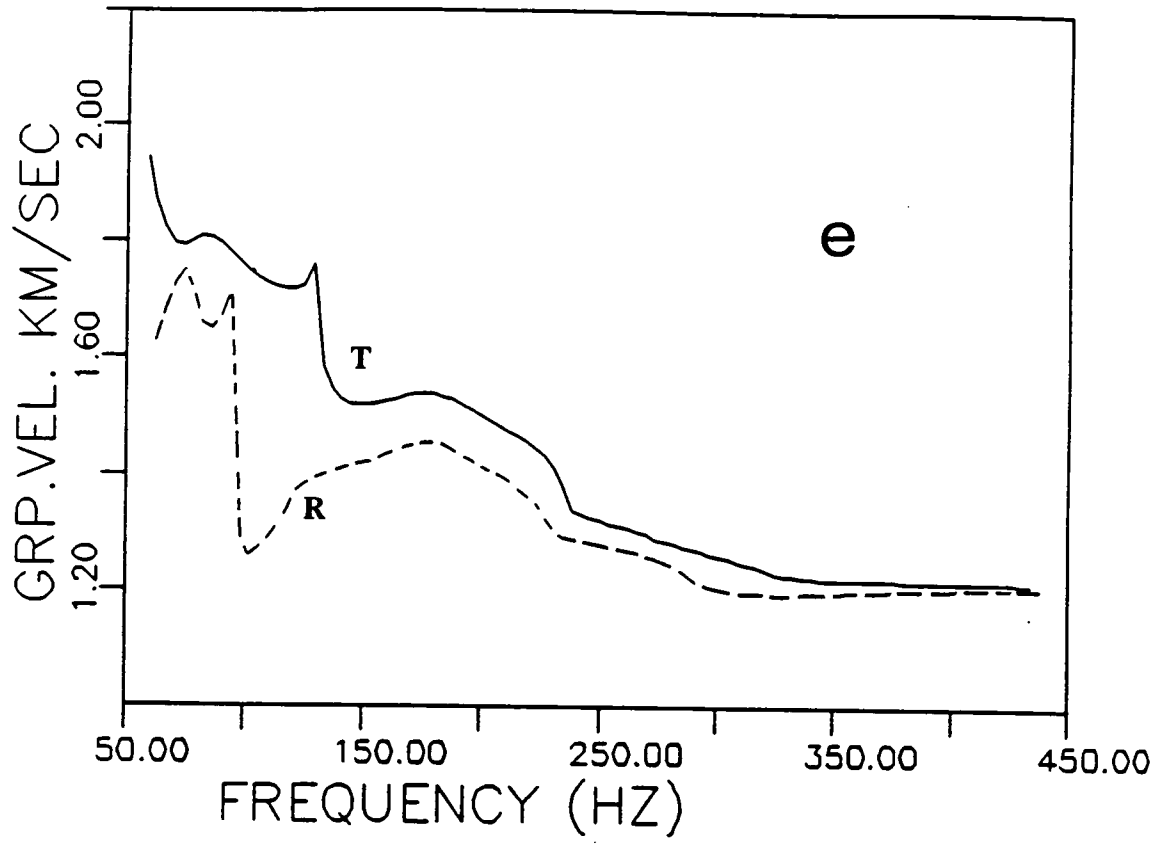

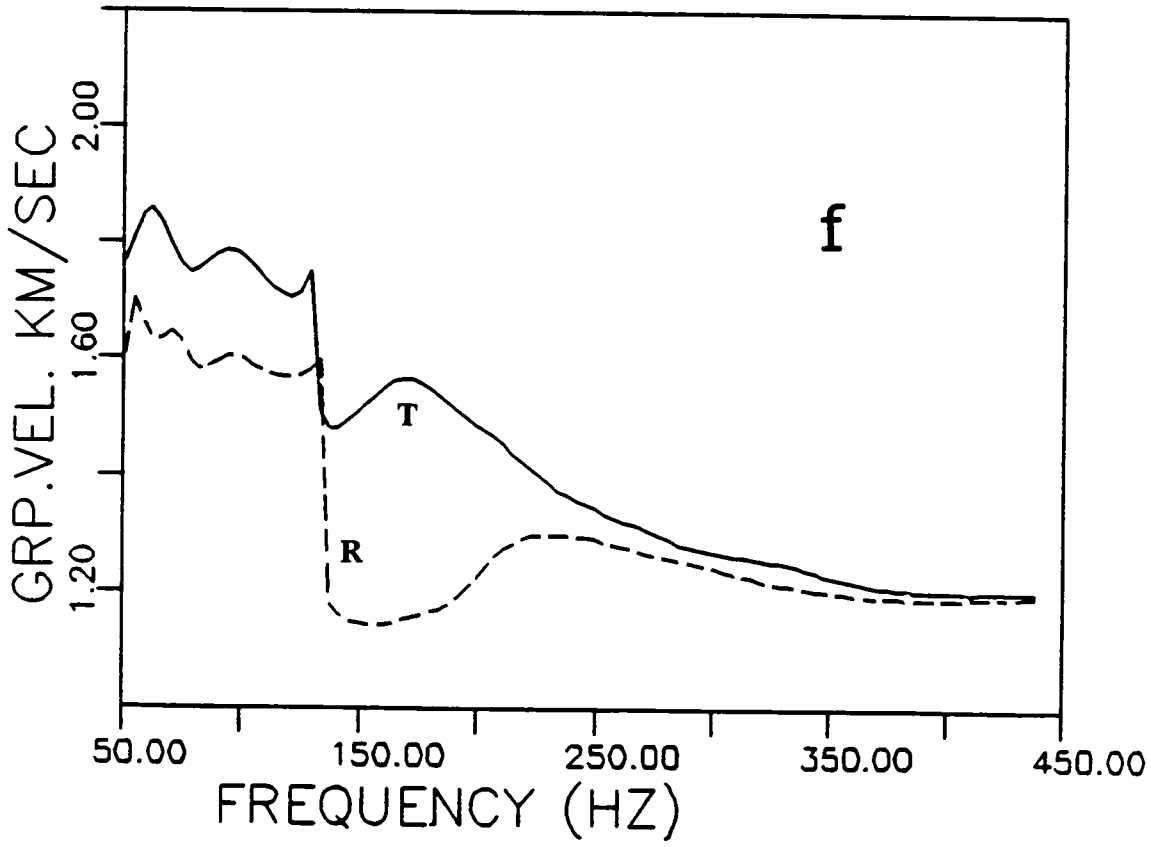

compared in Figure 6.11. We see that dispersion curves from these three directions are almost constantly separated from low frequency to high frequency with the maximum separation of 8-12%. In general, channel wave travels faster for raypath CH than for CF and CG, which is an indication of anisotropy. It is, however, noted that the data we analyzed here are not totally appropriate for the detection of azimuthal variation of dispersion. The data recorded from the raypath between CF and CH are not available to us except from raypath CG, so we cannot determine the fastest velocity direction accurately. Nevertheless, the data availabe do show azimuthal variation of dispersion.

It is sometimes suggested that these two discrepancies inferred from the dispersion analysis: coupling (identification of the same mode from radial and transverse components) and azimuthal variation of dispersion, that cannot be explained by isotropic theoretical models, may be due to anisotropy.

6.5.3 Comparison with theoretical dispersion

Figure 6.12 compares the dispersion of the synthetic (short dashed line) to the observed (long dashed line) Love waves from source site 9. The smoothed curves (solid line) are the theoretical group velocity dispersion calculated for the *isotropic* reference model (Table 6.1) using the extended phase recursion technique described in Appendix B. In general, the dispersion of synthetic seismograms is in a good agreement with the observations in a whole range of frequency from 50 to 450 Hz.

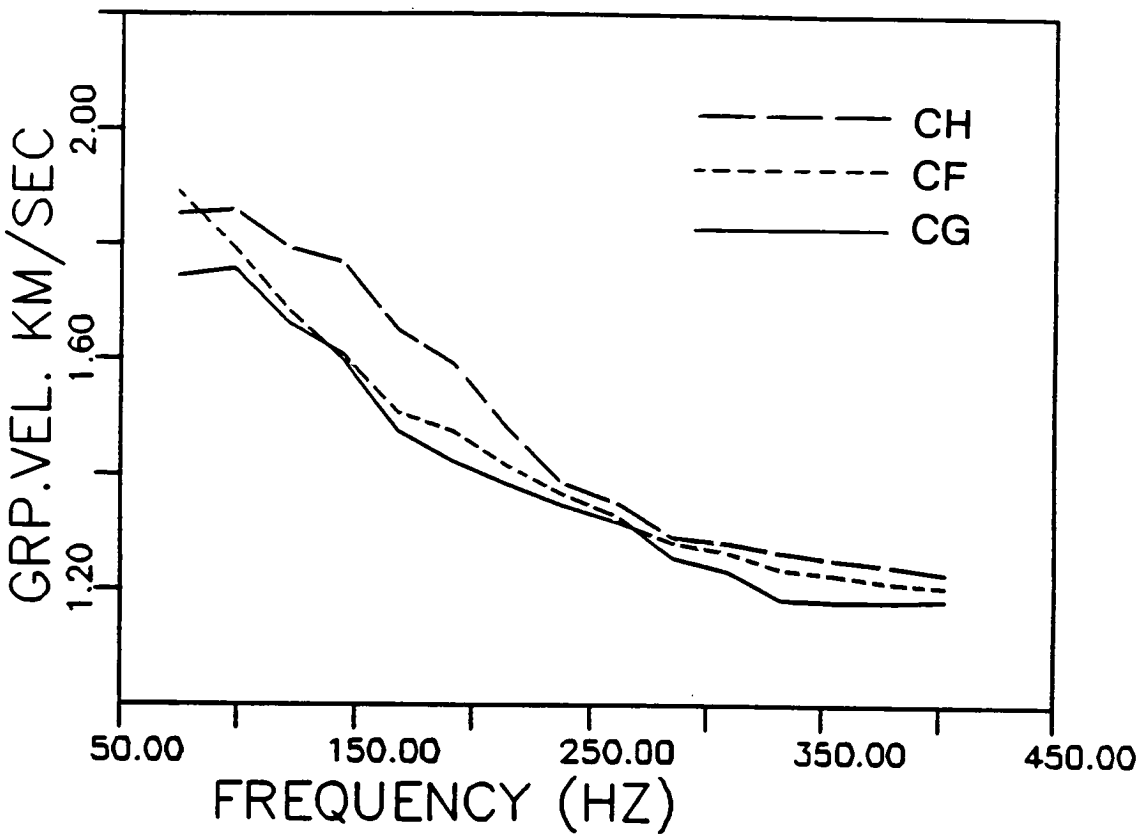

Figure 6.11 Stacked dispersion curves from three directions (raypath CH, CG, and CF) showing maximum anisotropy of 8-12%.

Figure 6.12 Comparison of dispersion of observed (long dashed line) with synthetic (short dashed line) Love wave seismograms and the theoretical Love wave dispersion of an isotropic reference model in Figure 6.1 (solid line). The theoretical Love wave dispersion is calculated by using the phase recursion method in Appendix B. (*a*) raypath CH and (*b*) raypath CF.

a

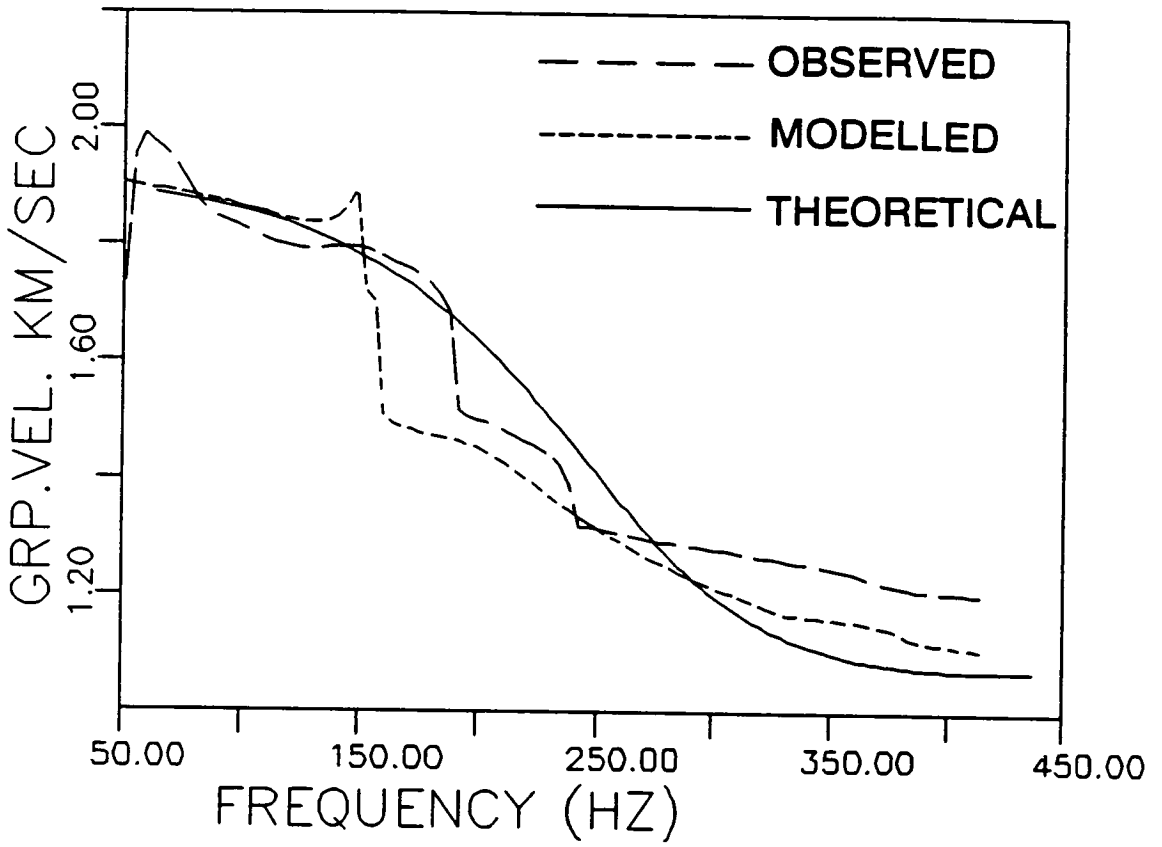
OBSERVED
MODELLED
THEORETICAL
GRP.VEL. KM/SEC
2.00
1.60
1.20
50.00
150.00
250.00
350.00
450.00
FREQUENCY (HZ)

b

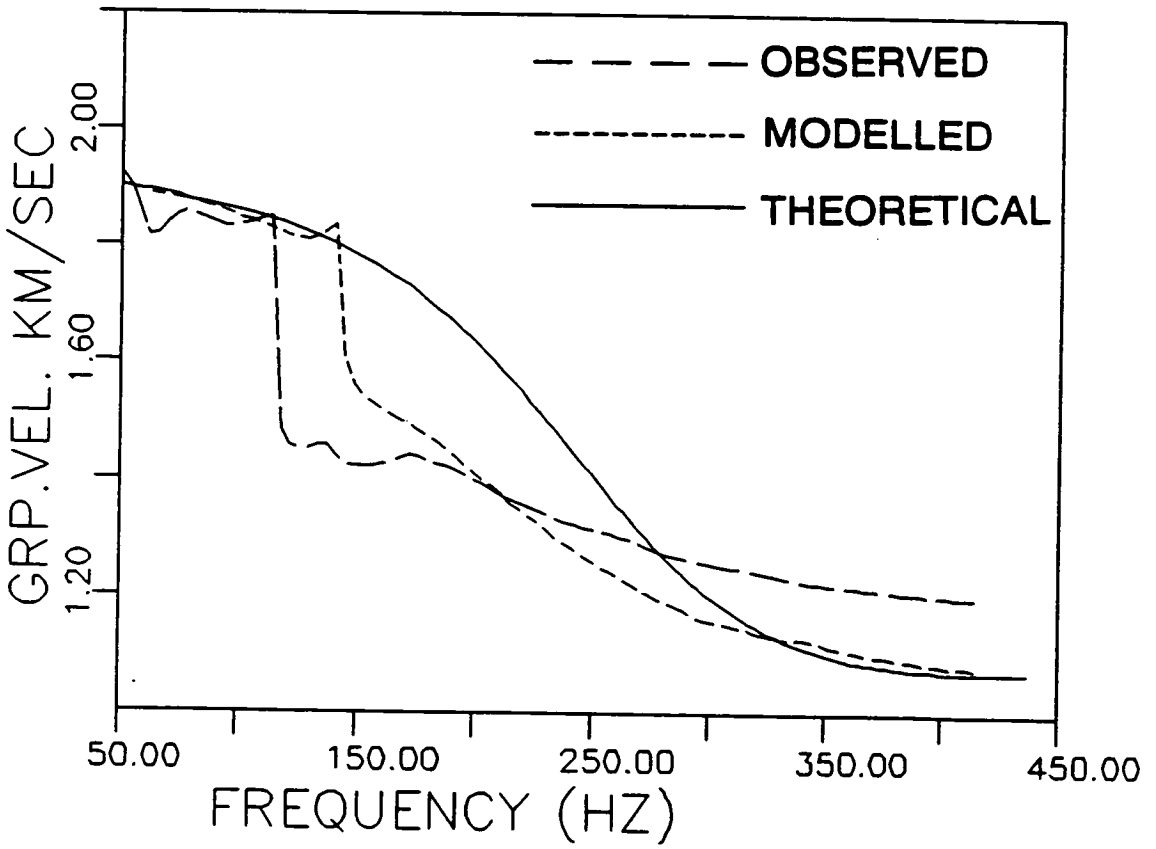
OBSERVED
MODELLED
THEORETICAL
GRP.VEL. KM/SEC
2.00
1.60
1.20
50.00
150.00
250.00
350.00
450.00
FREQUENCY (HZ)

Figure 6.13 compares the dispersion of radial (dashed line) and transverse components (solid line) of theoretical seismograms for the raypath CH, we see a perfect comfirmation of coupled Love-wave modes on the radial component. This is again similar to the observation in Figure 6.10.

We have already found the azimuthal variation of dispersion of channel waves from the observed data (Figure 6.11). This can be modelled by synthetic seismograms. Figure 6.14 compares stacked dispersion curves of synthetic seismograms for raypaths CH, CG and CF. The separation of dispersion curves from different raypaths relative to the crack orientations can be clearly seen for whole range of frequency, which is consistent with the observations in Figure 6.11. The fast direction is when the raypath is near the crack (cleat) normal (raypath CH) as expected for *shear-waves* in crack- induced anisotropic media, where the faster split shear-wave is in the plane through the crack normal. Therefore the existence of cleats in coal-seams is confirmed by comparison of dispersion between observed and synthetics. Note that variation of dispersion with direction for seismic surface waves have been widely used by seismologists to infer crustal and upper mantle anisotropy [for example, Smith and Dahlen 1973; Mindevalli and Mitchell 1989].

6.6 Particle motion anomalies

6.6.1 Relation to anisotropic symmetry: theory

We have found dispersion anomalies of observed Love channel waves. However, it is unlikely that anisotropic symmetry can be inferred from the dispersion alone with the limited azimuths of recording available, and polarization analysis is required. We prefer to use

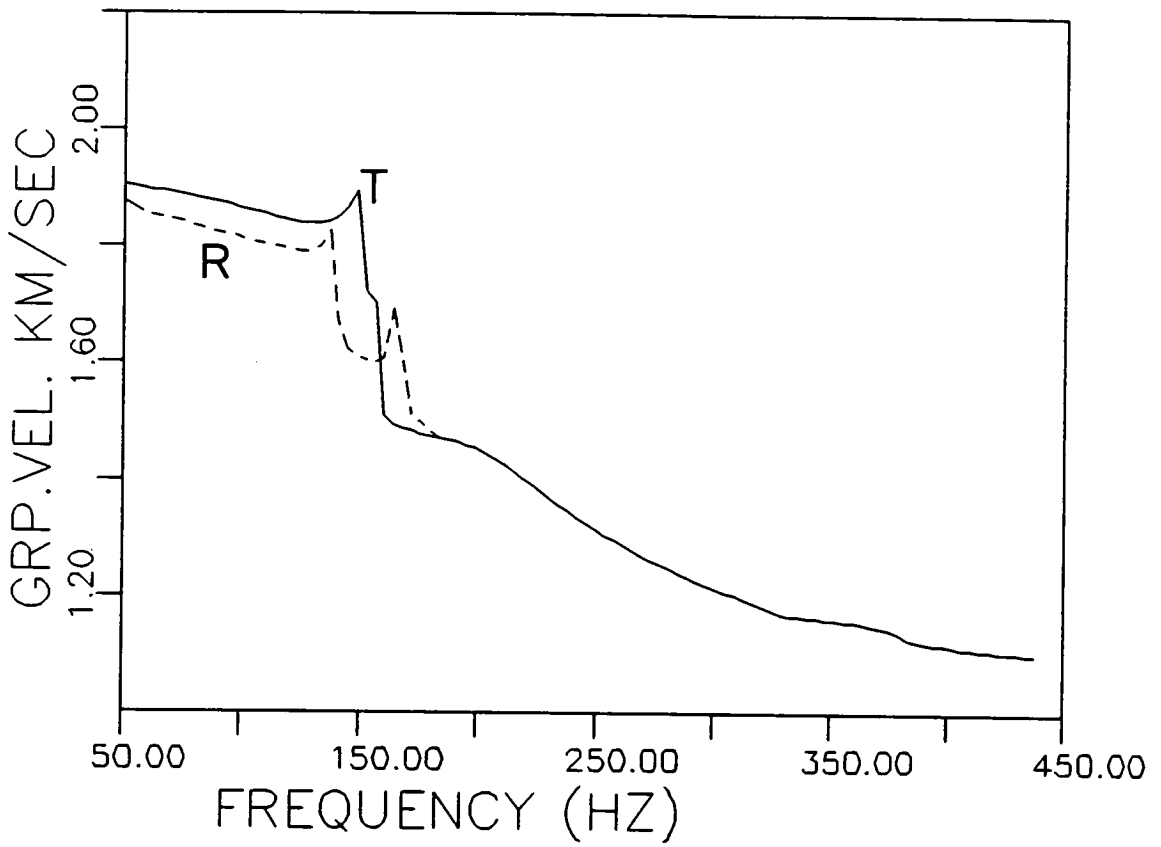

Figure 6.13 Comparison of dispersion inferred from radial (dashed line) and transverse (solid line) components of synthetic seismograms from raypath CH.

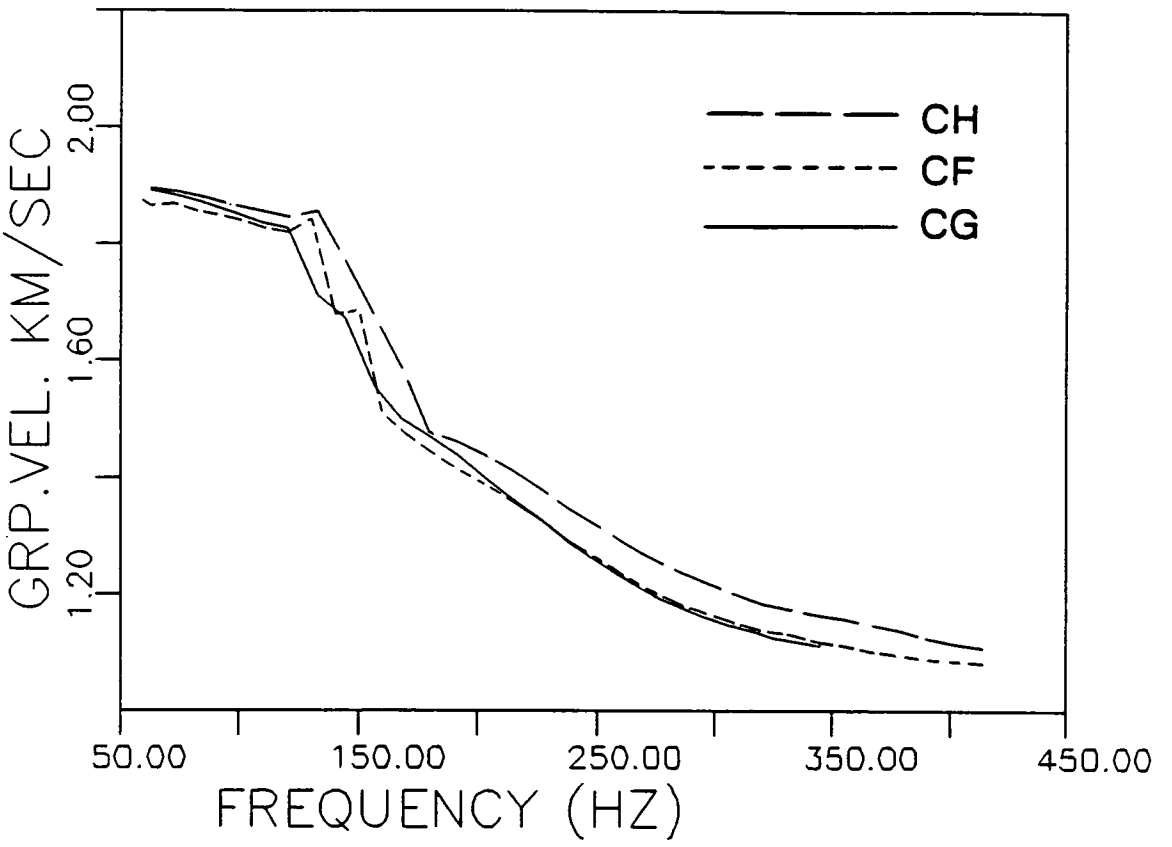

Figure 6.14 Stacked dispersion curves from three dispersions (raypaths CH, CG, and CF) of the synthetic seismograms. The separation of dispersion curves from low to high frequency is similar to the observed in Figure 6.11.

polarization diagrams from raw unprocessed data. Polarization diagrams display the cross-sections of the particle displacements which show patterns of motion dominated by the anisotropic parameters along the wavepath. The previous chapters of this thesis have demonstrated the sensitivity of body wave PDs to the symmetry of anisotropy (for example, Figures 5.11 to 5.15 in Chapter 5). The sensitivity of surface-wave PDs to the symmetry of anisotropy have been studied previously by Crampin (1975). There is one family of generalized wave travelling in anisotropic media. The pure Love-waves in isotropic media are equivalent to the second generalized mode (2G). There are several anomalous particle motions, from which anisotropy is characterized. We summarize the possible types of particle polarization in general anisotropic media:

1. *Generalized motion* - there is a constant phase difference between the components of displacement not equal to zero or $\frac{1}{2}\pi$.
2. *Tilted Rayleigh motion* - particle motion is elliptical in a plane rotated from the sagittal plane about the propagation vector.
3. *Inclined Rayleigh motion* - motion is elliptical in a plane rotated from the sagittal plane about a vertical axis.
4. *Sloping Rayleigh motion* - motion is elliptical in the sagittal plane with a non-vertical axis to the ellipse.
5. *Rayleigh motion* - motion is elliptical in the sagittal plane with a vertical axis.
6. *Love motion* - motion is linear with transverse horizontal polarization.

The above link between the polarization of *surface waves* and anisotropy symmetry has been theoretically established by Crampin

(1975); Taylor and Crampin (1978), and observed for higher mode seismic surface waves by Crampin and King (1977); Kirkwood and Crampin (1981b). There are generally three distinct particle motions: *inclined*, *tilted* and *sloping*, each of which is related to the propagation direction with respect to the symmetry plane of anisotropy. Waves travelling parallel to any of the vertical symmetry planes have *pure* Rayleigh or *pure* Love motion as in purely homogeneous isotropic media. In general, if waves travel in any other direction, three distinct particle motions (2,3,4 shown above) are often observed. Figure 6.15 shows three the distinct particle motion characteristics of symmetry orientations: (a) *inclined-Rayleigh motion* - when there is a horizontal plane of symmetry, (b) *tilted- Rayleigh motion* - when propagation at right angle to vertical plane of symmetry, and (c) *sloping-Rayleigh motion* - when propagation with the sagittal plane of symmetry. Hence, it offers the possibility of analysis of these particle motions of channel waves in determining the symmetry of existing anisotropy. Note that the above theory is for *surface waves*, and we suggest it still holds for more generalized *channel waves*.

6.6.2 Particle motion anomalies

The most obvious anomalies on the rotated seismograms in Figure 6.2 occur in Love-type motions. Wherever there is a dispersive wavetrain on the transverse component, this is coupled to a small horizontal radial component (source 6 and 9) and also vertical components (source 6), and this has already been confirmed from the dispersion analysis. The wave mode on the transverse component is clearly the second generalized mode (2G), corresponding to the Love

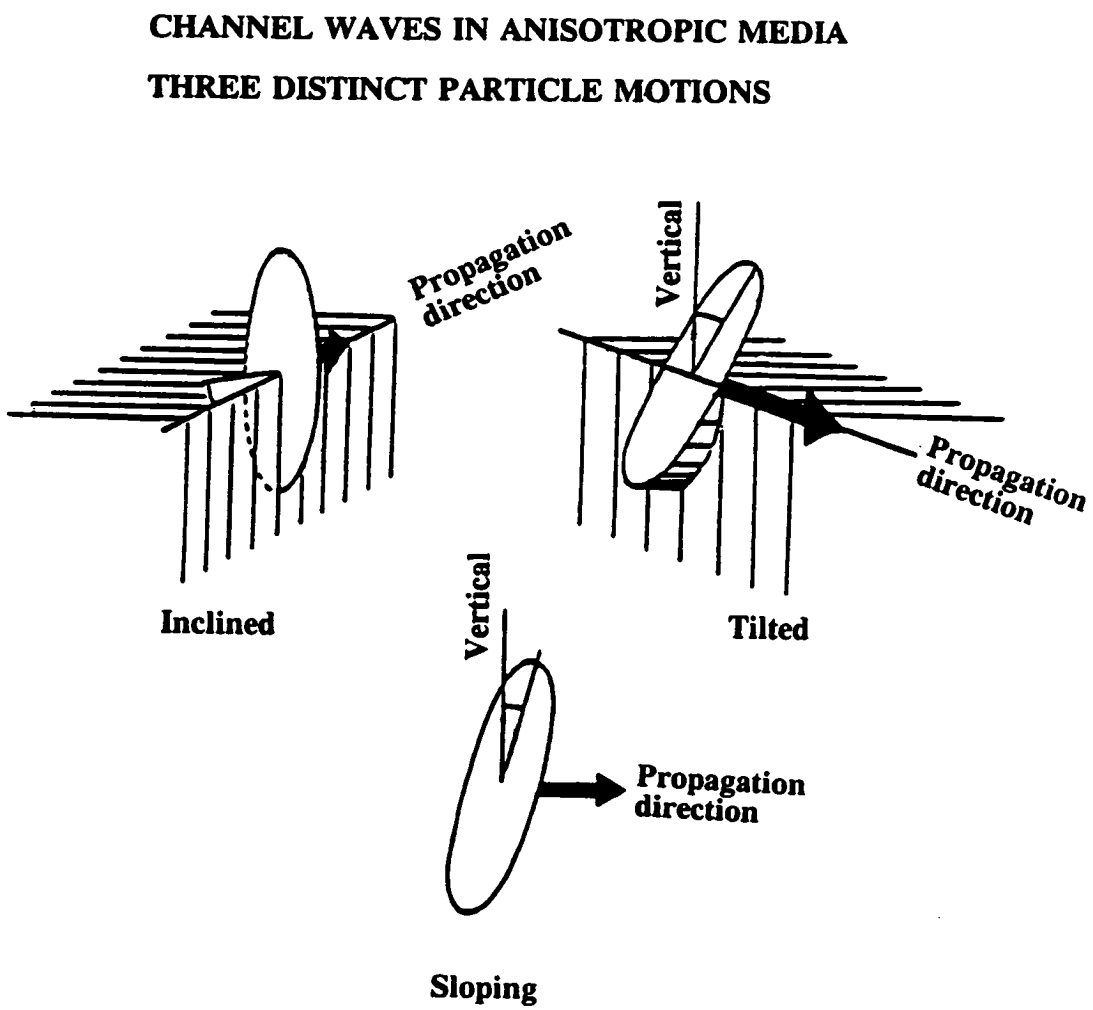

Figure 6.15 Three types of generalized channel-wave particle motion characteristic of propagation in particular symmetry directions: (*a*) inclined-Rayleigh motion - propagation in a horizontal plane of symmetry, (*b*) tilted-Rayleigh motion - propgation at right angle to a vertical plane of symmetry, and (*c*) sloping-Rayleigh motion - propagation in a sagittal plane of symmetry (after Crampin, 1975).

wave motion in isotropic media. This is apparent at all frequencies, and radial and transverse components are nearly ½π out of phase over several cycles. The relative phase of radial and transverse components appears to change gradually with frequencies.

The particle motion plots highlight this noticeable feature of coupling anomaly on the seismograms. Figure 6.16 shows observed particle motion plots of Love channel waves (or more precisely called 2G mode, we shall call it 2G only when it might be confused with Love-type motions in isotropic media, otherwise Love wave is called throughout). Love-type waves have particle motions, which are elliptical rather than linear in the horizontal plane as expected from the behaviour of Love waves in isotropic media. The observed particle motion is clearly inclined Rayleigh-type. The polarization ellipse is constantly deviated between 15° and 25° away from the transverse direction, which is clearest on the records from raypath CF in Figure 6.16(b). Because there is no vertical component records for source borehole 9 and the vertical components from source borehole 6 are not reliable, it is difficult to identify tilted and sloping particle motions. We assume that the coal-seam is symmetrical (the cutoff frequency tends to be zero), the vertical motion is cancelled when both source and geophones are in the centre of coal-seam, it is, therefore, unlikely to find tilted or sloping particle motions for fundamental modes. Nevertheless, the observed inclined PDs in most of the records show constant distinct characteristics, which cannot be easily explained by the expected Love wave in homogeneous isotropic media.

The particle motions of Love waves from the synthetic seismograms are displayed in Figure 6.17. Although the exact patterns of the

Figure 6.16 Observed inclined particle-motions of Love channel waves in the horizontal plane for the raypaths CF, CH and CG [impact sources orientated 45° (R)ight and (L)eft to the raypath CG], each PD corresponding to a time interval of 5 milliseconds.

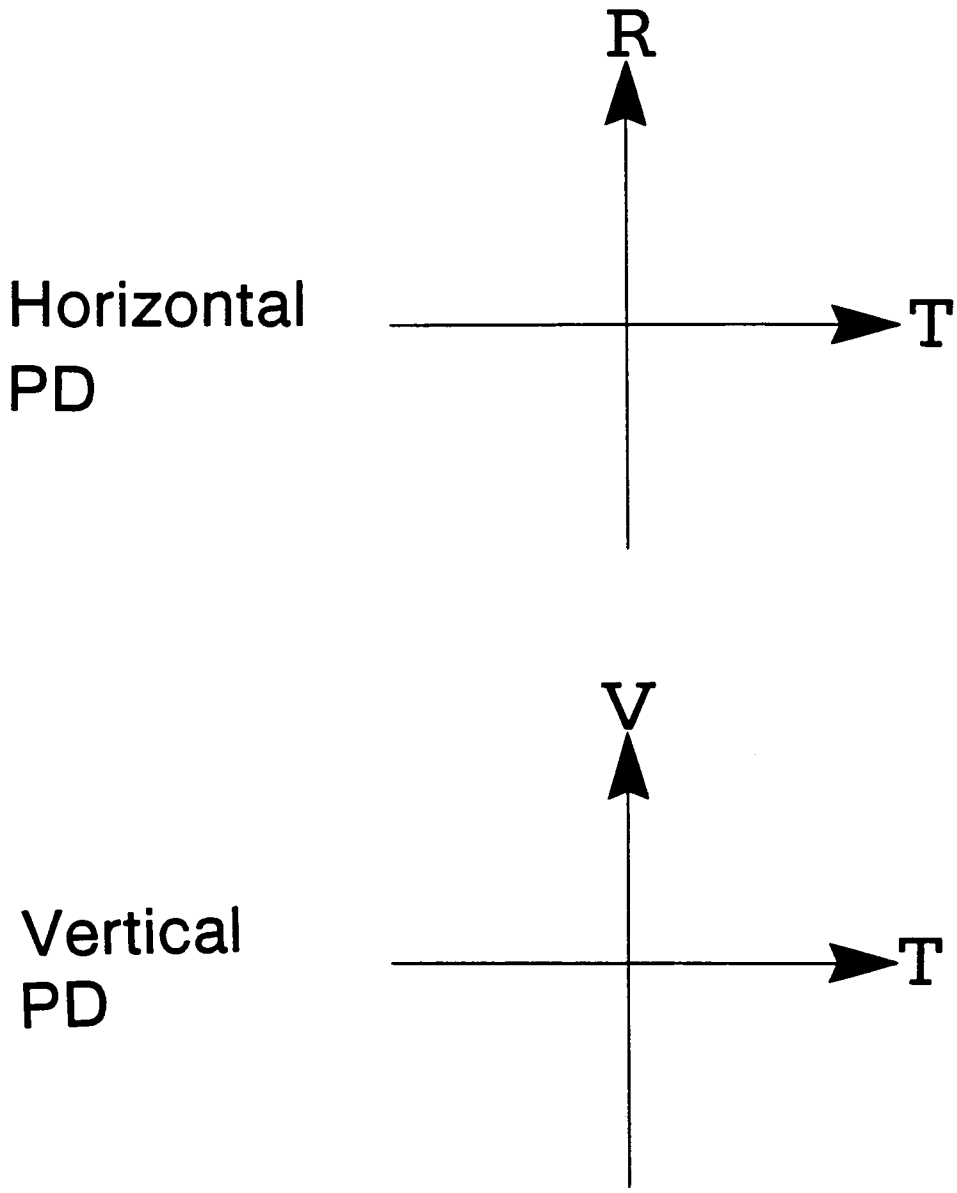

Figure 6.16 Key to the particle motion plots.

Figure 6.16 (cont.)

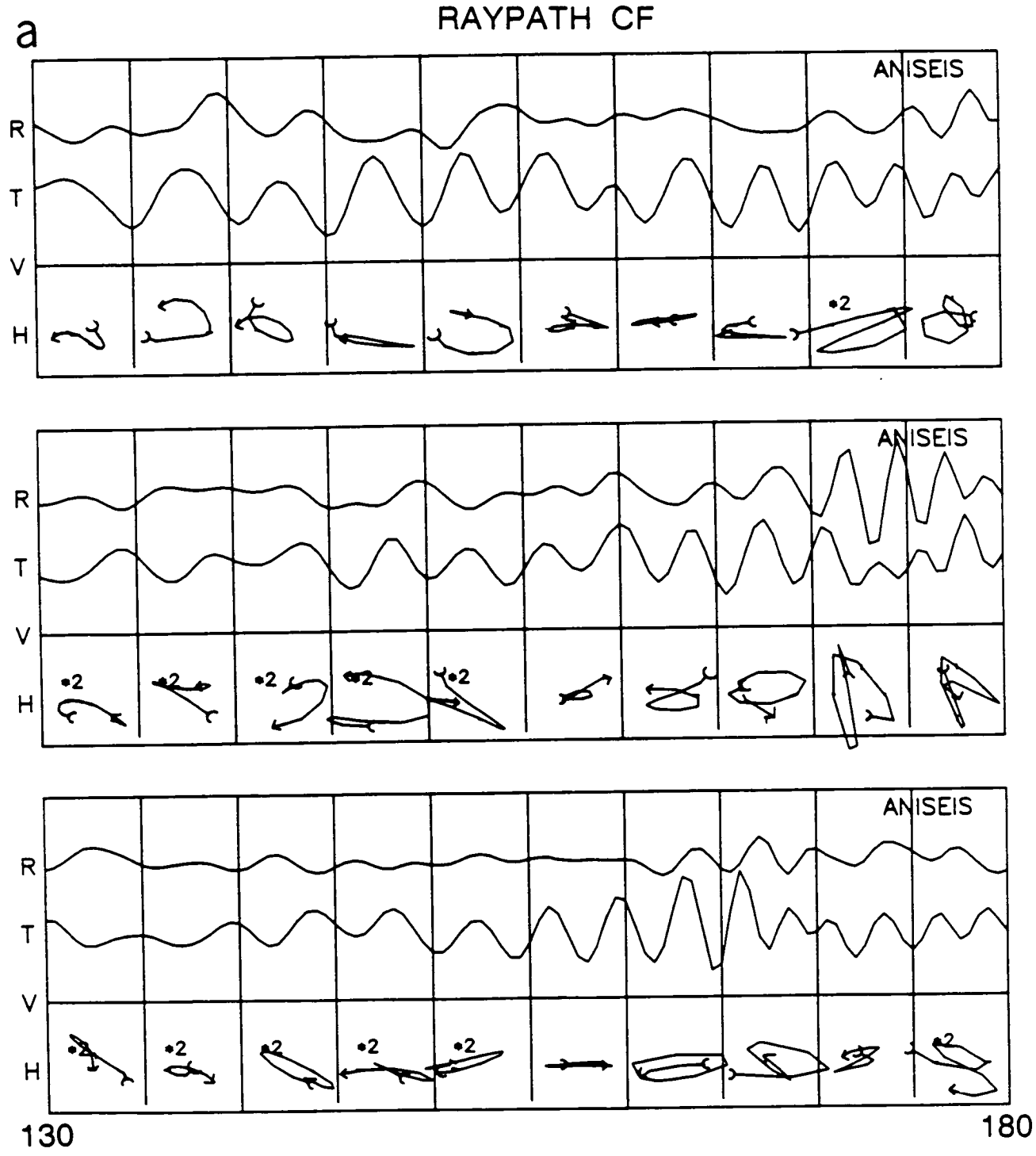

Figure 6.16 (cont.)

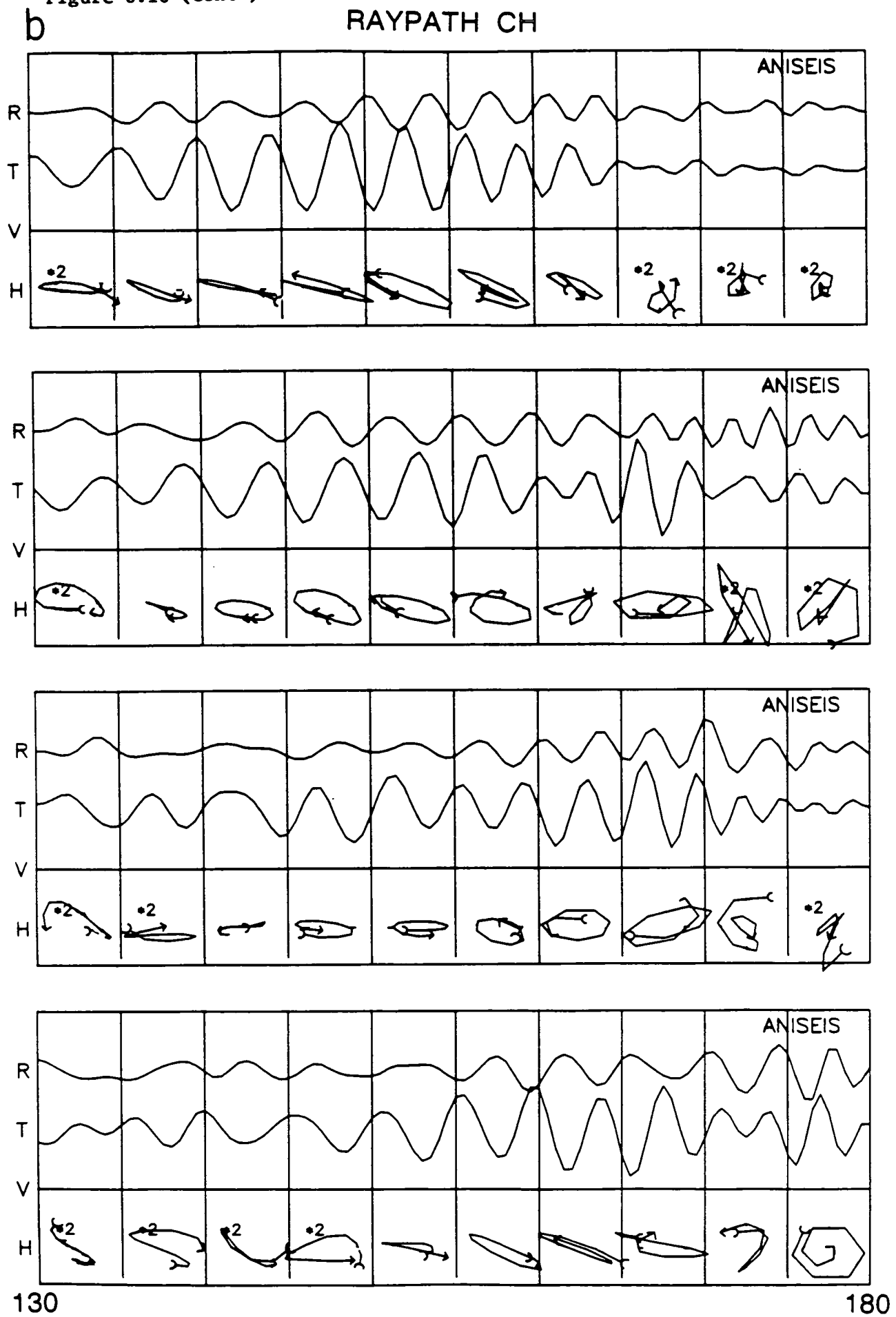

Figure 6.16 (cont.)

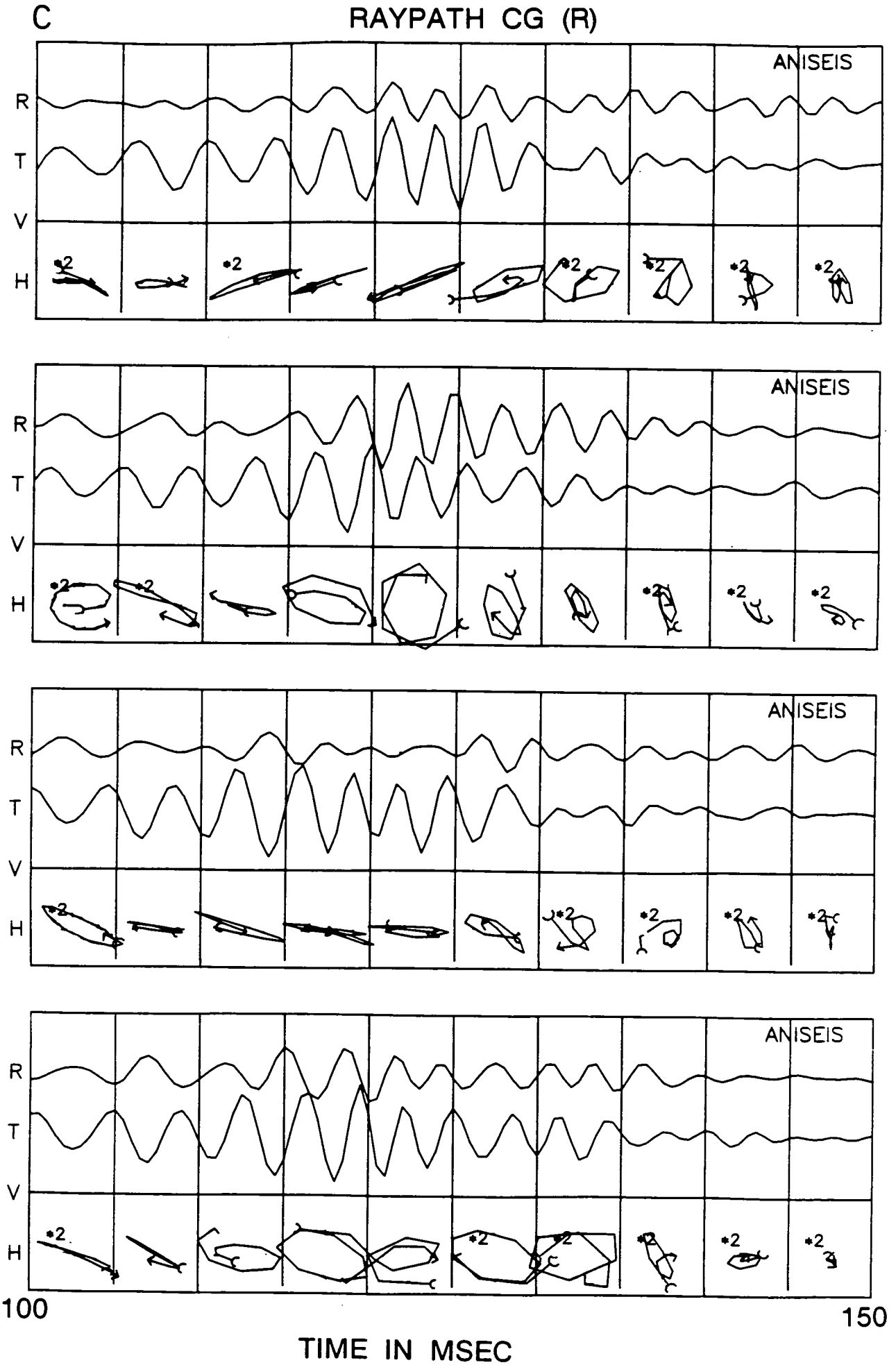

Figure 6.16 (cont.)

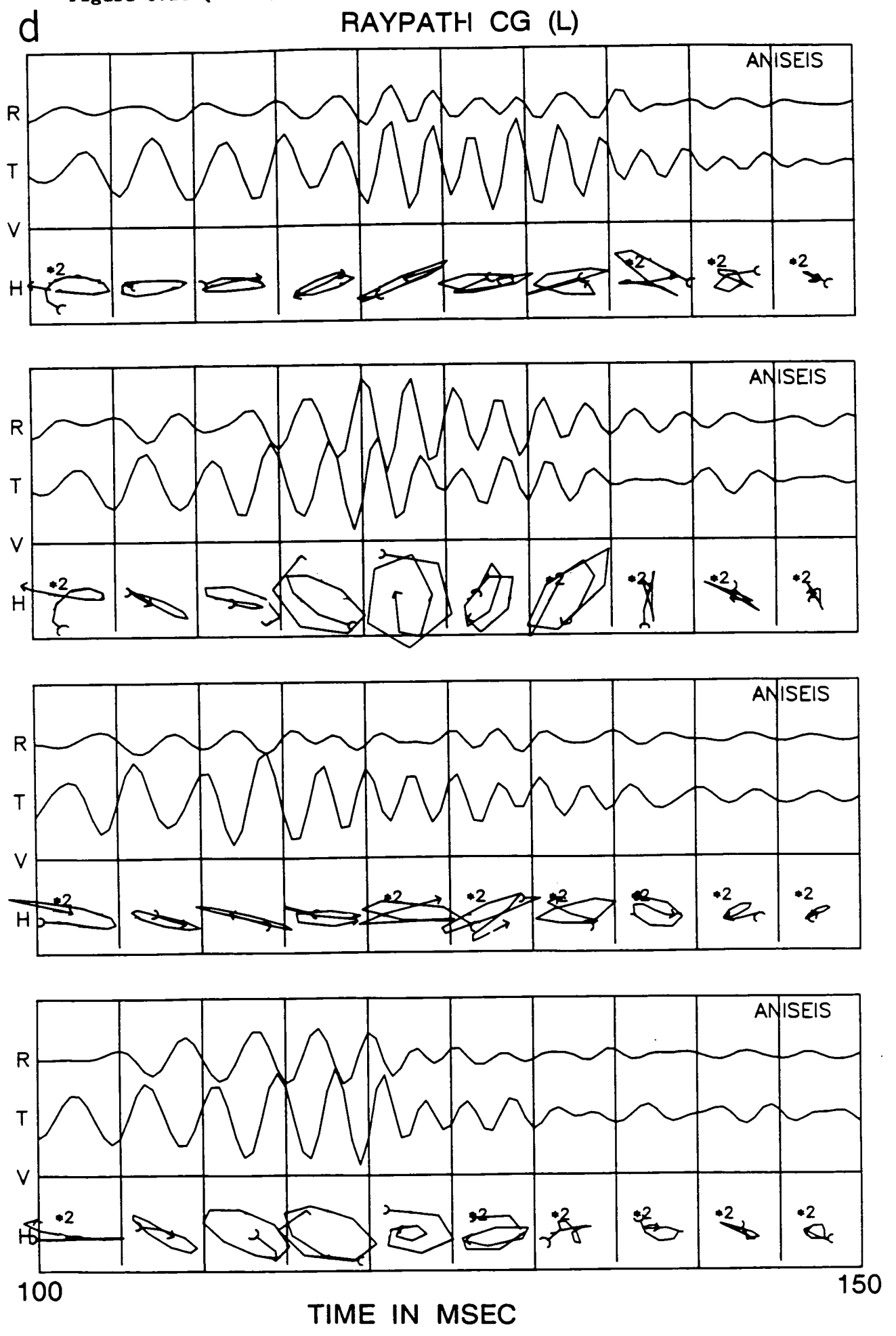

Figure 6.17 Particle motions of synthetic seismograms with the same notations as Figure 6.16.

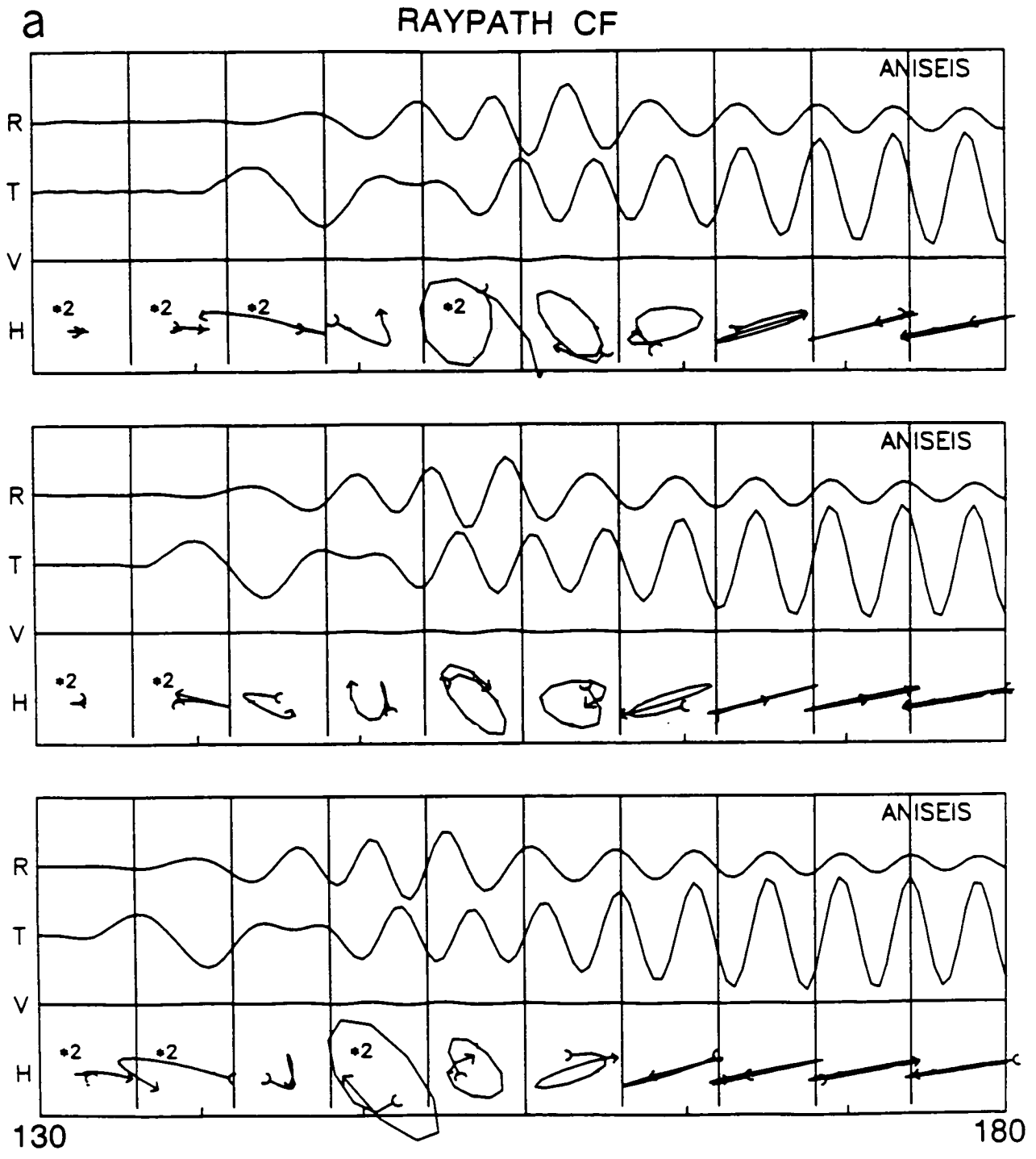

Figure 6.17 (cont.)

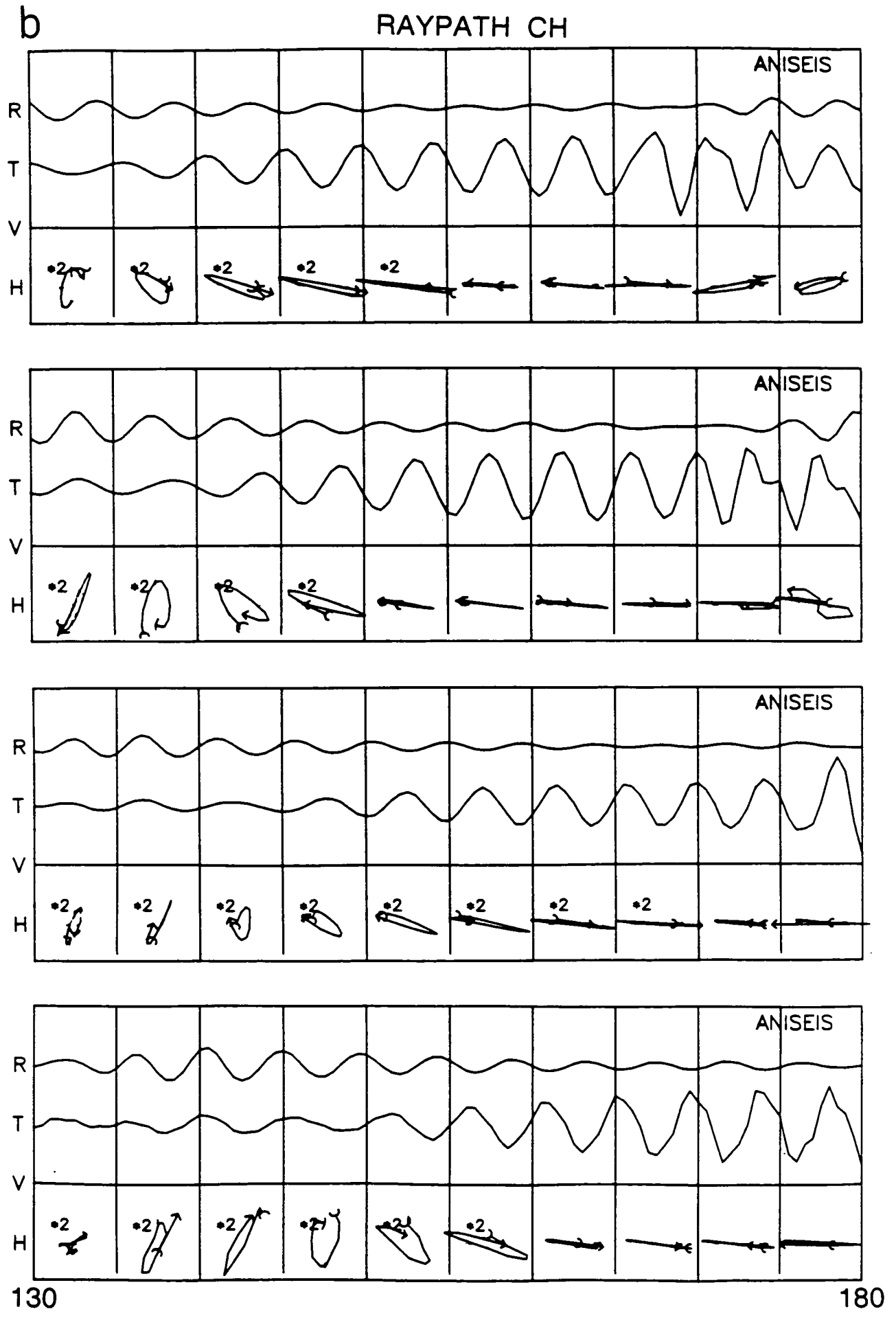

Figure 6.17 (cont.)

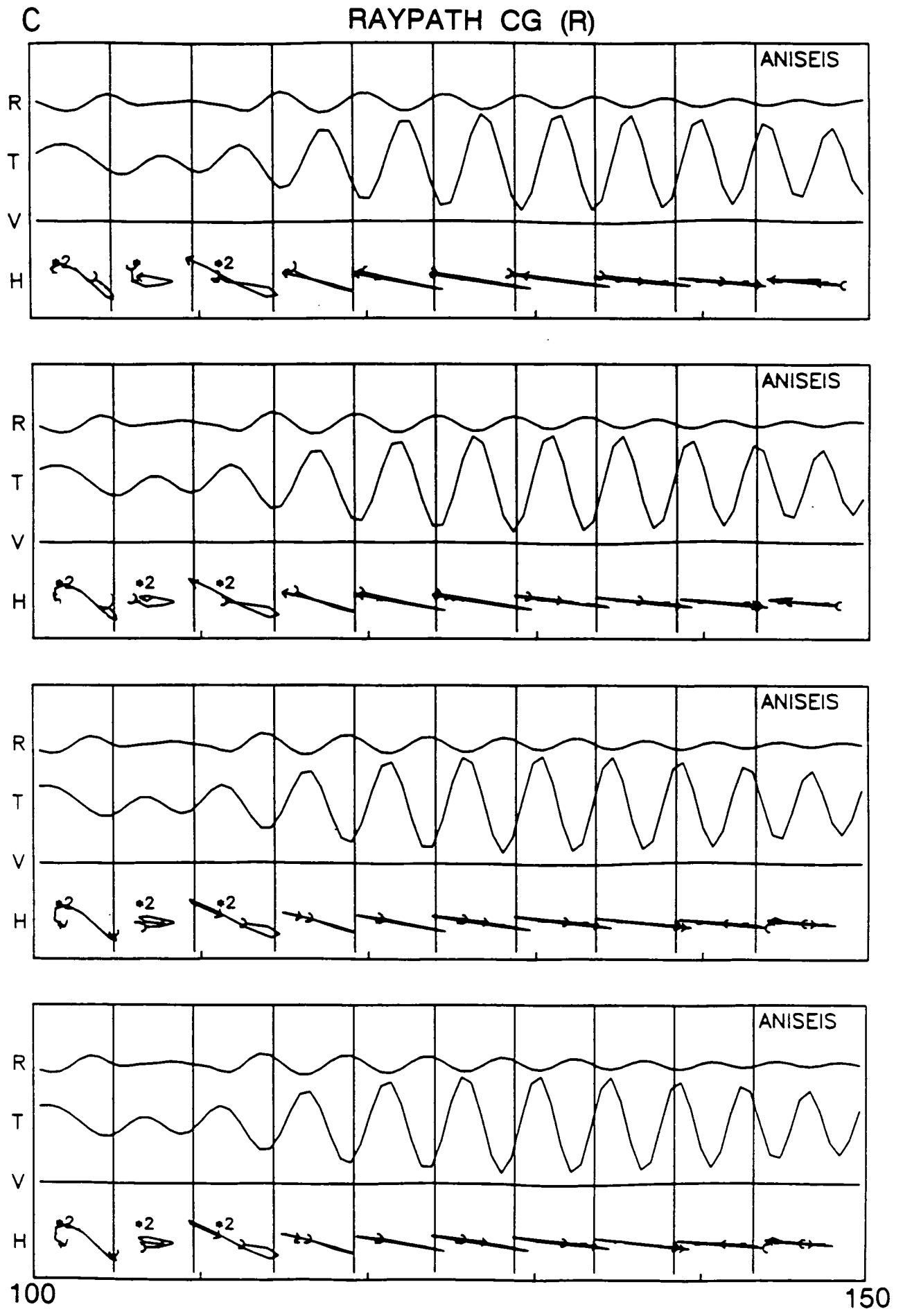

Figure 6.17 (cont.)

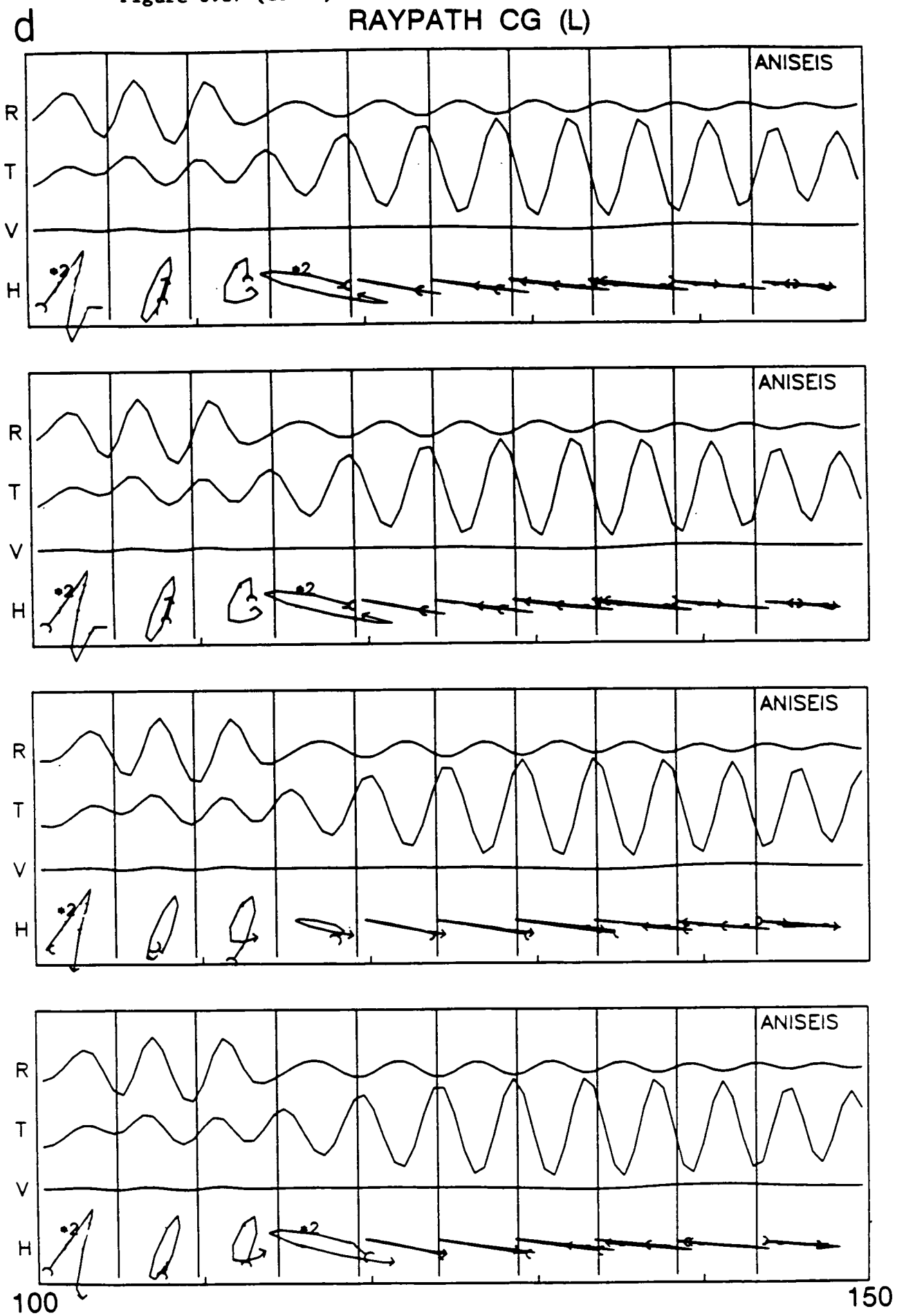

observed particle motions are not fully modelled, the polarization patterns of all the synthetic seismograms are inclined about 20° from the transverse axis, which is clear for the low frequency parts, but it is changing for intermediate frequency. The synthetic seismograms also show consistently ½π out of phase between the radial and transverse components. This consistent polarization inclination and relative phases in the radial and transverse components are in general quite similar to the observations. Note that due to the constant attenuation factor used in our modelling, the relative amplitudes of the radial and transverse components which affect the particle motions were not fully reproduced.

6.6.3 Implication of observed polarization patterns: anisotropy or inhomogeneity ?

Observed particle motions of Love waves are elliptical and inclined to about 15° to 25° from the transverse direction which are not expected from Love waves in isotropic media. Similar observations were also observed for seismic surface waves (see references by Crampin and co-authors on surface waves). Breitzke *et al.* (1987) give a good example (Figure 9 in their paper) of the inclined particle motions of Love channel waves. They stated that the observed particle motions are almost linear, but in fact, they display elliptical particle motions. Breitzke *et al.* found that the polarization angle of Love waves is constantly about 30° to the radial axis (y-axis in their notation), however, they could not explain this *discrepancy* between the analyzed and the expected polarization angle of Love channel waves (in isotropic media). If anisotropy is considered, such a "discrepancy" can be easily explained. The polarizations they have observed show typical

inclined particle motion in the horizontal plane, which are very similar to the observations in Figure 6.16.

One possible mechanism of the elliptical particle motions of Love waves could be scattering from the surface or roadways, or inhomogeneities near the recording sites. In comparison of the seismograms from sources 6 and 9, we have already ruled out the possibility of the roadway surface effects and suggested that the irregularity of seismograms could be due to some sort of inhomogeneities.

Inhomogeneities near the recording sites may cause the strains associated with incoming seismic waves to produce an elliptical motion. This has been studied by Rodgers (1968), Gupta and Blandford (1983). It is unlikely that this could produce a strong alignment of polarizations, and certainly different sites should show rather different anomalies (irregularity). This of course can make it difficult to identify the effect of anisotropy if a single observation is available. So, only when similar anomalies can be observed at several recording sites, will it be possible to say they are caused by anisotropic alignment along the raypaths. The inclined Love wave particle motions were observed at most of the raypaths available. Clearly, inhomogeneity cannot be the only cause.

It is also worth noting that there is a *residual coupling* if the rotation of seismograms by equation (6.3) is not correct or recorded components not being exactly parallel and perpendicular to the roadway face. However, the important fact is that an elliptical motion is always elliptical whatever the direction of rotation is. In isotropic media (and also transversely isotropic media with a

vertical symmetry axis), Love-wave should be *linearly* polarized in transverse direction. If the rotation is wrong, it will still be *linearly* polarized on the horizontal plane, but not in the transverse direction due to the *residual coupling* (Figure 6.18). This is one of the reasons why we say polarization diagram is more sensitive to anisotropy than seismograms. Clearly, any observed *elliptical motion* of the Love wave cannot be due to the residual coupling.

The relationship between channel wave particle motions and symmetry of anisotropy and the azimuthal variation of dispersion implies that transverse isotropy with a vertical symmetry axis is unlikely to cause this peculiarity since in such a medium Love waves should in any case be decoupled from Rayleigh waves although it may have significant influence on dispersion curves (Appendix B). The observed particle motion anomalies, and the symmetrical patterns into which they fit, can be explained by anisotropic alignment, that is vertical cleats in the coal-seam and the rocks. If aligned cleats or cracks are responsible for the observed effects, then cleats or cracks should have a horizontal plane of symmetry, which means the cracks have to be vertical. The synthetic models shown in Figure 6.17 are in general consistent with the observations in Figure 6.16, as is the dispersion.

6.7 The Florence in-seam seismic data: a further evidence of anisotropy

6.7.1 The Florence data: field geometry and observations

We have an additional in-seam seismic data available. The data were also collected by the British Coal and recorded on three-

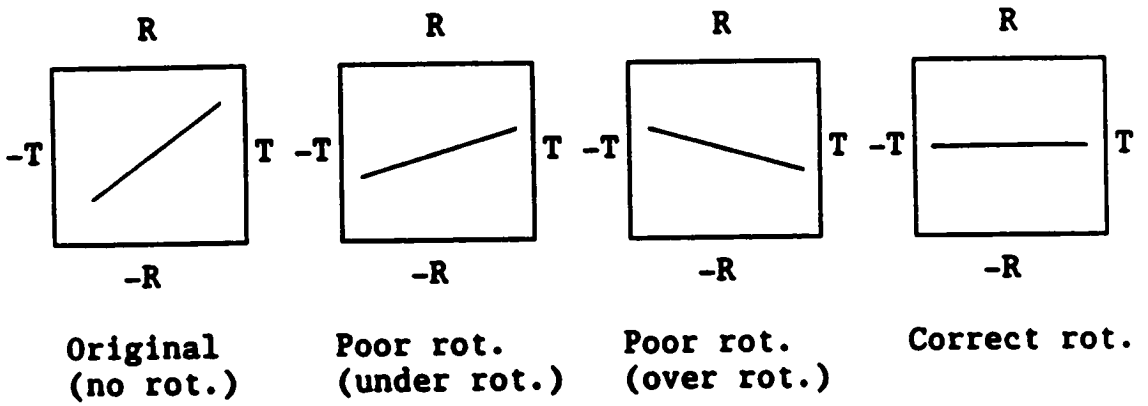

Figure 6.18 Residual coupling due to incorrect rotation.

component geophones. The recording geometry (Figure 6.19) is similar to the Harworth in-seam seismics discussed above. Three impact sources similar to Figure 6.1 were used. Figure 6.20 shows rotated three-component seismograms recorded at eight geophones from three impact sources at source hole 7 (denoted 7L, 7R and 7C in Figure 6.19). The suggested velocity structure is shown in Table 6.4. There is evidence of an intermediate layer between the Rowburst and Rider seams. This is made up in part of mudstone and in part dirt. The velocity values used to get a close Love wave dispersion fit (Roth, personal communication). Sonic logs are not sufficiently resolved to assist here. Roth suggested that the dirt band is gradually extended from 1.2m to 2m. We are unable to model such a dipping layer since the reflectivity method does not allow a dipping layer to be included. Instead, we look for evidence of anisotropy, which may be inferred from the observations.

Observed seismograms (Figure 6.20) show typical channel wave arrivals which in general appear in all three components, but the largest amplitudes are all in transverse components. The radial and transverse motions are constantly $\pi/2$ out of phase, which is similar to the Harworth data, whereas the vertical and transverse motions are in phase. The eight geophones in Figure 6.19 cover a small range of azimuths of only 10° (source position is at 7), it is therefore unlikely to find azimuthal dispersion variation. Figure 6.21 (a) compares the dispersion curves of Love waves (transverse components) from geophone 1, 3 and 6 in Figure 6.20 (c), and there is no distinct separation. Note that effects of dirt bands on dispersions can be found in a theoretical study of Räder *et al.* (1985).

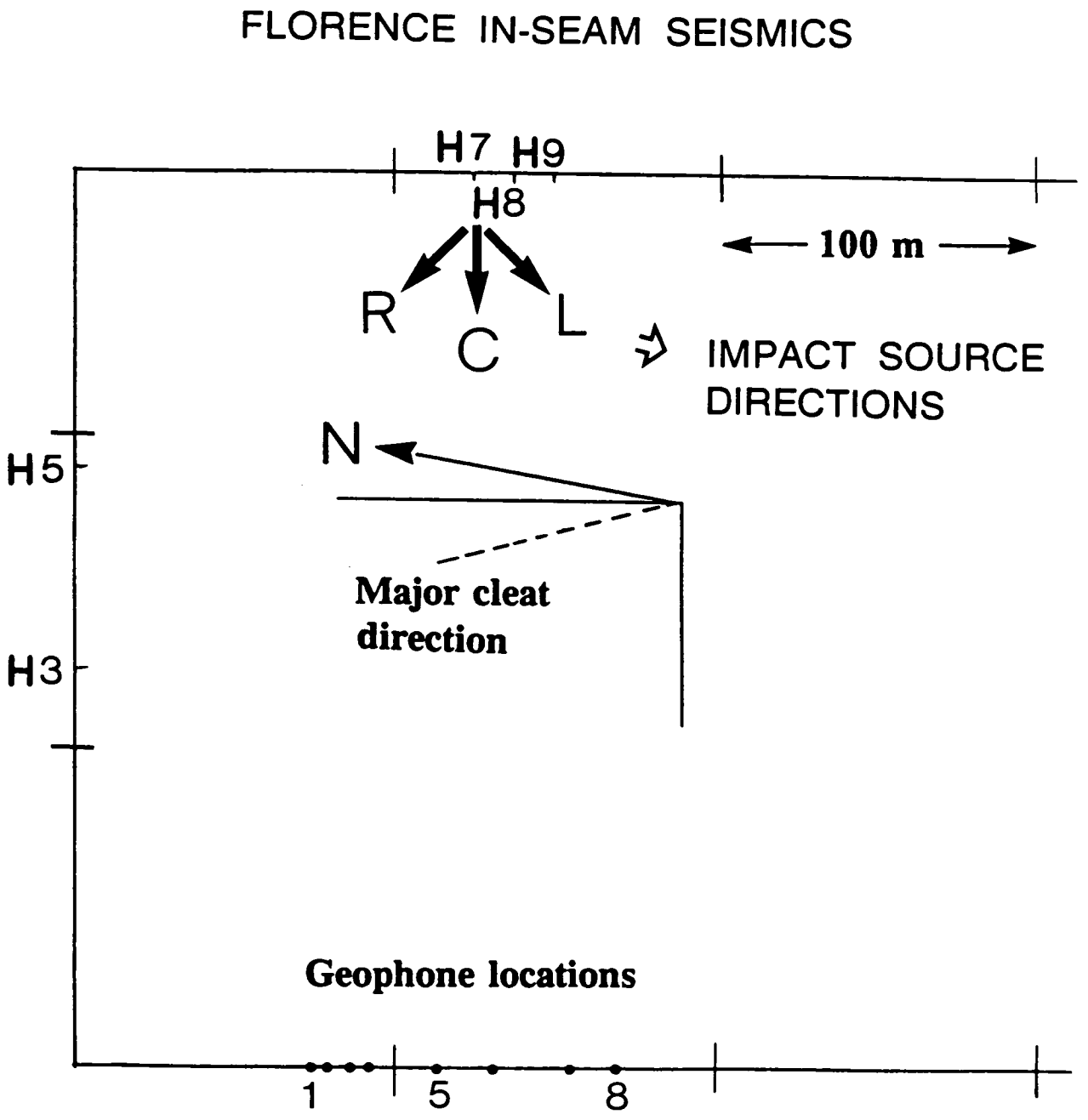

Figure 6.19 Plan geometry of the Florence in-seam seismic survey. Source sites are denoted by H3, H5, H7, H8, and H9, and 8 three-component geophones are represented by the black dots. The data set available to us is from three impact source directions 7L, 7C and 7R (same as the Harworth in-seam seismic geometry in Figure 6.2) at H7.

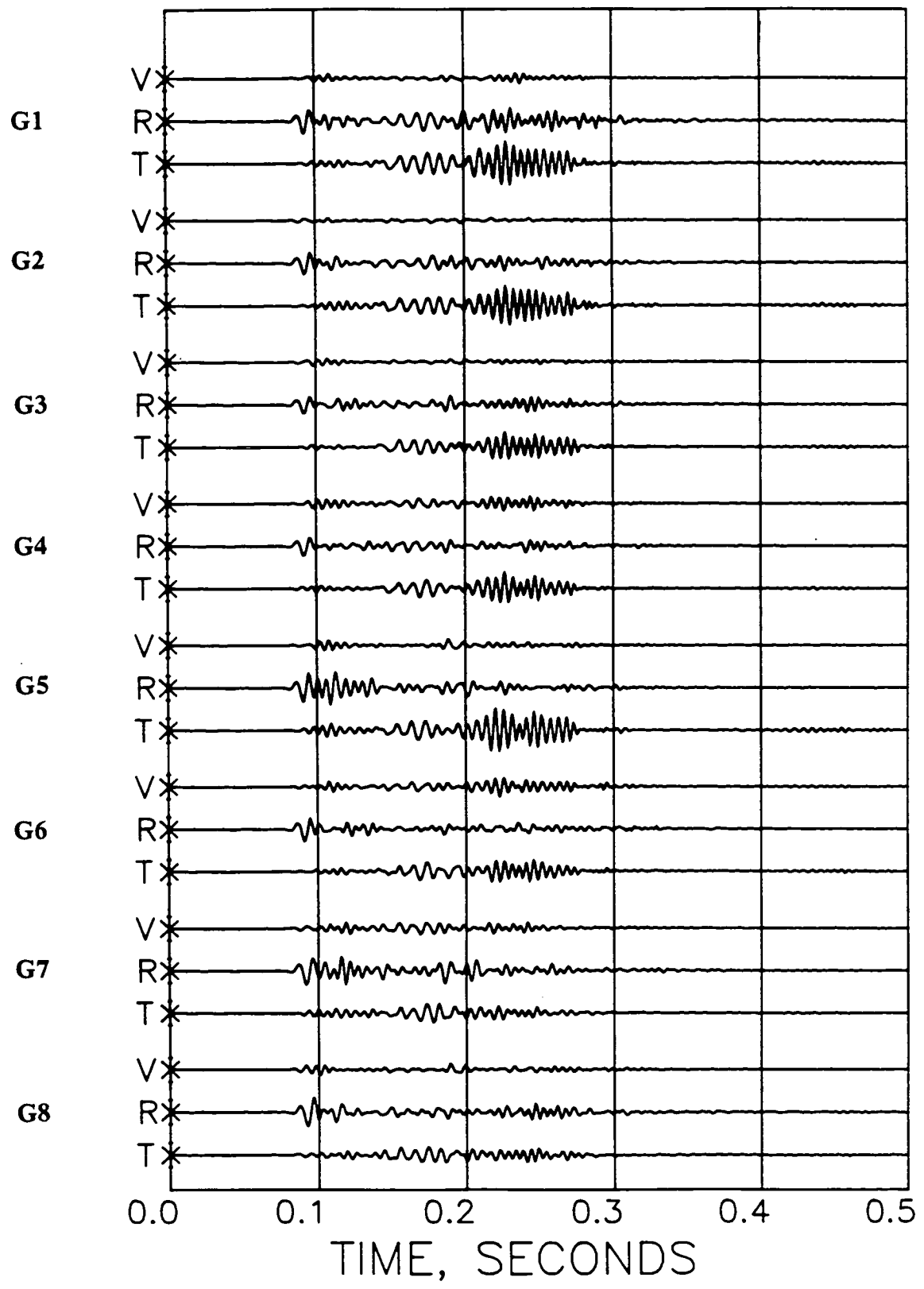

Figure 6.20 Three-component seismograms recorded at geophones 1 to 8 from the Florence in-seam seismics with the geometry in Figure 6.22. (*a*) impact source orientation 7L, (*b*) 7C, and (*c*) 7R.

Figure 6.20 (cont.)

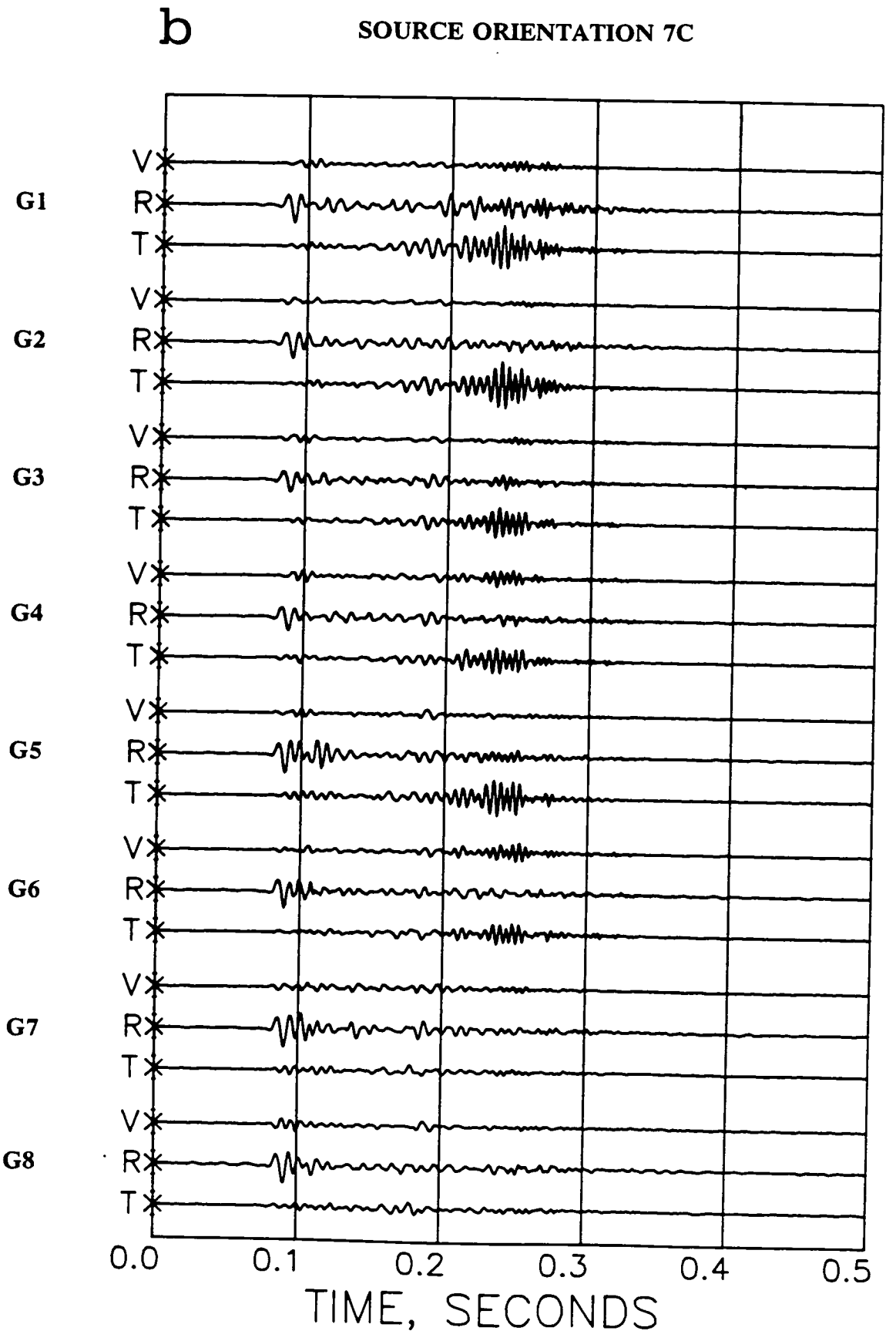

Figure 6.20 (cont.)

C SOURCE ORIENTATION 7R

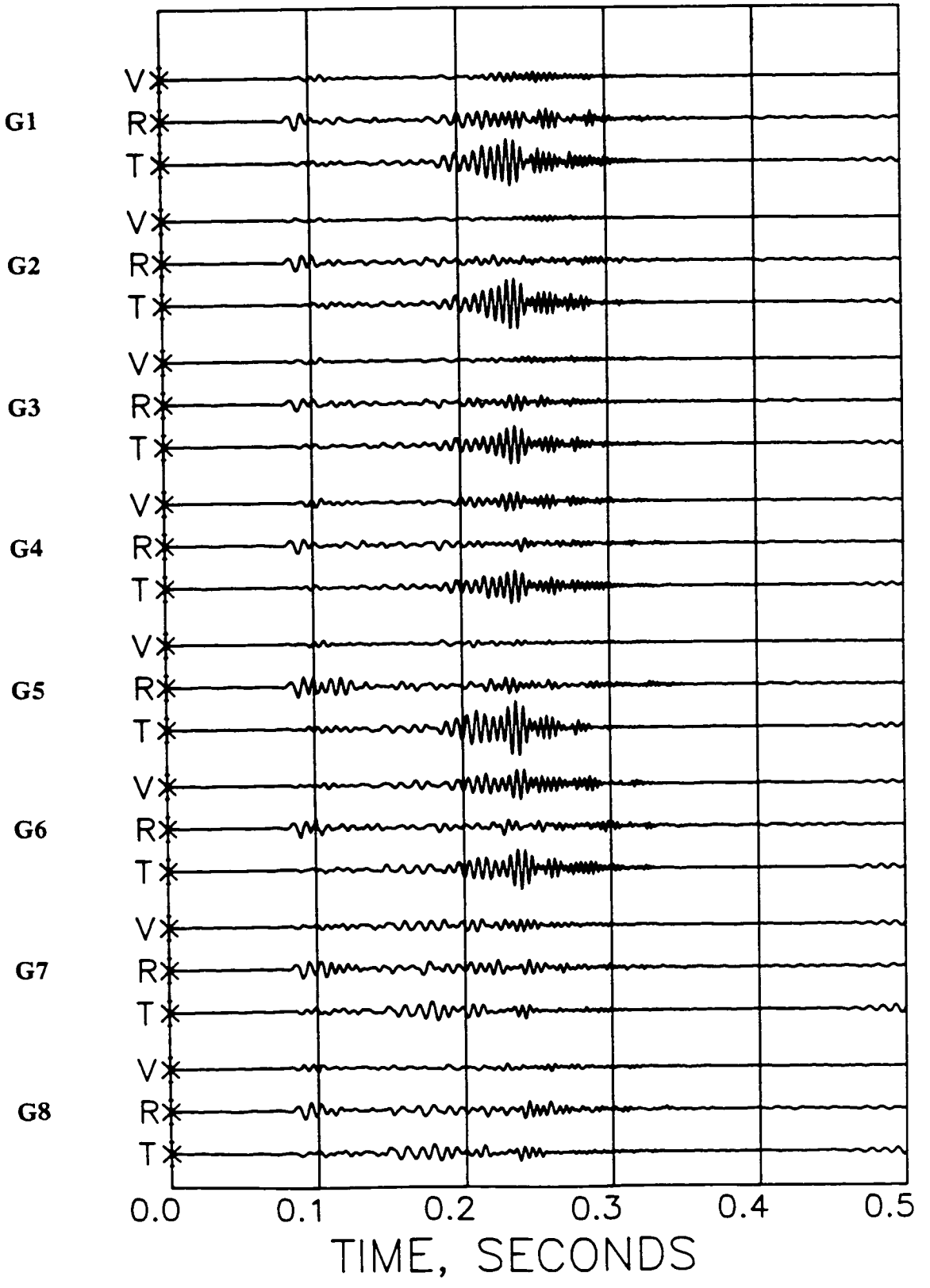

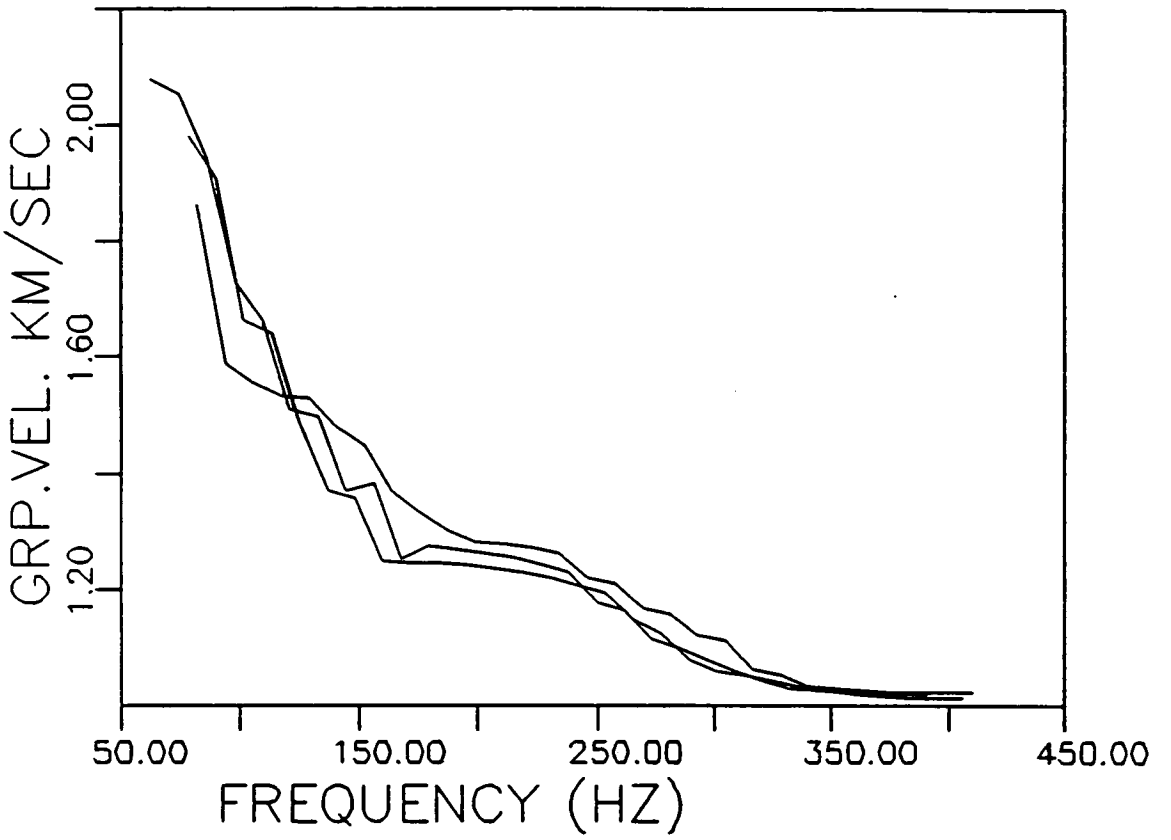

Figure 6.21 Comparison of dispersion curves of Love waves (transverse components) from geophones 1, 3 and 6 in Figure 6.20 (c). There is no distinct separation of dispersion.

Table 6.4 The velocity structure of the Florence data (Bruce Roth, personal communication)

	Depth (m)	Density (g/cm^3)	V_P (m/s)	V_S (m/s)
	540	2.7	3800	2000
Rowhurst Rider	0.7	1.4	1700	1000
Dirt Band	1.2	2.2	3200	1600
Rowhurst	1.8	1.35	1700	1000
	∞	2.6	3800	2000

6.7.2 The Florence data: 2G anomalies

The noticeable anomalies lie on the Love channel waves, or 2G mode. Figure 6.22 compares dispersion characteristics of radial (short dashed line), vertical (long dashed line), and transverse (solid line) components from geophone 1 in Figure 6.20 (c). The distinct features of all three components suggest that all three components record the same mode. This is an typical example of many observations showing 2G coupling.

Figure 6.23 is the particle motion plots of the observed records in horizontal radial-transverse plane (H) and vertical-transverse plane (N) for two impact source orientations (7L and 7R). The particle motions are in general elliptical in these two planes, and inclined 15° to 20° clockwise in the horizontal plane, which are very similar to Figure 6.16. This is constant from geophones 1 to 5. The elliptical particle motions also on vertical-transverse plane indicate that the observed PDs are probablly the combination of inclined- and tilted-Rayleigh motions. Cleat or crack orientation is believed to be 20° anti-clockwise from the roadway (Bruce personal communication). These complicated PDs may be related to some sort of general anisotropy, possibly the combination of fine layering- induced transverse isotropy and cleat-induced azmuthal anisotropy, which leads to an orthorhombic symmetry.

6.7.3 The Florence data: amplitude variations

Assuming the major cleat orientation anti-clockwise 20° from the roadway direction, we plot the relative amplitudes against angle from the crack normal in Figure 6.24, we find a linear increase of amplitude with the angle from the crack normal (geometrical spreading has been corrected). The maximum amplitude is almost

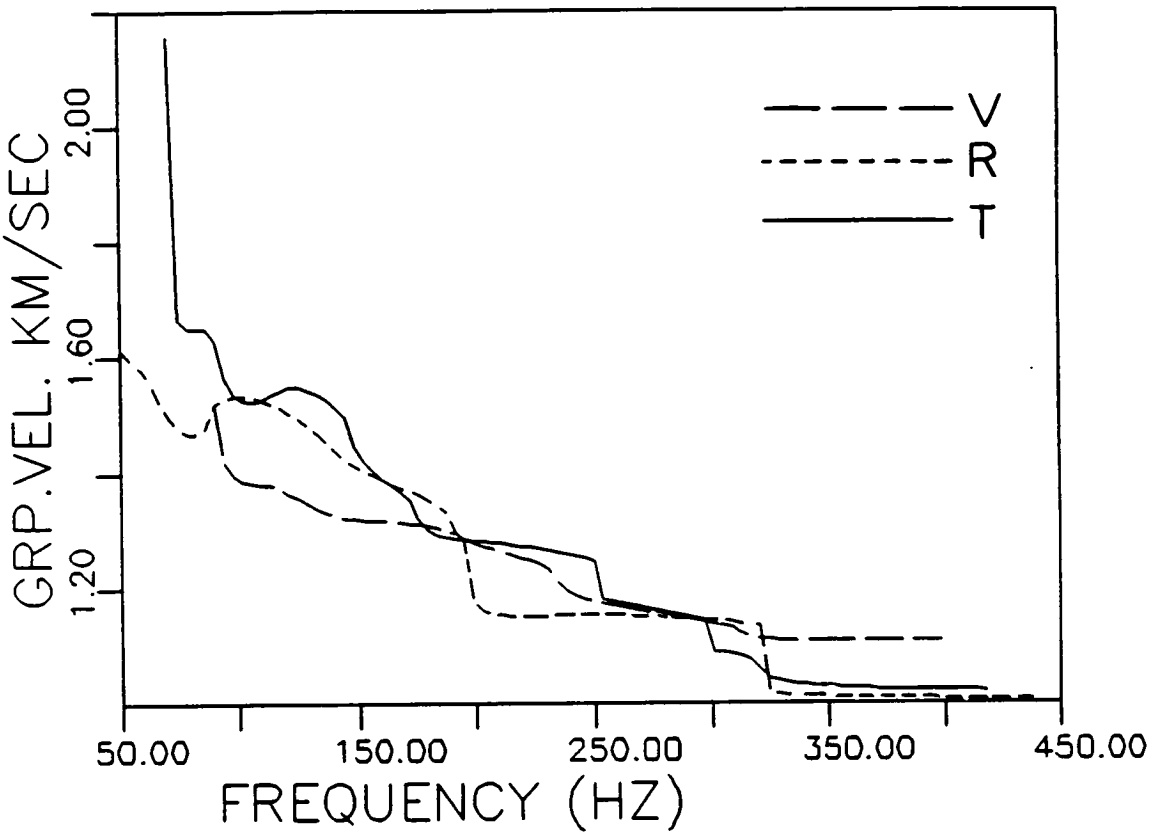

Figure 6.22 Comparison of dispersion curves of radial (short dashed line), vertical (long dashed line) and transverse (solid) components from geophone 1 in Figure 6.20 (c). The distinct features in all three components suggest that all three components record the same mode. This is a typical example of the many observations.

Figure 6.23 Observed particle motions of the Florence data in horizontal radial-transverse plane (H) and vertical-transverse plane (N) (see key to PDs in Figure 6.16). (*a*) and (*b*) for impact source 7L, and (*c*) and (*d*) for impact source 7R. Each PD corresponds to the time interval of 5 milliseconds (geophone numbers are shown on the left).

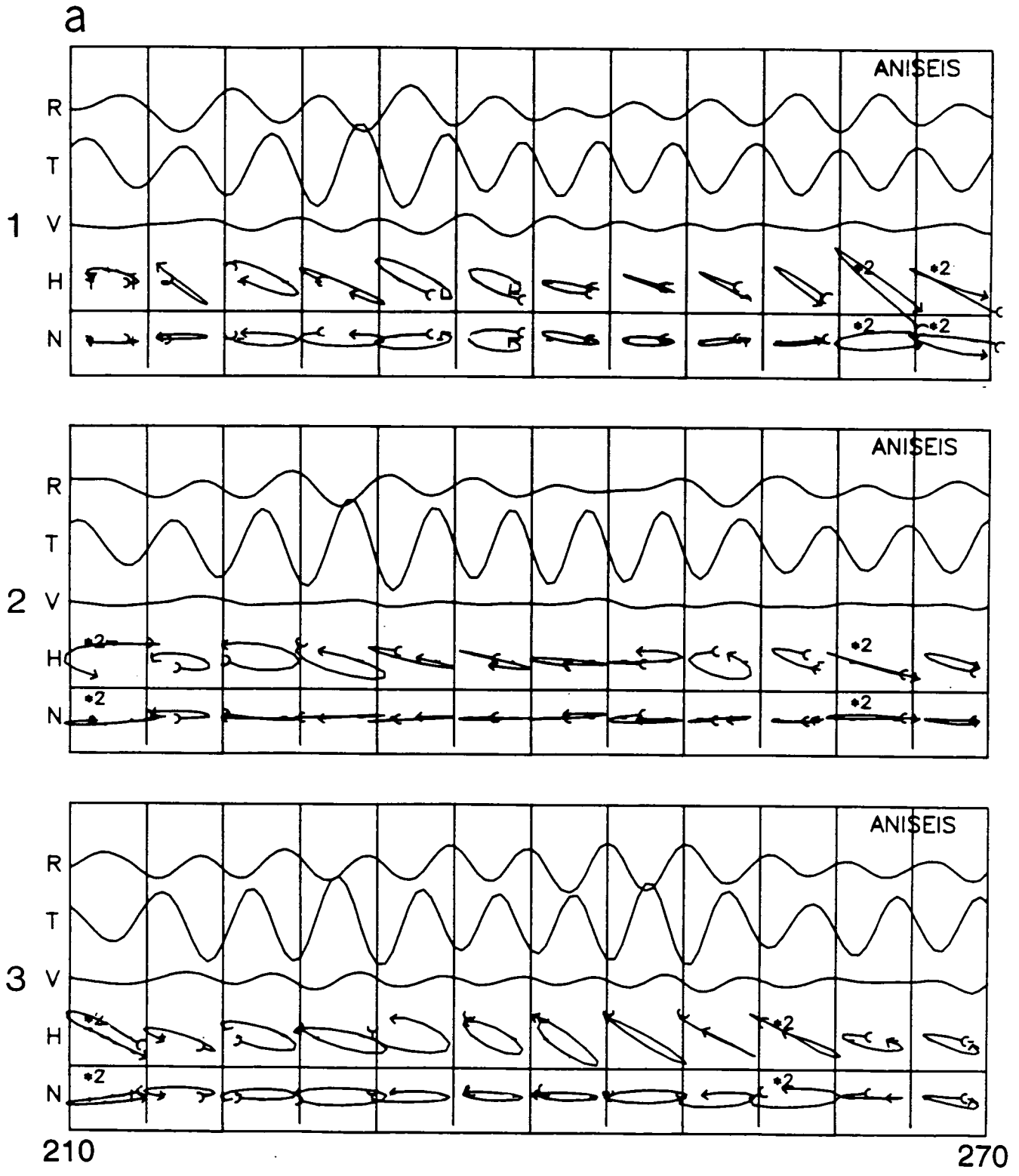

Figure 6.23 (cont.)

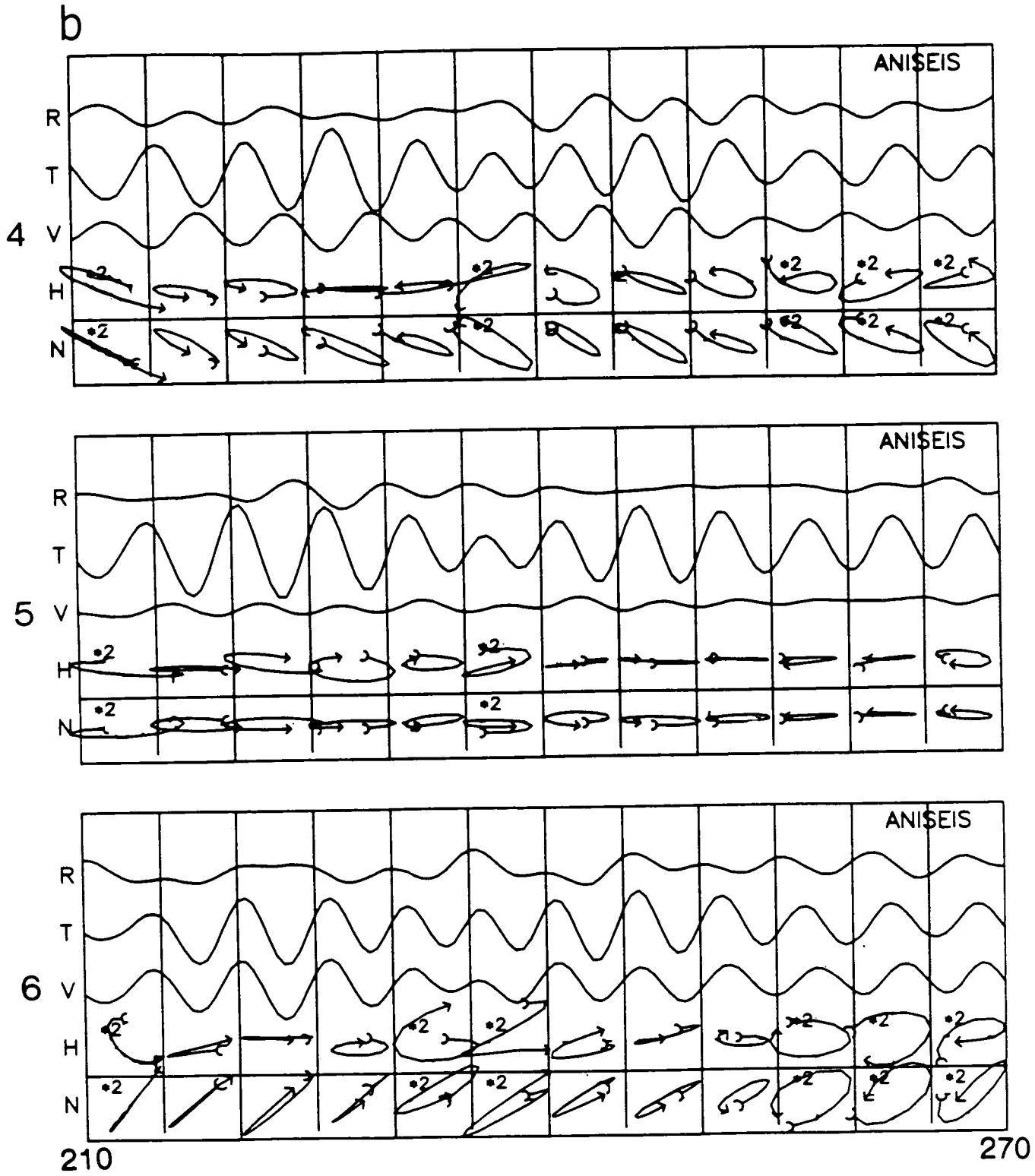

Figure 6.23 (cont.)

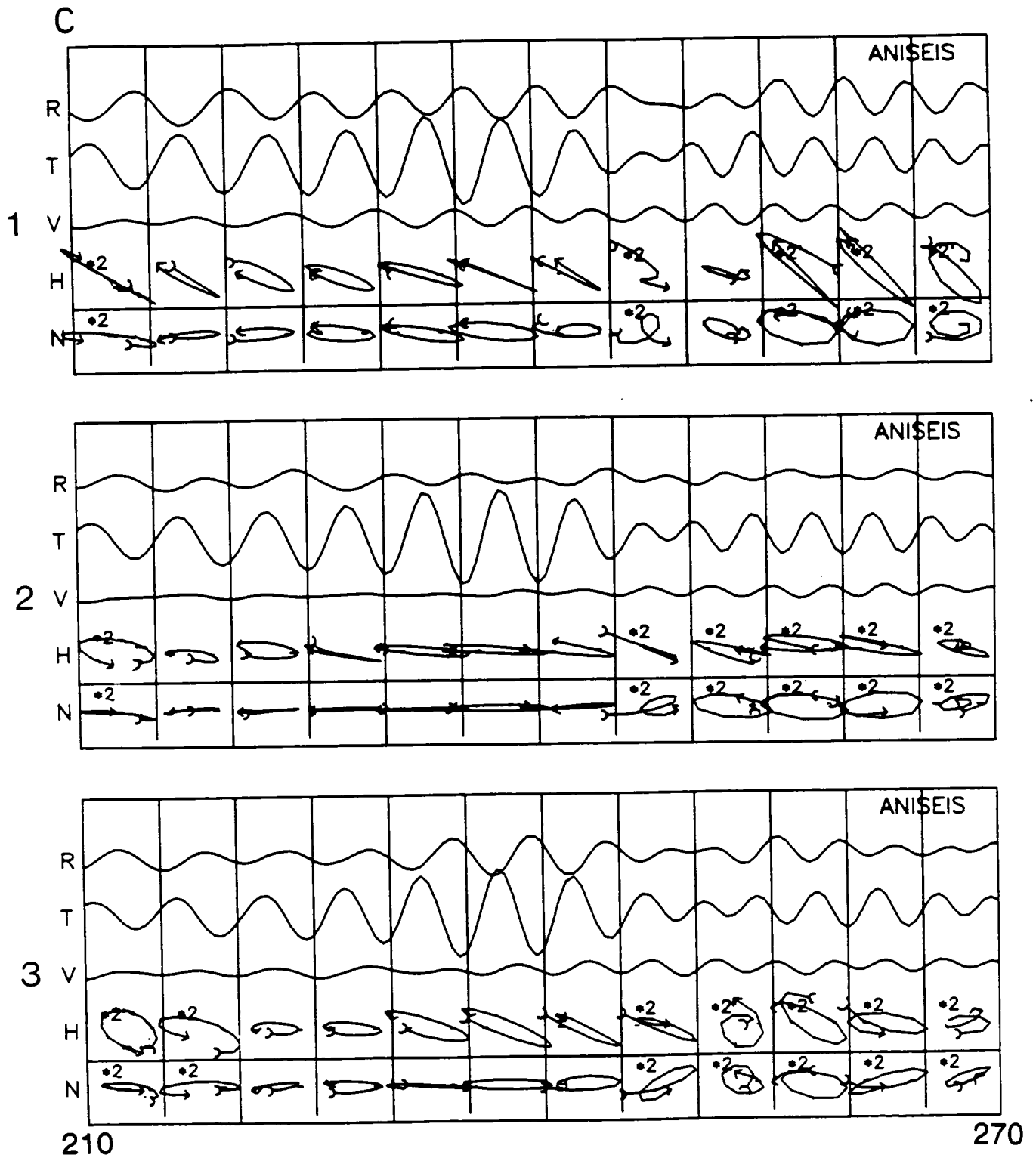

Figure 6.23 (cont.)

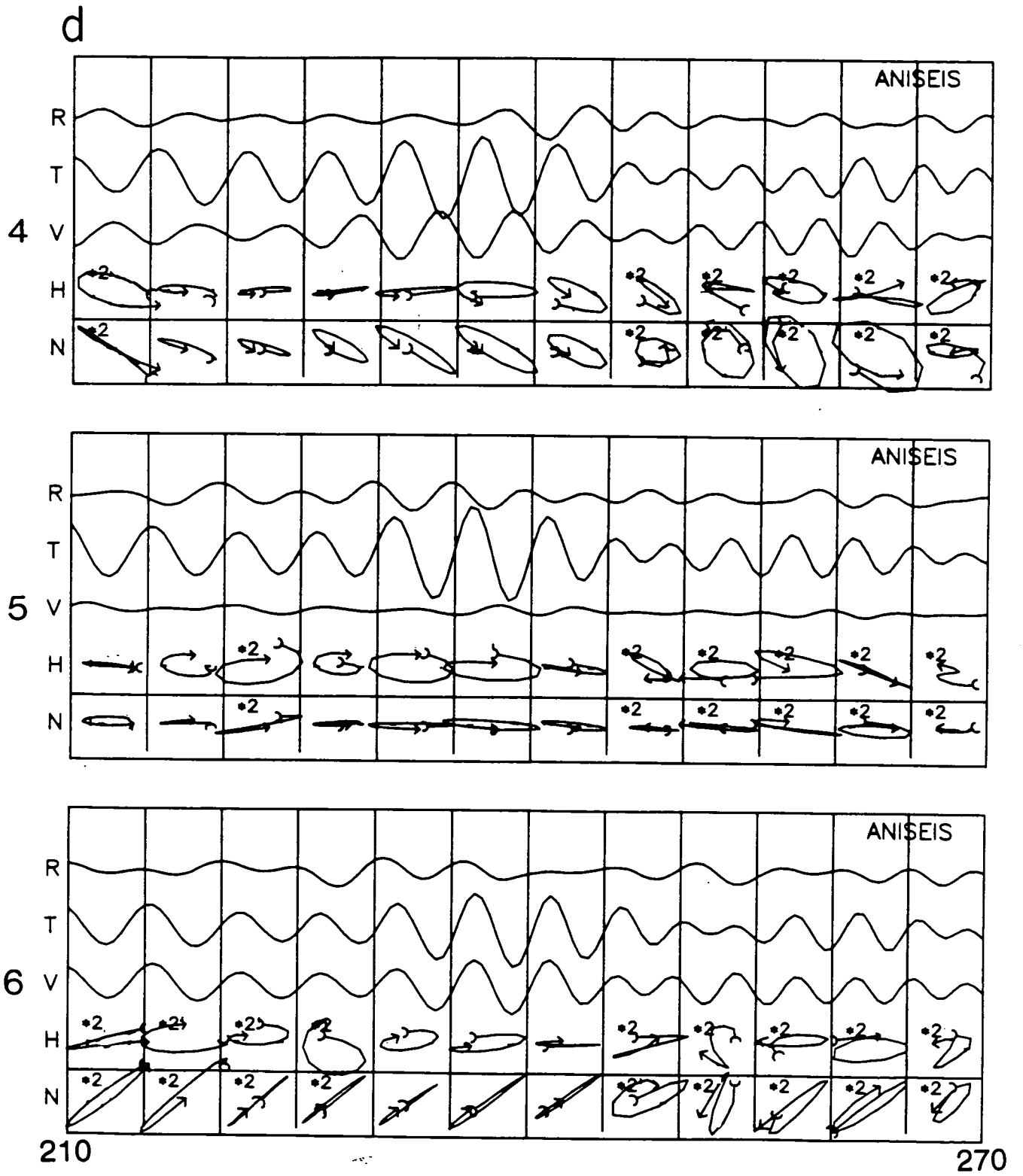

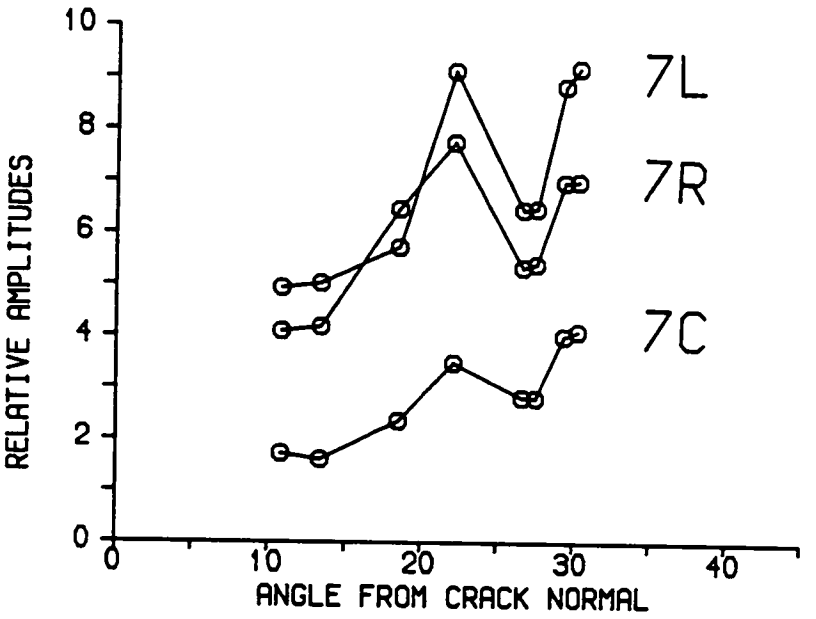

Figure 6.23 Love channel-wave amplitude (transverse component) variation with direction (crack normal) for three different source orientations in Figure 6.21. The amplitudes have been normalized to maximum of 10.

twice large of the minimum. The large variation of the Love wave amplitudes could be due to the anisotropic attenuation, because it seems that over only 10° azimuths, the attenuation variation is far too larger than expected. If this was due to different attenuations, it would indicate that attenuation had a significant effect on channel wave amplitudes. It certainly cannot be only due to the aligned cracks. Some sort of intrinsic anisotropy or recording instrumentation response might be responsible. Nevertheless the observed amplitude variation in a small range of azimuths suggests that attenuation is important for channel waves, and attenuation variation should be considered in the modelling of channel wave data.

6.7.4 The Florence data: discussion

The suggested velocity structure of the Florence coal-seam model is very complicated. It contains a dirt band between two coal-seams with its thickness increases from 1.2m to 2m. Such structure is not appropriate for presently available synthetic modelling technique. On the other hand, the data we analyzed here only covers a range of only 10° from the crack normal, so it is unlikely to estimate any symmetry of possible anisotropy. However, dispersion, particle motion and amplitude (attenuation) anomalies have been found. All these variations or anomalies are related to anisotropy, but not transverse isotropy since it requires some sort of azimuthal anisotropy. We suggest that the aligned cleats, which often exist in coal-seams, must be at least partly responsible.

6.8 Discussion

We acknowledge that a more detailed fit to the data than has been possible here would be required. Figure 6.5 is a good first-order match between fullwave synthetic seismograms and observed in-seam seismograms. 10% variation of modelling parameters (such as attenuation, crack densities in rocks and coal-seams) does not alter the synthetic seismograms and polarizations significantly.

Fine layering-induced transverse isotropy with a vertical symmetry axis is clearly present in coal-seams, but in this study, we have not included this kind of anisotropy in our modelling since transverse isotropy alone does not account for many observed anomalies, such as the coupling of Love waves in radial components, azimuthal dispersion variations and particle motion anomalies, although it may have a significant influence on detailed dispersion characteristics (Appendix B). A more realistic coal-seam model should have orthorhombic symmetry due to the presence of both fine-layering transverse isotropy with a vertical symmetry axis and verically aligned cleat-induced azimuthal anisotropy (Szab 1984; Szwilski 1984). Such a combination might be expected to have some effects on both channel-wave particle motions (as it does to body waves, Crampin 1989) and dispersion. For a more detailed analysis this should be considered.

There are apparently some discrepancies between observed and synthetics. Some may be attributed to the fine layering transverse isotropy, slight irregular coal-seam/rock boundaries, dirt band effects, difference in source and geophone positions, possiblly slighly asymmetrical coal-seam structures, and slightly different

crack orientations in coal-seams and rocks. In view of the fact that the observed records show scattering Love channel waves, all these factors are possible. Note also that a constant attenuation is assumed in our modelling, this is clearly not adequate, if an anisotropic attenuation factor was used, the match would be improved.

6.9 Conclusions

We suggest that the observations and modelling give a strong indication of the likely anisotropy symmetry in coal-seams, and demonstrate the need of polarization studies. We have shown that fullwave synthetic seismograms of channel waves in anisotropic coal-seams can match the observed travel-times, amplitudes and frequences of in-seam seismograms (dispersion), including the cross coupling of signals on different components which is a marked feature of the observed seismograms. The most important results from this study are summarized as follows:

1) It is apparent that observed channel waves are the results of anisotropy. Anisotropy is revealed by coupling in seismograms, dispersion, particle motion anomalies and possibly amplitude variations (attenuation anisotropy).

2) Anisotropy of the country rock, although probably not as strong as the anisotropy of the coal-seam, may still have a significant effect on the behaviour of the channel waves.

3) Seismograms, dispersion and polarization diagrams are sensitive to the crack/cleat orientation and density. This may help to explain the observed minima and maxima in amplitudes, which may indicate attenuation anisotropy.

4) The effects of attenuation on high frequency channel waves are important, and need to be taken into account when using synthetic seismograms to interpret channel wave data. This includes attenuation in the country rocks as well as the coal-seam. For the synthetic seismograms in Figure 6.5, the attenuation factor in the coal-seam is $Q = 50$, and in the country rock $Q = 100$. Matching synthetic to observed seismograms is likely to give good estimates of the effective attenuation of channel waves.

5) The source radiation is crucial to the seismograms. Synthetic seismograms vary with orientation, source frequency, and source shape. This probably makes inversion of in-seam seismic channel wave data difficult. In most examples, a source wavelength approximately two times the thickness of the seam (about 270Hz) seems appropriate. Note that it is possible that source radiation patterns in anisotropic media may differ considerably from these in isotropic media that we used in this study.

CHAPTER 7

CHANNEL WAVES IN ANISOTROPIC WAVEGUIDES: II, APPLICATION TO A CRACKED RESERVOIR

7.1 Introduction

There are typically four types of waveguides which are often seen in seismology, these are (a) the free surface and upper crust low-velocity zones; (b) an active fault zone; (c) a coal seam; and (d) a cracked hydrocarbon reservoir. Surface waveguides are sufficient for surface wave propagations, and the upper crust low-velocity zone may be attributed to sometimes observed surface waves and crustal channel waves [for example, Panza *et al.* (1972)]. A recent paper by Leary *et al.* (1987) has found that an active fault zone has a large crack density, which results in a low-velocity zone around the fault, such an area is an anisotropic waveguide and trapped modes have been observed in a VSP experiment.

In the previous Chapter 6, we analyzed and modelled the channel wave data recorded in a coal seam waveguide. Channel wave technique has not so far, to our knowledge, been applied in an oilfield. It remains to be seen that channel waves can be generated in and propagate through oilfield reservoirs. As an additional interest, in this chapter, we shall show some examples of observed records of hydraulic fracturing events. We shall not attempt to match the observations as we did in the previous chapters, and instead we calculate synthetic seismograms from a simple two-fracture model and

suggest that observed records of hydraulic fracturing events are due to the modes trapped between two or more fluid-filled fractures or treatment induced low-velocity zones.

7.2 Observational evidences

Hydraulic fracturing for enhancing the recovery of hydrocarbons has become a common reservoir engineering practice. The basic concept and practices can be found in the following papers and cited references, Hubbert and Willis (1957); Fehler (1981); Aki *et al.* (1982); Roberts and Crampin (1986); and Mahrer and Mauk (1987), which we shall not repeat.

Figure 7.1 shows some typical downwell recordings of microseismic events recorded during pressurization of a hydraulic fracturing. Figure 7.2 was recorded in another commercial treatment of hydraulic fracturing pumping. The precise position of the geophones is unknown, nor is the orientation of the geophone components with respect to the borehole. Both figures show some similarities. It is seen that there is a difference in the frequency content of the shear-wave coda between the vertical (Z or V) and horizontal components (X, Y or H1, H2). However, the principal characteristics of most, but not all of the seismograms is the large amplitude, low frequency wavetrain which begins at, or soon after, the onset of the shear-waves [as has been identified by Booth (1982)]. This wavetrain propagates with no measurable dispersion and suffers very little attenuation.

There are other examples which have been published by many

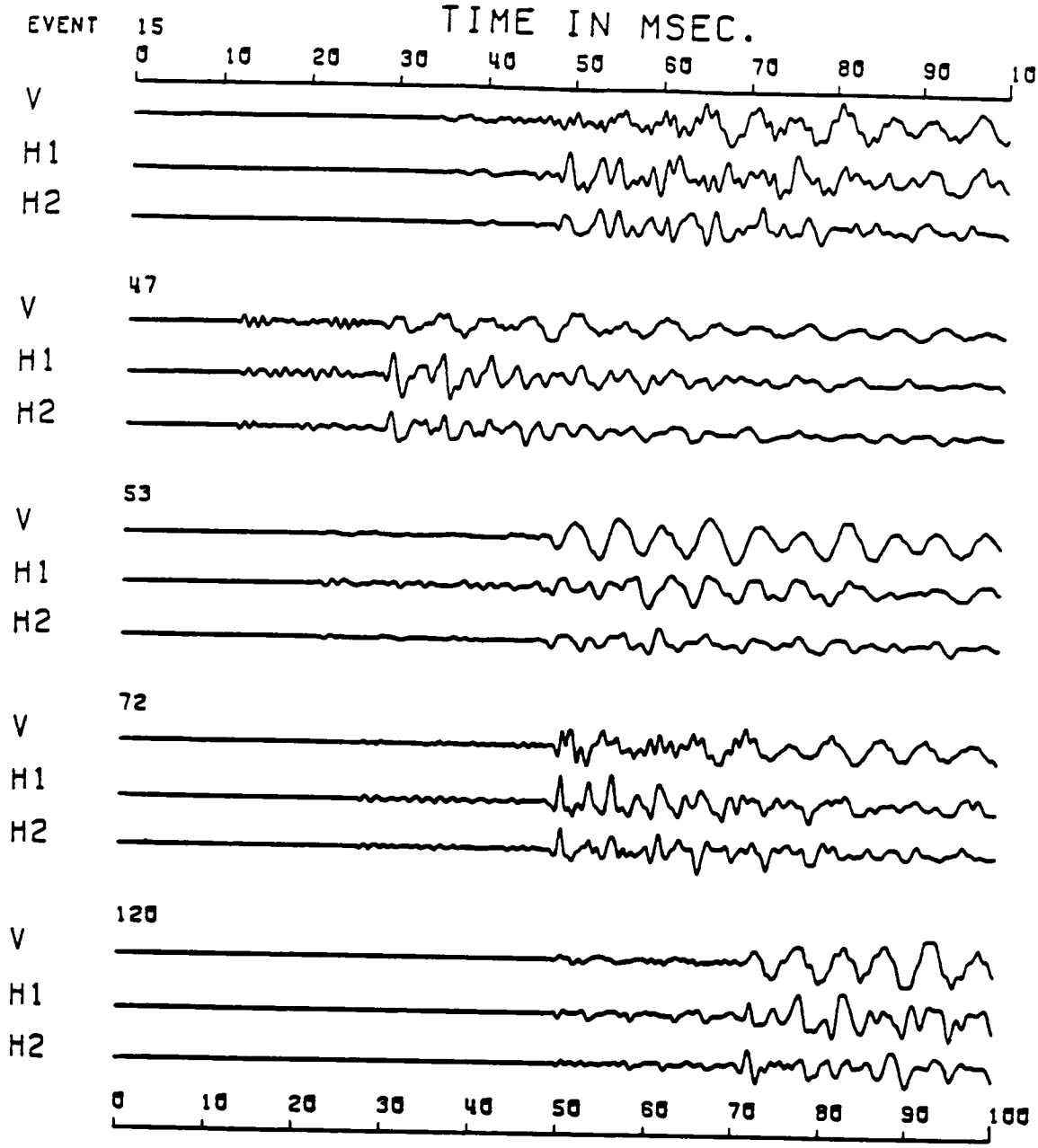

Figure 7.1 A selection of seismograms of microseismic events recorded by a three-component geophone package. The V component is parallel to the axis of the borehole. The horizontal components H1 and H2 are orthogonal to V, but their exact orientation is unknown.

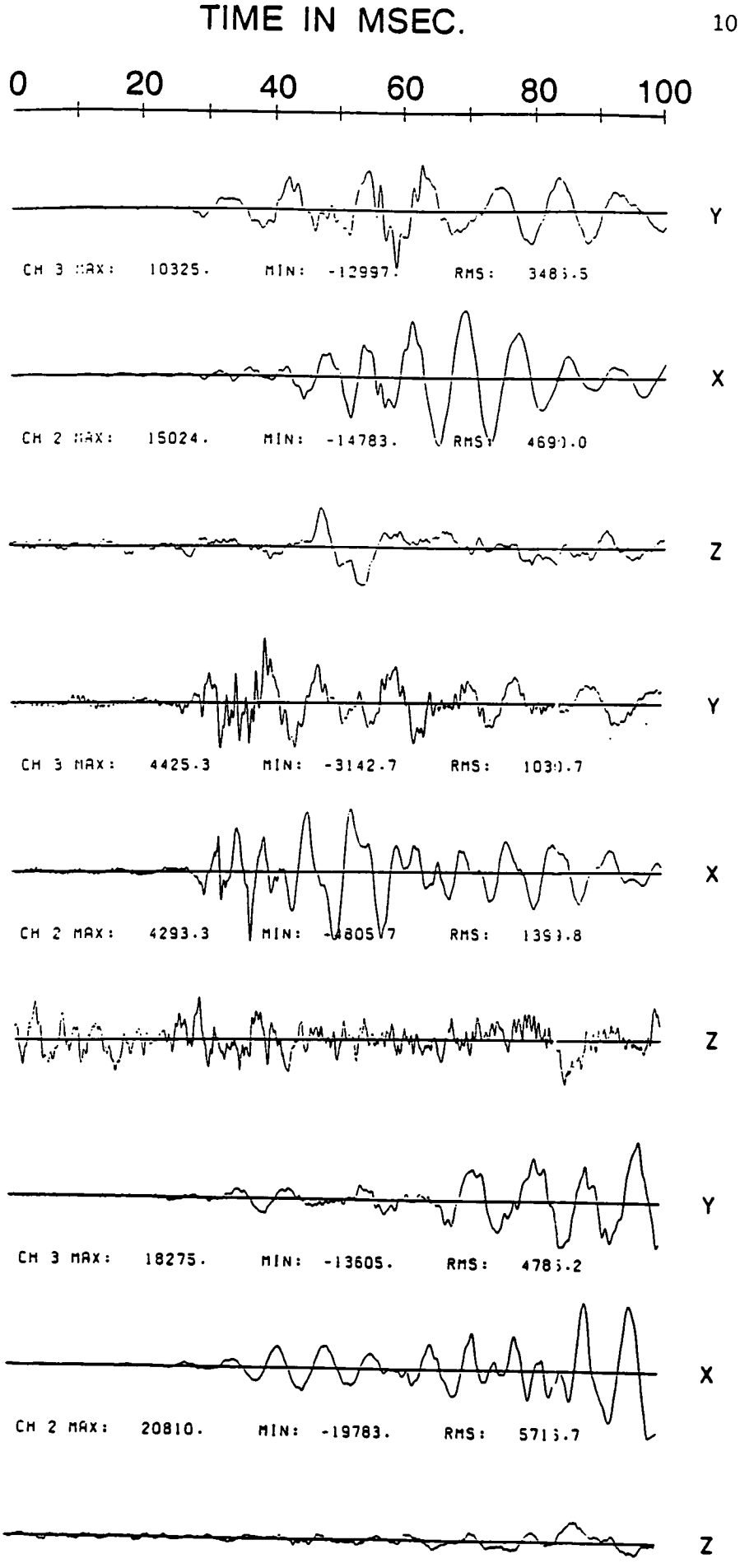

Figure 7.2 A selection of seismograms of microseismic events recorded at a commercial hydraulic fracture treatment.

authors. Observations of Figure 2 of Fehler (1981), Figure 4 and Figure 13 of Aki *et al.* (1982) and Figure 1 of Mahrer and Mauk (1987) show the same characteristics as the records in Figures 7.1 and 7.2. This feature indicates that the observed records are not conventional body waves. It is suggested that such a characteristic feature is typical for most of the acoustic events observed during hydraulic fracturing treatments. Booth (1982) suggested that this characteristics wavetrain could be due to the presence of a waveguide or a channel.

Mahrer and Mauk (1987) used the finite difference method to calculate synthetic seismograms for a low-velocity zone surrounding a hydraulic fracture in order to model observed microseismic records during hydraulic fracturing treatments. Rayleigh-type channel waves were observed, which, they suggested, showed some of the observed characteristic features.

7.3 Physical models

Hydraulic fracture treatments induce microseismic activity which can be observed using a triaxial seismic sonde located in the treatment wellbore. Records of this activity display properties typically associated with finite dimension waveguides. Mahrer and Mauk (1987) suggested that a hydraulic fracture is surrounded by an extended dilatant region. The importance of dilatancy is the reduction of seismic velocities, that is the creation of an low-velocity zone. Laboratory experiments carried out by Nur (1989) and Wang and Nur (1988) have found that both *P*- and shear-wave

velocities in oil reservoir rocks may reduce as much as 20 to 50% during thermal recovery (steam flooding, fire flooding or hot-water flooding), with the results of low-velocity reservoirs.

Hydraulic pressurization also opens new fractures. Figure 7.3 shows an example of the inferred geometry of the circular path in a commercial geothermal reservoir (after Booth 1982). The borehole GT-2B and EE-1 are connected by a system of natural joints and two large parallel fractures orthogonal to the direction of minimum tectonic stress, which were created by two separate hydraulic pressurizations of borehole EE-1. The thickness of the slab of rocks between these two fractures is estimated to be of the order of 10m. This slab is likely to be cracked as the result of thermal contraction on cooling during pressurization of the circulation system.

The suggested hydraulic fracturing models, either induced low-velocity zones or two or more large fractures, are all related to channels or waveguides, in which channel waves may propagate if the recording geometry is appropriate.

7.4 Synthetic seismograms

We only calculate the synthetic seismograms for a simple two-fractured model, which consists of a channel between two thin plane water-filled large cracks, surrounded by anisotropic halfspaces (Figure 7.4). It is believed that the channel is permeated by hexagonal columnar microcracks caused by thermal contraction (Booth 1982 and Crampin, personal communication), and

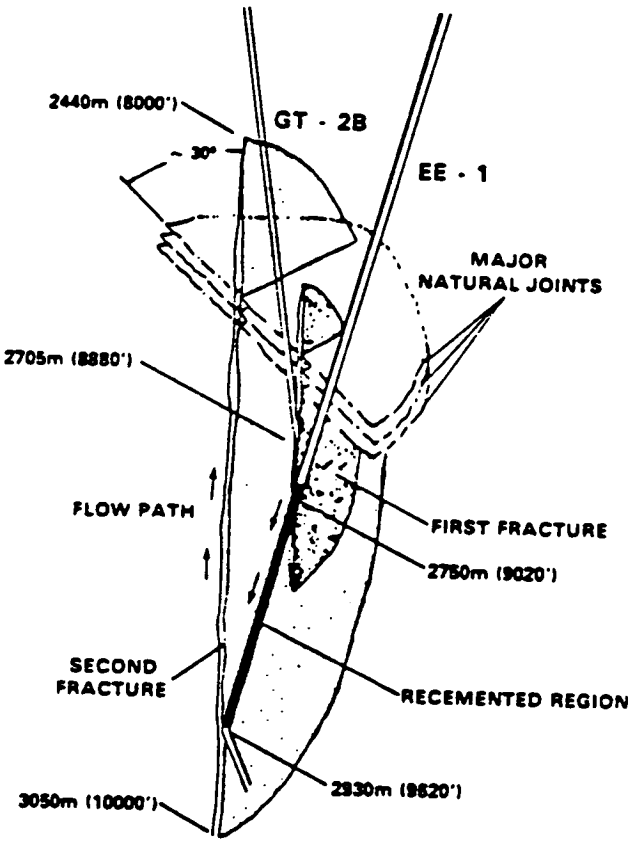

Figure 7.3 The inferred geometry of the circular path in a geothermal reservoir. The boreholes GT-2B and EE-1 are connected by a system of natural joints and two large parallel fractures. These fractures were created by two separate hydraulic pressurizations of the borehole EE-1.

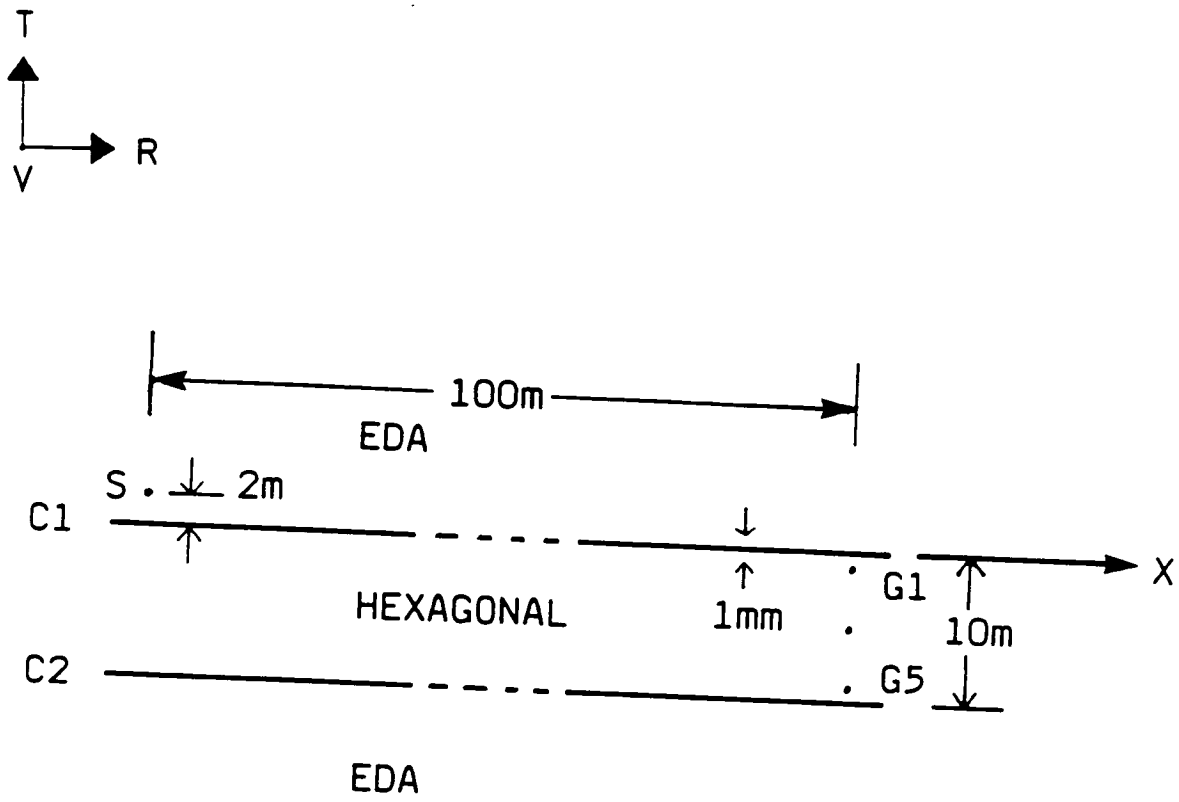

Figure 7.4 The model structure: two major 1mm thick water-filled cracks C1 and C2 on either side of a cracked slab which is modelled by an anisotropic medium with hexagonal symmetry, of thickness 10m. The geophones are located at depths of 1, 3, 5, 7 and 9 m in the channel. On either side of the channel are EDA-cracks perpendicular to the major fractures (the elastic constants of all the anisotropic materials are in Table 7.1).

thus it is anisotropic (the elastic constants are in Table 7.1).

The synthetic seismograms shown Figures 7.5 and 7.6 are calculated for the model in Figure 7.4 with different source types (the source is either 2m above or in one of the fractures. The source shape is the same as Figure 5.6 of Chapter 5, but with the frequency of 800Hz (the frequency of the recorded seismograms in Figure 7.1). All the seismograms show complicated motions, which are dependent of source and geophone positions. But in general the shear-waves are displayed with low frequency coda. If the source is in the channel (not shown here), the recorded seismograms will be similar to the channel waves observed in coal-seams (see Chapter 6). Booth (1982) suggested that arrivals appearing on the seismograms are the interferences of direct waves, waves reflected from the major cracks and reverberations within the channel. The shear arrivals frequently interfere to produce large-amplitude arrivals with low frequencies. This feature is most marked on the normal-component seismograms from geophone nearest to the major cracks. Similar features appear to be characteristic of some of the hydraulic fracturing downwell records (Figures 7.1 and 7.2), and may, we suggest, indicate that the geophone is very near to one of the major-cracks.

The most remarkable feature of the synthetic seismograms is the difference in the records for different positions of the receivers and sources and also difference in the frequency contents between radial and transverse components. It is suggested that the recording geophones and sources are crucial to the seismic signals observed. The seismograms are sensitive to the details of the

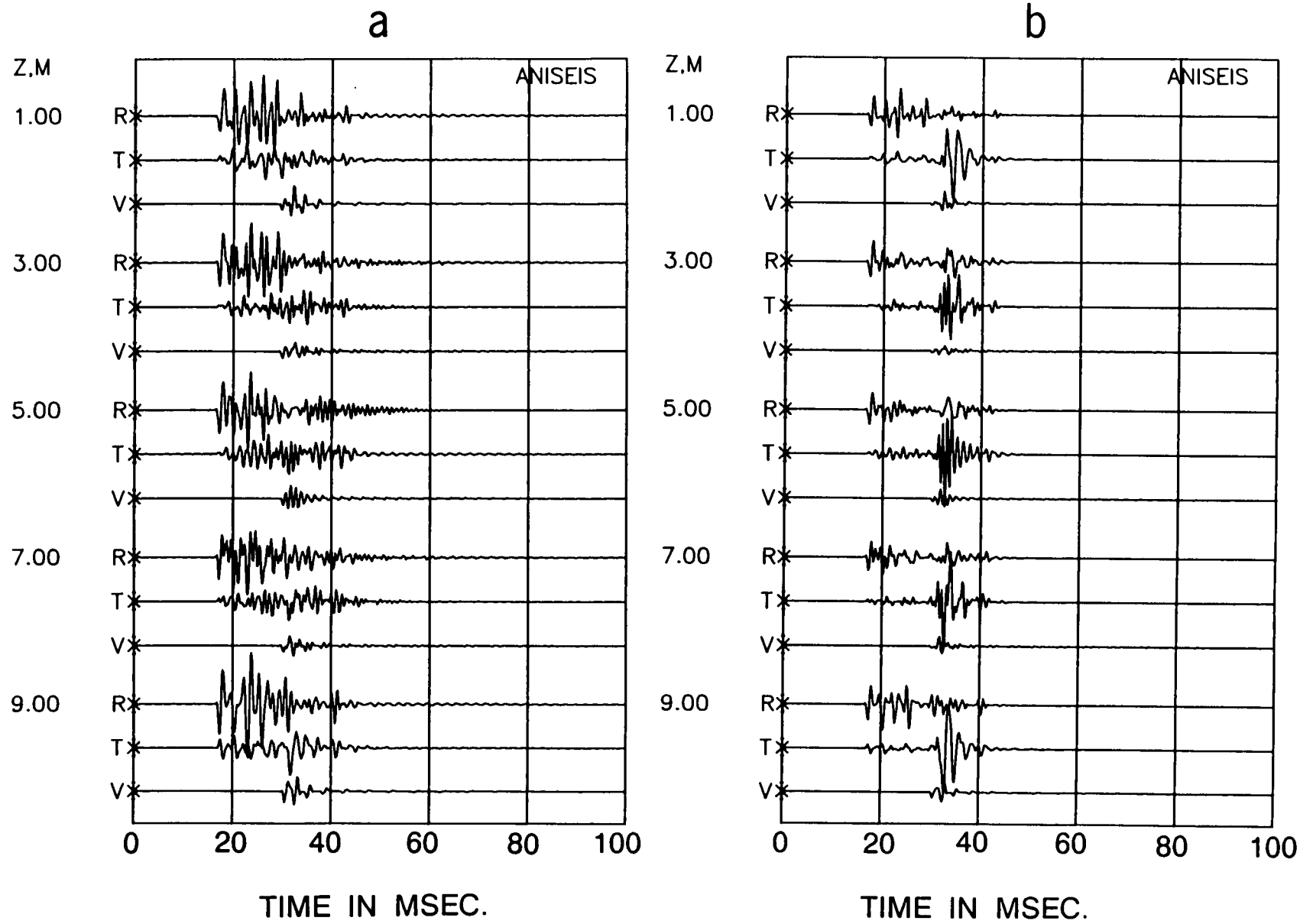

Figure 7.5 Seismograms calculated for two-fracture model in Figure 7.2 with 5 geophones located at depths of 1, 3, 5, 7 and 9m in the channel. The synthetic seismograms are calculated for a source pulse of 800Hz (source time function same as that used in Chapter 5). (*a*) a *SH45SV* source 2m above the channel and (*b*) a *SH45Sv* source in one large fracture.

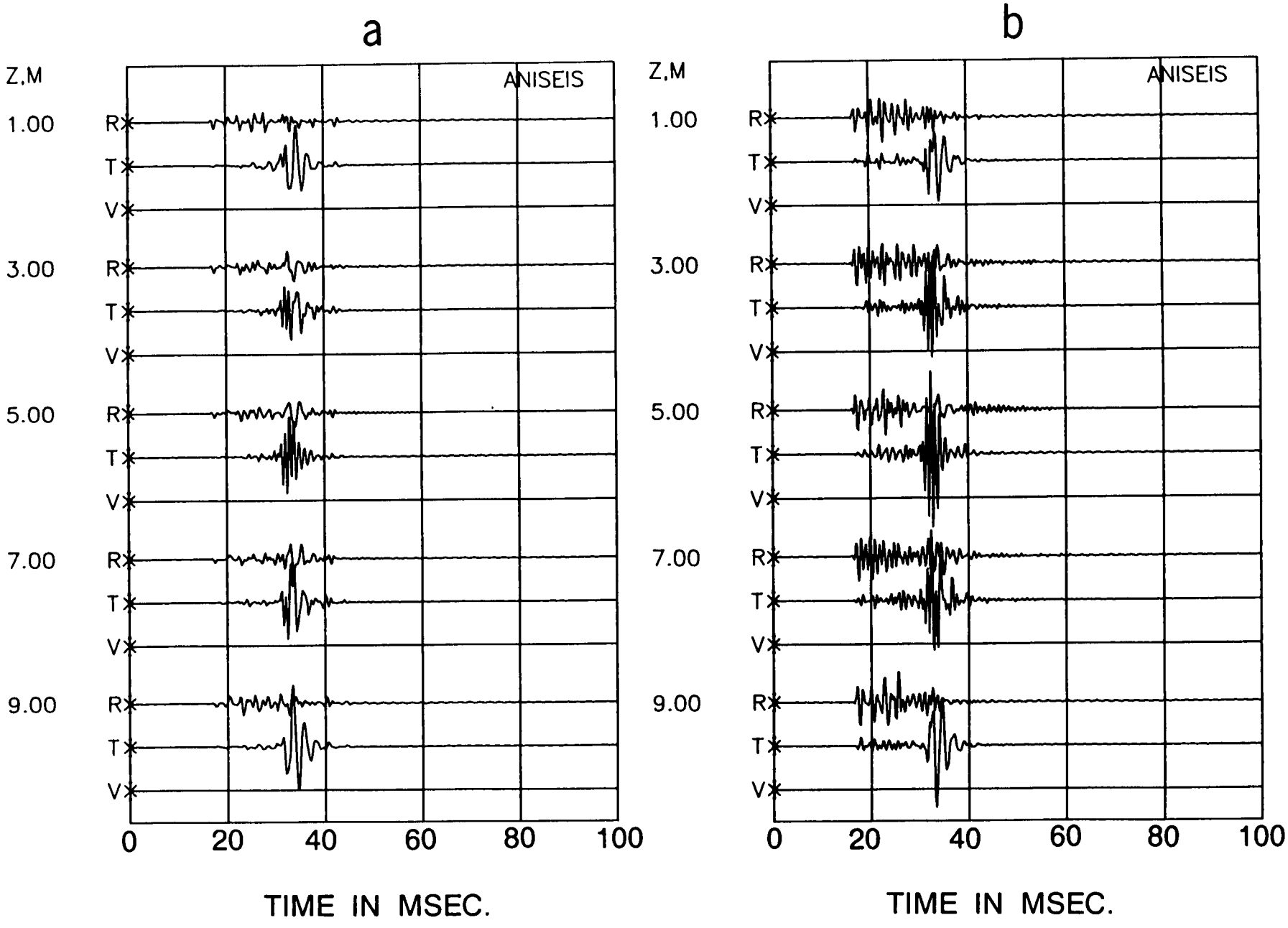

Figure 7.6 Same as Figure 7.6, but (*a*) a vertical force point source and (*b*) an explosive source in one of the large fractures.

Table 7.1 Elastic constants (in Pascals x 10^9) of the anisotropic material with hexagonal symmetry which models the cracked slab: a random distribution of coplanar normal saturated cracks in an isotropic matrix with V_P = 5.8, V_S = 3.35 km/s, and ρ = 2.6 gm/cm³. The crack density is 0.1. The axis of symmetry is paralel to the x_3 axis.

c_{1111} = 83.806,	c_{2222} = 83.806,	c_{3333} = 87.303
c_{2233} = 28.799	c_{3311} = 28.799,	c_{1122} = 31.532
c_{2323} = 26.213	c_{1313} = 26.213,	c_{1212} = 26.137

crack/geophone/ source geometry.

The simple modelling suggests that the low frequency shear-wave coda on observed seismograms is due to Love- and Rayleigh-type channel waves, which are generated most efficiently when the source is located within the channel as we discussed in the previous Chapter 6.

7.5 Discussion and conclusions

This is a very preliminary modelling. The synthetic seismograms and observed hydrofracturing records show several unusual features, which require more detailed investigations. Some of these features may be entirely dependent on particular details of the cracked structure, and may be, we suggest, interpreted in terms of interface waves along a single fracture.

Interface waves along a single fracture have been found in the theoretical studies by Pyrak-Nolt and Cook (1987) for Schoenberg's fracture model [a fracture can be modelled as a linear slip interface across which the stress is continuous, but the displacement is discontinuous (Schoenberg 1980)], by Ferrazzini and Aki (1987) for Fehler's fracture model [a very thin fluid-filled layer (Fehler 1982)] (see Appendix C for details). If interfaces along a single fracture exists, then some of the observed low frequency coda waves may be interpreted as a result of interferences of shear-waves with interface waves. This could have an important implication in interpreting acoustic events during hydraulic fracture treatments (Ferrazzini and Aki 1987).

In Chapter 3, we have shown that the geometry of cross-hole observations, with shear-waves propagating nearly horizontally, is not really appropriate for monitoring shear-wave splitting. However, analyzing channel waves, which propagate as trapped modes in low-velocity zones, as happens throughout most sedimentary reservoirs, offers some promise for recognizing small changes to reservoir rocks. We speculate that analyzing channel waves observed in cross- hole surveys offers good prospects for monitor enhanced oil recovery and will play an important role in the future reservoir seismology.

CHAPTER 8

CONCLUSIONS, DISCUSSION AND THE FUTURE

"There is no way that it can be accomplished easily, I am still searching for an approach to it." [*Qüyuan (B.C. an ancient Chinese poet), from "Gone with Complaints"*].

8.1 Introduction: conclusions from this thesis

Using synthetic seismograms, we have shown that anisotropy must be assumed if a precise interpretation of cross-hole and channel wave data is required. We have also demonstrated the effects of internal interfaces on shear-wave particle motions. The main results of this thesis are:

Chapter 3 and Chapter 4: Shear-wave splitting in cross-hole surveys

1. Synthetic modelling suggests that shear-wave splitting can be observed in cross-hole surveys. It is, however, more difficult to extract anisotropy information from cross-hole surveys than from VSPs.
2. Shear-wave splitting is observed from an inverted VSP, where the transverse motions are not expected from a borehole explosion source in a borehole. The modelling of this small data set supports the conclusion 1.

Chapter 5: Shear-wave polarizations at a single interface

1. A single interface may distort both transmitted and reflected shear-wave particle motions. The distortion is much more severe for reflected shear-waves than for transmitted shear-waves.

2. In the presence of anisotropy the interface will only alter the patterns in polarization diagrams, it will not alter the first motions of the shear-wave onsets since they are controlled by the symmetry of anisotropy (orientation of EDA-cracks). It is suggested that there are some difficulties of analyzing shear-wave reflection data in the presence of anisotropy.

Chapter 6 and Chapter 7: Channel waves in anisotropic waveguides

1. High frequency in-seam seismic channel waves have been modelled using synthetic seismograms. The amplitude, dispersion polarization and cross coupling of synthetic channel waves in coal-seams are in general consistent with the observations if cleat-induced anisotropy is taken into account.
2. Channel wave analysis as part of a reservoir study may help to extract information about the internal properties and fluid flow in hydrocarbon reservoirs (see more discussion later in this chapter).

The two main techniques: cross-hole surveys and in-seam seismics, employed in this thesis are closely related. The effects of an interface on shear-wave polarization as described in Chapter 5 is frequently encountered in cross-hole surveys, offset VSPs, and reflection seismics, hence it is *not* independent of the other two. A theme common to all these chapters is the use of synthetic seismograms and polarization diagrams to model observations and to identify the effects of anisotropy, in particular crack-induced anisotropy. Since there is no direct inversion procedures for detailed particle motion, forward modelling at present places the

closest constraint on the interpretation of observed records (Crampin *et al.* 1986). The important part of this thesis is the extension of shear-wave analysis to channel-waves.

In this chapter we turn to the discussion of these conclusions for the investigation of anisotropy. This includes recovery of shear-wave anisotropy information from various interferences, application of cross-hole surveys and channel waves, using EDA to describe reservoirs, and attenuation in cracked rocks.

8.2 Recovery of shear-wave splitting from various interferences

We are beginning to realize the importance of seismic anisotropy. The most diagnostic tool for the interpretation of anisotropy is polarization diagrams. In Chapter 5 we have investigated the effects of interfaces on shear-wave particle-motions. However, apart from various causes of anisotropy that we described in Chapter 2, anomalous particle-motions caused by phase shifts are due to a variety of mechanisms, which we shall summarize as follows:

(1) The free surface effects, including a *S*-to-*P* mode conversion, the irregular topography and the low-velocity zone near the surface. This can be found in the following references: Nuttli (1961, 1964); Nuttli and Whitmore (1962); Evans (1984); Booth and Crampin (1985); Yardley and Crampin (1989);
(2) Inhomogeneity near recording sites and along raypaths (Rodgers 1968; Cormier 1981; Gupta and Blandford 1983);
(3) Internal interface (including dipping interface) interferences

with both reflected and transmitted shear-waves (Jouma and Helbig 1987; Liu and Crampin 1989, see also Chapter 5);

(4) Noise effects (random noise, coherent low frequency noise), instrumentation responses, etc.

Distortion of shear-wave particle motions due to various factors makes it difficult to extract information about shear-wave splitting such as shear-wave first motions and the time delays between split shear waves. Interaction of shear-waves with interfaces restricts the analysis of shear-wave data in reflection seismics when anisotropy exists (Chapter 5). Identifying anomalous elliptical motions caused by the above mentioned factors is essential for our understanding of anisotropy-induced shear-wave splitting. There are several automated techniques (reviewed by MacBeth and Crampin 1989a, and others presented at SEG Summer Workshop on Recording and Processing Vector Wavefield Data in Utah, August 1989) that attempt to extract information about anisotropy from shear-wave data. All these techniques are based on the assumptions of small incident angles and simple structures. They may work very well for purely homogeneous anisotropic media without taking the effects of above distortion into consideration. However, the reliability of these techniques in the *real* Earth remains unanswered. Fortunately, some modelling techniques can handle some of these difficulties. One such technique, the reflectivity method (Booth 1982a), can model the free surface and interface effects for shear-waves. It is thus fair to assume that the current trial and error forward modelling is still one of the most important tools for seismic data interpretations.

Seismic inversion, a popular subject in the modern seismology, has been successful in seismic data interpretation. In fact, a major goal of the exploration geophysicist is to solve the geophysical inverse problem, namely determination or estimation of the physical properties of the subsurface from surface and/or borehole data. Very recently, seismologists have tried to extend this method to the study of anisotropy (for example, Dellinger 1989). The major difficulty is not only the many parameters involved, but three-dimensional variation of elastic properties. Sometimes, the solution of inversion for *anisotropy* is not unique even though the same technique may be unique for *isotropic* case, such as the state-space approach (Meadow and Coen 1986). Pattern recognition has also been developing rapidly both theoretically and practically as part of the development in computer science. As more and more people come to realize the importance of seismic anisotropy, it will be interesting to see how this technique can be adopted to discriminate 3D patterns of shear-wave polarizations. Before any inversion technique is applied to a study in anisotropy, the effects of interferences described above need to be fully resolved.

8.3 Where do we go from here ? - the future of cross-hole surveys

Exploration geophysics has so far mainly focused on the surface (even in a VSP a surface source is used). In order to extract more information about the internal properties of hydrocarbon reservoirs and to monitor enhanced oil recovery processing, "*We should take the sources and receivers into boreholes and begin to work on cross-hole shear-wave techniques.*" This was stated by Roger Turpening in replying to the question "*where do we go from here?*" in the SEG Research Workshop on Recording and Processing Vector Wave Field Data

in Snowbird, Utah, August 1989. He argues that "*...the obvious answer is: into borehole naturally...*". In Chapter 3 and 4, we have demonstrated some of the difficulties of cross-hole surveys in extracting information about anisotropy. This does not contradict the many advantages of cross-hole surveys that we mentioned in the beginning of Chapter 3. There are so many disadvantages of surface data. Just as reflection seismics, particularly CDP technique, has played a significant role in oil exploration, and VSP in oil recovery in the past 20 years, the cross-hole technique will have a great potential in the future oil production.

Actually, the subject of cross-hole technique has attracted many geophysicists, particularly on cross-hole tomography, known as the computer tomography (CT) technique. It is the process by which information characterizing the first arrivals is inverted for the velocity or attenuation structure in the area defined by the borehole. In travel time tomography the first arrival times between a series of downhole sources and receivers can be used to construct a tomographic image of the *P*- and shear-wave velocities between the boreholes. Amplitude tomography uses the amplitudes of the first arrivals to make an image of the quality factor Q or the dissipation factor (internal friction) Q^{-1}. This technique can be found in Wong *et al.* (1985); Bregman *et al.* (1989), and among many others. As most of the cross-hole surveys have been carried out in crystalline rocks, anisotropy should clearly be considered. Anisotropic cross-hole tomography will be a new challenge to geophysicists.

Channel-wave analysis is another possible application in cross-hole seismology. In Chapter 6 we have studied the channel waves in a coal seam, and identified several anomalies.

Particularly, studies of channel waves observed in a cross-hole survey [including channel-wave tomography as developed by the British Coal (Jackson 1985)] may help to estimate the geometry and contents of EDA-cracks (fluid or gas-filled) since channel waves are more sensitive to attenuation and small amount of anisotropy than body waves (shear-waves). In seismology, with anisotropy, we normally refer to as seismic velocity variations with direction. For body wave this is, of course, important. However, anisotropy may also imply *dispersion variations*, or *attenuation variations*. The dispersion and attenuation anisotropy may *not* be significant for body waves (since body waves are not essentially dispersive), but all three types of anisotropy can be significant for surface or channel waves. It is, therefore, not surprising that the high frequency channel wave may provide more detailed information about *in situ* cracks than body waves.

8.4 Using EDA to describe cracked reservoirs

Fractures (cracks) can be an important feature of hydrocarbon reservoirs where their presence (either naturally occurring or induced) increases the productive capacity. Many reservoirs with a low matrix permeability would not be commercially attractive without a natural or induced fracture system. While there is no question as to the importance of fractures with respect to formation permeability there is the matter of the contribution that fractures make the reservoir storage capacity or more specifically the porosity (Hensel 1986). The assignments of porosity in a dual porosity system (matrix and fractures) may be critical in estimating the reserves and ultimate production of hydrocarbons.

An oil or gas reservoir contains various pores and cracks or fractures, which form a circular path for the transport of fluids, such as oil and gas. Table 8.1 lists the properties of reservoirs that have the most important impact on oil recovery (after Nur 1989). Comparing with the EDA-crack parameters listed in Table 3.2 of Chapter 3, it is clear that reservoirs exhibit EDA-cracking and estimates of these EDA-cracks should yield more detailed information about the reservoir properties. It, therefore, offers a possibility of monitoring reservoir development during enhanced oil recovery by using seismic method (this is sometimes called reservoir seismology). To succeed in reservoir description and recovery monitoring, high frequency and broad-band seismic data must be obtained. Nur (1989) suggests that the key for success is to take advantage of the existance of wells, by placing sources and receivers in them to carry out a cross-hole survey (the idea that has also been put forward by Turpening). In Chapter 7 we suggest that channel waves may be observed in hydrocarbon reservoirs. Together with cross-hole survey channel waves will play an important role in future reservoir seismology.

8.5 Attenuation anisotropy and intrinsic attenuation in cracked rocks

There is much interest in attenuation study. Like seismic anisotropy, attenuation has always been a subject that many geophysicists have paid their attention to. Many of the proposed mechanisms for attenuation of wave motion would cause the attenuation to vary with the direction of propagation through the imperfectly elastic material (Crampin 1981). Attenuation may be caused by scattering at the faces of cracks or pores (Chatterjee *et al.* 1980), bubble movements in partially saturated cracks (Mavko and

Table 8.1 Reservoir properties that have the most important impact on oil recovery (after Nur 1989).

1. Mineralogy

2. Rock properties

   Porosity

   Saturations (oil, water, gas)

   Permeability

   Rock compressibility

3. Fluid properties

   Fluid viscosity

   Hydrocarbon chemistry

   Wetability

   Fluid compressibility

   Fluid chemistry

4. Environmental factors

   Pore pressure

   Stress

   Temperature

...and their spatial and temporal variations.

Nur 1979), liquid squirting in fully saturated cracks (O'Connell and Budiansky 1977) and friction in thin cracks and along grain boundaries (Johnston *et al.* 1979; Toksöz *et al.* 1979). It is clear that a variety of mechanisms are possible and the only common feature is that the major cause of attenuation is due to the presence of cracks or pores. Crampin (1978, 1985a) suggested that most systems of cracks in the Earth's crust display overall alignments. Attenuation caused by such aligned cracks will result in anisotropy velocity and attenuation. Crampin (1981) initially used the complex elastic constants to model cracked media with real part modelling velocity variation and imaginary part attenuation variation. This has later been extended to the Hudson crack theory (Hudson 1980b, 1981). Attenuation from his theory is due to the scattering at the faces of aligned cracks (either dry or saturated cracks). He further extended his theory to include partially saturated cracks (1988), which may have significant effects on attenuation.

All the analyses in this thesis are either assuming attenuation is constant (Chapter 6) or its effect is negligible (rest of this thesis). If attenuation anisotropy was considered in Chapter 6, the match of synthetics to observations of the in-seam seismic channel waves in Chapter 6 would improve. Hudson theory results in attenuation variation being largely dependent on frequency, which satisfies the famous Rayleigh Law, that is attenuation is a power 3 of frequency. This is not consistent with channel wave attenuation in coal seams. The attenuation of channel waves holds a linear relation with frequency in most coal seams (Buchanan *et al.* 1983).

This is one reason why in Chapter 6 we did not consider anisotropy attenuation due to cracks. New formulation based on Hudson theory is currently under development (Crampin and Peacock, personal communications).

Preliminary calculations by Crampin (personal communication) suggest that the differential attenuation of the two split shear-waves is likely to be sensitive to variations in viscosity of the pore fluid, and variations in the proportion of gas to liquid in the pore-space. This could have important implication during operations such as enhanced oil recovery.

8.6 Future shear-wave anisotropy study in China

I would like to finish this thesis by speculating about shear-wave anisotropy studies in China. Shear-wave splitting above small earthquakes has been observed across North America, the USSR, Europe, Africa (see references cited by Crampin 1987a; Lovell *et al.* 1989), and also Japan (Kaneshima *et al.* 1988a, 1988b, 1989). To my knowledge, shear-wave splitting has not so far been reported in China, although laboratory experiments have been undertaken (Chen Yong, personal communication).

Chinese scientists have found, in the earlier 1980's, that shear-wave polarizations from the precursory swarms of the Haichen Earthquake were very stable. They suggested that they played an important role in the prediction of Haichen Earthquake (Gu and Cao 1980). If such "*stable shear-wave polarizations*" is the shear-wave polarization alignment, EDA-cracks must be responsible for this. However, they did not go further to relate the stress to the

polarizations alignment they found. It is of interest to see if such a stable polarization alignment is consistent with the maximum compressional or minimum tensional stress direction in that region. I did not analyze any earthquake data in this thesis, but the basic theory is similar. It remains to be seen if shear-wave splitting will be observed in China, which would have a great benefit for the Chinese earthquake prediction studies.

China is rich in oil resources and coal supplies. The VSPs have been widely carried out in almost all the large oil fields, such as the Sichuan Gas Field and the Daqin Oil Field, the largest oil field in China. Shear-wave VSP study has just begun (He Qiao-deng, personal communication). However, the author knows little about the recent development there. This is clearly this new technique which will be employed in the Chinese oil industry in the future.

APPENDIX A

COMPLEX TRANSMISSION/REFLECTION COEFFICIENTS AND PHASE SHIFTS

Let us take an incident *SV*-wave as an example. The displacement of the incident downgoing *SV*-wave with amplitude S_1 is described by

$$\mathbf{u}_{SV} = S_1(\cos\beta_1, 0, \sin\beta_1)\exp[j\omega(\sin\beta_1/V_{S1}x' - \cos\beta_1/V_{S1}z' - t)], \quad \text{(A-1)}$$

where j is the imaginary unit, β_1 is the incident angle, $\sin\beta_1/V_{S1} = p$ is the ray parameter in the $x'\,y'\,z'$ coordinate system, ω is the angular frequency ($\omega = 2\pi f$), t is time, and V_{S1} is the shear-wave velocity in the medium 1 (See Figure 5.1 of Chapter 5). When a *SV*-wave is incident on an isotropic interface from medium 1 to medium 2, the transmitted downgoing *SV*-wave has a displacement of the following form:

$$\mathbf{u}_{SV} = S_1(\cos\beta_2, 0, \sin\beta_2)\,T_{SV}\exp[j\omega(px' - \cos\beta_2/V_{S2}z' - t)], \quad \text{(A-2)}$$

where V_{S2} is the shear-wave velocity in medium 2, β_2 is the angle between the transmitted wave and the normal to the interface. T_{SV} is the transmission coefficient (equation 5.2 in Chapter 5), and is the function of all the parameters defined in section 5.2 of Chapter 5.

The incident angle β_1 can be freely chosen between 0° and 90°, but the other angles (which determine upgoing reflected *SV-to-P* conversion, downgoing transmitted *SV-to-P* conversion and *SV*-waves) are controlled by Snell's law. When the incident angle β_1 is

greater than the first critical angle $\alpha_{c1} = \sin^{-1}(V_{S1}/V_{P2})$, T_{SV} becomes complex. From mathematics, we know that a complex number $z = x+jy$ can be written as $r\exp(j\phi)$, where $r = (x^2+y^2)^{1/2}$ and $\phi = \tan^{-1}(y/x)$. r is called the *amplitude* and ϕ is called the *phase* of z. A complex T_{SV} can therefore be written as

$$T_{SV} = |T_{SV}|\exp(j\phi) \qquad \text{(A-3)}$$

A complex transmission coefficient of *SV*-waves means that the amplitude of the incident wave is multiplied by $|T_{SV}|$ and the phase is shifted by ϕ. Using equation (A-3), we rewrite (A-2) as:

$$\mathbf{u}_{SV} = S_1(\cos\beta_2, 0, \sin\beta_2)|T_{SV}|\exp[j\omega(px' - \cos\beta_2/V_{S2}z' - t)+j\phi], \qquad \text{(A-4)}$$

so that the resultant downgoing transmitted *SV*-wave will experience a shift of ϕ. It should be noted that the transmission coefficient of a *SH*-wave is always real. Similarly, the reflection coefficient of a *SV*-wave can also be complex. The resultant phase shifts will inevitably lead to an elliptical motion defined by equation (5-6) in Chapter 5. Detailed derivation can be found in Kanasewich (1981).

APPENDIX B

LOVE WAVE DISPERSION IN TRANSVERSELY ISOTROPIC MEDIA WITH A VERTICAL SYMMETRY AXIS

B.1 Phase recursion algorithm

Love-type channel wave dispersion in multilayered isotropic media has been calculated using the phase recursion method of Räder *et al.* (1985). We now extend this method to include transversely isotropic (TI) layers by defining an anisotropic factor following Anderson (1961, 1962). We consider a layered structure as shown in Figure B.1. All the materials are either transversely isotropic or isotropic. The equation of Love-type motion in TI media in the ith layer is written as

$$N_i \frac{\partial^2 u_i}{\partial x^2} + L_i \frac{\partial^2 u_i}{\partial z^2} = \rho_i \frac{\partial^2 u_i}{\partial t^2} , \qquad \text{(B-1)}$$

where u_i is the displacement on the y-component in the ith layer. L_i and N_i are two elastic constants c_{2233} (or c_{44}) and c_{1212} (or c_{66}) of a transversely isotropic medium with density ρ_i. L_i and N_i are related to the horizontal and vertical velocities (V_H and V_V) of *SH*-waves by

$$N_i = \rho_i (V_H)_i^2, \quad \text{and} \quad L_i = \rho_i (V_V)_i^2. \qquad \text{(B-2)}$$

In isotropic media, N_i and L_i are equal, *i.e.* $N_i = L_i = \rho_i (V_S)^2$, where V_S is the shear-wave velocity in isotropic media. The

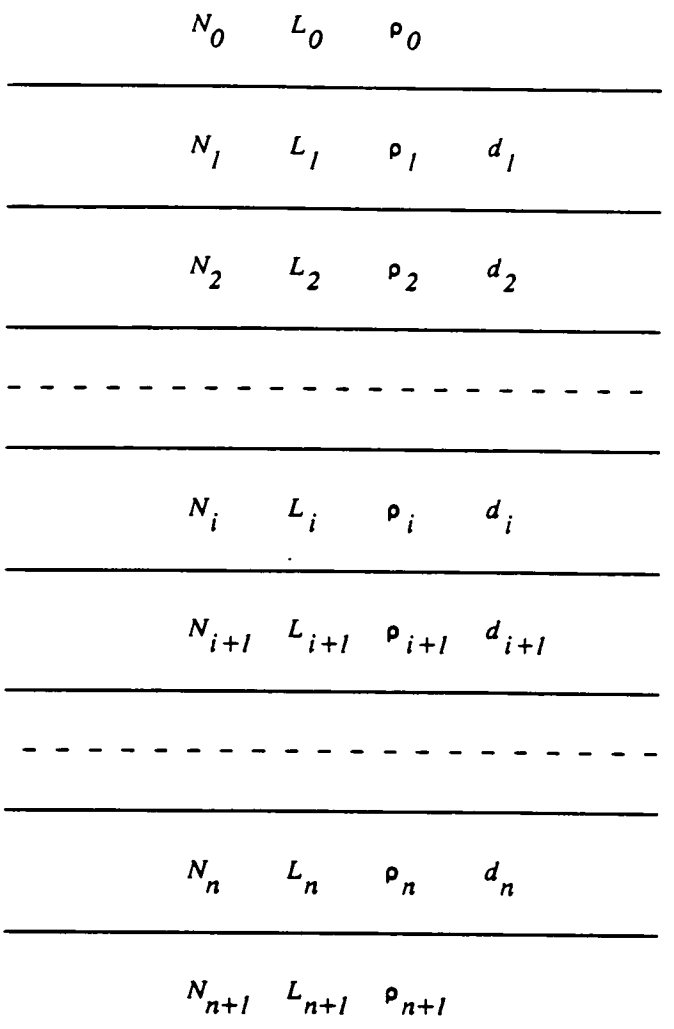

Figure B.1 Configuration of multilayered transversely isotropic structure used for the calculation of Love-wave dispersion. N_i and L_i are the corresponding elastic constants c_{44} and c_{66} of ith layer, repectively. d_i and ρ_i are the thickness and density of ith layer.

displacement $u_i(x, z, t)$ may be expressed as a funtion of time t, and position x and z by

$$u_i(x, z, t) = A_i(z)\exp[j\omega(t - x/c)], \tag{B-3}$$

where $A_i(z)$ is the z-dependent amplitude function in the ith layer, $\omega = 2\pi f$ is the angular frequency, j is the imaginary unit, and c is the phase velocity. By putting (B-3) into the equation of motion (B-1), we obtain the following differential equation of $A_i(z)$

$$\frac{\partial^2 A_i(z)}{\partial z^2} = -\omega^2 A_i(z)[\rho_i/L_i - N_i/(c^2 L_i)] = -\omega^2 \gamma_i^2 A_i(z), \tag{B-4}$$

where

$$\gamma_i = [\rho_i/L_i - N_i/(c^2 L_i)]^{1/2}. \tag{B-5}$$

It can be written in another form:

$$\gamma_i = (N_i/L_i)^{1/2}(\rho_i/N_i - 1/c^2)^{1/2} = \eta_i \gamma_i^{\circ}, \tag{B-6}$$

where

$$\gamma_i^{\circ} = (\rho_i/N_i - 1/c^2)^{1/2} = [(1/V_H)_i^2 - 1/c^2]^{1/2}. \tag{B-7}$$

Comparing equation (B-7) with equation (4) of Räder *et al.* (1985), we find that γ_i° is the expression for isotropic media. We define $\eta_i = (N_i/L_i)^{1/2} = (V_H/V_V)_i$ as an anisotropic factor [Anderson 1962, Note that Anderson originally defined the anisotropic factor as $\eta_i = N_i/L_i = (V_H/V_V)_i^2$]. This parameter is introduced so that it is now possible to use the computer program for isotropic media to determine channel (and surface) wave dispersion in transversely

isotropic media if the isotropic parameter γ_i° is substituted by $\eta_i \gamma_i^\circ$.

The differential equation (B-4) has the following general solution in the local coordinate system of the interface $z = z_i$:

$$A_i(z) = B_i \exp[-j\omega\nu_i(z - z_i)] + C_i \exp[j\omega\nu_i(z - z_i)], \qquad \text{(B-8)}$$

where the first term of equation (B-8) represents a downgoing wave in layer i, and the second term an upgoing wave. The superposition of both waves may yield a standing wave due to a constructive interference between the interface $z = z_i$ and $z = z_{i+1}$. However, this can only hold if the difference between their phases are $2m\pi$ ($m = 0, 1, 2...$). Following Räder *et al.* (1985), we assume the amplitudes of these waves are related by

$$C_i = B_i \exp(2j\xi_i), \qquad \text{(B-9)}$$

where ξ_i is the resultant complex phase shift between downgoing waves incident on the ith interface and upgoing waves incident on the $(i+1)$th interface resulting from all individual phase shifts caused by different traveltimes through layers and reflections at the interfaces.

Using this relation, the displacement coefficient $A_i(z)$ of *SH*-type wave in the ith layer may be written as

$$A_i(z) = B_i\{\exp[-j\omega\nu_i(z - z_i)] + \exp[j\omega\nu_i(z - z_i) + \xi_i]\}$$

$$= D_i \cos[\omega \nu_i (z - z_i) + \xi_i), \tag{B-10}$$

and

$$D_i = 2B_i \exp(j\xi_i).$$

The displacement coefficients of *SH*-type waves radiating in the two halfspaces can be written as

$$A_o(z) = D_o \exp[j\omega \nu_o (z - z_1)],$$

and (B-11)

$$A_n(z) = D_n \exp[-j\omega \nu_n (z - z_n)].$$

As the displacement and stress must be continuous at each interface, it leads to

$$D_i \cos(\omega \nu_i d_i + \xi_i) = D_{i+1} \cos(\xi_{i+1}),$$

and (B-12)

$$L_i \nu_i D_i \sin(\omega \nu_{i+1} d_i + \xi_i) = L_{i+1} \nu_{i+1} D_{i+1} \sin(\xi_{i+1}).$$

This is a standard eigenvalue problem. For a nontrivial solution of this homogeneous equation system the determinant of the matrix of coefficients is required to be zero, *i.e.*

$$\begin{vmatrix} \cos(\omega \nu_i d_i + \xi_i) & \cos(\xi_{i+1}) \\ L_i \nu_i \sin(\omega \nu_{i+1} + \xi_i) & L_{i+1} \nu_{i+1} \sin(\xi_{i+1}) \end{vmatrix} = 0$$

This yields

$$L_{i+1} \nu_{i+1} \tan(\xi_{i+1}) = L_i \nu_i \tan(\xi_i + \omega \nu_i d_i), \tag{B-13}$$

From this recursion equation, a set of unknown phase shifts ξ_i at

successive interfaces may be computed with the starting phase shift ξ_1 at the top interface, which is

$$\xi_1 = \tan^{-1}[-jL_0\nu_0/(L_1\nu_1)]. \tag{B-14}$$

As the Love channel wave develops by constructive interference of the resulting phase shifts, the final phase shift value ξ_n at the bottom interface is determined in the same way and must satisfy

$$\xi_n = \tan^{-1}[jL_n\nu_n/(L_{n-1}\nu_{n-1})]. \tag{B-15}$$

This is the dispersion equation of the layered model relating the frequency ω and the phase velocity c implicitly. For a given frequency ω, the phase velocities c for different modes may be iteratively computed with the above phase shift equations using the root-finding technique [such as the Newton-Raphson method or the Müller method for non-linear systems of equations (Nonweiler 1984)]. This algorithm requires only the inverse tangent of complex numbers, it works fast and is accurate in the high frequency range.

Finally, the method can also be used to calculate dispersion curves and amplitude-depth distribution of Love surface waves. In this case the starting value of recursion is

$$\xi_1 = 0, \tag{B-16}$$

on account of the phase shift of the SH-wave reflected at the free surface from below.

B.2 Group velocity

The kinematic group velocity V_g is the gradient of the frequency ω with respect to the wave number κ. In general anisotropic media, the group velocity is

$$V_g = (\partial\omega/\partial\kappa_1,\ \partial\omega/\partial\kappa_2,\ \partial\omega/\partial\kappa_3)^T, \tag{B-17}$$

(Crampin 1977). For channel wave propagation in a plane of symmetry, *i.e.* along the plane of fine layers, symmetry considerations demonstrate that the energy of Love waves (*SH*-motion) is confined to the symmetry plane and we have $\partial\omega/\partial\kappa_1=0$ and $\partial\omega/\partial\kappa_3=0$. Thus the equation of the group velocity of Love wave can be written as

$$V_g = (0,\ \partial\omega/\partial\kappa_2,\ 0)^T, \tag{B-18}$$

Alternatively, we can use the method described by Aki and Richards (1980), for channel waves (same as surface waves), we define the energy integrals

$$I_1 = \frac{1}{2}\int_0^\infty \rho(z)A(z)\,dz, \qquad I_2 = \frac{1}{2}\int_0^\infty L(z)A(z)\,dz, \tag{B-19}$$

the group velocity can then be written as

$$V_g = I_2/cI_1. \tag{B-20}$$

This gives the group velocity in terms of integrals, and is numerically more stable than differentiation of equation (B-17) (Aki and Richards 1980).

B.3 Numerical example: effects of transverse isotropy on Love channel wave dispersion

Coal seams are transversely isotropic with a vertical symmetry axis due to horizontal fine layering and the presence of overburden. Szabo (1984) suggested that for most coal seams the ratio between horizontal and vertical velocities is approximately 1.16, which gives about 14% of shear-wave anisotropy [say the horizontal shear-wave velocity is 1000 m/s for coal seams, $(V_{max}-V_{min})/V_{max}$ x 100% = (1000-1000/1.16)/1000 =13.8%]. We now use the phase recursion method described above to show the effects of TI on Love-type channel-wave dispersion.

Figure B.2 shows an example of Love-type channel wave dispersion curves of the fundamental (F), the first (1) and the second (2) higher modes for an isotropic reference coal-seam model (Model 2 in Table 6.1 of Chapter 6). The cut-off frequency of the fundamental mode is zero as the model is symmetrical. The cut-off frequencies of the first and second higher modes approach about 320 and 600 Hz, respectively. Note that there are also minima in the group velocity dispersion curves, which correspond to the Airy phases.

Figures B.3, B.4 and B.5 show Love-type channel wave dispersion curves of the fundamental modes calculated for three different horizontal to vertical shear-wave velocity ratio (V_H/V_V = 1.2, 1.15, and 1.0). Figure B.3 is for the isotropic rocks and the TI coal, Figure B.4 is for the isotropic coal and TI rocks, and Figure B.5 is for both TI coal and rocks. It is clear that transverse isotropy in both coal seam and country rocks has effects on the Love channel

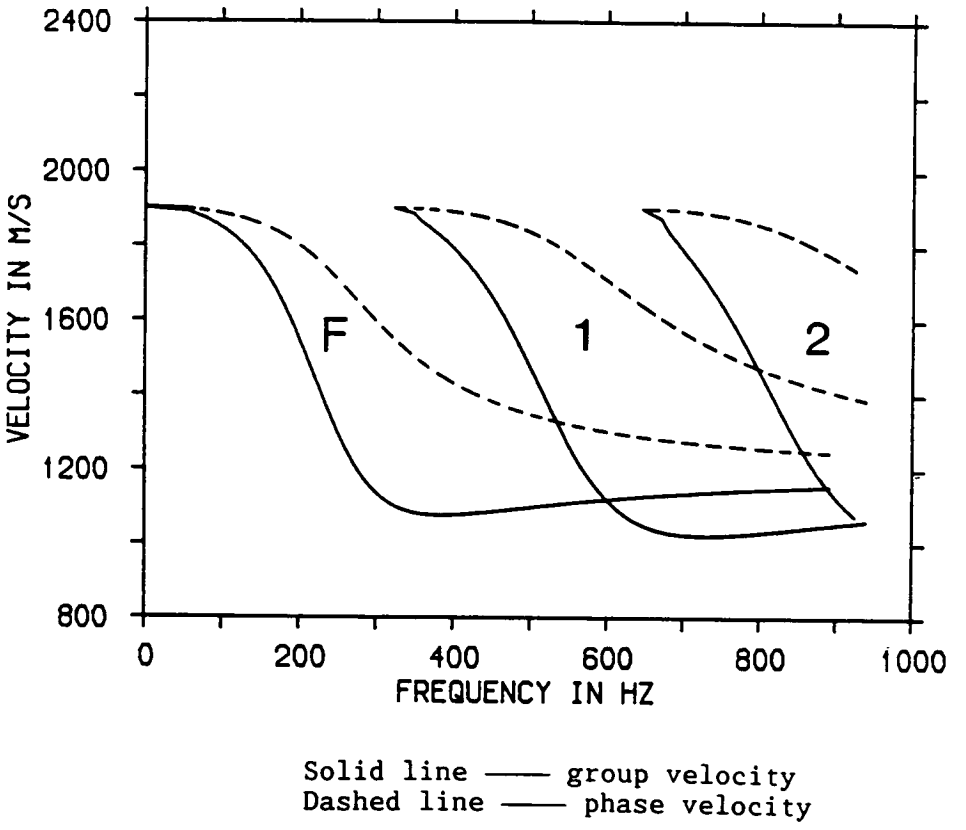

Figure B.2 Love-type channel wave dispersion curves of the fundamental (F), the first (1) and the second (2) higher modes for an isotropic reference coal-seam model (Model 2 in Table 6.1 of Chapter 6).

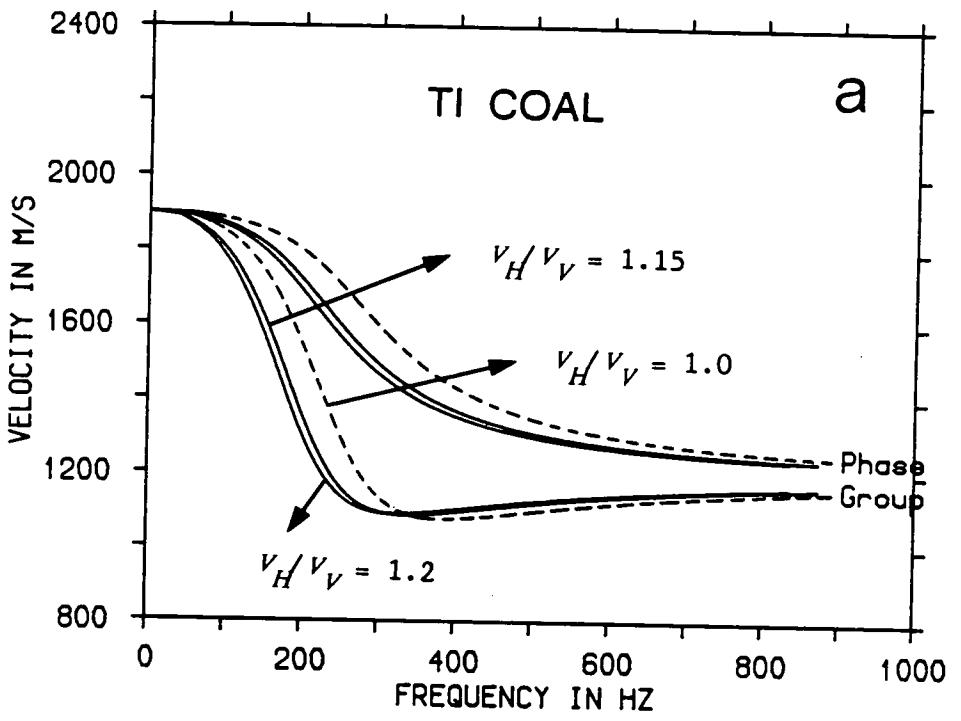

Figure B.3 Comparison of dispersion curves of the fundamental modes calculated for three different horizontal to vertical shear-wave velocity ratios in the coal-seam (a model with transversely isotropic coal seam and isotropic rocks). The dashed line is for the isotropic reference model.

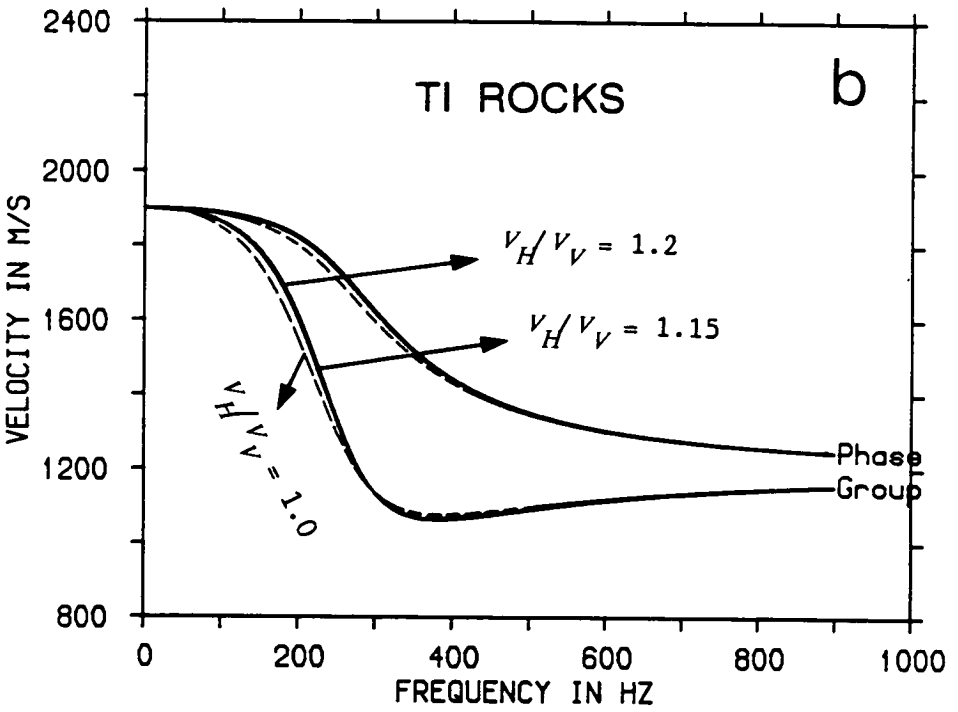

Figure B.4 The notation is the same as in Figure B.3, but for the isotropic coal seam and the transversely isotropic rocks. The dashed line is for the isotropic reference model.

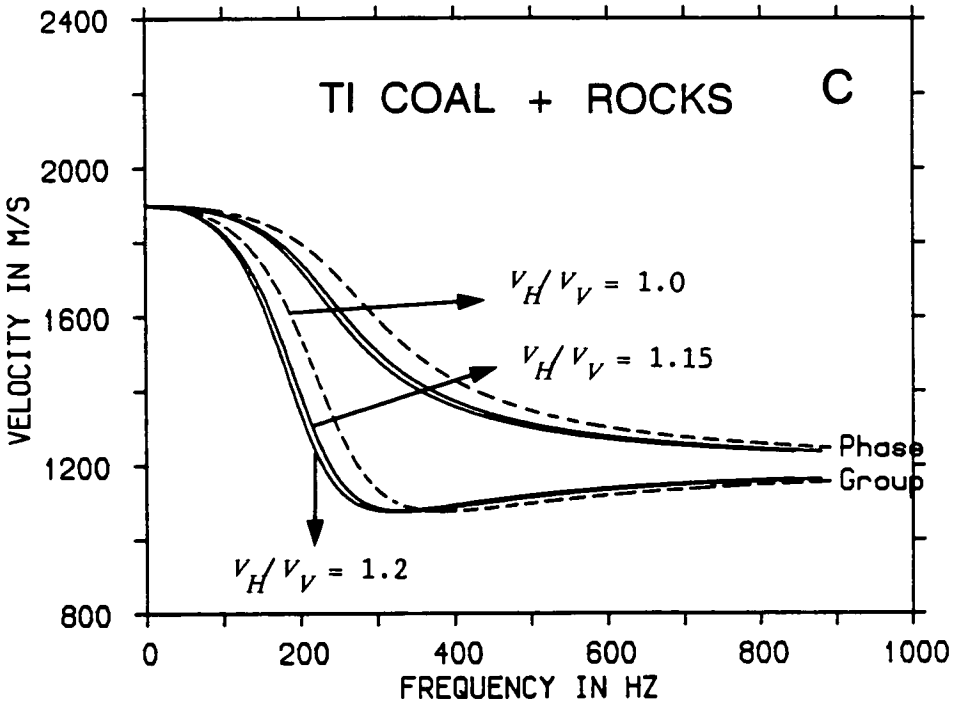

Figure B.5 The notation is the same as in Figure B.3, but both the coal seam and the country rocks are transversely isotropic. The dashed line is for the isotropic reference model.

wave dispersion, but the effects are more significant if anisotropy exists in the coal seam (Figure B.3) or in both coal seam and the country rocks (B.5). Nevertheless, from this simple model we may conclude that anisotropy (both TI and more general anisotropy such as crack-induced) both in coal seams and country rocks should be considered in the modelling although TI in the rocks has less effect than TI in the coal seam.

It is expected that more general anisotropy (such as crack-induced anisotropy or its combination with TI, which results in an orthorhombic symmetry) should have rather different effects on the Love-type channel wave dispersion, such as the azimuthal variation of dispersion curves which we observed in Chapter 6. The effects would be similar to the seismic surface waves which have been investigated previously by Crampin and Taylor (1971), Crampin and King (1977) and Kirkwood and Crampin (1981a, b). Note that Crampin's method (1970) can be used to calculate the channel wave dispersion in multilayered media. This is currently under modification (Crampin and Lou, personal communications).

B.4 Inversion of Love wave dispersion

It is possible to invert Love wave dispersion in TI media. The group velocity dispersion data can be extracted using the multiple filter technique of Dziewonski *et al.* (1969). We denote $\mathbf{V}^{obs} = (V_1^{obs}, V_2^{obs}, \ldots V_N^{obs})^T$ the observed group velocity corresponding to frequency $\mathbf{F} = (F_1, F_2, \ldots F_N)^T$ and $\mathbf{V}^{est} = (V_1^{est}, V_2^{est}, \ldots V_N^{est})^T$ the estimated group velocity. For a transversely isotropic medium, we have four parameters defining a layer if we only invert Love waves.

These are horizontal and vertical velocities (or elastic constants c_{2323} and c_{1212}), density and thickness (for top and bottom halfspace, there are only three parameters since thicknesses disappear). For a defined structure, we can use the phase recursion method to calculate the Love wave dispersion, and then compute the least square error between estimated and observed by

$$err = \{\sum_i [(V_i^{est} - V_i^{obs})/N]^2\}^{1/2}, \qquad \text{(B-21)}$$

where err is the prediction error between observed and estimated for a given structure. We start with initial values of a simple model determined by trial and error procedure, we perturb the model parameter one after another and use the phase recursion method to obtain the new dispersion V_i^{est}, corresponding to the perturbed model, until the given error value is satisfied [this is similar to the general inversion technique described by Aki and Richards (1980)].

APPENDIX C

INTERFACE WAVES ALONG A FRACTURE: IMPLICATIONS FOR HYDRAULIC FRACTURING EVENTS

C.1 Fracture models

Physically, a natural fracture is a very narrow, fluid-filled planar structure with an opening of the order of millimetres to tens of millimetres and a length and height which are of the order of metres to tens of metres or more. There are two fracture models which have been suggested to model a natural large fracture. One is proposed by Schoenberg (1980) and another by Fehler (1982). Schoenberg's fracture is modelled by representing the fracture as a boundary between two elastic half spaces subjected to the following boundary conditions: continuous stress, but discontinous displacements (Schoenberg 1980; Pyrak-Nolt and Cook 1987). Fehler's fracture is considered as a very thin layer (1mm to 3mm) which is fluid-filled. The fluid layer is described by viscosity, bulk modulus and fluid density (Fehler 1982).

C.2 Elastic waves along the Schoenberg's fracture

Pyrak-Nolt and Cook (1987) found two interface waves which may propagate along the Schoenberg's fracture. The two waves are not Stoneley waves since the Stoneley wave doesn't exist if the material properties of the half-spaces on either side of the fracture are the same. The two waves are considered as to be the coupled Rayleigh waves. In the limit of low stiffness or high frequency, the

fracture behaves as two free surfaces each of which supports a Rayleigh wave. As stiffness is increased, the coupling increases between the two Rayleigh waves, resulting two new waves which display different combinations of the original Rayleigh wave particle motions.

C.3 Elastic waves along the Fehler's fracture

Fehler's fracture model seems more realistic since the conditions for Schoenberg's model are hardly satisfied in the real earth. Along Fehler's fracture, there will also be possible for an interface wave to propagate. Ferrazzini and Aki (1987) developed a theory for such an interface along a liquid-filled fracture boundary. This wave is similar to a tube wave along a liquid-filled borehole, but different in that as the wavelength increases to infinity, both the phase and group velocities approach zero. This wave has been observed in laboratory experiments (Tang and Chen 1988). The dispersion relation of this wave is given theoretically (see also Ferrazzini and Aki 1987; Tang and Chen 1988; Paillet and White 1982).

C.4 Implications

The above theories have suggested that there possibly exist interface waves (two from Schoenburg's model and one for Fehler's model) along either Schoenberg's or Fehler's fracture. However, this requires to be further confirmed in field observations. The synthetic seismograms in Chapter 7 show complicated characteristics, some may be due to the interface waves along the large fractures

(Fehler's fracture in our case). If interface waves do exist, it may have an important implication. It may play an important role in the long-period events observed in geothermal areas and may explain their signal duration and low frequency (Ferrazzini and Aki 1987).

REFERENCES

Aki, K., Fehler, M., Aamodt, R.L., Albright, J.N., Potter, R.M., Pearson, V.M. & Tester, J.W., 1982, Interpretation of seismic data from hydraulic fracturing experiments at the Fenton Hill, New Mexico hot dry rock geothermal site *J.Geophys.Res.*, **87**, 936-944.

Aki, K. & Richards, P.G., 1980, *Quantitative Seismology, Theory and Method*, Freeman, San Francisco.

Alford, R.M., 1986, Shear data in the presence of azimuthal anisotropy: Dilley, Texas, *56th Ann.Internat.Mtg., Soc.Explor. Geophys., Expanded abstracts*, 476-479.

Anderson, D.L., 1961, Elastic wave propagation in layered anisotropic medium, *J.Geophys.Res.*, **66**, 2953-2963.

Anderson, D.L., 1962, Love wave dispersion in heterogeneous anisotropic media, *Geophysics*, **27**, 445-454.

Anderson, D.L., Minster, B. & Cole, D., 1974, The effects of oriented cracks on seismic velocities, *J.Geophys.Res.*, **79**, 4011-4015.

Atkinson, B.K., 1982, Subcritical crack propagation in rocks: theory, experimental results and applications, *J.Struct.Geol.*, **4**, 41-56.

Atkinson, B.K., 1984, Subcritical crack growth in geological materials, *J.Geophys.Res.*, **89**, 4077-4114.

Ave'Lallemant, H.G. & Carter, N.L., 1970, Syntectonic recrystallization of olivine and modes of flow in the upper mantle, *Bull.Geol.Soc.Am.*, **81**, 2203-2220.

Babuska, V., 1984, *P*-wave velocity anisotropy in crystalline rocks, *Geophys.J.R.astr.Soc.*, **76**, 113-119.

Backus, G.E., 1962, Long-wave elastic anisotropy produced by horizontal laying, *J.Geophys.Res.*, **67**, 4427-4440.

Bamford, D. & Crampin, S., 1977, Seismic anisotropy - the state of the art, *Geophys.J.R.astr.Soc.*, **49**, 1-8.

Bamford, D., Jentsch, M. & Prodehl, C., 1979, P_n anisotropy studies in the northern Britain and the eastern and western United States, *Geophys.J.R.astr.Soc.*, **57**, 397-429.

Banik, N.C., 1984, Velocity anisotropy of shales and depth estimation in the North Sea Basin, *Geophysics*, **49**, 1411-1419.

Becker, D.F. & Perelberg, A.I., 1986, Seismic detection of subsurface fracture, *56th Ann.Internat.Mtg., Soc.Explor.Geophys., Expanded abstracts*, 466-468.

Benhama, A., Cliet, C., Dubesset, M., 1988, Study and applications of spatial directional filtering in three-component recording, *Geophysical Prospecting*, **36**, 591-613.

Berryman, J.G., 1979, Long-wave elastic anisotropy in transversely isotropic media, *Geophysics*, **44**, 896-917.

Bodoky, A. & Bodoky, T., 1983, Preliminary results of numerical modelling of "seam wave", *Geophysical Prospecting*, **29**, 129-140.

Bois, P., Laporte, M., Lavergne, M. & Thomas, G., 1972, Well-to-well seismic measurements, *Geophysics*, **37**, 471-480.

Booth, D.C., 1982, *The anisotropic reflectivity technique*, PhD Thesis, University of Edinburgh.

Booth, D.C. & Crampin, S., 1983a, The anisotropic reflectivity technique: theory, *Geophys.J.R.astr.Soc.*, **72**, 755-766.

Booth, D.C. & Crampin, S., 1983b, The anisotropic reflectivity technique: anomalous reflected arrivals from an anisotropic upper mantle, *Geophys.J.R.astr.Soc.*, **72**, 767-782.

Booth, D.C. & Crampin, S., 1985, Shear-wave polarizations on a curved wavefront at an isotropic free surface, *Geophys.J.R. astr.Soc.*, **83**, 31-45.

Booth, D.C., Crampin, S., Evan, R. & Roberts, G., 1985, Shear-wave polarizations near the North Anatolian Fault - I: Evidence for anisotropy-induced shear-wave splitting, *Geophys.J.R.astr.Soc.*, **83**, 61-73.

Booth, D.C., Crampin, S., Lovell, J.H. & Chiu, J.-M., 1989, Temporal changes in shear-wave splitting during an earthquake swarm in Arkansas, *J.Geophys.Res.*, submitted.

Breitzke, M., Dresen, L., Csokas, J., Gyulai, A. & Ormos, T., 1987, Parameter estimation and fault detection by three-component seismic and geoelectrical surveys in a coal mine, *Geophysical Prospecting*, **35**, 832-863.

Brekhovskikh, L.M., 1960, *Waves in layered media*, Academic Press, New York.

Buchanan, D.J., 1978, The propagation of attenuated *SH* channel waves, *Geophysical Prospecting*, **26**, 17-28.

Buchanan, D.J., Davis, R., Jackson, P.J. & Taylor, P.M., 1981, Fault location by channel wave seismology in the United Kingdom coal seams, *Geophysics*, **7**, 994-1002.

Buchanan, D.J., Jackson, P.J. & Davis, R., 1983, Attenuation and anisotropy of channal waves, *Geophysics*, **48**, 133-147.

Budiansky, B. & O'Connell, R.J., 1976, Elastic moduli of a cracked solid, *Int.J.Solids Structures*, **12**, 81-97.

Bullen, K.E. & Bolt, B.A., 1985, *An introduction to the theory of seismology*, Cambridge Univ.Press.

Burton, P.W., 1974, Estimations of Q^{-1} from seismic Rayleigh waves, *Geophys.J.R.astr.Soc.*, **36**, 167-189.

Burton, P.W. & Blamey, C., 1972, A computer program to detect the spectrum and dispersion characteristic of a transient seismic signal, *UKAEA AWRE REPORT* No.0/48/72 (HMSO).

Bush, I., 1989, *Modelling shear-wave anisotropy in the Paris Basin*, PhD thesis, University of Edinburgh.

Bush, I. & Crampin, S., 1987, Observation of EDA and PTL anisotropy in shear-wave VSP's, *57th Ann.Internat.Mtg., Soc.Explor.Geophys., Expanded Abstract*, 476-479.

Çerveny, V., 1979, Accuracy of ray theoretical seismograms, *J.Geophys.*, **46**, 135-149.

Çerveny, V. & Ravindra, R., 1971, *Theory of seismic headwaves*, University of Toronto Press.

Chapman, C.H. & Shearer, P.M., 1989, Ray tracing in azimuthally anisotropic media - II: Quasi-shear wave coupling, *Geophys.J.*, **96**, 65-83.

Chacko, S., 1989, Porosity identification using amplitude variations with offset: Examples from South Sumatra, *Geophysics*, **54**, 942-951.

Chatterjee, A.K., Mal, A.K., Knopoff, L. & Hudson, J.A., 1980, Attenuation of elastic waves in a cracked, fluid-saturated solid, *Math.Proc.Camb.Phil.Soc.*, **88**, 547-561.

Chen, T.-C., Booth, D.C. & Crampin, S., 1987, Shear-wave polarizations near the North Anatolian Fault - III: Observations of temporal changes, *Geophys.J.R.astr.Soc.*, **91**, 287-311.

Christensen, N.I. & Salisbury, M.H., 1979, Seismic anisotropy in the oceanic upper mantle: evidence from the Bay of Islands ophiolite complex, *J.Geophys.Res.*, **84**, 4601-4610.

Cormier, V.F., 1984, The polarization of *S* waves in a heterogeneous isotropic Earth model, *J.Geophys.*, **56**, 20-23.

Crampin, S., 1970, The dispersion of surface waves in multilayered anisotropic media, *Geophys.J.R.astr.Soc.*, **21**, 387-402.

Crampin, S., 1975, Distinctive particle motion of surface waves as a diagnostic of anisotropic layering, *Geophys.J.R.astr.Soc.*,.**40**, 177-186.

Crampin, S., 1977, A review of the effects of anisotropic layering on the propagation of seismic waves, *Geophys.J.R.astr.Soc.*, **49**, 9-27.

Crampin, S., 1978, Seismic-wave propagation through a cracked solid: polarization as a possible dilatancy diagnostic, *Geophys.J.R. astr.Soc.*, **53**, 467-496.

Crampin, S., 1981, A review of wave motion in anisotropic and cracked elastic-media, *Wave Motion*, **3**, 343-391.

Crampin, S., 1984, Effective anisotropic elastic constants for wave propagation through cracked solids, *Geophys.J.R.astr.Soc.*, **76**, 135-145.

Crampin, S., 1985a, Evidence for aligned cracks in the Earth's crust, *First Break*, **3**, 12-15.

Crampin, S., 1985b, Evaluation of anisotropy by shear-wave splitting, *Geophysics*, **50**, 142-152.

Crampin, S., 1987a, Geological and industrial implications of extensive-dilatancy anisotropy, *Nature*, **328**, 491-496.

Crampin, S., 1987b, Crack porosity and alignment from shear-wave VSPs, in Danbom, S.H. and Domenico, S.N., Eds, *Shear-wave Exploration, Soc.Explor.Geophys.*, 227-251.

Crampin, S., 1987c, The basis for earthquake prediction, *Geophys.J. R.astr.Soc.*, **91**, 331-347.

Crampin, S., 1988, Non-parallel shear-wave polarizations in sedimentary basins, *57th Ann.Internat.Mtg., Soc.Explor.Geophys., Expanded abstract*, 1130-1132.

Crampin, S., 1989, Effects of singularities on shear-wave propagation in sedimentary basin, *J.Geophys.Res.*, submitted.

Crampin, S. & Atkinson, B.K., 1985, Microcracks in the Earth's crust, *First Break*, **3**, 16-20.

Crampin, S. & Booth, D.C., 1985, Shear-wave polarization near-the North Anatolian Fault - II: Interpretation in terms of crack-induced anisotropy, *Geophys.J.R.astr.Soc.*, **83**, 75-92.

Crampin, S. & Booth, D.C., 1989, Shear-wave splitting showing hydraulic dilation of pre-existing joints in granite, *Scientific Drilling*, **1**, 21-26.

Crampin, S., Booth, D.C., Evans, J.R., Peacock, S. & Fletcher, J.B., 1989, Changes in shear-wave splitting at Anza near the time of the North Palm Springs earthquake, *J.Geophys.Res.*, submitted.

Crampin, S., Bush, I., Naville, C. & Taylor, D.B., 1986, Estimating the internal structure of reservoirs with shear-wave VSPs, *The Leading Edge*, **5**, 35-39.

Crampin, S., Chesnokov, E.M. & Hipkin, R.A., 1984a, Seismic anisotropy - the state of the art, II, *Geophys.J.R.astr.Soc.*, **76**, 1-16.

Crampin, S., Evans, J.R. & Atkinson, B.K., 1984b, Earthquake prediction a new physical basis, *Geophys.J.R.astr.Soc.*, **76**, 147-156.

Crampin, S., Evans, J.R., Üçer, S.B., Doyle, M., Davis, J.P., Yegorkina, G.V. & Miller, A., 1980, Observations of dilatancy-induced polarization anomalies and earthquake prediction, *Nature*, **286**, 874-879.

Crampin, S., Evans, J.R. & Üçer, S.B., 1985, Analysis of records of local earthquakes: the Turkish Dilatancy Projects, *Geophys.J.R. astr.Soc.*, **83**, 1-16.

Crampin, S. & King, D.W., 1977, Evidence for anisotropy in the upper mantle beneath Eurasia from the polarization of higher mode seismic surface waves, *Geophys.J.R.astr.Soc.*, **49**, 59-85.

Crampin, S. & Taylor, D.B., 1971, The propagation of surface waves in anisotropic media, *Geophys.J.R.astr.Soc.*, **25**, 71-87.

Crampin, S. & Yedlin, M., 1981, Shear-wave singularities of wave propagation in anisotropic media, *J.Geophys.*, **49**, 43-46.

Crary, A.P., 1954, Seismic studies on Fletcher's ice Island, T-3, *Transactions, AGU*, **35**, 293-300.

Davis, E.E. & Clowes, R.M., 1986, High velocities and seismic anisotropy in Pleistocene turbidetes off the Western Canada, *Geophys.J.R.astr.Soc.*, **84**, 381-399.

Dellinger, J., 1989, Statistical traveltime inversion, *presented at 51st EAEG Ann.Mtg. Berlin, 1989.*

Dieulesain, E. & Royer, D., 1980, *Elastic waves in solids*, in French, by Masson & Cie, Editeurs, Paris, translated by Wiley, New York.

Douma, J., 1988, The effect of the aspect-ratio on crack-induced anisotropy, *Geophysical Prospecting*, **36**, 614-632.

Douma, J. & Helbig, K., 1987, What can the polarization of shear waves tell us?, *First Break*, **5**, 95-104.

Dresen, L. & Freystätter, S., 1976, Rayleigh channel waves for the in-seam seismic detection of discontinuities, *J.Geophys.*, **42**, 111-129.

Duff, G.F.D., 1960, The Cauchy problem for elastic wave propagation in anisotropic media, *Phil.Trans.R.Soc.*, A, **252**, 249-273.

Dziewonski, A., Bloch, S. & Landisman, M., 1969, A technique for the analysis of transient seismic signals, *Bull.Seism.Soc.Am.*, **59**, 427-444.

Edelmann, H.A.K., 1985, Shear-wave energy sources, in *Seismic shear waves, Part B: applications*, edt by Gerhard Dohr, Geophysical Press, London, **15B**, 134-141.

Eshelby, J.D., 1957, The determination of the elastic wavefield of an ellipsoid inclusion, *Proc.R.Soc., London*, A, **241**, 376-396.

Evans, J.R., 1984, Effects of the free surface on shear waves, *Geophys.J.R.astr.Soc.*, **76**, 165-172.

Ewing, W.M., Jardetzky, W.S. & Press, F., 1957, *Elastic waves in layered media*, McGraw-Hill Book Co., New York.

Fehler, M., 1981, Changes in *P* wave velocity during operation of a hot dry rock geothermal system, *J.Geophys.Res.*, **86**, 2925-2928.

Fehler, M., 1982, Interaction of seismic waves with a viscous liquid layer, *Bull.Seism.Soc.Am.*, **72**, 55-72.

Fehler, M. & Pearson, C., 1984, Cross-hole seismic surveys: application for studying subsurface fracture systems at a hot dry rock geothermal site, *Geophysics*, **49**, 37-45.

Ferrazzini, V. Aki, K., 1987, Slow waves trapped in a fluid-filled infinite cracks: implication for vocanic tremor, *J.Geophys.Res.*, **92**, 9215-9223.

Francis, T.J.G., 1969, Generation of seismic anisotropy in the upper mantle along the mid-ocean ridges, *Nature*, **221**, 162-165.

Franssens, G.R., Lagasse, P.E. & Mason, I.M., 1985, Study of the leaking channel modes of in-seam exploration seismology by means of synthetic seismograms, *Geophysics*, **50**, 414-424.

Freystätter, S. & Dresen, L., 1978, The influence of obliquely dipping discontinuities on the use of Rayleigh channel waves for the in-seam seismic reflection method, *Geophysical Prospecting*, **26**, 1-15.

Fuchs, K., 1983, Recently formed elastic anisotropy and petrological models for the continental subcrustal lithosphere in southern Germany, *Phys.Earth Planet.Int.*, **31**, 93-118.

Futterman, W.I., 1962, Dispersive body waves, *J.Geophys.Res.*, **67**, 5279-5291,

Fyfe, W.S., Price, N.J. & Thompson, A.B., 1978, Fluids in the Earth's crust, *in Developments in geochemistry, 1*, Elsevier, Amsterdam.

Garbin, H.D. & Knopoff, L., 1973, The compressional modulus of a material permeated by a random distribution of circular cracks, *Quart.App.Math.*, **3**, 453-464.

Garbin, H.D. & Knopoff, L., 1975a, The shear modulus of a material permeated by a random distribution of circular cracks, *Quart.App.Math.*, **33**, 269-300.

Garbin, H.D. & Knopoff, L., 1975b, Elastic moduli of a medium with liquid-filled cracks, *Quart.App.Math.*, **33**, 301-303.

Greenhalgh, S.A., Burns, D. & Mason, I., 1986, A cross-hole and face-to-borehole in-seam seismic experiment at the Invincible Colliery, Australia, *Geophysical Prospecting*, **34**, 30-55.

Gu,H.D. & Cao, T.Q., 1980, Precursory earthquake swarm and the polarization of S-waves (in Chinese), *Acta Seis.Sinica*, **2**, 243-355.

Gupta, I.N. & Blandford, R.R., 1983, A mechanism for generation of short-period transverse motion from explosions, *Bull.Seism.Soc. Am.*, **73**, 571-579.

Heelan, P.A., 1953, Radiation from a cylindrical source of finite length, *Geophsysics*, **18**, 686-896.

Helbig, K., 1958, Elastische wellen in anisotropen medien, *Beitr. Geophys.*, **67**, 177-211.

Helbig, K., 1984, Anisotropy and dispersion in periodically layered media, *Geophysics*, **49**, 364-373.

Hensel, W.M., 1987, A perspective look at fracture porosity, *presented at 1987 Ann.Tech.Conf. Soc.Petr.Eng., Dallas*, 571-578.

Hess, H., 1964, Seismic anisotropy of the uppermost mantle under oceans, *Nature*, **203**, 629-631.

House, L., 1987, Locating microearthquakes induced by hydraulic fracturing in crystalline rock, *Geophys.Res.Lett.*, **14**, 919-921.

Hubbert, M.K. Willis, D.G., 1957, Mechanics of hydraulic fracturing, *Trans.AIME*, **210**, 153-170.

Hudson, J.A., 1980a, *The excitation and propagation of elastic waves*, Cambridge University Press.

Hudson, J.A., 1980b, Overall properties of a cracked solid, *Math. Proc.Camb.Phil.Soc.*, **88**, 371-384.

Hudson, J.A., 1981, Wave speeds and attenuation of elastic waves in material containing cracks, *Geophys.J.R.astr.Soc.*, **64**, 133-150.

Hudson, J.A., 1986, A higher order approximation to the wave propagation constants for a cracked solid, *Geophys.J.R.astr.Soc.*, **87**, 265-274.

Hudson, J.A., 1988, Seismic wave propagation through material containing partially saturated cracks, *Geophys.J.*, **92**, 33-37.

Hyndman, P.D. & Shearer, P.M., 1989, Water in the lower continental crust: Modelling magnetotelluric and seismic reflection results, *Geophys.J.Int.*, **98**, 343-365.

Igel, H., 1989, *Analyzing shear-wave splitting*, Diplomarbeit, Geophysikalisches Insitut der Universität Karlsruhe.

Igel, H. & Crampin, S., 1989, Extracting shear-wave polarizations from different source orientations: Synthetic modelling, *J.Geophys.Res.*, submitted.

Ingram, R.E., 1952, Vibration angles of *S* waves, *Bull.Seism.Soc.Am.*, **42**, 145-151.

Jackson, P.J., 1985, Horizontal seismics in coal seams: its use by the UK coal industry, *First Break*, 3 (11), 15-24.

Jackson, P.J., 1989, Measuring seismic wave polarizations, *abstract presented at 51st EAEG Meeting, Berlin, 1989.*

Jackson, P.J., Onions, K.R. & Westerman, A.R., 1989, Use of inverted VSP to enhance the exploration value of boreholes, *First Break*, 7 (6), 233-246.

Johnson, D.H., Toksöz, M.N. & Timur, A., 1979, Attenuation of seismic waves in dry and saturated cracks: II, Mechanism, *Geophysics*, **44**, 491-511.

Johnson, T.C., Hamilton, E.C. & Berger, W.H., 1977, Physical properties of calcareous sediments: control by dissolution at depth, *Marine Geology*, **24**, 259-277.

Johnston, D.H., 1986, VSP detection of fracture-induced velocity anisotropy, *56th Ann.Internat.Mtg., Soc.Explor.Geophys., Expanded abstracts*, 464-466.

Kaarsberg, E.A., 1960, Elasticity studies of isotropic and anisotropic rock samples, *Trans.Soc.Min.Engrs.*, **241**, 470-475.

Kanasewich, E.R., 1981, *Time sequence analysis in geophysics*, The University of Alberta Press.

Kaneshima, S., Ando, M. & Crampin, S., 1987, Shear-wave splitting above small earthquakes in the Kinki district of Japan, *Phys. Earth & Planet Int.*, **45**, 45-58.

Kaneshima, S., Ito, H. & Sugihara, M., 1988, Shear-wave splitting observed above small earthquakes in a geothermal area of Japan, *Geophys.J.*, **94**, 399-411.

Kaneshima, S., Ito, H. & Sugihara, M., 1989, Shear-wave polarization anisotropy observed in a rift zone in Japan, *Tectonophysics*, **157**, 281-300.

Keith, C.M. & Crampin, S., 1977a, Seismic body waves in anisotropic media: reflection and refraction at a plane interface, *Geophys. J.R.astr.Soc.*, **49**, 181-203.

Keith, C.M. & Crampin, S., 1977b, Seismic body waves in anisotropic media: propagation through a layer, *Geophys.J.R.astr.Soc.*, **49**, 209-223.

Keith, C.M. & Crampin, S., 1977c, Seismic body waves in anisotropic media: synthetic seismograms, *Geophys.J.R.astr.Soc.*, **49**, 225-243.

Kennett, B.N.K., 1983, *Seismic wave propagation in stratified media*, Cambridge University Press.

Kerner, C. & Dresen, L., 1985, The influence of dirt bands and faults on the propagation of Love seam waves, *J.Geophys.*, **57**, 77-89.

Keys, R.G., 1989, Polarity reversals in reflections from layered media, *Geophysics*, **54**, 900-905.

Kirkwood, S.C. & Crampin, S., 1981a, Surface-wave propagation in an ocean basin with an anisotropic upper mantle: observations of polarization anomalies, *Geophys.J.R.astr.Soc.*, **64**, 487-497.

Kirkwood, S.C. & Crampin, S., 1981b, Surface-wave propagation in an ocean basin with an anisotropic upper mantle: numerical modelling, *Geophys.J.R.astr.Soc.*, **64**, 463-485.

Korn, M. & Stöckl, H., 1982, Reflection and transmission of Love channel waves at coal seam discontinuities computed with a finite difference method, *J.Geophys.*, **50**, 171-176.

Krajewski, P., Dresen, L., Schott, W. & Rüter, H., 1987, Studies of roadway modes in a coal seam by dispersion and polarization analysis: a case history, *Geophysical Prospecting*, **35**, 767-786.

Kraut, E.A., 1963, Recent advances in the theory of anisotropic elastic wave propagation, *Rev.Geophys.*, **1**, 401-448.

Krey, Th., 1963, Channel waves as a tool of applied geophysics in coal mining, *Geophysics*, **38**, 701-715.

Krey, Th., Arnetzl, H. & Knecht, M., 1982, Theoretical and practical aspects of absorption in the application of in-seam seismic coal exploration, *Geophysics*, **47**, 1645-1656.

Lagasse, P.E. & Mason, I.M., 1975, Guided modes in coal seams and their application to underground seismic surveying, *Proc.IEEE Ultrasonic Symp., Los Angeles*, 64-67.

Leary, P. & Li Y.-G., 1986, VSP fracture study of Mojave desert hydeofracture borehole, *EOS*, **67**, 1116 (abstract).

Leary, P., Li, Y.-G. Aki, K., 1987, Observation and modelling of fault zone fracture seismic anisotropy: I, *P*, *SV* and *SH* travel times, *Geophys.J.R.astr.Soc.*, **91**, 461-485.

Lee, M.W., 1987, Particle displacements on the wall of a borehole from incident plane waves, *Geophysics*, **52**, 1290-1296.

Levin, F.K., 1978, The reflection, refraction, and diffraction of waves in media with an elliptical velocity dependence, *Geophysics*, **43**, 528-537.

Levin, F.K., 1979, Seismic velocity in transversely isotropic media *Geophysics*, **44**, 918-936.

Levin, F.K., 1986, When reflection coefficients are zero, *Geophysics*, **51**, 736-741.

Li, X.-Y. & Crampin, S., 1989, Analyzing shear-wave splitting in three-component surface reflection surveys, *abstract presented at*

SEG Research Workshop on Recording and Processing Vector Wavefield Data, Snowbird, Utah 1989.

Li, Y.-G., Leary, P.C. & Aki, K., 1986, Seismic ray tracing for VSP observations in homogeneous fractured rock at Oroville, *EOS*, **67**, 117 (abstract).

Li, Y.-G., Leary, P.C. & Henyey, T.L., 1988, Stress orientation inferred from shear wave splitting in basement rock at Cajon Pass, *Geophys.Res.Lett.*, **15**, 997-1000.

Lighthill, M.J., 1960, Anisotropic wave motions, *Phil.Trans.R.Soc. Lond.*, **252**, 397-470.

Liu, E. & Crampin, S., 1989, Effects of an internal interface on shear-wave polarizations: comparison with anisotropy-induced splitting, *J.Geophys.Res.*, in press.

Liu, E., Crampin, S. & Booth, D.C., 1989, Shear-wave splitting in cross-hole surveys: Modelling, *Geophysics*, **54**, 57-65.

Liu, E., Crampin, S. & Roth, B., 1989a, Detection of anisotropy by in-seam seismic channel waves, *presented at 51st EAEG Meeting Berlin*, 1989.

Liu, E., Crampin, S. & Roth, B., 1989b, Anisotropic modelling of in-seam seismic channel waves, *Geophysical Prospecting*, in preparation.

Liu, E., Crampin, S. & Yardley, G., 1989, The polarization of reflected shear-waves, *Nature*, submitted.

Love, A.E.H., 1944, *A treatise on the mathematical theory of elasticity*, 4th ed. Dover, New York.

Lovell, J.H., Crampin, S. & Shepherd, T., 1989, Stress in the Earth's crust: the link between geochemistry and EDA, *J.Geol. Soc.*, submitted.

Lynn, H.B. & Thomsen, L.A., 1986, Reflection shear-wave data along the principal axes of azimuthal anisotropy, *56th Ann.Internat. Mtg., Soc.Explor.Geophys., Expanded abstracts*, 473-476.

MacBeth, C. & Crampin, S., 1989a, Automatic technique for measuring the effects of anisotropy, *Geophysical Prospecting*, submitted.

MacBeth, C. & Crampin, S., 1989b, Spectral method for measuring the effects of anisotropy, *Geophys.J.Int.*, submitted.

MacBeth, C. & Crampin, S., 1989c, Automatic processing of seismic data in the presence of anisotropy, *Geophysics*, submitted.

Mahrer, K.D. Mauk, F.J., 1987, Seismic wave motion for a new model of hydraulic fracture with an induced low-velocity zone, *J.Geophys.Res.*, **92**, 9293-9309.

Majer, E.L., McEvilly, T.V., Eastwood, F.S. Myer, L.R., 1988,

Fracture detection using *P*-wave and *S*-wave vertical seismic profiling at The Geysers, *Geophysics*, **53**, 76-84.

Mason, I.M., Buahanan, D.J. & Booer, A.K., 1980, Channel wave mapping of coal seams in the United Kingdom, *Geophysics*, **45**, 1131-1143.

Mason, I.M., Greenhalgh, S.A. & Hatherly, P., 1985, A channel wave transmission study in the Newcastle coal measures, Australia, *Geoexploration*, **23**, 395-413.

Mavko, G.M. & Nur, A., 1979, Wave attenuation in partially saturated rocks, *Geophysics*, **44**, 161-178.

Meadows, M. & Coen, S., 1986, Exact inversion of plane-layered isotropic and anisotropic elastic media by the state-space approach, *Geophysics*, **51**, 2031-2050.

McCann, D.M., Baria, R., Jackson, P.D. & Green, A.S.P., 1986, Application of cross-hole seismic measurements in site investigation surveys, *Geophysics*, **51**, 914-929.

McCann, D.M., Grainger, P. & McCann, C., 1975, Inter-borehole acoustic measurements and their use in engineering geology, *Geophysical Prospecting*, **23**, 50-69.

Musgrave, M.J.P., 1954, The propagation of elastic waves in crystal and other anisotropic media, *Proc.R.Soc., London*, A, **226**, 339-355.

Narr, W. & Burruss, R.C., 1984, Origin of reservoir fracture in Little Knife Field, North Dakota, *Am.Ass.Petro.Geosts.Bull.*, **68**, 1087-1099.

Nishizawa, O., 1982, Seismic velocity anisotropy in a medium containing oriented cracks-transversely isotropic case, *J.Phys.Earth*, **30**, 331-347.

Nicoletis, L., Client, C. & Leveuvre, F., 1988, Shear-wave splitting measurements from multi-shot VSP data, *58th Ann.Internat.Mtg., Soc.Explor.Geophys., Expanded abstract.*

Nonweiler, T.R.F., 1984, *Computational mathematics: a introduction to numerical approximation*, Ellis Horwood, London.

Nur, A., 1989, Four-dimensional seismology and (true) direct detection of hydrocarbons: the petrophysical basis, *The Leading Edge*, **8** (9), 30-36.

Nur, A. & Simmons, G., 1969, Stress-induced velocity anisotropy in rock: an experimental study, *J.Geophys.Res.*, **74**, 6667-6674.

Nuttli, O., 1961, The effect of the Earth's surface on the *S*-wave particle motion, *Bull.Seism.Soc.Am.*, **51**, 237-246.

Nuttli, O., 1964, The determination of *S*-wave polarization angles for an Earth model with crustal layering, *Bull.Seism.Soc.Am.*, **54**, 1429-1440.

Nuttli, O. & Whitmore, J.D., 1962, On the determination of the polarization of the *S* wave, *Bull.Seism.Soc.Am.*, **52**, 95-107.

O'Connell, R.J. & Budiansky, B., 1974, Seismic velocities in dry and saturated cracked solids, *J.Geophys.Res.*, **79**, 5412-5426.

O'Connell, R.J. & Budiansky, B., 1977, Viscoelastic properties of fluid-saturated crack solids, *J.Geophys.Res.*, **82**, 5719-5735.

Ostrander, W.J., 1984, Plane-wave reflection coefficients for gas sands at nonnormal angles of incidence, *Geophysics*, **49**, 1637-1648.

Paillet, F.L. &White, J.E., 1982, Acoustic modes of propagation in the borehole and their relationship to rock properties, *Geophysics*, **47**, 1215-1228.

Panza, G.F., Schwab, F.A. & Knopoff, L., 1972, Channel and crustal Rayleigh waves, *Geophys.J.R.astr.Soc.*, **30**, 273-280.

Paulsson, B.N.P. & King, M.S., 1980, Between-hole acoustic surveying and monitoring of a granite rock mass, *Int.J.Rock Mech.Min.Sci. & Geomech.Abstr.*, **17**, 371-376.

Peacock, S., 1986, *Shear-wave splitting in the Earth's crust*, PhD thesis, University of Edinburgh.

Peacock, S., 1988, Laboratory and computer models of cracked media, *Geophys.J.*, **92**, 532.

Peacock, S. & Crampin, S., 1985, Shear-wave vibrator signals in transversely isotropic shale, *Geophysics*, **50**, 1285-1293.

Peacock, S., Crampin, S., Booth, D.C. & Fletcher, J.B., 1988, Shear-wave splitting in the Anza seismic gap, southern California: temporal variations as possible precursors, *J.Geophys.Res.*, **93**, 3339-3356.

Peselnick, L. & Nicolas, A., 1978, Seismic anisotropy in an ophilite peridotite: application to oceanic upper mantle, *J.Geophys.Res.*, **83**, 1227-1235.

Postma, G.W., 1955, Wave propagation in a stratified medium, *Geophysics*, **20**, 780-806.

Puzyrev, N.N., Obolentseva, I.R., Trigubov, A.V. & Gorshkalev, S.B., 1984, On the anisotropy of sedimentary rocks from shear-wave analysis, *Geophys.J.R.astr.Soc.*, **76**, 243-252.

Pyrak-Nolte, L.J. & Cook, G.W., 1987, Elastic interface waves along a fracture, *Geophys.Res.Lett.*, **14**, 1107-1110.

Räder, D., Schott, W., Dresen, L. & Rüter, H., 1985, Calculation of dispersion curves and amplitude-depth distributions of Love channel waves in horizontally-layered media, *Geophysical Prospecting*, **33**, 800-816.

Rendleman, C.A. & Levin, F.K., 1988, Reflection maxima for reflections from single interfaces, *Geophysics*, **53**, 271-275.

Roberson, J.D. & Corrigan, D., 1983, Radiation patterns of a shear-wave vibrator in near-surface shale, *Geophysics*, **48**, 19-26.

Roberts, G. & Crampin, S., 1986, Shear-wave polarization in a Hot Dry Rock geothermal reservoir: anisotropic effects of fractures, *Int.J.Rock Mech.Min.Sci. & Geomech.Abstr.*, **23**, 291-302.

Rodgers, P.W., 1968, The response of the horizontal pendulum seismometer to Rayleigh and Love waves, tilt and free osillations of the Earth, *Bull.Seism.Soc.Am.*, **58**, 1384-1406.

Sayers, C.M., 1989, Seismic anisotropy of the inner core, *Geophys. Res.Lett.*, **16**, 267-270.

Schoenberg, M., 1980, Elastic wave behavior across linear slip interface, *J.Acoust.Soc.Am.*, **68**, 1516-1521.

Schoenberg, M., 1983, Reflection of elastic waves from periodical stratified media with interfacial slip, *Geophysical Prospecting*, **31**, 265-292.

Schoenberg, M., 1986, Fluid and solid motion in the neighborhood of a fluid-filled borehole due to the passage of a low-frequency elastic plane wave, *Geophysics*, **51**, 1191-1205.

Schoenberg, M. & Douma, J., 1988, Elastic wave propagation in media with parallel fractures and aligned cracks, *Geophysical Prospecting*, **36**, 571-590.

Schoenberg, M. & Muir, F., 1989, A calculus for finely lauered anisotropic media, *Geophysics*, **54**, 581-589.

Shearer, P.M. & Chapman, C.H., 1989, Ray tracing in azimuthally anisotropic media - I: Results for models of aligned cracks in the upper crust, *Geophys.J.*, **96**, 51-64.

Shearer, P.M., Toy, K.M. & Orcutt, J.A., 1988, Axi-symmetric Earth models and inner-core anisotropy, *Nature*, **333**, 228-232.

Shih, X.R., Meyer, R.P. & Schneider, J.F., 1988, An automated, analytic method to determine shear-wave anisotropy, *Tectonophysics*, in press.

Silver, P.G. & Chan, W.W., 1988, Implications for continental structure and evolution from seismic anisotropy, *Nature*, **335**, 34-39.

Smith, M.L. & Dahlen, F.A., 1973, The azimuthal dependence of Love and Rayleigh wave propagation in a slightly anisotropic medium, *J.Geophys.Res.*, **78**, 3321-3333.

Smith, B.D. & Ward, S.H., 1974, On the computation of polarization ellipse parameters, *Geophysics*, **39**, 867-869.

Spears, D.A. & Caswell, S.A., 1986, Mineral matter coals: cleat minerals and their origin in some coals from the English midlands, *Internat.J.Coal Geol.*, **6**, 107-125.

Szab, T.L., 1984, A representative Poisson's ratio for coal, *Int.J. Rock Mech.Min.Sci. & Geomech.Abstr.*, **18**, 531-533.

Szwilski, A.B., 1984, Determination of the anisotropic elastic moduli of coal, *Int.J.Rock Mech.Min.Sci. & Geomech.Abstr.*, **21**, 3-12.

Tang, X.M. Cheng, C.H., 1988, Wave propagation in a fluid-filled fracture - an experimental study, *Geophys.Res.Lett.*, **15**, 1463-1466.

Taylor, D.B., 1987, *ANISEIS II Manual: Summary*, Macroc Ltd.

Taylor, D.B. & Crampin, S., 1978, Surface waves in anisotropic media: propagation in a homogeneous piezoelectric halfspace, *Proc.R.Soc. Lond.*, **364**, 161-179.

Terry, N.B., 1959, The dependence of the elastic behaviour of coal on the microcrack structure, *Quart.J.Fuel Sci.*, **38**, 125-146.

Thill, R.E., 1978, Acoustic cross-borehole apparatus for determining *in situ* elastic properties and structural integrity of rock masses, *Proc. 19th U.S Rock Mech.Symposium, 121-129.*

Thomsen, L., 1986, Weak elastic anisotropy, *Geophysics*, **51**, 1954-1966.

Toksöz, W.N., Johnston, D.H. & Timur, A., 1979, Attenuation of seismic waves in dry and saturated rocks: I, Laboratory measurements, *Geophysics*, **44**, 681-690.

Wang, Z. Nur, A., 1988, Monitoring the thermal recovery with the use of seismic method (in Chinese), *Oil Geophysical prospecting*, **24**, 144-154.

Waters, K.H., 1978, *Reflection seismology: a tool for energy exploration*, Wiley, New York.

Ward, C.R., 1984, *Coal geology and coal technology*, Black Scientific Publication.

White, J.E., 1983, *Underground sounding, application of seismic waves*, Elesvier, Amsterdam.

White, J.E., Martineau-Nicoletis, L. & Monash, C., 1983, Measured anisotropy in Pierre shale, *Geophysical Prospecting*, **31**, 709-725.

White, J.E. & Sengbush, R.L., 1963, Shear waves from explosive sources, *Geophysics*, **28**, 1001-1019.

Willis, H.A., Rethford, G.L. & Bielanski, E., 1986, Azimuthal anisotropy: occurrence and effect on shear-wave data quality, *56th ann.Internat.Mtg., Soc.Explor.Geophys., Expanded abstracts*, 479-481.

Winterstein, D.F., 1986, Anisotropy effects in *P*-wave and *SH*-wave stacking velocities contain information on lithology, *Geophysics*, **51**, 661-672.

Wong, J., Hurley, P. & West, G.F., 1983, Crosshole seismology and seismic imaging in crystalline rocks, *Geophys.Res.Lett.*, **10**, 686-689.

Wright, J., 1987, The effects of transverse isotropy on reflection amplitude versus offset, *Geophysics*, **52**, 564-567.

Xu,S. & King, M.S., 1988, Shear-wave birefringence and directional permeability in fractured rocks, *presented at the Cambore School of Mines Borehole Seismic Conference*, 1988.

Yardley, G. & Crampin, S., Extensive-dilatancy anisotropy: information contents of reflection surveys and VSPs, *Geophysical Prospecting*, submitted.

Young, G.B. & Braile, L.W., 1976, A computer program for the application of Zoeppritz's amplitude equations and Knott's energy equations, *Bull.Seism.Soc.Am.*, **66**, 1881-1885.

Enclosed in back cover:

Liu, E., Crampin, S. and Booth, D.C., 1989, Shear-wave splitting in cross-hole surveys: modelling, *Geophysics*, **54**, 57-65.

(Permission of a photocopy of the above paper has been granted by Michael Schoenberg, editor of Geophysics on 24th October 1989.)

GEOPHYSICS. VOL. 54. NO. 1 (JANUARY 1989); P. 57–65. 8 FIGS.

Shear-wave splitting in cross-hole surveys: Modeling

Enru Liu*, Stuart Crampin‡, and David C. Booth‡

ABSTRACT

Shear-wave splitting, diagnostic of some form of effective seismic anisotropy, is observed along almost all near-vertical raypaths through the crust. The splitting is caused by propagation through distributions of stress-aligned vertical parallel fluid-filled cracks, microcracks, and preferentially oriented pore space that exist in most crustal rocks. Shear waves have severe interactions with the free surface and may be seriously disturbed by the surface and by near-surface layers.

In principle, cross-hole surveys (CHSs) should be free of much of the near-surface interference and could be used for investigating shear waves at higher frequencies and greater resolution along shorter raypaths than is possible with reflection surveys and VSPs. Synthetic seismograms are examined to estimate the effects of vertical cracks on the behavior of shear waves in CHS experiments. The azimuth of the CHS section relative to the strike of the cracks is crucial to the amount of information about seismic anisotropy that can be extracted from such surveys. Interpretation of data from only a few boreholes located at azimuths chosen from other considerations is likely to be difficult and inconclusive. Application to interpreting acoustic events generated by hydraulic pumping is likely to be more successful.

INTRODUCTION

Shear-wave splitting has recently been observed in many shear-wave reflection surveys (surface-to-surface) in sedimentary basins across North America (Alford, 1986; Lynn and Thomsen, 1986; Willis et al., 1986), in shear-wave vertical seismic profiles (VSPs) (surface-to-subsurface) in sedimentary rocks (Johnston, 1986; Becker and Perelberg, 1986; Crampin et al., 1986) and in mixed metamorphic regimes (Majer et al., 1985; Leary and Li, 1986; Li et al., 1986), and above small earthquakes in many seismic areas around the world (reviewed by Crampin, 1987a). It appears that shear-wave splitting is characteristic of almost all shear-wave propagation in at least the upper 20 km of the crust. The splitting is principally caused by *extensive-dilatancy anisotropy*, or *EDA*: the distributions of stress-aligned parallel vertical fluid-filled microcracks, cracks, and preferentially oriented pore space which pervade most rocks in the crust (Crampin et al., 1984; Crampin, 1985a, 1987a). We shall refer to these fluid-filled inclusions as EDA cracks.

At present, all published records of shear-wave splitting involve shear waves generated, recorded, or both generated and recorded at the free surface. Shear waves, however, may suffer severe scattering at the free surface and by irregular topography within a wavelength or two of the recording site (Evans, 1984; Booth and Crampin, 1985). In principle, cross-hole surveys (CHSs), where both source and receiver are subsurface, should be free of many of the difficulties associated with long raypaths and near-surface interference when shear waves are either generated or recorded at the surface (Fehler and Pearson, 1984). CHSs should allow shear-wave splitting to be monitored along shorter raypaths at higher frequencies; the resulting shorter wavelengths would increase the resolution with which we could specify the effective anisotropy of EDA cracks within the rock mass. Such information might not be of direct use in discovering new reservoirs but should enable fractured beds and the structure of EDA cracks to be identified in known reservoirs and some of the parameters to be estimated so that the internal structure could be evaluated. The orientations of the in-situ stress-aligned microcracks are expected to be directly related to the orientations of hydraulic fractures and preferred directions of flow in hydrocarbon reservoirs.

The major surveying distinction is that the raypaths for VSPs and reflection surveys are usually within $\pm 45°$ of the vertical (often much closer to vertical), whereas the raypaths for CHSs are usually within $\pm 45°$ of the horizontal. This difference requires different field techniques and different schemes of analysis when surveying vertically oriented cracks. Below, we examine the behavior of shear waves propagating through cracked rock by analyzing shear-wave splitting on synthetic seismograms along horizontal and nearly horizontal raypaths.

Presented at the 57th Annual International Meeting, Society of Exploration Geophysicists. Manuscript received by the Editor December 14, 1987; revised manuscript received July 6, 1988.
*British Geological Survey and University of Edinburgh, Edinburgh, Scotland.
‡British Geological Survey, Murchison House, West Mains Road, Edinburgh EH9 3LA, Scotland, UK.

SHEAR WAVES IN CRACKED ROCK

EDA cracks are aligned by stress relationships similar to those orienting hydraulic fractures in intact rock (Crampin, 1987a). Consequently, where the vertical stress is greater than the minimum horizontal compression, which is usually the case below the immediate surface layers, fluid-filled microcracks are aligned nearly vertically and perpendicular to the direction of minimum compression (Crampin, 1987a). We consider cracked rock where the dimensions of the cracks are several times smaller than the wavelengths of the shear waves. This is little restriction, since the minimum wavelength of observed shear waves is usually measured in meters (often many tens of meters) and EDA cracks are expected to be principally microcracks with dimensions less than a few millimeters, or at most open fractures of one or two meters (Crampin, 1987a). Such aligned cracks are effectively anisotropic to seismic waves (Crampin, 1984). A rock containing parallel vertical cracks in an isotropic matrix is transversely isotropic with a horizontal axis of cylindrical symmetry perpendicular to the face of the cracks.

Shear waves propagating through aligned cracks generally split into two components with different vector displacements (polarizations) traveling at different velocities, where both velocities and displacements are fixed for the particular raypath through the cracked rock (Crampin, 1981, 1984). This phenomenon is known as shear-wave splitting or shear-wave birefringence. Figure 1 shows a schematic illustration of shear-wave splitting. A shear wave propagating nearly vertically through EDA cracks splits into two phases with polarizations parallel and perpendicular to the face of the cracks. The phase with polarization parallel to the cracks meets less acoustic impedance, travels faster, and is less attenuated than the phase with polarization normal to the crack face. The splitting has inserted into the three-dimensional (3-D) particle motion characteristic waveforms, which are preserved for any subsequent propagation through isotropic rock. Note that splitting does not occur when the incident shear wave is polarized parallel (or perpendicular) to the crack face, so that only the faster (or slower) phase is excited. When the slower shear wave is excited, additional motion orthogonal to the expected polarizations occurs, behavior which has been observed on many occasions. Wave propagation through rock containing such aligned cracks may be simulated by propagation through a homogeneous, purely elastic anisotropic solid that has the same patterns of velocity (and attenuation) as the cracked rock (Crampin, 1978).

Figure 2 shows the velocity variations of body waves propagating through distributions of thin parallel liquid-filled cracks with two crack densities. The crack densities are specified by $CD = Na^3/v$, where N is the number of cracks of radius a in volume v. Figure 2a shows the velocity variations for $CD = 0.1$, where the velocity anisotropy is large enough for the group and phase velocities to be clearly separated; Figure 2b shows the velocity variations for $CD = 0.04$, which is a crack density commonly found in the Earth in sedimentary (Crampin et al., 1986), metamorphic (Crampin and Booth, 1985), and igneous rocks (Roberts and Crampin, 1986). A crack density of 0.04 is equivalent to a crack with a diameter less than 0.7 in each unit cube. The three body waves are a quasi P-wave qP with nearly longitudinal displacement, and two quasi shear waves qSP and qSR polarized (P)arallel and

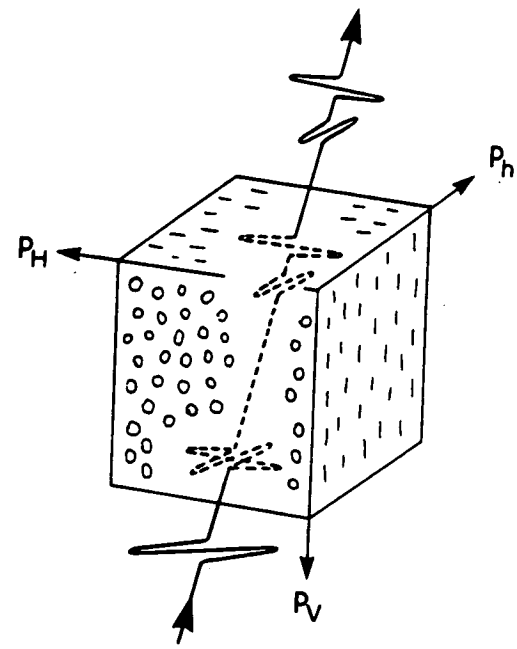

FIG. 1. Schematic illustration of shear-wave splitting in aligned EDA cracks in the crust. The cracks are aligned by the typical stress relationships in the subsurface crust. P_V, P_H, and P_h are the vertical, maximum, and minimum horizontal compressional stresses, respectively. P_V and P_H are at least two or three times greater than P_h.

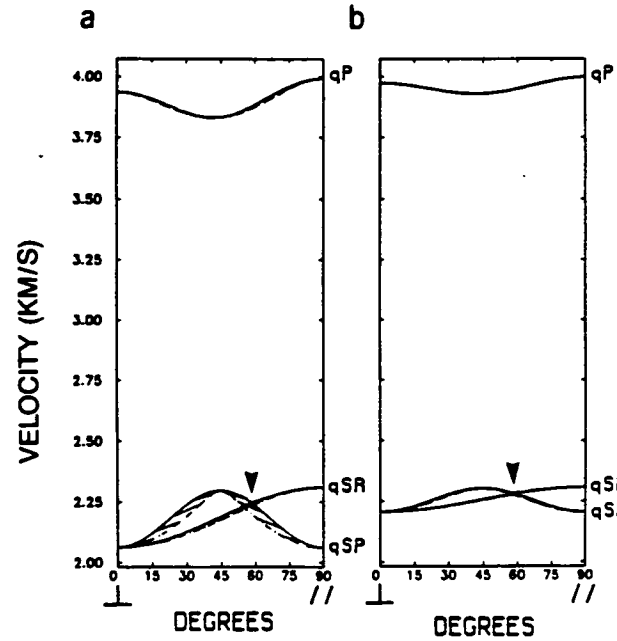

FIG. 2. Velocity variations of the three body waves [quasi P-wave qP and quasi S waves (parallel qSP and right angle qSR)] propagating through distributions of thin parallel liquid-filled cracks in an isotropic rock with velocities $V_P = 4.0$ and $V_S = 2.309$ km/s. The propagation directions range from perpendicular (0°) to parallel (90°) to the cracks. The solid lines are the phase velocities and broken lines are the group velocities which are joined to the equivalent phase velocity at every 10° of phase velocity. Arrowheads mark directions where the two velocity surfaces intersect in line singularities. The crack densities are (a) $CD = 0.1$; and (b) $CD = 0.04$.

at (R)ight angles, respectively, to the plane through the crack normals. Figure 2 was calculated using Hudson's (1980, 1981) theoretical formulations following Crampin (1984). Note that Hudson's formulations also model velocity and attenuation due to cracks for specified aspect ratios and both gaseous and viscous fluid contents. These refinements generally produce only second-order differences to the effects of thin liquid-filled cracks on shear-wave propagation; for simplicity, they are not considered in this paper.

The behavior of shear-wave splitting along nearly vertical raypaths can be conveniently specified by mapping the polarizations and delays between the split shear waves in equal-area projections (polar maps) over an upper or lower hemisphere of directions. Thus, Figure 3a shows a polar map of the horizontal strike of the polarization of the leading (faster) shear wave for a hemisphere of directions of plane waves propagating through parallel vertical liquid-filled cracks. The cracks strike east-west and have the same crack density as for Figure 2b. Figure 3a shows that the polarization of the leading shear wave is parallel to the strike of the cracks for a broad band of directions across the center of the projection, as suggested by Figure 1. The abrupt change in polarization on either side of the central band is caused by the intersection of the velocity curves of the two shear-wave polarizations at 60° from the crack normal (30° from the vertical) marked by an arrowhead in Figure 2. Figure 3b shows contoured delays between the split shear waves for a normalized path length. Such polar projections, although suitable for specifying the behavior of shear waves along raypaths within ±45° of the vertical, are not appropriate for describing the behavior of shear waves along more nearly horizontal raypaths expected in CHSs.

The remarkable feature of shear-wave splitting in parallel vertical cracks displayed in these polar projections is that the faster shear wave is polarized parallel to the strike of the vertical cracks for a broad band of directions across the center of the projection, including almost the whole of the shear-wave window (Booth and Crampin, 1985). This diagnostic feature is seen in almost all observations of shear waves along nearly vertical raypaths in the crust (Crampin, 1987a). The time delays between the split shear waves reach maximum values in the same broad band. We show that CHS experiments in similar crack distributions do not display such diagnostic phenomena.

THE BEHAVIOR OF SHEAR WAVES IN CYLINDRICAL PROJECTIONS

We display the behavior of shear-wave splitting in CHSs by cylindrical projections of the polarizations and delays over a full range of raypaths (360° of azimuth and dips from +90° downward to −90° upward). Figure 4 shows Plate Carée cylindrical projections (equal steps of latitude and longitude) of the particle polarizations of the leading split shear wave to subsurface geophones in (a) horizontal (R)adial and (T)ransverse and (b) (V)ertical and (T)ransverse cross-sections for $CD = 0.1$. Thus, Figure 4 shows the polarizations of the leading shear-wave arrivals radiating from a point source as seen by (a) horizontal instruments and (b) vertical and transverse

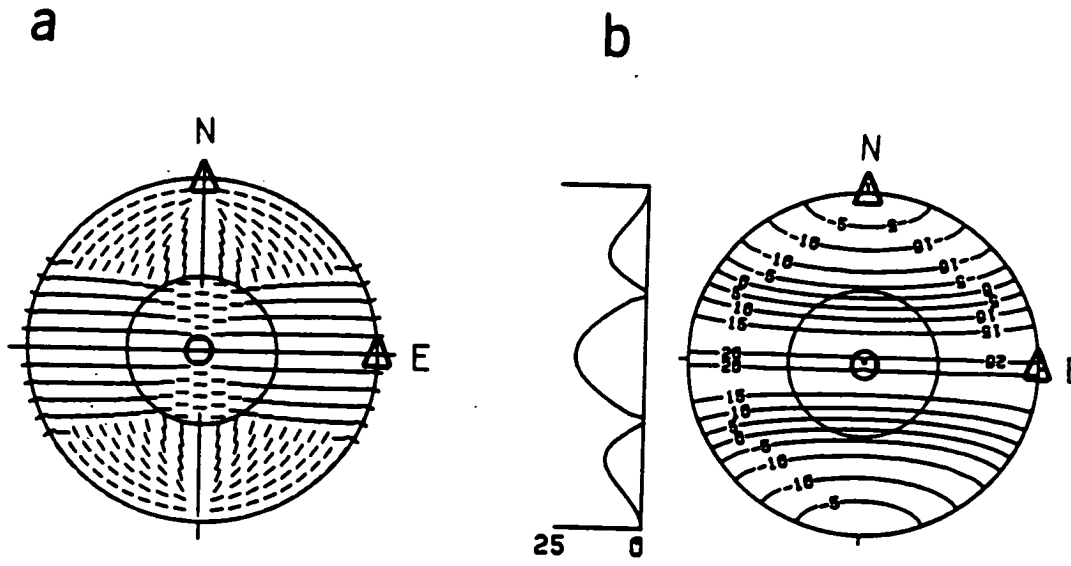

FIG. 3. Polar equal-area projections over a hemisphere of directions of the (a) polarizations in the (R)adial-(T)ransverse plane and (b) time delays of plane split shear waves propagating at the group (ray) velocity through the thin parallel liquid-filled cracks of Figure 2b ($CD = 0.04$) aligned vertically and striking east-west. The inner circles mark the shear-wave windows at the free surface at arcsin (V_S/V_P) = 35.26° and are marked as a scale. The bars in (a) are the horizontal components of the displacements of the leading (faster) split normalized shear wave, and the time delays between the split shear waves in (b) are contoured in milliseconds for a normalized pathlength of 1 km. A north-south section of the delays is to the left of the contour plot. Values for vertical directions are circled, and values for horizontal north and horizontal east are marked with triangles.

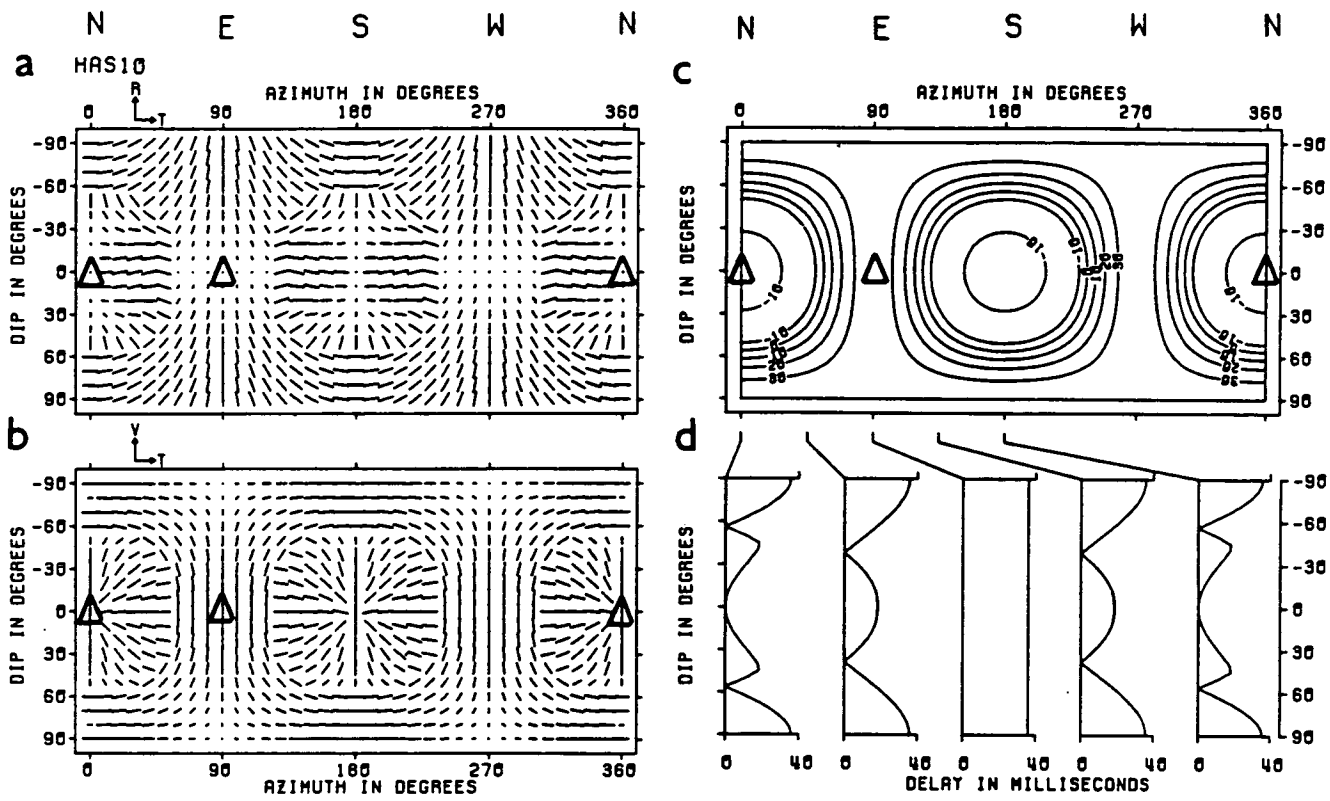

FIG. 4. Cylindrical projections of the polarizations and time delays of the split shear waves propagating through the thin parallel liquid-filled cracks of Figure 2a ($CD = 0.1$) aligned vertically and striking east-west, for the full range of raypath directions from upward ($-90°$) to downward ($90°$) to a geophone from azimuths of $0°$ to $360°$ east of north (clockwise from north). Polarizations of the leading split shear wave are projected onto (a) horizontal, marked (R)adial and (T)ransverse and (b) (V)ertical and (T)ransverse cross-sections for a fixed amplitude of displacement. The length of the symbol indicates the amplitude of a normalized leading split shear wave for the appropriate direction. Values for horizontal north and horizontal east are marked with triangles corresponding to the triangles in Figure 3. Values for vertical directions (circled in Figure 3) lie along the $-90°$ dip coordinates in Figure 4. Time delays in (c) are contoured in milliseconds for a normalized pathlength of 1 km, and the cross-sections of the contours in (d) are at the five specified azimuths in (c).

instruments on the walls of a cylinder. The cylinder has then been opened out. (Figure 4 is a cylindrical map of the radiation in all directions from a point source, whereas Figure 3 is a polar map of one hemisphere.) Figure 4c shows contours and Figure 4d, sections of delays between the split shear waves for plane waves propagating at the group (ray) velocity through the same parallel vertical liquid-filled cracks striking east-west with a crack density of $CD = 0.1$ as in Figure 2a.

Figure 5 shows the same variations as Figure 4 for the smaller crack density ($CD = 0.04$) in Figure 2b. The principal effect of the reduced crack density is the smaller time delays in Figures 5c and 5d. There are also minor differences between the shapes of the contours caused by the differences between the variations of group velocity seen in Figures 2a and 2b. Figure 6 shows polarizations and delays of shear waves propagating through the same cracks as Figure 5 but with the plane of the cracks dipping at 70°.

The variations with direction of the polarizations and delays in Figures 5 and 6 show distinctive patterns in which the orientations of the cracks and relative crack densities can be easily evaluated, given observations from a sufficient range of directions. However, the patterns lack any strongly diagnostic features, such as the pattern of parallel polarizations in the polar projections in Figure 3. In practice, CHS observations are usually confined to raypaths between a limited number of approximately vertical boreholes usually at relative azimuths which have been fixed by other considerations. Thus, in most CHS surveys the behavior of shear-wave splitting can be examined only along a few vertical stripes at arbitrary azimuths in cylindrical projections. The interpretation of the polarizations and delays in terms of crack orientations and crack densities from a few vertical stripes is possible in noise-free conditions for an appropriate choice of azimuths and range of dips, but the interpretation of a few vertical stripes at arbitrary azimuths, particularly where irregularities in the rock may cause scatter in the observations, is likely to be difficult and inconclusive.

SYNTHETIC SEISMOGRAMS FROM ADJACENT BOREHOLES

The principal effect of shear-wave splitting is to introduce subtle phase and amplitude changes into the different components of motion. These may be observed by meticulously comparing the relative displacements of parallel time series, or by easily recognizable patterns in polarization diagrams

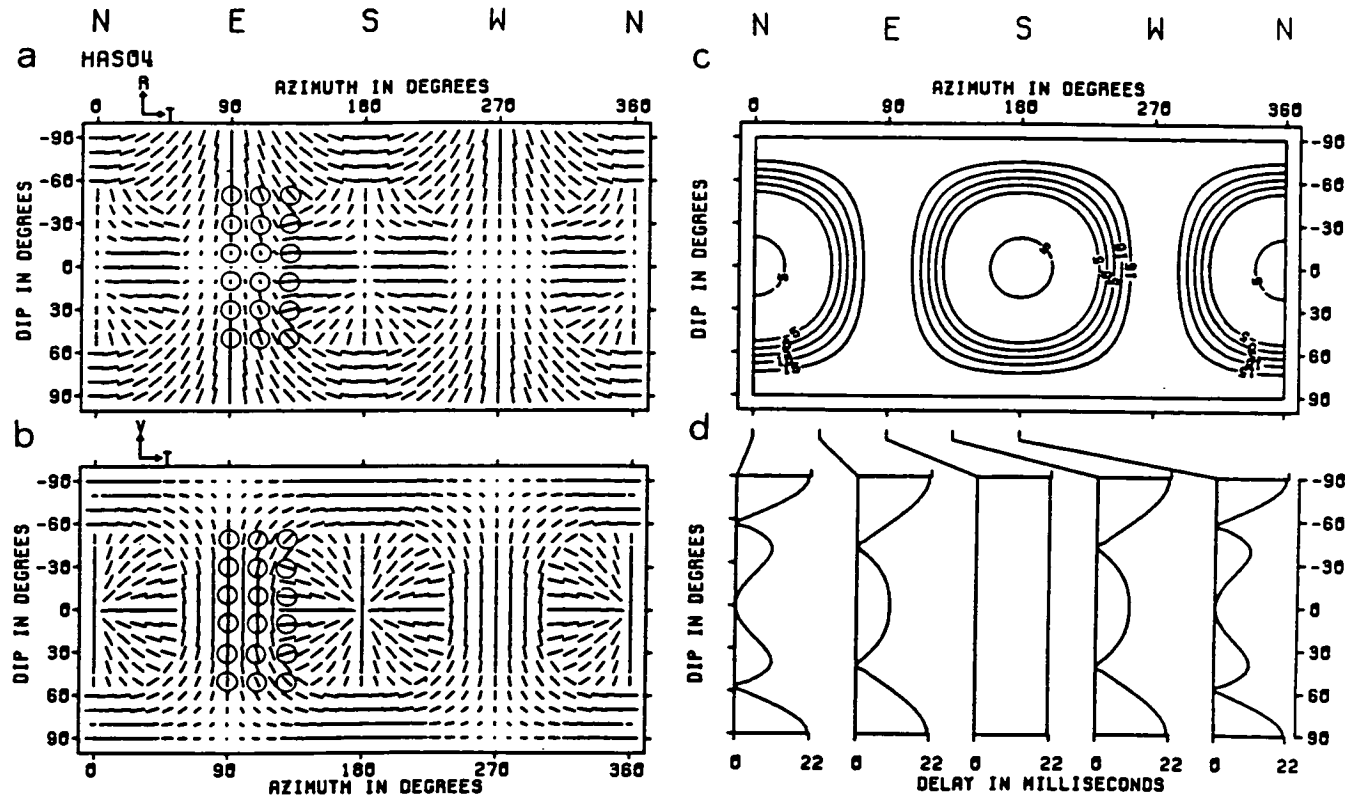

FIG. 5. Cylindrical projections for shear waves propagating through the thin parallel vertical cracks of Figure 2b for a crack density of $CD = 0.04$. The circles mark the directions of propagation of the synthetic seismograms in Figure 7. Notation as in Figure 4.

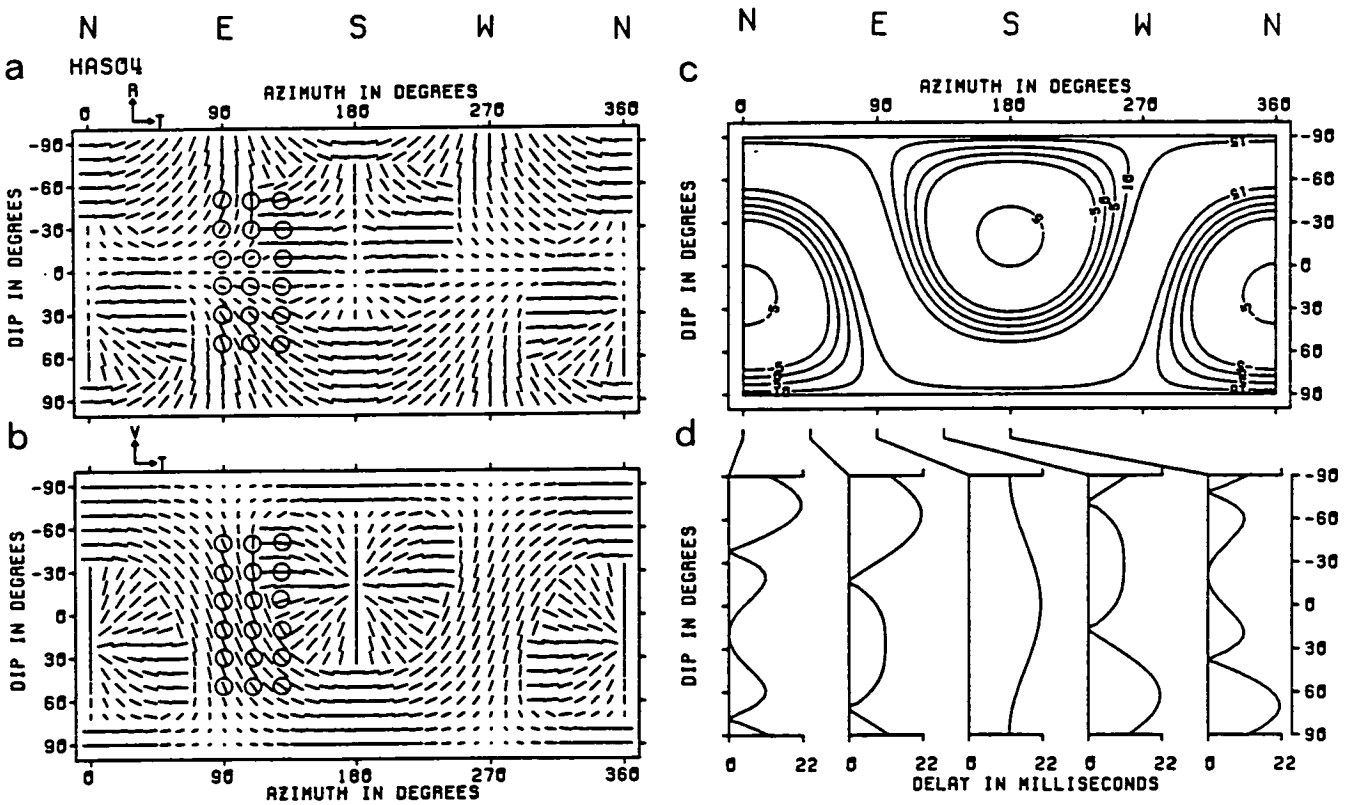

FIG. 6. Cylindrical projections for the same cracks as Figure 5 but dipping at 70° to the north. The circles mark the directions of propagation of the synthetic seismograms in Figure 8. Notation as in Figure 4.

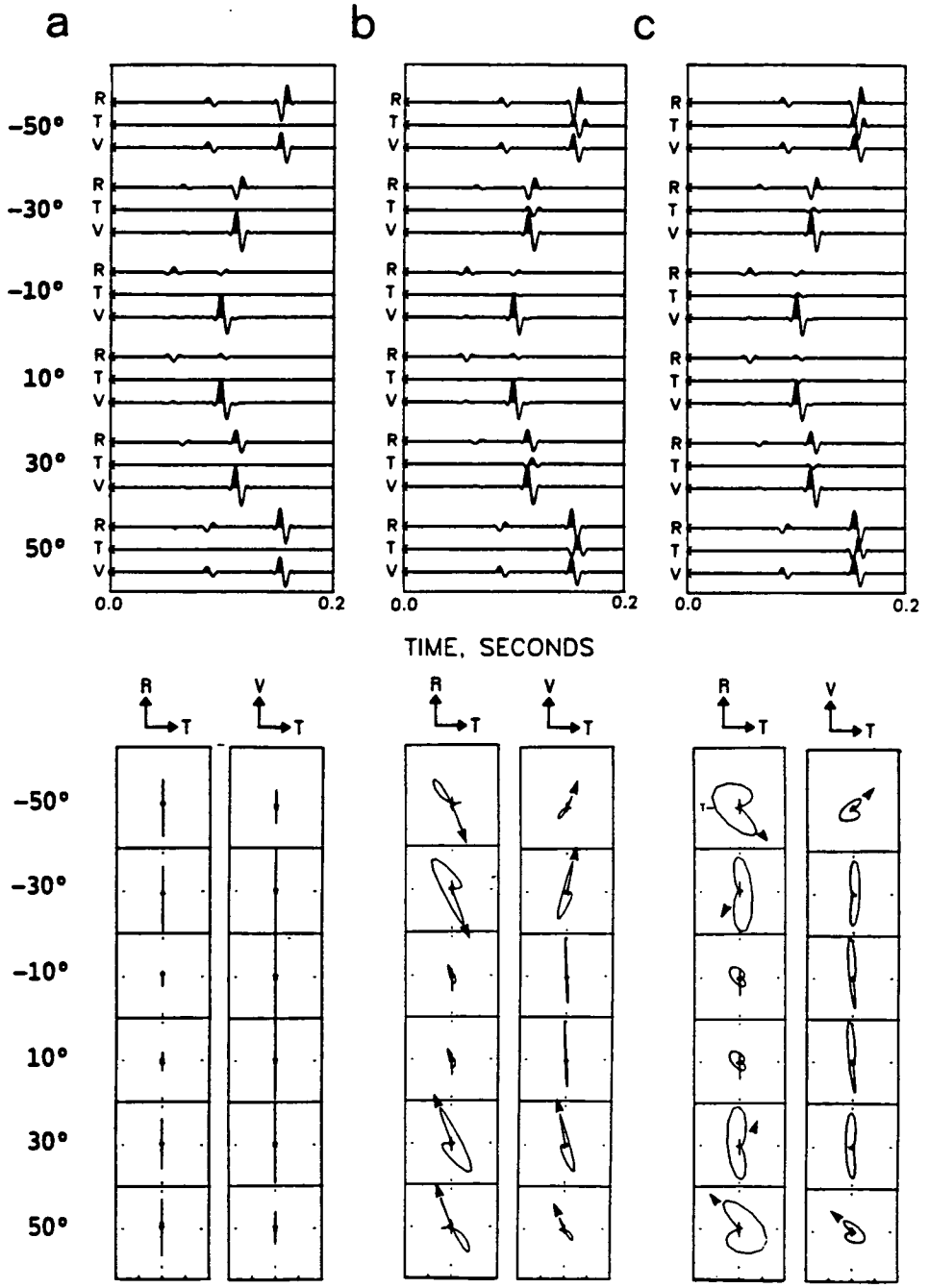

FIG. 7. Seismograms and polarization diagrams of shear waves through the same uniform space as Figure 5. Six three-component geophones in a vertical borehole are arranged at depths to give the raypaths identified in Figure 5 (dips of $-50°$ to $50°$) relative to vertical point forces (dominant frequency of 80 Hz) in vertical boreholes offset 200 m at azimuths of (a) N 90°E, (b) N 110°E, and (c) N 130°E. Upper diagrams are three-component synthetic seismograms aligned (V)ertical, and horizontal (R)adial and (T)ransverse to the azimuth of arrival. Lower diagrams are corresponding polarization diagrams for horizontal and vertical-transverse cross-sections of the particle displacements, and labeled (V)ertical, (R)adial, and (T)ransverse. Arrowheads indicate the initial directions of the first motions of the shear waves corresponding to the polarizations identified in Figure 5. Seismograms and polarization diagrams show the true relative amplitudes in each vertical column.

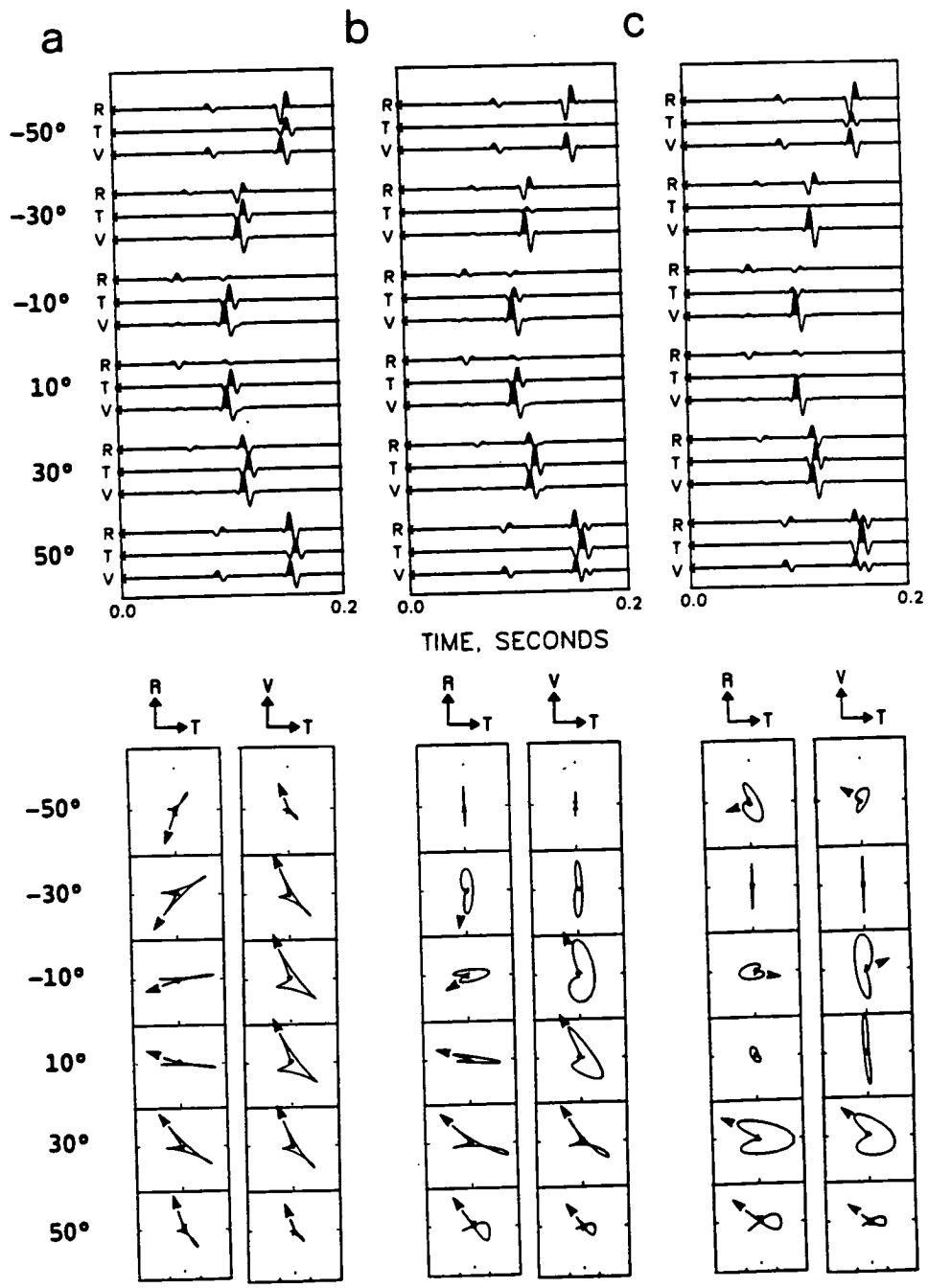

FIG. 8. Seismograms and polarization diagrams for synthetic seismograms through the same uniform space as Figure 6 (cracks dipping 70° to the north) along the marked raypaths. Geometry of paths and notation is the same as in Figure 7.

(Crampin, 1985b). (Polarization diagrams, also known as hodograms, are orthogonal cross-sections of the particle displacements for short time intervals along the wavetrains.) The patterns are characteristic of the particular phase and amplitude differences between the different shear-wave phases (Crampin, 1985b). Numerous observations suggest that the patterns are stable and can be identified even in the presence of considerable noise. Figure 7 shows synthetic seismograms and polarization diagrams for shear waves from a point source propagating through a uniform space containing the thin parallel vertical cracks of Figure 2b striking east-west, giving the same structure as used for Figure 5. The synthetic seismograms have been calculated by the ANISEIS program package. Synthetic seismograms are shown at six three-component geophones placed in a vertical borehole at depths to give relative dips of $-50°$, $-30°$, $-10°$, 10°, 30°, and 50° from vertical point forces, with offset from the borehole at 200 m, at azimuths N 90°E, N 110°E, and N 130°E corresponding to the circled arrivals in Figure 5. This geometry gives signals that can be compared directly with the polarizations and delays in Figure 5.

The arrowheads in the polarization diagrams in Figure 7, marking the initial directions of motion of the leading split shear waves radiating from a point source, correspond to the polarizations in the marked directions in Figure 5. The places where arrowheads are omitted are where there is no splitting either because the radiated shear wave is polarized very close to one of the fixed polarizations through the anisotropic rock so that the other split shear wave is not excited, as in Figure 7a, or because the time delays between the split shear waves are too small to cause significant splitting at the dominant period of the signal, as elsewhere in Figure 7.

Figure 8 shows synthetic seismograms and polarization diagrams for shear waves propagating through the same structure as Figure 7 but with cracks dipping 70° to the north, corresponding to the marked raypaths in the cylindrical projection in Figure 6. The notation is the same as in Figure 7.

The polarization diagrams in Figures 7 and 8 display patterns of particle displacements with the abrupt changes in direction typical of impulsive single-cycle shear waves propagating through cracked rock (Crampin, 1985b, 1987b). The polarizations of the initial motion of the leading split shear waves with curved wavefronts are very similar to the polarizations of the plane waves along the group velocity (ray) directions in Figures 5 and 6, respectively. The measured inconsistencies are less than 3° and are caused by the different behavior of group velocity for curved and plane wavefronts in anisotropic rocks. (The point source is about seven wavelengths from the geophone borehole.) A plane wave travels at the phase velocity and the two polarizations of the shear waves are strictly orthogonal, whereas a ray from a point source (with a curved wavefront) travels at the group velocity and, in general, will have different polarizations from the plane wave at the same angle of incidence. Consequently, for a point source the two split shear waves will not be strictly orthogonal.

DISCUSSION

There are at least four parameters of EDA cracks of interest to the reservoir engineer that can be extracted from seismic observations of shear-wave splitting. These are the crack geometry, particularly the strike and dip of the cracks, the aspect ratio of the cracks, and the crack dimensions.

The strike of parallel cracks

The polarization of the leading split shear wave along nearly vertical raypaths gives estimates of the strike of the nearly vertical parallel cracks. This type of polarization is observed in many different circumstances in the Earth (see the review by Crampin, 1987a). There is no such distinctive behavior in CHSs. The strike could be identified by the symmetrical behavior at a range of azimuths spanning the direction of strike, but, except by chance, observations between suitable boreholes are unlikely to be available. However, determination of strike might be possible for a range of sources from a horizontal borehole or tunnel with three-component geophones at some distance away from the line of the tunnel.

The dip of parallel cracks

Dip is difficult to identify from nearly vertical raypaths unless observations are available from a range of azimuths and angles of incidence in an appropriate range of directions. CHSs display the effects of dip as asymmetries in the polarization patterns between upward and downward propagating waves, as in Figure 8, where the cracks dip at 70°, in contrast to Figure 7, where the cracks are vertical. At azimuths parallel to the strike of the cracks, as in Figure 8, the dip can be read directly from the dip of the polarization of the leading shear wave.

The aspect ratio of the cracks

Changes in aspect ratio change the directions where the two split shear waves intersect (see Figure 2 in Crampin, 1987b) and change the position of the line of transition between the nearly orthogonal polarizations in polar and cylindrical projections in Figures 3 to 6. A larger aspect ratio increases the width of the broad band of parallel polarizations in polar projections and increases the diameter of the circular features in the cylindrical projections. Such changes in aspect ratio have been identified along nearly vertical raypaths in seismic gaps where the stress is changing before earthquakes (Peacock et al., 1988). It does not seem likely that the positions of these transition zones can be easily identified in CHSs.

Crack dimensions

The dimensions of EDA cracks may range from submicrometer to a few millimeters in intact rock and up to a few meters in fractured beds (Crampin, 1987a). The elastic constants, and hence the velocity variations and shear-wave splitting, are more sensitive to the dimensionless crack density Na^3/v than the crack dimensions (see the theoretical formulations of Hudson, 1980, 1981, or Crampin, 1984). It is likely that attenuation will be more sensitive than velocity variations to the dimensions of the cracks. If the cause of attenuation in cracked rock can be established, measurement of attenuation is likely to be a particularly valuable technique, because with a known source polarization, the relative attenuations of

the split shear waves can be compared directly because they will have propagated along very similar raypaths.

Note that the interpretation in this paper is based on the effects of a single parallel vertical crack set. We believe assuming a single crack set is justified. There are now observations of shear-wave splitting from over 50 different locations (see Crampin, 1987a). Relatively few of the data show scatter and are difficult to interpret, and the majority show clear patterns of 3-D variation; wherever a pattern can be seen, it suggests vertical cracks striking perpendicular to the minimum horizontal stress, as illustrated in Figure 1. To our knowledge, no shear-wave polarizations anywhere suggest other than nearly parallel vertical cracks. The physical reasons for this have been discussed elsewhere (Crampin, 1987a).

CONCLUSIONS

The theoretical and numerical examples presented here suggest that information about the internal structure causing shear-wave splitting is unlikely to be extracted easily from CHS experiments unless sufficient observations can be made at a range of azimuths. A large number of boreholes at suitable azimuths or a horizontal borehole are not expected to be commonly available. Note, however, that the dip of near-vertical parallel cracks can be estimated from polarization diagrams at a specific range of CHS azimuths.

As always with shear-wave splitting observed in the subsurface (away from the severe interactions with the free surface), detailed interpretation is possible with synthetic seismograms. However, this type of interpretation will be more difficult for CHSs than for VSPs, because CHSs appear to give less easily recognized information about the parameters of the cracks; and there will be less control over the initial parameters for the modeling procedure.

Note that we have only modeled synthetic seismograms from borehole shear-wave sources that radiate *SV* waves, reflecting current technology. A source of *SH* waves would produce different patterns of polarization, for example, by exciting the second slower split shear wave with orthogonal polarizations in Figure 7a; but the conclusions of this paper are unlikely to be changed significantly.

Shear-wave CHS surveys will be expensive and consequently rarely attempted. We suggest that the major applications of the results of this paper are likely to be in interpreting acoustic events induced by hydraulic pumping. Interpreting acoustic events recorded by down-well three-component geophones should yield unique information about the initial stress distribution and the developing system of cracks.

ACKNOWLEDGMENTS

We thank Applied Geophysical Software Inc. and Macroc Ltd for approval to use the ANISEIS package for plotting Figures 2 and 3 and for calculating the synthetic seismograms. We also thank Franklyn Levin for his comments on the manuscript. This work was supported by the Natural Environment Research Council with some indirect support from U.S. Geological Survey contract no. 14-08-0001-G1380. The sponsorship of one of the authors (EL) by the British Council and the Chinese Government is gratefully acknowledged. The paper is published with the approval of the Director of the British Geological Survey (NERC).

REFERENCES

Alford, R. M., 1986, Shear data in the presence of azimuthal anisotropy: Dilley, Texas: 56th Ann. Internat. Mtg., Soc. Explor. Geophys., Expanded Abstracts, 476–479.

Becker, D. F., and Perelberg, A. I., 1986, Seismic detection of subsurface fractures: 56th Ann. Internat. Mtg., Soc. Explor. Geophys., Expanded Abstracts, 466–468.

Booth, D. C., and Crampin, S., 1985, Shear-wave polarizations on a curved wavefront at an isotropic free-surface: Geophys. J. Roy. Astr. Soc., **83**, 31–45.

Crampin, S., 1978, Seismic wave propagation through a cracked solid: polarization as a possible dilatancy diagnostic: Geophys. J. Roy. Astr. Soc., **53**, 467–496.

——— 1981, A review of wave motion in anisotropic and cracked elastic-media: Wave Motion, **3**, 343–391.

——— 1984, Effective elastic constants for wave propagation through cracked solids, *in* Crampin, S., Hipkin, R. G., and Chesnokov, E. M., Eds., Proc. of the First Internat. Workshop on Seismic Anisotropy: Geophys. J. Roy. Astr. Soc., **76**, 135–145.

——— 1985a, Evidence for aligned cracks in the earth's crust: First Break, **3**, no. 3, 12–15.

——— 1985b, Evaluation of anisotropy by shear-wave splitting: Geophysics, **50**, 142–152.

——— 1987a, Geological and industrial implications of extensive-dilatancy anisotropy: Nature, **328**, 491–496.

——— 1987b, Crack porosity and alignment from shear-wave VSPs, *in* Danbom, S. H., and Domenico, S. N., Eds., Shear-wave exploration: Soc. Explor. Geophys., 227–251.

Crampin, S., and Booth, D. C., 1985, Shear-wave polarizations near the North Anatolian Fault—II. Interpretation in terms of crack-induced anisotropy: Geophys. J. Roy. Astr. Soc., **83**, 75–92.

Crampin, S., Bush, I., Naville, C., and Taylor, D. B., 1986, Estimating the internal structure of reservoirs with shear-wave VSPs: The Leading Edge, **5**, no. 11, 35–39.

Crampin, S., Evans, R., and Atkinson, B. K., 1984, Earthquake prediction: a new physical basis, *in* Crampin, S., Hipkin, R. G., and Chesnokov, E. M., Eds., Proc. of the First Internat. Workshop on Seismic Anisotropy: Geophys. J. Roy. Astr. Soc., **76**, 147–156.

Evans, R., 1984, Effects of the free surface on shear wavetrains: *in* Crampin, S., Hipkin, R. G., and Chesnokov, E. M., Eds., Proc. of the First Internat. Workshop on Seismic Anisotropy: Geophys. J. Roy. Astr. Soc., **76**, 165–172.

Fehler, M., and Pearson, C., 1984, Cross-hole seismic survey: Application for studying subsurface fracture systems at a hot dry rock geothermal site: Geophysics, **49**, 37–45.

Hudson, J. A., 1980, Overall properties of a cracked solid: Math. Proc. Cambridge Phil. Soc., **88**, 371–384.

——— 1981, Wave speeds and attenuation of elastic waves in material containing cracks: Geophys. J. Roy. Astr. Soc., **64**, 133–150.

Johnston, D. H., 1986, VSP detection of fracture-induced velocity anisotropy: 56th Ann. Internat. Mtg., Soc. Explor. Geophys., Expanded Abstracts, 464–466.

Leary, P. C., and Li, Y.-G., 1986, VSP fracture study of Mojave desert hydrofracture borehole: EOS, **67**, 1116 (abstract).

Li, Y.-G., Leary, P. C., and Aki, K., 1986, Seismic ray tracing for VSP observations in homogeneous fractured rock at Oroville: EOS, **67**, 1117 (abstract).

Lynn, H. B., and Thomsen, L. A., 1986, Reflection shear-wave data along the principal axes of azimuthal anisotropy: 56th Ann. Internat. Mtg., Soc. Explor. Geophys., Expanded Abstracts, 473–476.

Majer, E. L., McEvilly, T. V., and Eastwood, F. S., 1985, Fracture mapping using shear-wave profiling: EOS, **66**, 950 (abstract).

Peacock, S., Crampin, S., Booth, D. C., and Fletcher, J. B., 1988, Shear wave splitting in the Anza seismic gap, Southern California: temporal variations as possible precursors: J. Geophys. Res., **93**, 3339–3356.

Roberts, G., and Crampin, S., 1986, Shear-wave polarizations in a Hot-Dry-Rock geothermal reservoir: anisotropic effects of fractures: Internat. J. Rock Mech. Min. Sci., **23**, 291–302.

Willis, H. A., Rethford, G. L., and Bielanski, E., 1986, Azimuthal anisotropy: occurrence and effect on shear-wave data quality: 56th Ann. Internat. Mtg., Soc. Explor. Geophys., Expanded Abstracts, 479–481.